IN-SITU AND COMPUTATIONAL STUDIES OF ETHANOL ELECTROOXIDATION REACTION: RATIONAL CATALYST DESIGN STRATEGIES

Evans Angwenyi Monyoncho

A thesis submitted to the

Faculty of Graduate and Postdoctoral Studies

in partial fulfilment of the requirements for the

Doctor of Philosophy in Chemistry

Department of Chemistry and Biomolecular Sciences

Faculties of Science and Engineering

University of Ottawa

Table of Contents

List of Tables

List of Figures

Legend

AA-DEFCs		Alkaline-acid direct ethanol fuel cells
AFCs		Alkaline fuel cell
AEM		Anion-exchange membranes
AEMFCs		Anion-exchange membrane fuel cells
ALD		Atomic Layer Deposition
ADC		Analog to Digital Converter
ATR-IR		Attenuated total reflection infrared
d		Average particle size (diameter) (nm)
CA		Chronoamperometry
CaF_2		Calcium fluoride
CV		Cyclic voltammetry
DAAFCs		Direct alcohol alkaline fuel cells
DAFCs		Direct alcohol fuel cells
DEFCs		Direct ethanol fuel cells
DE-SOFCs		Direct ethanol solid oxide fuel cells
DFT		Density functional theory
DMFCs		Direct methanol fuel cells
DRIFT		Diffuse reflectance infrared Fourier transform
EOR		Ethanol oxidation reaction
ECSA		Electrochemical active surface area
EMIRS		Electrochemically modulated infrared spectroscopy
FTIR		Fourier Transform infrared
FWHM		Full-width at half maximum
GC		Glassy carbon
Hg/HgO	or	Mercury-mercury oxide reference electrode
MMO		
H.P.		High Pass filter
I		Current
IR		Infrared
k		Rate constant
KOH		Potassium hydroxide
LIA		Lock-in amplifier
LN-MCT		Nitrogen cooled mercury cadmium telluride detector
L.P.		Low pass filter
MPD		Maximum power density
MEA		Membrane electrode assembly
MIR		Mid-infrared
MSE		Mercury-mercurous sulphate reference electrode
MSEFS		Mean squared electric field strength
$NaBH_4$		Sodium borohydride salt
NBs		Nano-bars
NEB		Nudged-elastic band
NRs		Nano-rods
NPs		Nanoparticles

OCV	Open circuit voltage
PAW	Projected augmented wave
PBE	Perdew, Burke, and Erzenhorf functional
$Pd(DBA)_2$	Bis(dibenzylidene acetone)palladium(0)
PEM-IRRAS	Photoelastic-modulation infrared reflection-absorption spectroscopy
PEMFCs	Proton exchange membrane fuel cells
PMA – 50 XL	Photoelastic modulator accessory box/chamber
R	Universal gas constant (8.314 $J \cdot mol^{-1} \cdot K^{-1}$)
$R.F._{(bulk)}$	Reflectance factor for bulk species
$R.F._{(surf)}$	Reflectance factor for surface species
RHE	Reversible hydrogen electrode
SEIRAS	Surface-enhanced infrared reflection absorption spectroscopy
SERS	Surface-enhanced Raman spectroscopy
SFG	Sum frequency generation
SPAIR	Single potential alteration infrared
SSD	Synchronous sampling demodulator
STEM	Scanning Transmission Electron Microscopy
SNIFTIR	subtractively normalized interfacial Fourier transform infrared spectroscopy
T	Temperature
TEM	Transmission electron microscopy
TS	Transition states
VASP	Vienna *Ab-initio* Simulation Package
WE	Working electrode
XPS	X-ray photoelectron spectroscopy
XRD	X-ray diffraction
θ	Bragg angle (radians)
λ	X-ray wavelength (m)

Abstract

Fuel cells represent a promising technology for clean power generation because they convert chemical energy (fuel) into electrical energy with high efficiency and low-to-none emission of pollutants.[1–4] Direct ethanol fuel cells (DEFCs) have several advantages compared to the most studied hydrogen and methanol fuel cells. First and foremost, ethanol is a non-toxic liquid, which lowers the investment of handling facilities because the current infrastructure for gasoline can be largely used.[5,6] Second, ethanol can be conveniently produced from biomass, hence is carbon neutral which mitigates increasing atmospheric CO_2. Last but not least, if completely oxidized to CO_2, ethanol has a higher energy density than methanol since it can deliver 12 electrons per molecule. The almost exclusive oxidation to acetic acid overshadows the attractiveness of DEFCs considerably, as the energy density is divided by 3. The standard potential of acetic acid formation indicates that a reaction path including acetic acid, leads to inevitable potential losses of about 0.4 V (difference between ideal potential for CO_2 and acetic acid "production").[7]

The development of alkaline DEFCs had also been hampered by the lack of stable and efficient anion exchange membranes. Fortunately, this challenge has been well tackled in recent years,[8,9] making the development of alkaline fuel cells (AFCs) which are of particular technological interest due to their simple designs and ability to operate at low temperatures (25-100 °C). In alkaline conditions, the kinetic of both the cathodic oxygen reduction and the anodic ethanol oxidation is facilitated. Furthermore, the expensive Pt catalyst can be replaced by the lower-cost and more active transition metals such as Pd.[10–14]

The main objectives of this project are: i) to provide detailed fundamental understanding of ethanol oxidation reaction on transition metal surfaces in alkaline media, ii) to propose the best rational catalyst design strategies to cleave the C–C bond during ethanol electrooxidation. To

achieve these goals two methodologies are used, i.e., in-situ identification of ethanol electrooxidation products using polarization modulation infrared reflection absorption spectroscopy (PM-IRRAS) and mechanistic investigation using computational studies in the framework of density functional theory (DFT). The PM-IRRAS technique was advanced in this project to the level of distinguishing electrooxidation products at the surface of the nanoparticles (electrode) and in the bulk-phase of the electrolyte. This new PM-IRRAS utility makes it possible to detect molecules such as CO_2 which desorbs from the catalyst surface as soon as they are formed. The DFT insights in this project, provides an explanation as to why it is difficult to break the C–C bond in ethanol and is used for screening the top candidate metals for further studies.

Resume

Les piles à combustible représentent une technologie prometteuse pour la production d'énergie propre puisqu'elles convertissent l'énergie chimique (carburant) en énergie électrique avec un rendement élevé et des émissions de polluants faibles à nulles. Les cellules à combustible à éthanol directes (DEFC) La plupart des piles à combustible hydrogène et méthanol étudiées. D'abord et avant tout, l'éthanol est un liquide non toxique, ce qui réduit l'investissement des installations de manutention parce que l'infrastructure actuelle de l'essence peut être largement utilisée. Deuxièmement, l'éthanol peut être commodément produit à partir de biomasse, donc neutre en carbone qui atténue l'augmentation CO_2 atmosphérique. Enfin, si complètement oxydé en CO_2, l'éthanol a une densité d'énergie plus élevée que le méthanol puisqu'il peut livrer 12 électrons par molécule. L'oxydation presque exclusive de l'acide acétique masque l'attractivité des DEFC considérablement, puisque la densité d'énergie est divisée par 3. Le potentiel standard de formation d'acide acétique indique qu'une voie de réaction comprenant de l'acide acétique conduit à des pertes potentielles inévitables d'environ 0,4 V (différence Entre le potentiel idéal de production de CO_2 et d'acide acétique).

Le développement des DEFC alcalines a également été entravé par l'absence de membranes échangeuses d'anions stables et efficaces. Ce défi a heureusement été relevé ces dernières années, ce qui rend le développement de piles à combustible alcalines (AFC) qui présentent un intérêt technologique particulier en raison de leur conception simple et de leur aptitude à fonctionner à basse température (25-100°C). Dans des conditions alcalines, la cinétique de la réduction de l'oxygène cathodique et de l'oxydation de l'éthanol anodique est facilitée. En outre, le catalyseur Pt onéreux peut être remplacé par des métaux de transition à moindre coût et plus actifs tels que Pd.

Les principaux objectifs de ce projet sont les suivants: i) fournir une compréhension fondamentale détaillée de la réaction d'oxydation de l'éthanol sur les surfaces de métaux de transition en milieu alcalin, ii) proposer les meilleures stratégies de conception rationnelle des catalyseurs pour cliver la liaison C-C pendant l'électrooxydation de l'éthanol. Pour atteindre ces objectifs, deux méthodologies sont utilisées, c'est-à-dire l'identification in situ de produits d'électro-oxydation à l'éthanol utilisant la spectroscopie d'absorption par réflexion infrarouge à modulation de polarisation (PM-IRRAS) et l'étude mécanique à l'aide d'études informatiques dans le cadre de la théorie de la densité fonctionnelle. La technique PM-IRRAS a été avancée dans ce projet au niveau de la distinction des produits d'électrooxydation à la surface des nanoparticules (électrode) et dans la phase de masse de l'électrolyte. Ce nouvel utilitaire PM-IRRAS permet de détecter des molécules telles que le CO_2 qui se désorbe de la surface du catalyseur dès leur formation. Les perspectives de la DFT dans ce projet expliquent pourquoi il est difficile de rompre la liaison C-C dans l'éthanol et est utilisé pour le dépistage des meilleurs métaux candidats pour des études ultérieures.

Statement of contributions and collaborations

I hereby confirm that I am the sole author of this thesis. I planned and executed experimental studies, computational calculations, and the subsequent data analysis and presentation under the guidance of my supervisors Prof. Tom Woo and Prof. Elena Baranova. I am the first author of all the chapters presented in this thesis which have been published or submitted for publication elsewhere. However, there were invaluable contributions from various collaborators to different sections of the project as highlighted below.

In chapter 4, Prof. Vlad Zamlynny helped with theoretical simulation for the spectroelectrochemical system shown in Figure 4.7 and I used the software he developed to optimize experimental conditions for the PM-IRRAS. These theoretical simulation insights were critical in understanding and validating the conclusions reported in chapter 4. Dr. Spyridon Ntais helped with XPS data collection and analysis reported in chapters 6 and 7. In chapter 6, Felipo Soares (a summer student from Brazil) helped me during the synthesis and characterization of the Pd-Ru nanoparticles.

In chapter 7, the nanoparticles and their physical characterization was done by a Nicolas Brazeau (Masters Student) who worked in collaboration with Jhing-Jhou Wu and Prof. Chia-Liang Sun from Taiwan. I reproduced the electrochemical experiments, carried out PM-IRRAS and wrote the manuscript.

In chapter 8 and 9, Dr. Stephan Steinmann helped with transition state energy calculations (Figure 8.7 and 9.8b) and sections of computational methodologies. Dr. Carine Michel was instrumental in revising the reaction mechanism schematic shown in Figure 8.7 and handled the publication correspondences for chapter 8. Prof. Philippe Sautet and my supervisors helped and guided with insightful discussions.

Acknowledgments

The success of this project has been made possible via the effort of many individuals both directly and indirectly. Herein, I will mention some of them starting with my supervisors Prof. Tom Woo and Prof. Elena Baranova. I thank them for accepting me into their research groups and for their continued support and guidance throughout the period of the project. The project gave me a great opportunity to learn, travel, and collaborate with many individuals within and a broad Canada.

Many thanks to my collaboration team; computational chemists (Prof. Philippe Sautet, Dr. Carine Michel, and Dr. Stephan Steinmann) from ENS Lyon, France, and spectroscopist Prof. Vlad Zamlynny from Acadia University, Nova Scotia. It was an honour to visit ENS Lyon as part of my project. I was also glad to host Prof. Vlad Zamlynny at the University of Ottawa and welcomed his generous contribution of parts of his equipment for my project. Special thank you to Dr. Spyridon Ntais for his contribution with XPS experiments and data analysis. We had a great opportunity to work together at Canadian Light Source in Saskatoon in collaboration with Dr. Xiaoyu Cui. I thank Dr. Martin Couillard from National Research Council for his help with HAADF-STEM micrographs and for giving me opportunity to visit their facility here in Ottawa. I greatly thank these collaborators for the wonderful discussions we had throughout the project which are likely to continue for a while after this project.

Special thank you to Louis Tremblay and his Support staff (Franco Ziroldo and Gerard Nina) at the Department of Chemical and Biological Engineering. All the staff were very supportive and Louis provided a critical support in the machining of the spectroelectrochemical cell.

I also would like to thank my fellow research colleagues from Prof. Tom Woo's and Prof. Elena Baranova's research groups. From Prof. Woo's group, I would like to thank Dr. Tom

Daff, Dr. Eugene Kadantev, and Dr. Carlos Campana for their technical support in theoretical work. From Prof. Baranova's group, I would to thank, Dr. Anis Allagui, Dr. Rima Isaif, and Dr. Holly Dole for their support at the beginning of my project.

Many thanks to my Thesis and Examination Committee Members, Prof. Javier Giorgi, Prof. Maxim Berezovski, Prof. Edward Lai (Carleton), and Prof. Daniel Guay (INRS). I thank them for accepting to be part of my supervisory team and for their invaluable feedback on the project.

Nothing would have been possible without the financial support from many agencies. I thank Natural Sciences and Engineering Research Council (NSERC) of Canada for the graduate scholarship. I thank Canadian Light Source for the travel grant to their facility, Canada Foundation for Innovation (CFI) for computing resources and the spectrometer. Compute Canada (Sharcnet) provided additional computing resources. I thank the University of Ottawa, CNRS, and ENS Lyon for the travel grants to France provided in the framework of the Associated International Laboratory FUNCAT "Fundamental catalysis for green chemistry: From well-defined active sites to mechanistic explorations." I also acknowledge the literature and other support services provided by the Library at the University of Ottawa.

I thank my family for the support and love. My late father Christopher and my mother Zipporah for the hard work to send me to school. Many thanks to my brothers, sisters, and my Kids (Rebecca and Jordan) who always put a smile in my face. Above all, I thank God for the life and opportunity to pursue my studies to this level regardless of the many challenges along the way.

Chapter 1: Introduction

1.1 **Background and Motivation**

Fuel cells represent a promising technology for clean power generation because they convert chemical energy (fuel) into electrical energy with high efficiency and low-to-none emission of pollutants.[1–4] Among the various fuel cell technologies available, Direct Ethanol Fuel Cells (DEFCs) are more attractive compared to the mostly studied hydrogen and methanol fuel cells for a number of reasons:

i) Ethanol is a non-toxic liquid, which would mitigate high investment in storage and handling facilities because the current infrastructure for gasoline can be used,[5,6]

ii) Ethanol can be conveniently produced from biomass, hence is carbon neutral which mitigates increasing atmospheric CO_2,

iii) If completely oxidized to CO_2, ethanol has a higher energy density and efficiency than methanol.

There are a number of challenges that must be overcome before the commercialization of DEFCs. These challenges include; the lack of efficient catalysts which can selectively cleave the C–C bond during ethanol electrooxidation, lack of stable membranes and conducting porous ionomers, the issues of water and ethanol transport management, proper regulation of carbon dioxide, and the selection of the best electrolyte for the reaction. Chief among these challenges is the design of selective catalysts for the cleavage of the C–C bond. The success in this challenge will lead to an increase of the overall DEFCs efficiency from the current 14% to 43% hence making DEFCs the strongest competitor to hydrogen fuels cells which have an overall efficiency of 54%. Designing catalysts to break the C–C bond is a fundamental material question while the other challenges are more engineering in nature, which means they will become more attractive for research if the fundamental materials design question is resolved.

1.2 Objectives

The two main objectives of this project are: i) to provide detailed fundamental understanding of ethanol oxidation reaction on transition metal surfaces in alkaline media, ii) to propose strategies for the rational design of catalyst to cleave the C–C bond during ethanol electrooxidation and suggest the best candidate transition metals for consideration. To achieve these objectives, two methodologies are used:

a) Experimental *in-situ* identification of ethanol electrooxidation products using polarization modulation infrared reflection absorption spectroscopy (PM-IRRAS) and
b) Computational studies in the framework of density functional theory (DFT) for mechanistic insights of the reaction.

At the beginning of the project there were two parallel studies which were later merged together in the final stages. In the experimental studies, there was the need to develop the in-house spectroelectrochemical cell since they are not commercially available. Palladium (Pd) and Ruthenium (Ru) metals were selected based on the literature review in which they were revealed as the top candidates, where Pd acts as the main catalyst while Ru is used as the promoter. For this reason, detailed mechanistic computations were conducted on Pd then extended to other fcc and hcp transition metals in an effort to screen for the best candidate.

1.3 Thesis Structure

This section provides the link between the various chapters presented in this thesis and how together they help in achieving the objectives of the project. Chapter 2 is a comprehensive literature review highlighting the state-of-the-art in DEFCs. The review is selective with a special focus on; alkaline DEFCs, the reported monometallic and bimetallic catalyst studies, and discusses the mechanistic understanding of ethanol electrooxidation reaction available in the literature. Chapter 3 provides experimental and computational methodology details used in this project. Chapter 4 is an extended version of experimental methodologies specific to PM-IRRAS which provides technical experimental and data processing details. Chapter 5 is the initial detailed computational study for ethanol interaction on different facets of Pd surfaces (100, 110, and 111). Chapter 6 deals with ethanol electrooxidation on bimetallic Pd_xRu_{1-x}/C nanoparticles in alkaline solution followed by Chapter 7 where the effect of the metal-support interaction on ethanol electrooxidation is shown in the instance of Pd nanoparticles supported on metal oxides

(TiO_2, CeO_2, and SnO_2). Chapter 8, merges experimental PM-IRRAS and DFT insights to explain why it is very difficult to selectively break the C–C bond during ethanol electrooxidation. Chapter 9 is a theoretical study on screening for the best candidate transition metals for ethanol electrooxidation followed by the general conclusions and recommendations for further work in chapter 10. I hope you will enjoy walking through the path of my journey in the past four years of the project. Welcome on-board and enjoy the reading.

Chapter 2: Literature Review

Publication: E. A. Monyoncho, T. K. Woo, and E. A. Baranova in *RSC SPR Electrochemistry 2016 book series* – submitted

2.1 **Introduction**

Fuel cell technology dates back to 1839 when Grove demonstrated that chemical energy from hydrogen and oxygen can be converted directly into electrical energy with high efficiency.[1] Therefore, by principle, fuel cells represent a promising technology for clean generation of power from chemicals compared to combustion Carnot engines. Fuel cells convert chemical energy (fuel) into electrical energy with higher energy efficiencies, i.e., 45% in electrical energy, 90% in total energy (electricity and heat production) compared to combustion engines with total efficiency of up to 40%.[2] In addition, fuel cells have low-to-none emission of pollutants.[2,3] There are several good review articles [4–12] and book chapters [13–15] reporting the status of direct ethanol fuel cells (DEFCs) at different periods since 2000. By 2002 DEFCs were conceived based on the significant progress done on proton exchange membrane fuel cells (PEMFCs). The motivation was that direct alcohol fuel cells (DAFCs) were to eliminate the need for the bulky and expensive reformers hence allowing the deployment of the technology for mobile applications.[12] However, this shift to DAFCs encountered other challenges such as: i) the complex and incomplete oxidation of alcohols leading to low fuel efficiencies, ii) the alcohol crossover, in particular methanol, through the proton exchange membrane, etc. These challenges became the focus of active research since then. Most investigators focused on direct methanol fuel cells (DMFCs) and DEFCs in acidic media. It was recognised that DEFCs were more promising than DMFCs if the C–C bond would be cleaved.[12] Cleaving the C–C bond was found to be favourable in alkaline conditions than in acidic media because the OH species readily accepts a proton which facilitates ethanol dehydrogenation. This finding sparked interest for

direct alcohol alkaline fuel cells (DAAFCs). In 2005, Varcoe and Slade reported alkaline anion-exchange membranes followed by reports on Platinum-free low temperature fuel cells by Tsivadze *et al*. in 2007.[16,17]

DEFCs have several advantages compared to the most studied hydrogen and methanol fuel cells:[5,18] i) ethanol is a non-toxic liquid, which lowers the investment of handling facilities because the current infrastructure for gasoline can be largely used, ii) ethanol can be conveniently produced from biomass, hence is carbon neutral which mitigates the increasing atmospheric CO_2, iii) ethanol is the smallest alcohol with the C–C bond, hence can serve as a model for the electro-oxidation of bigger compounds containing the C–C bonds, iv) ethanol has a higher energy density than methanol if completely oxidized to CO_2 since it can deliver 12 electrons per molecule following the anodic reaction in equation (2.1):[5]

$$CH_3CH_2OH + 12\ OH^- \rightarrow 2\ CO_2 + 9\ H_2O + 12\ e^- \qquad E_a^o = +0.19\ \text{V/RHE} \qquad 2.1$$

In DEFCs, Eq. 1 is counterbalanced at the cathode by the oxygen reduction reaction, generating a theoretical cell voltage of 1.14 V. However, in practice ethanol is known to be partially oxidized to acetic acid (acetate in alkaline media) giving a maximum of 4 electrons as shown in Eq. 2:

$$CH_3CH_2OH + 5\ OH^- \rightarrow CH_3COO^- + 4\ H_2O + 4\ e- \qquad E_a^o = -0.20\ \text{V/RHE} \qquad 2.2$$

The standard potential of acetic acid formation indicates that the reaction path leads to inevitable potential losses of about 0.4 V (the difference between ideal potential for CO_2 and acetic acid "production").[19]

The progress in the development of DEFCs is well documented since the concept was conceived in earlier 2000. At that time, McLean *et al*. reviewed the state of the art of alkaline fuel cell (AFC) technology based on publications covering the past twenty five years up to 2002.[20] Although popular in the 1970s and 1980s, the AFC had fallen out of favour with the technical community in the light of the rapid development of proton exchange membrane fuel cells (PEMFCs). AFCs had been shown to provide high power densities and achieve long lifetimes in certain applications, and appeared to compete favourably with ambient air PEMFCs. In the review, McLean *et al*. examined the overall technology of AFCs, i.e., the power density, the lifetime performance, and the potential solutions were discussed. They presented a rough cost comparison between ambient air AFCs and PEMFCs. Overall, they showed that AFCs had

potential to succeed in certain market niche applications, but lacked research and development support to refine the technology into successful market offerings.

The mechanistic understanding of ethanol electrooxidation reaction was reviewed in 2008 by Koper *et al.*[15] They highlighted that the synergy between single-crystal *in-situ* studies and DFT calculations were beginning to unravel the kinetic and thermodynamic factors, the reaction pathways, and the structure sensitivity issues in electrocalysis with a special focus in their own work. Shortly after, Lamy *et al*. reviewed the working principles for DEFCs with a particular focus on solid alkaline membrane fuel cell.[14]

By 2010 there was realization in the community that direct alkaline fuel cells had many advantages compared to acidic counterparts.[11] The success leading up to this major shift from acidic to alkaline was the development of alkaline anion-exchange membranes (AEMs).[16,21–23] The use of AEMs have several advantages over conventional AFCs: i) the enhanced electro-kinetics of the reaction, ii) the potential to use non-noble metal catalysts, iii) the use of higher energy density fuels such as ethanol, ethylene glycol, and glycerol, iv) no carbonate precipitation since there was no mobile cation (Na^+ or K^+) which mitigates the issue of progressive carbonation of the alkaline electrolyte, v) no electrolyte weeping (flooding), vi) the reduced alcohol crossover, vii) the simplified water management due to the fact that the water is produced at the anode and consumed at the cathode, and viii) the reduced corrosion when working in alkaline media compared to acidic media.[11,24] Varcoe *et al*. have pointed out the importance and breakthrough of designing membrane electrode assembly (MEA) without metal cations (e.g. K^+, Na^+) present in alkaline fuel cells in which CO_2 is supplied to or generated at the electrodes to avoid undesirable carbonate precipitation, a major problem with traditional aqueous potassium hydroxide (KOH) electrolyte AFCs.[22] Antolini and Gonzalez reviewed the progress of the catalysts and membranes tested for alkaline direct alcohol fuel cells fuelled by methanol, ethanol, and ethylene glycol as of 2010.[11] The same year (2010) Zhao et al. presented a comprehensive review on the development of AEM DEFCs including the aspects of catalysts design, AEMs, and single-cell design and performance.[25]

In 2012, Yu *et al*. reviewed developments in AFCs, considering different types of fuels, novel catalysts and AEM.[9] They showed AFC systems and configurations particularly the new designs for portable devices. They pointed out that further development of DAFCs will rely on: i) the improved AEMs with good ionic conductivity and stability, ii) the low cost non-Pt catalysts with

high activity, and iii) the catalyst stability towards various fuels and oxidants. Rabis *et al.* presented a perspective summarizing the most outstanding contributions covering ten years (2002 to 2012) in terms of activity and durability of the catalyst materials for ethanol oxidation and oxygen reduction reaction, respectively.[10] They provided an outlook towards the development of new catalyst support materials with improved performance/stability, the use of advanced characterization techniques, and the fundamental studies of reaction mechanisms and degradation processes as areas deserving attention from researchers.[10]

In 2013, Almeida and Andrade reviewed the trends in DEFCs with special attention to: i) the systematic study toward the preparation of effective catalyst formulations by use combinatorial method, ii) the oxidation of ethanol in amorphous alloys containing low amounts of Pt, and iii) the use of non-noble materials as catalysts.[13] Singh *et al*. reviewed the status of the efforts in developing low cost and efficient electrocatalysts (the preparation and structural characterization catalysts) so as to decrease the over-potential for alcohol oxidation reaction and oxygen reduction reaction.[26] Brouzgou *et al*. reviewed the comparison in performance of PEM-DEFCs and AEM-DEFCs.[8] They pointed out that Pt-containing or Pt-free PEM-DEFCs that use acid proton-exchange membranes (typically Nafion type) exhibited relatively low performance, while AEM-DEFCs exhibited better performance values. They noted that the best value ever reported (peak power density was 360 mW cm^{-2} at 60 °C) had been obtained in a very promising alkaline-acid direct ethanol fuel cells (AA-DEFCs).

In 2014, Rao *et al.* reviewed the progress in ethanol electrooxidation reaction focusing on the thermodynamic process, the reaction mechanism, and the advantages and disadvantages of different electrocatalysts.[27] They discussed the factors affecting the reaction activity and selectivity such as supports, nanoparticle sizes, catalyst structure, and alloying of metals. Sharaf *et al.* although focusing on hydrogen fuel cells provided a very good and concise review of fuel cell ranging from the fundamentals, history developments, the competing technologies, to the system evaluation factors.[6] They used the most current data from industry and academia to highlight the relations between fuel cell fundamentals and applications.

In 2015, Wang *et al.* presented an overview of the advances in the study of ethanol electrooxidation mechanism and the electrocatalytic materials with a focus on Pt- and Pd-based catalysts.[28] They discussed the mechanistic understanding of ethanol oxidation reaction (EOR) on Pt and Pd surfaces. They reported that consensuses from the mechanistic studies are that

sufficient active surface sites to facilitate the cleavage of the C–C bond and the adsorption of water or water residue were critical for obtaining a higher activity. They showed how this understanding had been applied to achieve improved performance on various Pt- and Pd-based catalysts. This was achieved by optimization of electronic and bifunctional effects, as well as by tuning the surface composition and structure of the catalysts. Badwal *et al*. reviewed various types of DEFCs currently under development with emphasis on ethanol sources and production methods, the fuel cell construction materials and their operating regime, the performance and life time issues and market applications.[29] An *et al.* reviewed the comparison of acidic and alkaline DEFCs, i.e., their working principles, cell performance, system efficiency, reaction products, and the cost.[5] Similarly, recently Akhairi and Kamarudin published an overview of the acidic and alkaline DEFCs.[4] The review focused on the work done on platinum and palladium as strong competitors and highlighted the outstanding problems such as the incomplete oxidation of ethanol to carbon dioxide, the need to optimize the performance of DEFCs at standard conditions, the discovery of suitable catalysts for higher tolerance to surface poison, the stability of the catalysts, the promotion of better diffusivity between the membranes and the electrodes, and the need to control the selectivity of the reaction.

From the above quick survey, it is evident that alkaline DEFCs are superior to their acidic counterparts. Therefore, the detailed review and focus of this thesis is on alkaline DEFCs. The literature review starts with the various prototypes of DEFCs which have been proposed to highlight current state-of-the-art of DEFCs, followed by an overview of catalyst designs with a focus on monometallic, bimetallic catalysts and metal oxide supports. Then I review the current understanding of EOR mechanism with emphasis to alkaline conditions. The review is ended with a summary of outstanding challenges for DEFCs and proposal of the strategies to deal with them.

2.2 **Direct ethanol fuel cells**

2.2.1 **Fuel Cell Designs**

There are five types of DEFC designs reported in the literature to date,[5,8,30] i) the proton-exchange membrane fuel cells (PEMFCs), ii) the Anion-exchange membrane fuel cells (AEM-FCs), iii) alkaline-anode membrane acid-cathode fuel cells (AA-FCs), iv) direct alkaline fuel

cells (DAFCs), and v) direct ethanol solid oxide fuel cells (DE-SOFCs). The first three are shown in Figure 2.1 and the last two are shown in Figures 2.2 and 2.3, respectively.

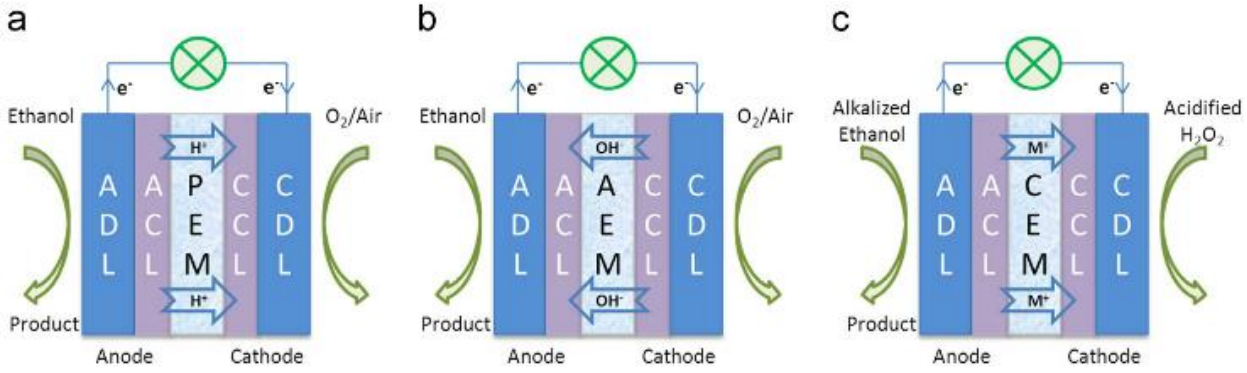

Figure 2.1: Fuel cell design schematics for (a) Proton Exchange Membrane (PEM), (b) Anion Exchange Membrane (AEM), and (c) Alkaline anode - acid cathode (AA). Reproduced with permission from [5]

The reactions for PEM-based, AEM-based, and AA for DEFCs are shown in equations 2.3–2.5, 2.6 – 2.8, and 2.9 – 2.11, respectively.

PEM-based DEFCs

Anode: $C_2H_5OH + 3H_2O \rightarrow 2CO_2 + 12[H^+ + e^-]$ 2.3

Cathode: $3O_2 + 12[H^+ + e^-] \rightarrow 6H_2O$ 2.4

Cell: $C_2H_5OH + 3O_2 \rightarrow 2CO_2 + 3H_2O$ 2.5

AEM-based EOR

Anode: $C_2H_5OH + 12OH^- \rightarrow 2CO_2 + 9H_2O + 12e^-$ 2.6

Cathode: $3O_2 + 6H_2O + 12\ e^- \rightarrow 12OH^-$ 2.7

Cell: $C_2H_5OH + 3O_2 \rightarrow 2CO_2 + 3H_2O$ 2.8

AA based EOR

Anode: $C_2H_5OH + 5MOH \rightarrow CH_3COOM + 4[M^+ + e-] + 4H_2O$ 2.9

where M = Na or K

Cathode: $2H_2O_2 + 2H_2SO_4 + 4e^- \rightarrow 2SO^{2-}_4 + 4H_2O$ 2.10

Cell: $C_2H_5OH + 5MOH + 2H_2O_2 + 2H_2SO_4 \rightarrow CH_3COOM + 2M_2SO_4 + 8H_2O$ 2.11

2.2.2 Cation/Proton – exchange Membranes (PEM) Fuel Cell Designs

Figure 2.1a shows the working principle of the first conceived fuel cell directly fed with the alcohol at the anode. The design had the advantage of avoiding the use of the bulk fuel reformer

used in PEMFCs.[12] Typically an aqueous solution of ethanol is circulated through the anodic compartment, and oxygen (or air) is circulated in the cathodic compartment. Later, it was realized that there were several challenges for design such as:[8] i) the acidic electrolyte membranes (mostly Nafion-based) were expensive, ii) the incomplete oxidation of ethanol to CO_2, instead acetaldehyde and acetic acid which liberates only 2 and 4 electrons, respectively greatly reduced the Faradaic efficiency of the fuel cell, iii) the sluggish reaction kinetics for EOR in acid media, leading to a large activation loss, iv) ethanol crossover from the anode to the cathode within the PEM which lead to a parasitic current generation, v) the need to use a cathode catalyst tolerant to ethanol, vi) the durability of the state-of-the-art catalysts employed such as PtRu/C and PtSn/C was in question. Therefore, there was need to develop other fuel cell designs to avoid the use of acidic electrolyte as presented below.

2.2.3 **Anion – exchange Membranes (AEM) Fuel Cell Designs**

The prospect of using an anionic membrane or a solid polymer electrolyte (SPE) in an alkaline fuel cell was first looked at by Agel *et al.* in 2000.[31] Their goal was to extend the concept of using cheaper SPE which were well developed in lithium-ion batteries into the fuel cell design. They characterized SPE for ionic conductivity, transport numbers, water content and assembled a prototype alkaline fuel cell to show the viability of the new design. They reported that the performance of the prototype fuel cell was greatly improved while using an interfacial solution between the electrodes and the membrane.[31] Figure 2.1b shows the working principle for AEM-DEFCs. This concept was rapidly explored in the community as evidenced by the articles and patents reviewed by Varcoe and Slade in 2005.[16] The advantages of this configuration are presented in the introduction.

The challenges for AEM-based DEFCs are: i) the incomplete oxidation of ethanol to CO_2 remain an issue, ii) the activity and durability of the Pd-based catalyst (the top candidates in the literature) for the EOR in alkaline media needs to be further enhanced, iii) enhancing the catalytic activity of non-Pt catalysts at the cathode to make them comparable to that of Pt is required. Currently, Ag-based cathode catalysts for the ORR in alkaline media are the leading candidates, iv) a significant improvement is needed to upgrade the OH^- conductivity, chemical, mechanical, and thermal stability of the existing AEMs. The OH^- conductivity can be improved by increasing the amount of charged groups in the membrane; however, there is a trade-off with

the mechanical properties. A loss of the mechanical properties by promoting excessive water uptake is the result of increasing the concentration of the charged groups. The thinness of the AEM is an important requirement related to mechanical stability. To keep good mechanical stability when immersed in water, an AEM as thin as ~50 µm is necessary. AEM suffers also of a poor chemical stability in alkaline media, stemming from the hydroxide attack on the cationic group. The result of this degradation is an important loss in the number of anionic exchange groups, and a decrease of the ionic conductivity. v) Improvements of the ionic conductivity and the thermal and chemical stability of the ionomers present within the catalyst layers are required.

2.2.4 **Alkaline anode – Acid cathode (AA) Fuel Cell Designs**

Figure 2.1c shows the working principle for alkaline-acid DEFCs. It consist of an alkaline anode, a membrane, and an acid cathode employing hydrogen peroxide as oxidant which boost the theoretical voltage from 1.14 V to 2.52 V.[30,32] Although, this design has been reported to deliver the highest power density (360 mW cm^{-2}), it has two major issues; i) the species crossover, and ii) the hydrogen peroxide decomposition.[33]

2.2.5 **Direct Alkaline Fuel Cells**

In direct alkaline fuel cell (DAFC) designs, an aqueous solution of ethanol and KOH/or NaOH is used in a flow type arrangement without the need for a membrane to separate the anode and the cathode as shown in Figure 2.2.[34]

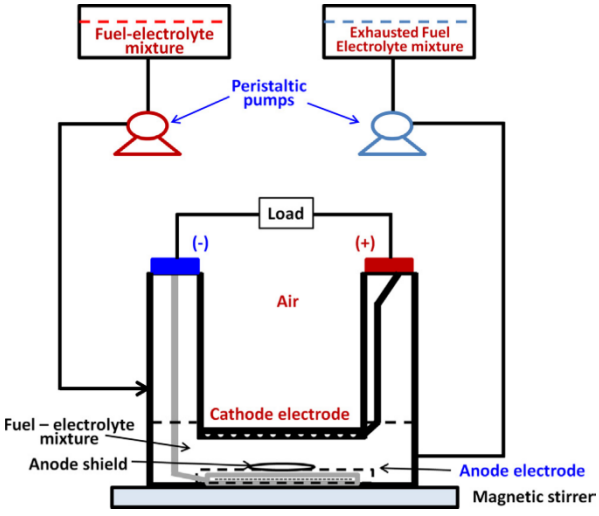

Figure 2.2: Schematic for direct alkaline fuel cell. Figure reproduced with permission from reference [34]

The electrode reactions are similar to AEM fuel cells, equations 2.6 – 2.8. This design has been mostly studied by Verma and Basu.[34–37] The best performance for this system was obtained with electrolyte concentration of 3 M KOH and 2 M Ethanol. However, it was reported that ethanol oxidation in this configuration proceeded to only acetaldehyde which involves only two electron. Therefore, considerable effort is required to optimise this technology which is promising for stationary power supply.

2.2.6 **Direct ethanol solid oxide fuel cells (DE-SOFCs)**

Last but not least is the direct ethanol solid oxide fuel cells (DE-SOFC) configuration shown in Figure 2.3.[38,39] This design marks the efforts towards using liquid fuels such as ethanol directly in the SOFCs.

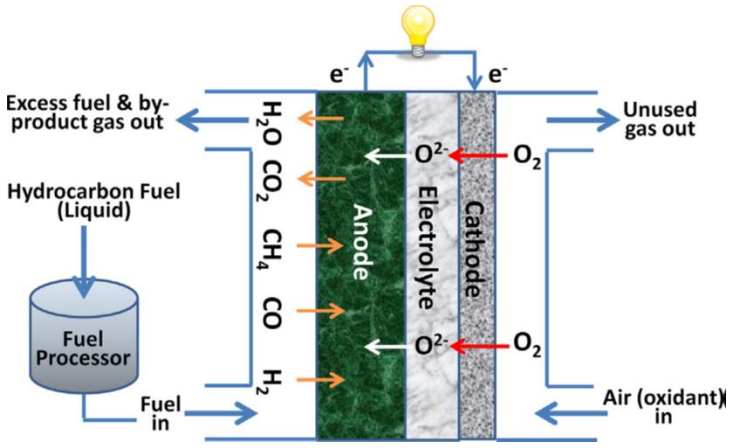

Figure 2.3: Schematic for a typical direct liquid SOFCs. Reproduced with permission from reference [38]

2.3 **Catalyst design strategies**

The development and design of efficient catalysts for breaking the C–C bond during ethanol electrooxidation is a central question in electrocatalysis. Many factors are known to influence the catalyst activity and selectivity such as chemical composition, morphology, size and shape of the catalyst in addition to the reaction conditions.[40–46] Therefore, the precise control of these parameters is crucial for the rational design of efficient and stable electrocatalysts for DEFCs. Figure 2.4, gives the summary of the common factors/parameters that control the catalytic performance of the catalyst.[43]

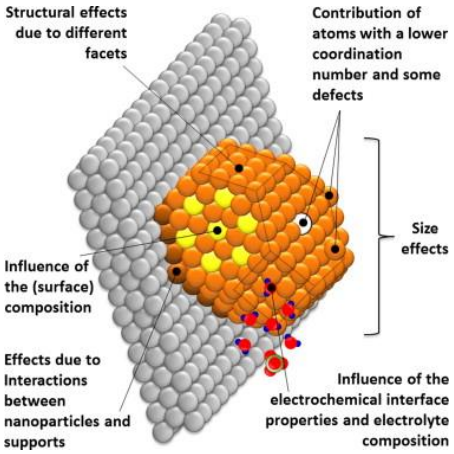

Figure 2.4: A schematic illustration of the complex factors and parameters that control the catalytic performance. Reproduced with permission from reference [43]

The efforts in the rational catalyst design strategies include the search for optimal formulations, the catalyst supports, and in the methodologies for catalyst preparations to tune the sizes, the morphologies and the surface composition. In this section, we first give an overview of the various methodologies reported, followed by a review of mono-, and bi-metallic catalysts for EOR in alkaline media.

2.3.1 **Methodologies for catalyst preparation**

There has been an excellent progress in the synthesis of electrocatalysts with different morphologies, mono- and multi-metallic nanoparticles with various compositions and well-controlled shapes.[41,47] It is now possible, to rationally design catalysts at the atomic-level to enhance the electrocatalytic performance, hence making it possible to correlate the nanoparticle structure with activity. Figure 2.5 shows the facets for different nanoparticle structure accessible for Au and Pd bimetallics.[47]

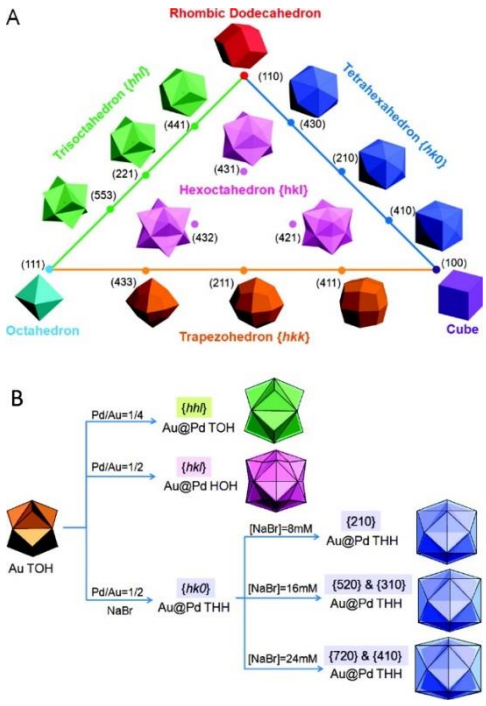

Figure 2.5: Schematics showing (a) the triangular diagram correlating fcc metal polyhedrons with different crystallographic facets and (b) illustrating the reaction regions that form Au@Pd NPs with different polyhedral shapes and different high-index facets. Reproduced with permission from reference [47]

During the nanoparticle synthesis, various approaches are used to reduce the metal ions as summarised in Table A.1 (see appendix) such as:[13] sodium borohydride reduction, polyol (alcohol–reduction), formic acid reduction, tannic acid, zinc, sodium silicate (Na_2SiO_3), gas phase reduction, thermal decomposition of polymeric precursors (Pechini method), and microwave-assisted heating method. A number of synthesis methods have been adopted such as: i) *Impregnation*, in which the support is mixed with a suitable metal precursor solution before the reduction of the metal ions. The method is best suited for monometallic catalysts.[32,48,49] ii) *Sequential impregnation / Colloidal* , in which a colloid precursor is first synthesised preferably in an organic solvent in the presence of a suitable surfactant before adding the supports.[50] The approach is better suited for the synthesis of polymetallic systems of uniform composition. iii) *Micro-emulsion*, in which the first step is the formation of the nanoparticles via a water-in-oil micro-emulsion reaction followed by a reduction step.[51–53] A micro-emulsion is formed by vigorous stirring or sonication and is thermodynamically stable. Nano-sized particles can spontaneously form within the micron size water droplets as a thermodynamically stable

microemulsion.[26] This method provides the ability to control the metallic composition and particle size with a narrow distribution.[53] iv) *Sol-Gel Derived*, in which the catalysts are prepared by the hydrolysis of acetylacetonate of the metal salt precursors in the presence of tetra methyl ammonium hydroxide followed by solution evaporation to form xerogel then thermal treatment under controlled atmosphere.[54]

Examination of the available literature for EOR reveals that there are four strategies commonly adapted to design catalysts: i) the use of high surface area carbon supports and/or reducible metal oxide supports, ii) the tuning of the catalyst structure and morphology which includes mesoporous, two- and three-dimensional structures with preferential facets, iii) the addition of the second or third ad-atoms on the catalyst surface, and iv) the tuning of the reaction conditions such as electrolyte pH, cations and anions.

2.3.2 **Catalyst support materials**

Catalyst supports are reported to play a significant role towards morphology, dispersion, activity, and selectivity of the catalysts.[55–57] Carbon is the most widely used support in the fuel cell research because it has high electrical conductivity and excellent structural properties which are important for fuel cell application.[58] Carbon has been widely used in PEMFCs and alkaline fuel cells for fabrication of the bipolar plate, the gas-diffusion layer and as a support for the active metal in the catalyst layer. Antolini has reviewed the application of carbon supports for Pt-based catalysts in fuel cells.[59] The novel carbon materials presented showed improved electrocatalytic properties and stability during fuel cells operation. Carbon nanotubes and aerogels have been investigated for use as catalyst support leading to the fabrication of more stable and active catalysts by reducing the undesirable carbon corrosion and degradation.[60] Graphene or graphene oxide materials are attractive alternative supports for dispersion and stabilization of the catalyst nanoparticles. Graphene is one atom thick nano-carbon materials which has attracted considerable attention in various applications including electrocatalysis.[61]

There are several reports showing the application of metal oxide supports such as CeO_2,[62–73] SnO_2,[62,64,74–82] TiO_2,[62,64,83–86] Mn_xO_y,[70,71,87] WO_x,[64,88] MoO_x,[64,89] RuO_2,[78] ZrO_2,[64,90] $CaSiO_2$,[91] MgO,[92,93] NiO/foam,[70,71,94–96] and CoO_x[70,71] as promising supports for EOR catalysts. These metal oxide supports have a significant effect on the catalytic activity of the catalysts because of

the interaction phenomenon known as "strong metal-support interaction" which was recognized by Tauster *et al*.[97,98] and advanced by Sanches and Gazquez.[99]

2.3.3 **Monometallic Catalysts**

2.3.3.1 **Platinum catalysts for ethanol electrooxidation reaction**

Platinum is one of the default catalyst metals for many reactions, as such it has been considered for EOR. Katayama *et al*. investigated the role of adsorbed OH^- species on Pt catalyst for EOR.[100] They did a comparative study between ionomer-coated Pt and highly oxophilic CeO_2 modified Pt electrode using *in situ* ATR-FTIR to monitor adsorption behaviour of adsorbed OH^-. They observed a distinct change in adsorption behaviour of adsorbed OH^- in blank KOH solution, which was attributed to the activity enhancement for EOR. This activity increase was not observed under acidic conditions. Hence, the pH has a significant effect not only on the reaction kinetics but also on the equilibrium properties of both solution and surface species. During EOR in alkaline media, the OH^- species are consumed which alters the local pH at the electrode surface, decreasing the reaction kinetics. Figueiredo *et al*. have shown the evidence of the local changing pH for EOR on Pt electrodes in alkaline media.[101] They used rotating ring-disc electrode experiments to monitor the local pH change during EOR. The current at the ring when polarized at the onset of hydrogen evolution (0.1 V vs RHE) served as a measure of the local pH in the vicinity of the electrode. Their results showed that the current at the ring at 0.1V became more negative during EOR, owing to a change in the equilibrium potential of the hydrogen evolution reaction caused by a change in the local pH. Lai *et al.* investigated EOR on Pt in electrolytes of varying pH and composition using electrochemical and surface-enhanced Raman spectroscopy (SERS) techniques.[102] The reaction activity increased significantly when the pH of the electrolyte was above 10 (as shown in Figure 2.6).

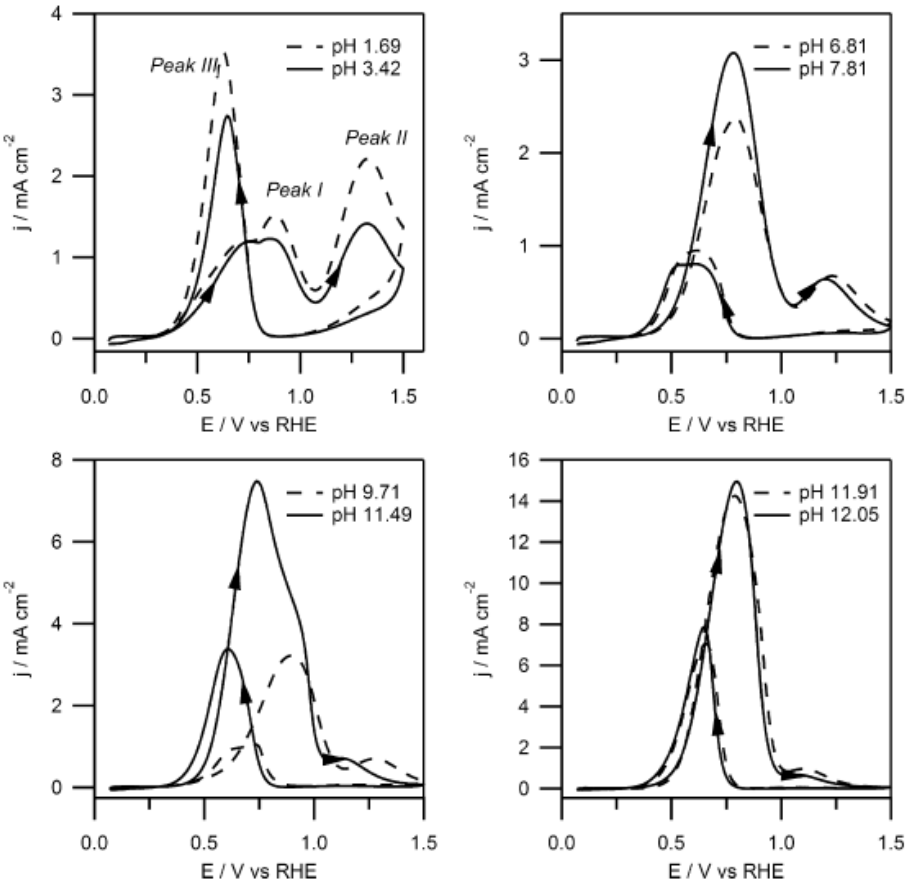

Figure 2.6: CVs for EOR (0.5 M EtOH + 0.1 M phosphate buffers) on polycrystalline Pt showing the effect of electrolyte pH. Reproduce with permission from reference [102]

According to their report, the reaction selectivity depends strongly on the nature of the electrolyte but to a smaller extent on the electrolyte pH.[102] These findings opened up the door to exploration of various electrolyte compositions. Of great interest from Lai *et al*. investigations, was the observation that the cleavage of the C–C bond was only observed on Pt in the absence of strongly adsorbed anions, which was attributed to the competition for the active sites. A comparative study of EOR on Pt electrode in acidic and alkaline media using DEMS was conducted by Cremers *et al*.[103] They reported that in the acidic environment the initial oxidation of ethanol was via acetaldehyde formation, which proceeded rather easily and was found to be highly reversible. They pointed out that the challenge in implementing DEFCs was to consequently oxidize acetaldehyde, a step that was particularly difficult as it must not proceed via acetic acid which cannot be oxidized further to CO_2.[104] In alkaline media, they found EOR to proceed rather faster and lead to a complete oxidation to CO_2, a promising approach for DEFCs.

Electrochemically reduced Pt oxide films were reported to be 29 times more active for EOR in than Pt films.[105] The superior activity was attributed to higher electrochemical active surface area and the existence of residual oxygen based on CV and XPS measurements. The concentration dependence for EOR on Pt in alkaline medium was studied using electrochemical and DEMS techniques by Bayer *et al*.[106,107] They showed that selectivity for EOR to CO_2 was favoured at lower concentrations and was only observed during CV and not during CA, indicating that formed intermediate(s) were playing a key role. They did a comparison to ethylene glycol, which showed significant CO_2 formation during CV and CA experiments with the tendency that low concentrations and low potentials yielded higher CO_2 current efficiencies. Although in acidic medium both alcohols exhibited a comparable electrochemical performance, in alkaline medium the current densities for ethylene glycol were substantially higher.[107]

The single-crystal Pt structural effects on EOR have been studied by several authors.[108–110] Buso-Rogero *et al*. used single-crystal Pt electrodes to show the effect of different facets (111, 110, and 100) for EOR using electrochemical and IRRAS techniques.[108] Although, the Pt(111) electrode displayed the highest currents and also the highest onset potential in CV, the CA showed that the activity decreased in the order of 110 > 100 > 111. Surprisingly, their IRRAS data showed that the C–C bond cleavage was not favoured in alkaline media. Lai and Koper studied irreversible adsorption of ethanol on Pt single crystal in alkaline solution using SERS.[109] They reported that EOR was very sensitive to the electrode surface structure, i.e., a higher concentration of low-coordination sites increased the current, lowered the over-potential required and lowered the deactivation rate. They found that the terrace length affected the quantity and nature of the adsorbed species, i.e., on Pt (110) only adsorbed CO was observed whereas adsorbed CH_x was only found on Pt (111) terrace sites.[109] Tripkovic *et al*. studied EOR on Pt(111), Pt(755), and Pt(332) surfaces in NaOH solution with a special focus on the oxygen-containing species generated and adsorbed on the surface.[110] They suggested the existence of reversible and irreversible adsorbed OH^- and PtO species in the potential region relevant for EOR. They suggested the role of these species in the reaction and proposed a dual path reaction mechanism as discussed in the mechanism section.[110]

There are studies which have looked at Pt nanoparticles for EOR in alkaline media.[111,112] Buso-Rogero *et al.* investigated EOR on Pt nanoparticles with different shapes and loadings using electrochemical and spectroscopic techniques.[111] The nanoparticles with a large amount of (100)

ordered domains showed higher current densities compared to nanoparticles with higher (111) domains. They reported that acetate was the main product with negligible amounts of CO_2, regardless of the type of Pt nanoparticles used. Sun *et al*. investigated the nanoparticle size effect for Pt nanoparticles supported on sulfonated graphene (Pt/sG) for EOR in alkaline solution.[112] They prepared five catalysts with various average particle sizes. They reported that 2.5 nm catalyst had the highest current density peak for EOR.[112]

The effect of the support on Pt activity has been explored by many research groups. Xu and Shen did a comparative study for Pt/C and Pt-CeO_2/C.[72,73] They reported that the electrode with a weight ratio of Pt to CeO_2 of 1.3 to 2.1 and a Pt loading of 0.30 mg cm^2 had the highest activity. Xu *et al*. studied EOR on MgO promoted Pt/C catalysts in alkaline media.[93] The promoted electrocatalysts were superior to pure Pt and the electrode with a weight ratio of Pt to MgO of 4:1 showed the highest activity for EOR. Bai *et al*. compared EOR on Pt-ZrO_2/C with Pt/C(20 wt.% E-TEK) using CV, Tafel plot, and impedance spectroscopy in alkaline.[90] They reported that molar ratio of Pt:ZrO_2 of 1:4 had the best catalytic activity for EOR. Recently, a comparative study of the effect of metal oxide support (support = TiO_2/C, ZrO_2/C, SnO_2/C, CeO_2/C, MoO_3, and WO_3) on Pt nanoparticles for EOR in alkaline media was reported.[64] Godoi *et al.* used *in-situ* XAS to show that Pt-support interaction produces changes in the Pt 5d band vacancy, which correlated to the EOR catalytic activity.[64] They observed the highest and lowest activities for Pt nanoparticles on TiO_2/C and CeO_2/C, respectively.[64] Using IRRAS technique, they reported that acetate was the main product and traces of CO_2 with different amounts for each support. They showed good correlation between fuel cell performances with electrochemical data.

2.3.3.2 **Palladium catalyst for ethanol electrooxidation**

Palladium is the strongest competitor to platinum catalysts so far based on reports in literature. In particular, Pd-based catalysts show high activity for EOR in alkaline media, hence has been extensively studied in the last decade. The influence of halide ions on EOR on Pd was reported by Kumar and Buttry, who found that halide ions decreased the peak currents monotonically as a function of increasing halide concentration.[113] The extent of poisoning, which also shifted the oxidation peak potential in more positive direction, was in the order of $I^- > Br^- > Cl^-$. This study highlighted the importance of thoroughly cleaning the nanoparticles prepared from palladium halide salt precursors. The effect of concentration has been studied using 8 wt.% Pd, on Vulcan

XC-72 in passive alkaline DEFC and it was reported that improved performance and stability was observed when the [hydroxyl]/[ethanol] = 1.[114] Carrera-Cerritos *et al*. investigated the performance and stability of Pd nanostructures (nanopolyhedral, nanobar and nano-rod particles) in DEFCs.[115] They studied the effect of the operation parameters, i.e., temperature and ethanol concentration on the maximum power density (MPD) and open circuit voltage (OCV). They reported that OCV values increased with increasing temperature for all of the catalysts at low ethanol concentration. Although, the MPD increased with temperature for all of the catalyst independent of the ethanol concentration, the effect of the temperature on the MPD for each Pd structure results in different slopes due to the different crystal faces.[115]

A study on single crystal Pd has been reported by Wang *et al*. who demonstrated the effectiveness of an electrochemical treatment consisting in cycles of constant potential oxidation and reduction of polycrystalline Pd surface in the enhancement of EOR.[116] The rise of the activity after the treatment was ascribed to the increase of both the surface area and density of low coordination surface atoms. With the aid of IRRAS, they showed that a change in the reaction products distribution also occurred, resulting in some cases, in an increased tendency to cleave the C–C bond.

Most of the studies have focused on the use of Pd nanoparticles. Assaud *et al.*, reported the use of three dimensional Pd clusters grown on TiO_2 nanotubes by atomic layer deposition for EOR.[117] They found that there existed not only a direct correlation between the catalytic activity and the particle size but also a steep increase of the response due to the enhancement of the metal-support interaction when the crystal structure of the TiO_2 nanotubes was modified by annealing at 450 °C in air. Rohwer *et al*. have reported a comparison of microwave and non-microwave treated Pd nanoparticles for EOR in alkaline medium.[118] Microwaved Pd nanocatalyst showed higher electrochemical active surface area, aggregation/uniformity dispersion, higher amounts of palladium oxides, and had remarkable activity for EOR. The morphological effect of Pd catalyst for EOR was investigated by Cerritos *et al*., who studied three different structures; nanoparticles (NP/C), nano-bars (NB/C) and nano-rods (NR/C) with preferentially exposed crystal faces supported on carbon black.[119] They reported considerable differences with the performance trend of peak oxidation potential of: NB/C < NP/C< NR/C < commercial Pd/C, indicating that NB/C catalyst enclosed by Pd(100) facets was the best catalysts. Cherevko *et al*. used high surface area Pd foams with roughness factors of more than

1000 and a specific surface area of 60 m^2 g^{-1} obtained by electrodeposition and reported them to have high activity towards the EOR.[120]

The effect of the catalyst support for Pd has been shown is several studies. For instance, Monyoncho *et al*. reported the promotional role of metal oxide supports (CeO_2, SnO_2, TiO_2) for EOR on Pd in alkaline media.[62] The monitored in-situ electrooxidation products using the PM-IRRAS which revealed that the supports influence the selectivity the reaction. They reported superior selectivity towards breaking the C–C bond to produce CO_2 on Pd/CeO_2 and acetate was the major product evident on all the catalysts, but at different ratios.[62] Safavi *et al*. have proposed the use of immobilized Pd nanoparticles in a well-structured composite of hydroxyapatite and carbon nanotubes EOR.[121] They demonstrated that the use of hydroxyapatite-carbon nanotubes composites lead to remarkable enhancements in the electrocatalytic activity, the kinetic parameters, and the durability of the catalyst. They attributed catalytic improvements to the synergetic effects between the immobilized Pd nanoparticles and the functionalities on the carbon nanotube-hydroxyapatite.[121] To avoid the use of metal oxides, Zhian *et al*. have conducted a study of EOR on bis(dibenzylidene acetone)palladium(0), $Pd(DBA)_2$, complex shown in Figure 2.7.[122] They reported that $Pd(DBA)_2$ had higher tolerance against poisoning intermediate/products for EOR, which was successfully employed as an anode catalyst in a passive air breathing DEFCs achieving a maximum power densities of 30, 31, 25 and 18 mW cm^2 for ethylene glycol, ethanol, glycerol and methanol, respectively.[122]

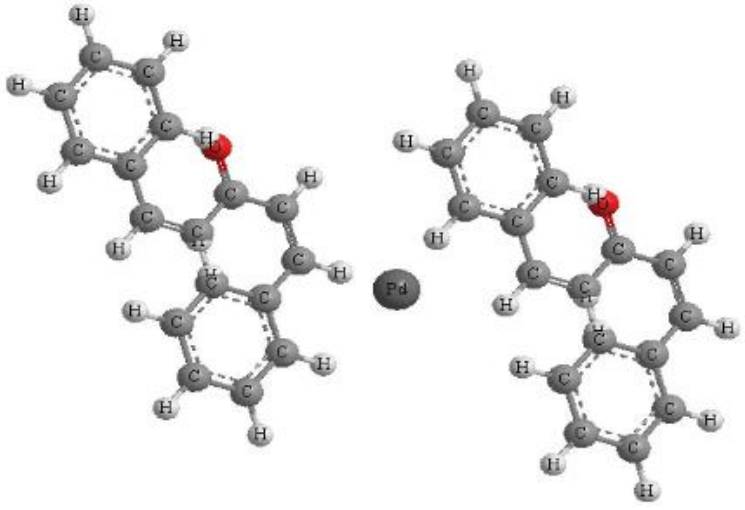

Figure 2.7: The structure of $Pd(DBA)_2$ catalyst. Reproduced with permission from reference [122]

Chen *et al*. conducted a comparative study of DEFCs build with a 2 μm thick layer of TiO_2 nanotube arrays doped with Pd nanoparticles (1.5 mg Pd cm^{-2}) and reported a maximum power densities were 210, 170, and 160 mW cm^{-2} at 80 °C for fuel cells fed with 10 wt. % aqueous solutions of ethanol, ethylene glycol, and glycerol, respectively in 2 M aqueous KOH.[123] The use of highly porous 3D-Graphene nanosheets synthesized using the sacrificial support method as a support for Pd nanoparticles was presented by Serov *et al*.[124] Their approach allowed the preparation of nanoparticles with smaller particle size distribution, higher surface area and showed good electrochemical activity and durability for EOR. Silva *et al*. described the use of Pd nanoparticles supported on physical mixtures of C + TiO_2 for EOR in alkaline media.[83] They prepared C/TiO_2 mass ratios of 100:0, 80:20, 60:40, 40:60, 20:80, and 0:100. They reported that Pd/C + TiO_2 (40:60) as the most promising mixture ratio. Chen *et al*. studied EOR on Pd/C promoted with $CaSiO_3$ in alkaline medium and demonstrate that the Pd/$CaSiO_3$ and C in wt.% 50:50 had higher current density (1408 mA mg^{-1}) than that of the Pd/C catalyst (743 mA mg^{-1}).[91] Li *et al*. investigated the effect of adding MgO to Pd/C catalyst for EOR in alkaline medium and reported a significant improvement in activity and in the poisoning resistance.[92] They reported that catalyst with a weight ratio of Pd to MgO of 2:1 to be the best in performance, the onset potential was negative shifted by 80 mV and the peak current density was 3.4 times higher than Pd/C.[92] Li *et al*. reported EOR on Pd nanoparticles supported on multi-wall carbon nanotubes synthesized on a carbon fiber paper (MWCNTs/CFP) in alkaline media which gave higher activity and stable performance than the commercial Pd/C and Pd/CFP.[125] The promotion role of oxide phases on Pd for the EOR was studied by Martinez *et al* who presented the evidence for the difference between an intrinsic effect obtained from an alloyed system and a synergistic effect produced by the presence of an oxide phase (SnO_2).[74] They interestingly showed that at 1M KOH, SnO_2 acted as a co-catalyst to provide OH^- ions to the interface layer which increased the turnover rate. However, acetate was reported to be the main the final products instead of the desired complete electrooxidation of ethanol to CO_2.[74] Pd nanoparticle-deposited MoO_x/C catalyst (Pd-MO/C) were considered by Lim *et al*. who showed a 35% higher mass activity compared to Pd/C catalyst for EOR.[89] They attributed the performance of Pd-MO/C to the high active surface area and the higher resistance to adsorbed CO. Uhm *et al*. synthesized well-ordered arrays of free-standing Pd–CeO_2 nano-bundles in an anodic alumina template via occlusion electrodeposition which showed dramatically enhanced activity for EOR compared to

pure Pd.[68] Chu *et al*. reported EOR activity enhancement on palladium-indium oxide supported on carbon nanotubes (Pd-In_2O_3/CNTs) composites prepared by via chemical reduction and hydrothermal reaction process.[126] The composite electrode with the mass ratio of Pd:In_2O_3 equals to 10:3 (with Palladium loading of 0.20 mg cm^{-2}) showed the highest electrocatalytic activity for EOR.[126]

2.3.3.3 **Comparative studies between Pt and Pd catalysts for ethanol electrooxidation**

Comparative studies between Pt and Pd for EOR in alkaline media have been conducted to determine the best candidate.[70,79,95,127–130] Xu *et al*. showed that Pd/C has a higher catalytic activity and better steady-state performance for EOR than Pt/C in alkaline media and the addition of oxides (CeO_2, NiO) significantly promoted the activity.[95] They found better performance for Pd or Pt supported on CeO_2 and NiO with weight ratio of 2:1 and 6:1, respectively. In another study, they reported EOR Pt and Pd electrocatalysts supported on carbon microspheres (CMS).[130] The results showed that nanoparticles supported on carbon microspheres gave better performance than those supported on carbon black and pointed out that although Pd was not a good catalyst for methanol oxidation; it was excellent catalyst for EOR in alkaline media than Pt. Hu *et al*. prepared Pt/C and Pd/C electrocatalysts supported on NiO by intermittent microwave heating (IMH) method and tested them for EOR in electrolyte with and without the presence of CO.[96] They reported that EOR on Pd-NiO/C electrocatalyst was better than Pt-NiO/C electrocatalyst. Bayer *et al*. studied EOR on Pt and Pd in alkaline medium using DEMS.[129] They reported that the reaction products and their current efficiencies depended strongly on the metal used. Acetate was the major reaction product while the current efficiency for CO_2 was low for both. However, the amount of acetate was higher for Pd electrode. At higher ethanol concentrations ethyl acetate was formed on Pt electrode but was absent on Pd electrode. Cantane and Lima have studied EOR on electrodeposited layers of Pd and Pt in alkaline electrolyte and monitored reaction products by online DEMS.[131] The DEMS evidenced similar amounts of CO_2 for Pd and Pt but Pd presented the higher production of ethyl acetate (acetic acid) and EOR on the Pd surface occurred to a higher extent in agreement to previous reports. They proposed a mechanism as presented in the mechanism.

2.3.4 **Bimetallic catalysts**

It is well known that bimetallic, trimetallic, and quaternary catalysts are better than monometallic catalysts.[42,132–142] We are going to focus our attention on the bimetallic work to understand the synergetic effect of the metals involved to determine the rationally for catalyst optimization for EOR in alkaline media. Table 3 gives the summary of the bimetallic catalysts and they corresponding monometallic catalysts tested for EOR in alkaline media.

Table A1: Summary of DEFCs and half-cell tests in alkaline media (See appendix)

2.3.4.1 **Bimetallic Platinum catalysts for ethanol electrooxidation in alkaline media**

There are many reports that Pt-M (M = Pd,[143–150] Sn,[151–158] Ru,[60,155,158–164] Mo,[159,165] W,[158] Bi,[166–168] Au,[102,128,148,169–173] Pb,[145,167,174–177] Rh,[178,179] Cu,[180] Co,[181] and Ag,[182,183]) etc. catalysts are significantly more active for the EOR than Pt alone. Here we examine a number of these studies to highlight what has been done.

Pt-Pd catalysts : The fabrication of Pt-Pd alloy nanoparticles on graphene nano-sheets (PtPdNPs/GNs) have been described by Chen *et al*.[143] They reported that varying the molar ratio of the starting precursors, nanoparticles with different shapes such as *spherical* (Pt_1Pd_1NPs), *nanoflowers* (Pd@PtNFs) and *nanodentrites* (Pt_3Pd_1NPs) could be produced on graphene nanosheets. Based on these observations, they proposed a plausible growth mechanism of PtPdNPs/GNs as shown in Figure 2.8.

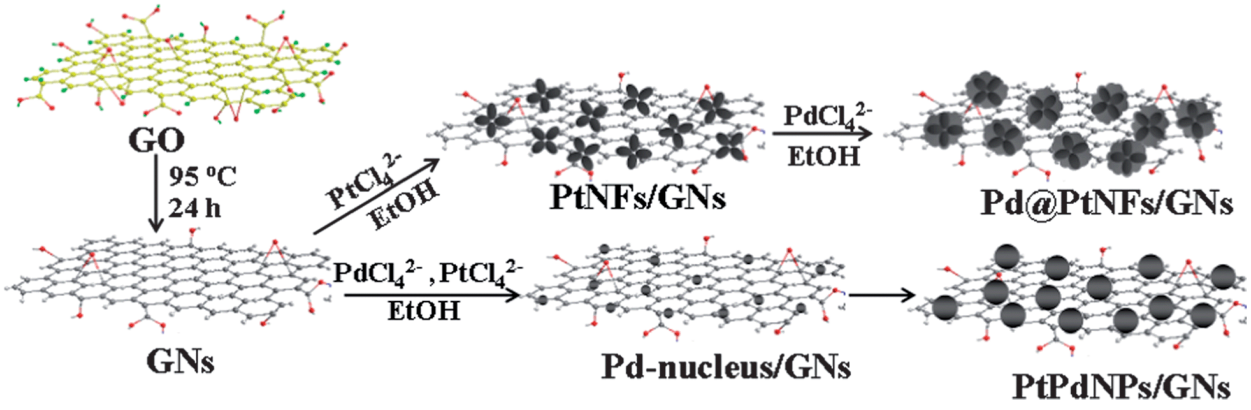

Figure 2.8: Proposed growth process for PtPdNPs on GNs. Reproduced with permission from reference [143]

The electrocatalytic properties of PtPdNPs/GNs for EOR exhibited higher activity and better tolerance to poisoning intermediates compared to PtPdNPs supported on carbon black (PtPdNPs/C).[143] Zhu *et al*. reported 3D PdPt bimetallic alloy nano-sponges which exhibited enhanced activity and stability towards EOR in an alkaline medium.[144,148] They developed a method to synthesize well-defined PdPt alloy nanowires, which exhibited significant activity enhancement towards EOR. Yang *et al*. reported an electrochemical method to synthesize PtPd alloy nanoparticles on Nafion-graphene film and demonstrated that the catalyst had good tolerance against poisoning by the reaction intermediates generated during EOR.[146] Datta *et al*. used poly-vinyl carbazole (PNVC), a conducting polymer composite matrix, crossed linked with vanadium pentoxide (V_2O_5) and embedded with PtPd nano-crystallites for EOR leading to higher currents compared to carbon supported counterpart.[147] Lin *et al*. reported a spontaneous reduction method to prepare PtPd with high activity for EOR.[149] They showed that $Pd_{77}Pt_{23}$ had the highest activity followed by $Pd_{87}Pt_{13}$, Pd, and Pt.

Pt-Ru catalysts: PtRu bimetallic is the oldest and most studied in the literature. Therefore, it is more appropriate here to refer the interested reader to a comprehensive review by Petri who discusses the three periods of Pt-Ru research:[162] (a) the initial period after discovery (1963-1970); (b) the observation and classification of basic tendencies (like the effects of compound segregation, structural features on the activity; up to 1990); and (c) the nano-structural studies and molecular level consideration of electrocatalytic phenomena in combination with advanced applied studies of materials, mechanistic, and applied aspects (after 1990 to 2008). The review focuses on the balance of various aspects of Pt-Ru electrochemical related to material science and electrocatalysis as well as to remember the early basic results being of importance for future understanding of Pt-Ru functional properties.[162] Gralec *et al*. have studied the role of the Kegging-type phosphomolybdate ($PMo_{12}O_{40}^{3-}$) ions adsorbed on C-supported PtRu and PtRu/C for EOR using CV, DEMS, and XPS.[159] They showed that modification of PtRu/C nanoparticles with phosphomolybdate ions lead to the suppression of the formation of surface Ru oxides which resulted into more than 40% activity increase for EOR at potentials > 700 mV.[159]

Pt-Sn catalysts: This bimetallic system has been extensively studied and here we mention a few selected studies. The structure-to-property relationship for EOR on PtSn in alkaline and acidic environments have been studied by Artyushkova *et al*.[151] They observed that transitioning

from acidic to an alkaline environment, changes the material structure and electrochemical reaction mechanisms. Electrocatalysts containing larger particles with larger relative amounts of metallic Pt and Sn performed better in acid media which they attributed to the inner-sphere electron transfer reaction on active PtSn alloy phase.[151] PtSn electrocatalysts containing larger amounts of oxidized Pt and Sn performed better in alkaline, which they suggested indicated that hydroxyl species that are natively present on oxidized Pt and Sn were promoting an outer-sphere electron transfer. Du *et al*. sought to explain why Pt-Sn nanoparticles are active electrocatalysts for EOR but inactive for splitting the C–C bond to CO_2 using microelectrode to monitor the amount of CO_2.[152] They reported that the composition and crystalline structure of the Sn element played an important role in the CO_2 generation. The non-alloyed Pt_{46}-$(SnO_2)_{54}$ core/shell particles demonstrated a strong capability for breaking the C–C bond than pure Pt and intermetallic Pt/Sn. The effect of ethanol concentration on the DEFCs with PtSn anode performance and products distribution was studied by Assumpcao *et al.* using in-situ single fuel cell/ATR-FTIR setup.[153] They performed experiments at 80° using commercial Pt_3Sn/C as anodic catalyst and the concentrations of ethanol solution were varied from 0.1 to 2.0 M. An increase in power density was observed with the increase of ethanol concentration up to 1.0 M, and the FTIR spectra band intensities revealed an increase of acetic acid/acetaldehyde ratio with increasing concentration of ethanol. Baranova *et al*. studied EOR on PtSn/C nanoparticles in alkaline media synthesized using a polyol reduction method.[154] They formed a bi-phase PtSn electrocatalysts where one group was composed of disordered PtSn alloys and the other group composed of PtSn alloys intimately mixed with a SnO_x. They reported that all catalysts were active during CV experiments but the bi-phase PtSn + SnOx nanoparticles had significantly higher current densities at lower over-potentials compared to the pure alloy PtSn catalysts.[154] They correlated the catalyst bulk and surface structure with the observed EOR in alkaline media demonstrating that 1 M KOH was the best when electrocatalyst contained higher amounts of both Pt and oxides. They reported that alloying of Pt with Sn improves intrinsic Pt catalytic activity and plausibly prevents Pt oxidation.[154]

Pt-Rh catalysts: For these catalysts, Calderon-Cardenas *et al*. have studied the effect of the composition and thermal treatment in H_2 of Pt-Rh/C materials with atomic ratios of Pt:Rh 3:1, 1:1 and 1:3 and metal loading of 40 wt.% for EOR in alkaline media.[178] They reported that thermally treated Pt-Rh catalysts in a hydrogen atmosphere showed greater stability and higher

current densities and suggested the necessity of exploring the effects of thermal treatments of the catalysts for EOR. Shen *et al*. prepared PtRh/C catalysts and compare their catalytic activities with that of Pt/C in alkaline media and reported that the peak current density on Pt_2Rh/C was about 2.4 times of that on Pt/C.[179] They ascribed the enhanced activity to the improved C–C bond cleavage in the presence of Rh and to the accelerated oxidation kinetics of adsorbed CO to CO_2 in alkaline media.

Pt-Pb catalysts: Gunji *et al*. synthesized Pt_3Pb(core)-PtPb(shell) nanoparticles on carbon black by converting nano-crystalline Pt to an ordered intermetallic compound with the reduction of Pb ions and tested them for EOR in alkaline media.[174] The nanoparticles exhibited enhanced catalytic activity and relatively stable cycle performance towards EOR in an alkaline solution. They attributed the improved performance to both the enhancement of ethanol dehydrogenation and the higher concentration of surface adsorbed OH^- on the modified PtPb surface in the Pt_3Pb-PtPb core-shell NPs. The mechanism for EOR on a Pt electrode modified with an irreversibly-deposited layer of Pb in alkaline solution was proposed by Christensen *et al*. based on in-situ IRRAS insights.[145] He *et al*. described an approach for the selective cleavage of the C–C bond using a solution-born co-catalyst based on Pb(IV) acetate, which they suggested controlled the mode of ethanol adsorption so as to facilitate the direct activation of the C–C bond as shown in Figure 2.9.[176]

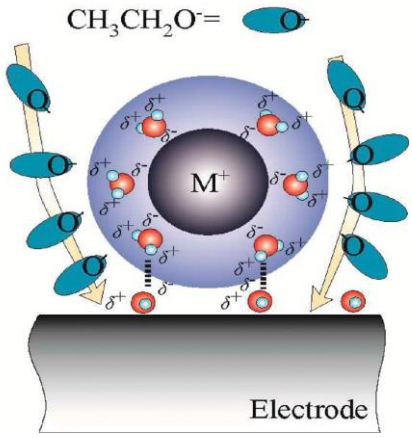

Figure 2.9: Schematic to show the noncovalent interactions with hydrate Pd cations that would lead to a preferred orientation of acetaldehyde and/or acetate anion with the CH_3 end pointing toward the surface as it approaches the electrode surface. Reproduced with permission from reference [176]

Matsumoto studied the electrocatalytic activities of a wide range of intermetallic bulk compounds for EOR in alkaline media including PtPb which had the lowest onset potential for ethanol oxidation of 20-30 mV less than that of pure Pt and Pd.[167] The current densities for PtPb were ≥ 17 times larger than those of pure Pt and Pd. Yang *et al*. synthesized Pt-PbO_x nanocomposite catalyst with a mean size of 3.23 nm with a much higher catalytic activity and a longer durability than Pt nanoparticles and commercial Pt black catalysts for EOR in alkaline media.[175] In-situ IRRAS data revealed that breaking the C–C bonds on Pt-PbOx was 5.17 times higher than that of the Pt nanoparticles.

Pt-Au catalysts: Mourdikoudis *et al*. synthesized PtAu hetero-nanostructures comprising the dimer (Pt-Au) and core-satellite (Pt@Au) configurations by means of a seeded growth procedure using Pt nano-dendrites as seeds.[169] They reported that the prepared PtAu bimetallic nanostructures were highly efficient catalysts for EOR in alkaline solution. Dutta *et al*. synthesized PtAu alloyed nanoparticles and reported improved half-cell activity for EOR and a considerable increase in the peak power density (>191%) in an in-house fabricated DEFCs.[170] da Silva *et al*. tested PtAu/C electrocatalysts in different atomic ratios and reported that the 50:50 as the most promising ratio for half-cell tests for EOR in alkaline media, while single fuel cell suggested a 70:30 ratio.[172] They attributed the discrepancy to the electrode architecture since 50:50 ratio yielded a much thicker electrode than the 70:30 catalyst because the Pt load was the same. Song *et al*. reported the preparation of hollow Au@Pt core-shell nanoparticles and used them for EOR in alkaline media which showed high current density in the forward scans.[173] Cherevko *et al*. prepared highly ordered Pt decorated Au nanowire arrays, Pt/Au NWA and studied the effect of shell materials for EOR in alkaline media and reported up to 4-fold increase in the ethanol oxidation peak current.[128]

Pt-Bi catalysts: Figueiredo *et al*. reported the enhancement of EOR activity on Pt/C by simple adsorption of Bi on the surface.[166] They reported that Bi promoted the cleavage of the C–C bond. Matsumoto *et al*. reported PtBi and $PtBi_2$ intermetallic compounds as promising electrocatalysts among the various bulk electrodes they examined which had lower onset potentials for the EOR and exhibited extremely stable oxidation currents of 4.8 and 3.3 mA cm^{-2} during the constant-potential electrolysis.[167] Tusi *et al*. prepared Pt/C, Bi/C and PtBi/C (Pt:Bi atomic ratios of 90:10, 70:30 and 50:50) electrocatalysts and showed that PtBi/C had significant increase of

performance for EOR in alkaline compared to Pt/C.[168] They noted that the performance of PtBi/C electrocatalysts for EOR was superior in alkaline medium compared to acid medium.

Pt-others: Li *et al*. synthesized a series of Mo-doped Pt/C catalysts with a microwave assisted technology and investigated the effects of Mo content on using CV, CA, and EIS.[165] They reported that the Pt_2Mo/C showed the highest current density and the slowest deterioration from intermediates/products poisoning. Kepenier *et al*. fabricated graphene supported PtCo catalysts (Pt:Co = 1:1, 1:7 and 1:44) by the rapid microwave heating method and reported that the molar ratio of 1:7 had highest activity.[181] Jin *et al*. prepared Pt/C catalysts modified by the potentiostatic deposition of Ag and reported a significant improvement in the activity of PtAg/C for ethanol oxidation in alkaline solution.[182] El-Maksoud *et al*. investigated the electrocatalytic effect of Pb, Tl, and Cd ad-atoms on Pt electrode for EOR in alkaline medium.[177] They reported that all three metal ad-atoms enhanced activity and Pb and Tl ad-atoms increased the oxidation rate by a factor of about 15, whereas Cd ad-atoms shifted the polarization curves negatively by a factor of about 5 at lower over-potentials.

2.3.4.2 **Bimetallic Palladium catalysts for ethanol electrooxidation**

Pd is considered the most active metal for EOR in alkaline media; hence a lot of effort has been directed towards improving its catalytic activity as evidenced from recent reviews.[1–4] Several bimetallic catalysts have been tested so far Pd-M (M=Ni,[17,184–203] Ru,[17,60,204–209] Au,[17,128,148,173,208,210–216] Ir,[217,218] Bi,[219–221] Sn,[75,185,188,216,222] V,[223] W,[224,225] Ag,[49–52] Cu,[226–232] Co,[17,233] Fe,[17] Mn,[57] Ti,[234,235] Rh,[236,237] Sb,[238] Te,[239] La,[240] and Pb.[241]). Herein we highlight a few of them.

Pd-Ni catalysts: PdNi combination has been extensively studied because Ni is very cheap. Obradovic *et al*. synthesized Pd-Ni/C using $NaBH_4$ reduction method which they reported to be up to three times more active for the EOR compared to Pd/C.[184] They found that maximum activity was attained after fifty cycles with the positive potential limit of 1.2 V/RHE regardless of whether they were performed in the electrolyte with or without ethanol, hence proposed that potential cycling induces reorganization of the catalyst surface bringing Pd and Ni sites to a more suitable arrangement for ethanol electrooxidation.[184] Moraes *et al*. have reported performance enhancement for alkaline DEFCs using non-functionalized and functionalized Vulcan carbon

supported Pd, PdNi, and PdNiSn anodic electrocatalysts produced by impregnation-reduction.[185] They reported that alkaline DEFCs with PdNiSn supported on functionalized Vulcan had the best performance which they attributed to improved textural properties.[185] Chen *et al.* prepared PdNi nano-catalysts supported on multi-walled carbon nanotube (MWCNT) using a modified polyol method.[187] They reported that the surface oxygen content in PdNi/MWCNT was higher than in Pd/MWCNT and Ni existed mainly in the form of hydroxides which were attributed to be responsible for the improved poison resistance. Wang and co-workers have demonstrated in a number of studies that de-alloying can be used to improve PdNi electrocatalysts.[186,189,192] They used Pd-Ni-P film prepared via electro-deposition on Au substrate and de-alloyed it by repetitive potential cycling in acidic media to leach out most of the Ni and P components and the resulting film showed significantly enhanced and durable activity for EOR. They used in-situ ATR-SEIRAS for reaction insights which revealed that the enhanced electrocatalysis correlated well with the enhanced formation of adsorbed CO and acetate.[186] This was an extension of their earlier work on Pd–Ni–P where they showed that Pd-Ni-P have double the number of electrocatalytically active sites (12.03%) compared with the Pd-Ni (6.04%) and Pd-black (5.12%) samples.[192] Dutta and Datta have investigated EOR on Pd_xNi_y/C in alkaline medium synthesized by simultaneous reduction of metal precursors using $NaBH_4$ method.[190] They attributed the improved catalytic activity on NiO present in the binary catalyst matrix. Ahmed and Jeon studied a series of graphene supported NixPdy binary alloyed catalysts for EOR and reported activities in the order $Ni_{75}Pd_{25}/G > Ni_0Pd_{100}/G > Ni_{25}Pd_{75}/G > Ni_{50}Pd_{50}/G$ as shown in Figure 2.10.[191]

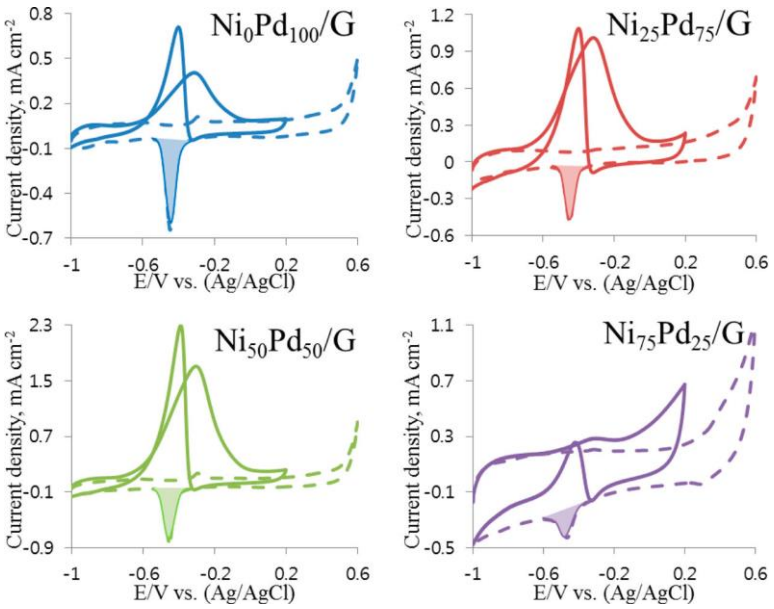

Figure 2.10: CVs of a series of graphene supported Ni_xPd_{100-x} recorded in 1 M KOH the absence (dotted lines) and presence of 0.1 M EtOH. Reproduced with permission from reference [191]

Sheikh *et al*. synthesized Pd-Ni/C catalysts by impregnation-reduction method and reported that $Pd_{40}Ni_{60}$/C had the best catalytic performance for EOR in alkaline medium, which they attributed to Ni hydroxides ($Ni(OH)_x$).[188] Lee *et al*. prepared highly monodisperse 5 nm Pd-Ni alloy nanoparticles by the reduction of $Pd(acac)_2$/$Ni(acac)_2$ mixtures with tert-butylamine-borane complex in the presence of oleic acid and oleylamine which exhibited higher activity and stability for EOR.[196] Miao *et al*. used to electroless co-plating to coat Pd-Ni nanoparticles on Si nanowires for EOR.[195,199] They reported that Pd-Ni/SiNWs electrode had higher activity and better long-term stability in an alkaline solution.[195] The work was an extension of their previous work on using silicon microchannel plates modified with Ni-Pd nanoparticles.[199]

Shen *et al*. performed a quantitative product analysis of EOR in an anion-exchange membrane DEFC that consisted of a PdNi/C anode and found that Pd_2Ni_3/C leads to a significant increase in the cell performance compared to Pd/C but did not improve the selectivity towards CO_2.[193,201] They observed that among the operating conditions tested (temperature, discharge current, and ethanol concentration) the operating temperature was the most significant parameter that affect the CO_2 selectivity: increasing the temperature from 60 to 100 °C increased the CO_2 current efficiency from 6.0% to 30.6% with the Pd/C. This work was an extension of their earlier studies.[7] Roy *et al*. prepared spherical Pd nanoparticles and dip-coated them Ni-foil and found

them to be superior electrocatalysts for EOR compared to the Ni-supported Pd electrode despite of them having less Pd^0 loading.[194] Qi *et al*. used de-alloying method to prepare $Pd_{40}Ni_{60}$ alloy from a ternary $Al_{75}Pd_{10}Ni_{15}$ in a 20 wt.% NaOH solution under free corrosion conditions.[198] They reported that $Pd_{40}Ni_{60}$ had enhanced electrocatalytic performance for EOR in alkaline media than nanoporous Pd. Zhang *et al.* prepared PdxNiy/C through a solution phase-based nanocapsule method and showed that onset potential for EOR on Pd_4Ni_5/C was negative shifted by 180 mV and the exchange current density was 33 times higher compared to Pd/C.[197] They proposed that surface Ni promoted refreshing Pd active sites, thus enhancing the overall reaction kinetics. Maiyalagan and Scott prepared Pd-Ni nanoparticles supported on carbon nanofibers by $NaBH_4$ reduction method and reported negative onset potential shift of 200 mV and four times increased peak current density for EOR on Pd-Ni/CNF compared to Pd/C.[202]

Pd-Ru catalyst: Monyoncho *et al*. prepared PdRu nanoparticles supported on carbon Pd_xRu_{1-x}/C (x = 1, 0.99, 0.95, 0.90, 0.80, 0.50) using a polyol method and reported that the resulting bimetallic catalysts were primarily a mix of Pd metal, Ru oxides and Pd oxides.[204] They found that addition of 1–10 at.% Ru to Pd not only lowered the onset oxidation potential for EOR but also produced higher current densities at lower potentials compared to Pd/C by itself. In particular, they singled out $Pd_{90}Ru_{10}$/C and $Pd_{99}Ru_1$/C which gave up to six times higher current densities than Pd/C at -0.96 V and -0.67 V vs MSE, respectively. Similarly, Ma *et al*. studied PdRu/C catalysts with various Pd:Ru atomic ratios synthesized by impregnation method and tested them in AEM-DEFCs.[205,206] They reported the anode with Pd_3Ru/C showed maximum power density as high as 176 mW cm^2 at 80 ºC which was about 1.8 times higher than Pd/C catalyst. Anindita *et al*. reported addition of Ru to Pd-0.5wt%C composite electrode increased the electrocatalytic activity greatly attaining a maximum at 20wt% i.e. (Pd-0.5wt%C-20wt% Ru) for EOR in alkaline media.[207]

Pd-Au catalysts: Cai *et al*. synthesized Pd nanotubes covered by high-density Au-islands which increased the mass activity by up to six times for EOR in alkaline media compared to Pd/C as shown in Figure 2.11.[210] They proposed a model to explain the relationship between the structure and the catalytic activity.

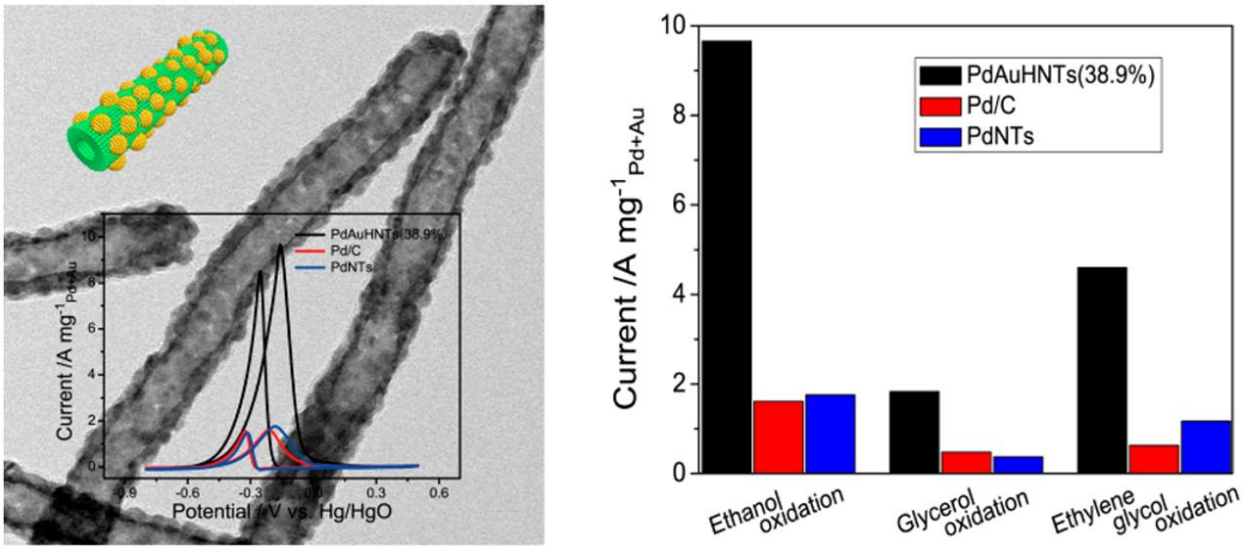

Figure 2.11: The controlled synthesis of Au-Island-covered Pd. Reproduced with permission from reference [210]

Hong *et al*. have demonstrated a rapid synthetic process for alloyed dendritic PdAu nanocrystals which are active for EOR in alkaline media.[211] The process involves mixing Na_2PdCl_4, $HAuCl_4$, polyvinylpyrrolidone and hydroquinone and heating at 50 °C for 15 min. Smiljanic *et al*. examined the catalytic properties of Pd/Au(111) nanostructures obtained by spontaneous deposition of Pd using $PdSO_4$ and $PdCl_2$ salts.[212] They reported that Pd/Au(111) nanostructures obtained using $PdCl_2$ salt had higher activity which they ascribed to the thinner and smoother Pd deposits on the surface, hence more convenient sites for the adsorption of ethanol and its subsequent oxidation steps. Song *et al*. prepared hollow Au@Pd core-shell nanoparticles using galvanic displacement with Ag which showed highest current density in forward scan for EOR in alkaline media.[173] Xu *et al*. prepare Pd-Au alloy electrocatalysts using dimethylformamide co-reduction method under an ultrasonic process and reported Pd_3Au/C exhibited an enhanced catalytic activity and stability for EOR compared to monometallic Pd/C catalyst.[213] Cheng *et al*. prepared highly ordered PdAu nanowire arrays using a combination of anodized Al oxide template-electrodeposition and Pd nanowire arrays reacting with $HAuCl_4$.[214] They found that the PdAu nanowires shifted onset oxidation potential by 123 mV more negative compared with that on the Pd nanowires.

Recently, Assaud *et al*. reported Pd nanoparticles of controlled particle size deposited by Atomic Layer Deposition (ALD) on electrochemically grown TiO_2 nanotubes (TNTs).[117] The particle size was controlled by the number of ALD cycles (Figure 2.12). They showed by TEM

that catalysts fully cover the inner and outer walls of the three-dimensional nanostructured TiO_2. The influence of TiO_2 nanotube support was demonstrated through the modification of the crystalline structure of the TNTs anatase TiO_2 phase obtained after annealing is more conductive than the amorphous TiO_2. Catalysts with the different number of ALD cycles were prepared and studied for EOR. Among the prepared electrocatalysts (N = 400-900 ALD cycles), the 500 ALD Pd/TNTs system showed the best catalytic activity and satisfactory stability in alkaline media (Figure 2.13).

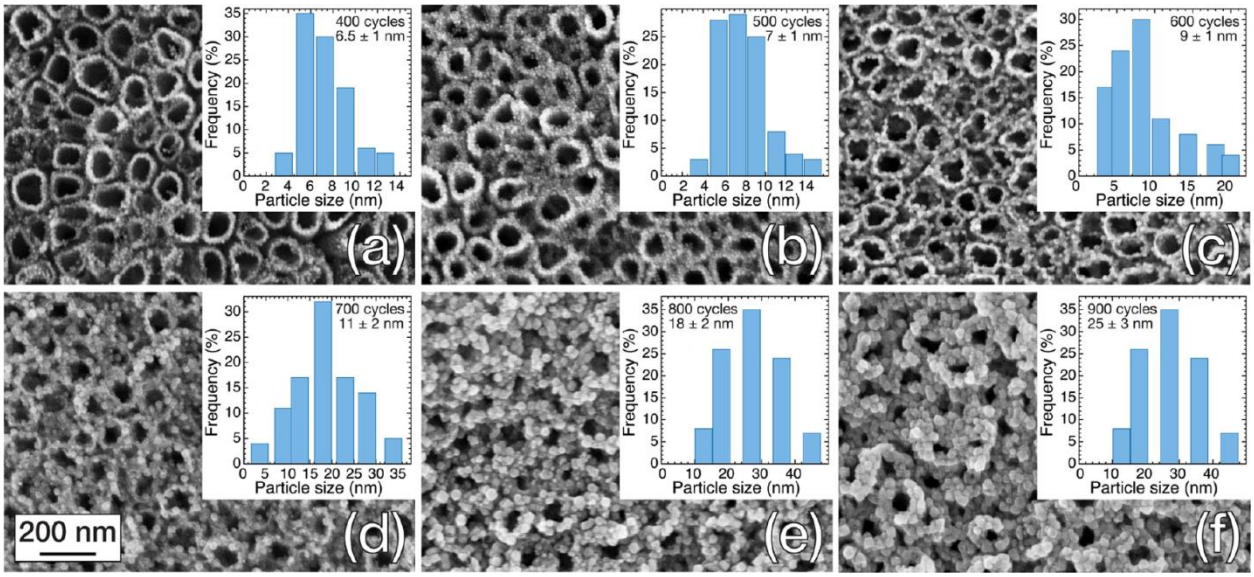

Figure 2.12: SEM micrographs of TNTs coated by Pd nanoparticles with an increasing number of ALD cycles: (a) 400, (b) 500, (c) 600, (d) 700, (e) 800, and (f) 900 cycles. Insets show the size distribution estimated, for each N, from the SEM pictures. Reproduced with permission from [117]

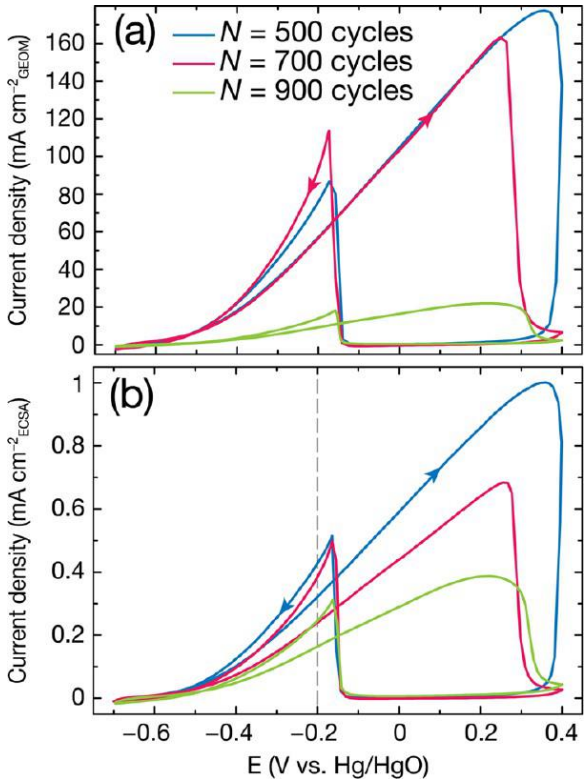

Figure 2.13: Cyclic voltammograms of Pd/TNTs with a various number of Pd ALD cycles on annealed TNTs in 1 M KOH + 1 M C_2H_5OH. Current density is given per geometrical area (a) and ECSA (b). The scan rate is 25 mV s^{-1}. Reproduced with permission from reference [117]

Zhu *et al*. decorated carbon-supported gold nanoparticles with monolayer of Pd atoms with different Pd:Au atomic ratios using chemical epitaxial seeded growth method and showed that PdAu nanoparticles had higher specific activities than Pd/C for EOR in alkaline media.[215] He *et al*. prepared carbon-supported Pd_4Au and $Pd_{2.5}Sn$ nanoparticles using a chemical reduction method and examined the kinetics for EOR using impedance spectroscopy and Tafel plots which showed that the reaction kinetics were somewhat more sluggish on the Pd-based alloy catalysts than on commercial Pt/C, but the alloy catalysts had higher tolerance to surface poisoning.[216] Pd_4Au/C displayed the best catalytic activity among the series of prepared catalysts for EOR in alkaline media.

Pd-Cu catalysts: Serov *et al*. used a sacrificial support method in combination with the thermal reduction of metal precursors to prepare unsupported uniformly-distributed PdCu catalysts with ratios of 1:3, 1:1, and 3:1.[226] They found that PdCu and Pd_3Cu electrocatalysts showed improved EOR activity, which they attributed to the presence of surface Cu sites favouring adsorbed OH^- species as confirmed by their DFT calculations in the paper.[226] Mao *et*

al. prepared a series of surface Pd rich Cu_xPd_y/C catalysts and reported Cu_1Pd_2/C stood out from the four sets tested for EOR in alkaline.[227] Cai *et al*. reported catalyst with Cu core-shell structure prepared by the galvanic replacement between Pd^{2+} ions and Cu particles (Cu@PdCu/C) which showed greatly improved durability, poisoning tolerance, and current density of 2.78 times higher than Pd/C for EOR.[230] Zhao *et al*. have demonstrated a one-pot, room temperature aqueous synthesis of submicrometer-sized PdCu networks as superior catalysts for EOR in alkaline medium.[229] Their composition-optimized $Pd_{73}Cu_{27}$ network showed superior performance for EOR and better tolerance of CO-like poisoning species compared to commercial Pd/C. Wang & Kang et al have worked on the development of high performance PdCu/C catalysts to enhance EOR performance.[231,232]

Pd-Sn catalysts: Mao *et al*. used impregnation reduction method to prepare carbon-supported PdSn–SnO_2 with higher catalytic activity for EOR in alkaline solution compared to Pd–Sn/C and Pd/C catalysts.[75] They attributed the higher activity to easy adsorption-dissociation of OH^- over the SnO_2 surface which changed the electronic effect and accelerated the adsorption of ethanol on the surface of Pd. Du *et al*. prepared a series of carbon-supported Pd–Sn binary alloyed catalysts using a polyol method among which $Pd_{86}Sn_{14}$/C catalyst showed much enhanced current densities.[8] They supplemented their study with DFT calculations which confirmed that Pd–Sn alloy structures leads to lower reaction energies for ethanol dehydrogenation compared to pure Pd crystal.

2.3.4.3 **Nickel-based and non-Platinum Group Metal catalysts for ethanol electrooxidation**

Ni-based bimetallic catalysts without Pt or Pd have been tested for EOR in alkaline media.[242–251] Zhan *et al*. synthesized well-dispersed mesoporous $NiCo_2O_4$ fibres using an easy-controlled template-free method with specific surface area of 54.469 $m^2\ g^{-1}$ and average pore size of 13.5 nm.[242] The catalysts exhibited significantly high EOR activity with higher current densities and lower onset potential compared to those of Co_3O_4 and NiO. Ren *et al*. reported a three-dimensional free-standing Ni nanoparticle aerogel with a graphene sheet network formed through the self-assembly aggregation of graphene accompanied by nickel nanoparticle in-situ loading on the graphene sheet during the hydrothermal reduction of graphene oxide and Ni ions.[243] The three-dimensional composite architecture revealed excellent EOR activity. Hassan and Hamid electrodeposited Ni-Cr_2O_3 nanocomposite supported on carbon electrodes for EOR

and showed that the catalytic activity of the fabricated electrodes increased with increasing the volume fraction percent (V_f%) of Cr_2O_3 in the deposited film up to 7 V_f%.[244] The Ni-Cr_2O_3/C (7 V_f%) electrode displayed significantly enhanced catalytic activity and stability towards EOR compared with Ni/C electrode. Yi *et al.* compared nanoporous Ni electrode synthesized by electrodeposition into alumina template with smooth Ni electrode and reported that nanoporous Ni electrode had dominant (111) facets and self-regulated NiOOH rich surface in KOH solution, which they ascribed to be active for EOR.[245] Tarasevich, Tsivadze, and co-workers conducted studies on anodic (RuNi/C) and cathodic (PtCo/C and CoN_4/C) catalysts, polybenzimidazole membrane, and membrane-electrode assemblies for alkaline ethanol-oxygen fuel cell.[246,249] They reported optimized atomic percent of Ru:Ni = 68:32 and the metal mass on carbonaceous support of 15-20% which was superior to commercial Pt/C and RuPt/C catalysts when calculated per unit mass of the precious metal. Using chromatographic analysis of the products, they reported the highest CO_2 yield at low electrolysis overvoltage and elevated temperature. The use of non-platinum group metals such as Au[102,208,252–257] and Rh[258,259] have also received attention especially Au-based but they are expensive for commercial applications, hence will not be discussed further.

2.4 **Ethanol electrooxidation reaction mechanism in alkaline media**

The understanding EOR mechanism is critical for the rational design of catalysts and in the reaction optimization for DEFCs. The synergy between experimental techniques and theoretical simulations has been employed to achieve this objective. A combination of pure electrochemical methods with state of the art *in-situ* analytical methods to monitor adsorbed intermediates/products is necessary to visualize the reaction paths. See the methodology chapter for more details on techniques used.

Ethanol electrooxidation mechanism has many pathways leading to controversial debates on the details in the literature. Nevertheless, there is a general consensus that EOR mechanism exhibits a "dual pathway".[110,256,287,288] Several reaction mechanism schematics have been presented to explain the mechanistic details.[102,110,145,155,170,176,287,289–298] Currently, there are two schematics which in our opinion are inclusive of all the other schematics reported in literature. One of the schematic is more general which was based on electrochemical experiments without proper identification of intermediates/products.[110,287] The second schematic is more detailed and

applicable to both acidic and alkaline conditions.[155] The first and more general schematic is shown in Figure 2.14 which shows a dual path reaction where in one path the reactive intermediates are weakly bound to the catalyst surface which leads to incomplete oxidation "C_2 pathway".[110,287] The other pathway involves the strongly bond intermediates which can be fully oxidized to CO_2 "C_1 pathway" if the right conditions are met, otherwise they can block the catalyst surface hence are called poisons.

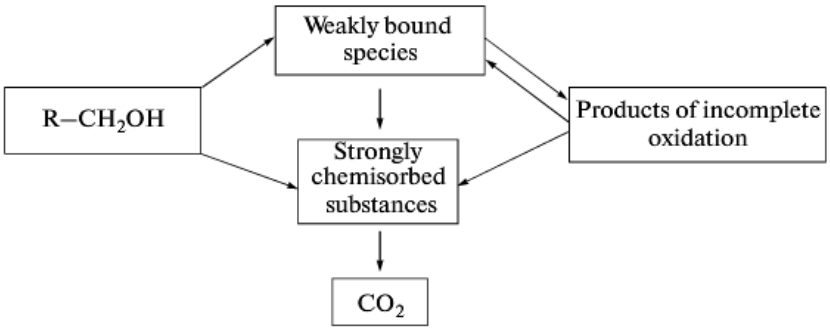

Figure 2.14: The proposed general "dual pathway" EOR mechanism scheme. Reproduced with permission from reference [287]

The arrows in Figure 2.14 show the interplay between the two pathways. In the dominant C_2 pathway, the C–C bond does not break and ethanol is oxidized to products such as acetaldehyde, acetic acid, acetate, germinal diols etc. depending on the electrolyte used. In the C_1 pathway, the C–C bond is broken and the fragments are oxidized into CO and eventually CO_2.

The second and more comprehensive schematic presented to date is shown in Figure 2.15.[155] It was based on cumulative experimental data from different groups and intuition.

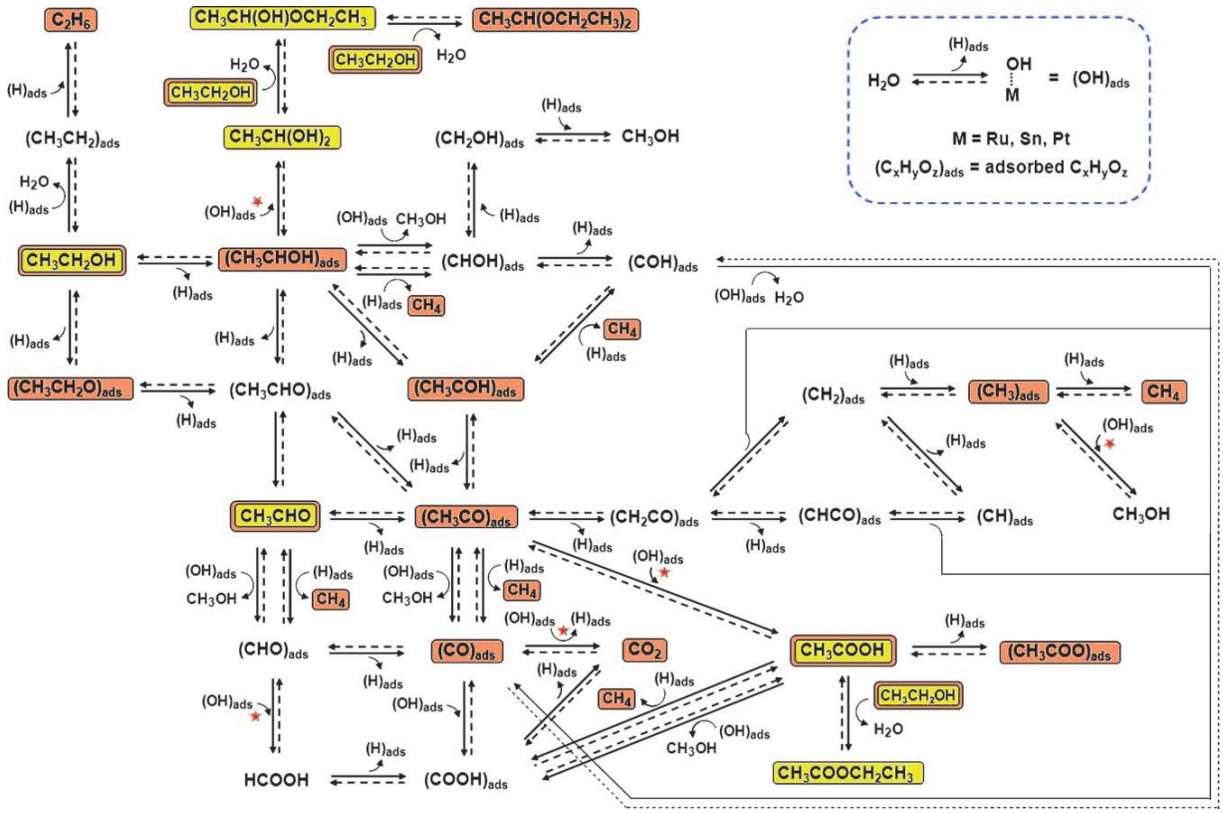

Figure 2.15: Schematic for EOR pathways on Pt-based catalyst proposed on the basis of NMR data and prior literature by 2011. The chemical species highlighted in yellow were observed by NMR while those highlighted in brown were observed by other analytical techniques in previous studies. Figure reproduced with permission from reference [155]

In the schematic, the yellow highlighted species were identified with NMR [155,286] while the brown highlighted species had been identified by DEMS, chromatography, and infrared spectroscopy. The reaction steps marked with red stars (*) are those in which OH_{ads} are involved and catalytic sites are regenerated due to reaction with OH_{ads}. Note that although, the schematics show the reaction paths in a stepwise manner it is possible some steps would happen in a concerted manner as suggested in literature.[299] The schematic is universal in a sense that it can be used to explain observations in both acidic and alkaline conditions. Therefore, the schematic in Figure 2.15 stands out among many schematics [102,110,145,155,170,176,287,289–298] in highlight experimental progress made in understanding EOR without theoretical insights. It is important to note that EOR intermediates/products are influenced by the nature of the catalyst, the electrolyte, and the applied potential. Therefore, not all the intermediates/products shown would be observed in each reaction.

The schematic in Figure 2.15 tells us that there are three possible routes for ethanol electrooxidation. The first two pathways are due to dehydrogenation which would lead either to adsorbed CH_3CHOH or CH_3CH_2O in the first step. In the second step, acetaldehyde is the central molecule. Following these first two steps in EOR, there are many other possibilities as shown in the schematic of which the details are not necessarily accurate as presented in the Figure 2.15. The third pathway is due to loss of the water molecule to form adsorbed CH_3CH_2 which can be reduced to ethane. Path three is specific to acidic media where ethane was observed as one of the products in low/cathodic potential. The key points we would like to highlight from Figure 2.15 are: i) Acetyl (CH_3CO) pathway leads to the cleaving of the C–C bond to form CO_2 but it faces a strong competition to formation of acetic acid and/or ethyl acetate instead based on quantitative analysis of the products, ii) the NMR technique was critical in identifying products such as ethyl acetate ($CH_3COOCH_2CH_3$), germinal diol ($CH_3CH(OH)_2$), and $CH_3CH(OH)OCH_2CH_3$, iii) the link of the reactions leading to some products is not explicitly presented such as $CH_3CH(OH)_2 \rightarrow CH_3COOH$, iv) the schematic does not incorporate first-principle insights available in literature. The last two points represents the weaknesses of the schematic which will be addressed in a different forum. Herein we focus our attention to what has been done for EOR in alkaline media particularly in addressing the question as to why it is difficult to break the C–C bond.

The understanding of EOR mechanism in alkaline conditions is at infancy, for only a few studies provide the molecular information.[300–302,295,303,104,272,304] The reason for the scarcity of EOR mechanism details was the fact that the produced CO_2 forms soluble carbonates in the presence of aqueous alkaline electrolyte, which makes it difficult to study using FTIR or model DEMS systems. Rao *et al*. overcame this obstacle by using alkaline polymer electrolyte membranes which gave them opportunity to observe CO_2 produced during EOR using fuel cell effluents coupled to DEMS system.[104,272] Hence, DEMS was the first technique to reveal that in alkaline conditions the C–C bond cleavage in ethanol is more efficient than in acidic media. Rao *et al*. demonstrated that CO_2 current efficiency was around 55% at 0.8 V/RHE at 60 °C for alkaline MEA compared to only 2% for acidic MEAs.[104,272] The fact was confirmed by Cremers *et al*. who reported that the kinetics for ethanol oxidation in alkaline media were higher than in acidic media under the same conditions.[103] In a subsequent study, Cremers *et al*. made some of interesting observations:[305] i) in alkaline medium ethanol adsorbates can only be desorbed in form of carbon dioxide and methane, ii) pre-adsorbed CO could not be reduced to methane at Pt

in alkaline conditions, hence they ascribed methane formation from ethanol adsorbates to an adsorbed CH_x or CO_xH_y species, iii) ethanol adsorbates in alkaline media can be oxidized in two potential regions, i.e., below and above 0.9 V/RHE, iv) the calculated number of electrons per molecule of CO_2 evolved in the potential region below 0.9 V/RHE was found to be two, independent of the adsorption potential. They claimed that a form of adsorbed CO_{ads} species was present on the electrode. They suggested that the higher calculated number of electrons per molecule of CO_2 in the potential region above 0.9 V/RHE pointed to the co-existence of more than one adsorbate species. The deviation of the number of electrons per molecule of CO_2 from the value of two in the potential region below 0.9 V/RHE for stripping experiments started in cathodic direction indicated an alteration of the adsorbate in the form of CO_{ads}, initially being present, or the co-existence of two adsorbate species. Their observation that no CO_2 formation was observed in the potential region above 0.9 V/RHE for stripping experiments started in cathodic direction, lead to their conclusion that the adsorbates which are oxidized in the potential region above 0.9 V/RHE are the ones which can be reduced to methane.[305] They later determined that in alkaline media CO_2 was only formed in the potential region of the oxidation of adsorbed CO.[107] Therefore, they inferred that in alkaline conditions, CO_2 was a produced from adsorbed ethanol and not from bulk ethanol. v) The efficiency of breaking the C–C bond is lower with increasing concentration of ethanol,[305] and comparison between Pd and Pt showed that on Pd, ethanol oxidation in alkaline media is almost selectively towards acetate formation. Similarly, on Au electrodes, acetate and ethyl acetate seemed to be the exclusive products with no cleaving of the C–C bond. They reported Ni to be a poor catalyst for EOR.[129]

It has been recognized that the inconsistencies of EOR details in literature both from experimental and computational studies were due to the sensitivities of the reaction to the surface structure of the electrode and the adsorbed ions.[297] Melke *et al*. summarized the available literature data by 2010 into the reaction schematic shown in Figure 2.16.[103,298,306–308]

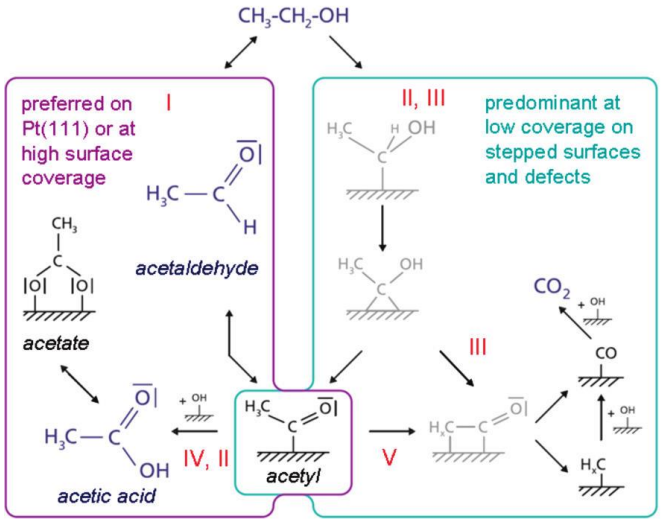

Figure 2.16: Summary of the ethanol oxidation reaction (EOR) mechanism on Pt. Path on the left is preferred in Pt(111) and at high surface coverages and the path on right side is dominant at low coverages on stepped surfaces and defects. Adsorbates pictured in black were found experimentally and molecules in blue are present in solution. Reproduced with permission from [297]

Figure 2.16, shows that there exist two main EOR paths governed by the reaction conditions and the structure/morphology of the catalyst used. Acetyl serves as a bridging intermediate between the two reaction paths, which means it will have a very small life-span once generated during the reaction due to the strong competition to either break the C–C bond or to the formation of acetic acid. The reaction path towards acetic acid (acetate) is preferred on close-packed surfaces such as Pt(111) and/or at high surface coverage (left side in Figure 2.16). On the other hand, full oxidation to CO_2 prefers open or stepped surfaces like Pt(110), Pt(100), and Pt(211) (right side in Figure 2.16) and low surface coverage. It has been suggested that the bond breaking takes place either within adsorbed CHCO or CH_2CO species,[77] and CH_x and CO are the strongly adsorbed intermediates.[305]

Fang *et al*. reported the mechanism for EOR on a Pd electrode in alkaline solution using cyclic voltammetry and *in-situ* infrared spectroscopy.[309] They observed the best performance at the pH = 14 (1M NaOH) and acetate was the main product for concentrations higher than 0.5 M NaOH. They reported that the C–C bond cleavage to form CO_2, occurred at pH $\leq$ 13 which was in agreement with online mass-spectrometry the results from Cantane and Lima evidencing CO_2 production over Pt and Pd in 0.01 M NaOH where acetic acid formation was almost absent.[131] Christensen *et al*. have shown that the interfacial pH drops at higher potentials due to the high consumption of OH^- which is not completely counterbalanced by the OH^- diffusion from the

bulk-phase.[295,303,310] This phenomenon leads to a transition from alkaline to acidic conditions at the interphase. The transition potential varies with the diffusion rate of OH^- which is dependent on the temperature and mass flow-rate. They reported that during electrooxidation reaction, ethanol is converted to acetate in alkaline pH but above the transition potential, acetic acid and traces of CO_2 are formed.[311]

A comparative study of EOR on Pd, Pt, and Rh in alkaline electrolyte through online DEMS experiments have shown similar amounts of CO_2 for the three metals but Pd electrode produced higher amounts of ethyl acetate (which they attributed to acetic acid formation).[131] The authors reported that on Pt and Rh the formation of CO_2 occurred mainly via oxidation of either the adsorbed CO or CHx species formed after dissociative adsorption of ethanol or the oxidation of the ethoxy species that takes place only at low potentials. This argument was based on the observation of methane for Pt and Rh electrodes during potential excursions to lower potentials which was lacking for the case of Pd electrode. These insights implied that the dissociative adsorption of ethanol or ethoxy species is inhibited at higher potentials on Pt and Rh as they pointed out.[131] For the case of Pd electrode, the reaction may be occurring via non-dissociative adsorption of ethanol or ethoxy species at lower potentials followed by oxidation to acetaldehyde and to acetic acid. Alternatively, they proposed a parallel reaction path where acetaldehyde molecules adsorbed on the Pd surface can be deprotonated, yielding a reaction intermediate in which the C–C bond can be easily broken and produce CO_2 after potential excursions to higher potentials.[131]

The question(s) on why is it difficult to break the C–C bond and at what intermediate does it occur during ethanol electrooxidation will be addressed in this thesis.[279]

2.5 Summary of Issues to be addressed for DEFCs

The top priority challenge for the successful development of DEFCs depends on the detailed understanding of the reaction mechanism which would pave way for the rational design of the catalysts capable of cleaving the C–C bond in ethanol. A break through in this endeavour will increase the overall DEFCs efficiency from the current 14% to 43% hence making them the strongest competitor to hydrogen fuels cells which have an efficiency of 54%.[29] Other issues which are more in the engineering development part include: membrane and ionomer

improvements, water and ethanol transport management, carbon dioxide regulation and electrolyte development.

2.5.1 **Reaction mechanism and rational catalysts design strategies**

Although, ethanol electrooxidation reaction kinetics is faster in alkaline conditions, efficient catalyst for complete oxidation of ethanol to CO_2 remains an outstanding challenge in the reviewed literature. Even after three decades of active research, there is still no selective catalyst for breaking the C–C bond. Therefore, efforts in the fundamental understanding of the reaction mechanism are required to pave the way for the rational design of efficient catalysts. On the cathode side, the challenge is how to enhance non-Pt catalysts to make them comparable to Pt for ORR.

2.5.2 **Membranes improvements**

Anion-exchange membrane can be grouped into two categories: the polyelectrolyte and the alkali-doped polymer membranes.[31] Membrane improvements in parameters such as composition, ionic conductivity, ethanol permeability, thermal and chemical stability are discussed elsewhere.[16,25,312] The main challenges with alkaline anion-exchange membranes are the low stability in OH^- and low OH^- conductivities. Therefore, efforts are required not only in developing new membrane formulations, but also the development of tools for characterising membrane properties such as water uptake, ethanol permeability, water diffusivity, and electro-osmotic coefficient.

2.5.3 **Ionomer improvements**

Ionomers are critical components of the fuel cell which helps to bind discrete catalyst particles which must form a porous conduction layer for the transfer of ions, electrons, and reactants/products.[313] Therefore, similar to membranes there is need to improve ionic conductivity, thermal and chemical stability, and making them soluble in nontoxic and cheap solvents.

2.5.4 **Water transport management**

Water management is a critical requirement for a long-term operation of DEFCs. Water is produced at the anode and consumed at the cathode which would lead to a high water crossover

from anode to cathode. Although, the water crossover phenomenon has the advantage of improving the ionic conductivity, too much water crossover would lead to the cathode flooding and hinder oxygen transport. Similarly, a low water crossover can facilitate oxygen transport but leads to mass transport loss for ORR which would result into high cathode activation loss.

2.5.5 **Ethanol transport management**

Maintaining proper circulation of the fuel (ethanol) is critical to obtaining the optimum current density and avoiding fuel waste due to incomplete reaction.[25] If ethanol concentration in the anode is too high will lead to the reduction of the coverage of OH^- and increase the anode activation loss. Secondly, high ethanol concentration will increase ethanol crossover that can reduce fuel utilization. On the other hand, too low ethanol concentration level in the anode will increase mass transport loss and reduce the optimum current. Therefore, efforts in the design of the anode flow field as well as determining the optimum operating conditions, such as ethanol concentration supplied to the flow field and the ethanol solution flow rate in the flow field and temperature are required.

2.5.6 **Carbon dioxide regulation**

It is cheaper to use air rather than oxygen in the fuel cells but this presents a challenge for alkaline fuel cells because air contains around 0.039% (volume fraction) of CO_2. Under standard conditions, this CO_2 will react with the OH^- generated by the ORR to form carbonate (CO_2^{3-}), which may affect cell performance in two aspects: [25] i) by decreasing the pH level in the cathode, thus affecting the kinetic of the ORR, and ii) by reducing the ionic conductivity in both the cathode and membrane, increasing the cell resistance. Hence, the problem associated with CO_2 from air is an issue that needs to be addressed in the future.

2.5.7 **Electrolyte (KOH, ionic liquids etc.)**

The fact that KOH reacts with CO_2 produced at the anode or from the air at the cathode presents a serious challenge. As discussed above KOH reacts with CO_2 to form carbonate which precipitates and blocks the pores of the membranes and the electrodes. At the cathode, KOH can reduce the hydrophobicity of the gas diffusion layer, thereby breaking the balance of mass transport between water and oxygen. Therefore, efforts in consideration of other possible

electrolyte formulations such as ionic liquids to mitigate the use of the KOH will be welcomed in the future studies.

2.6 **Conclusions and Outlook**

From the survey of the literature presented herein, it is clear that in the past two decades tremendous effort have been devoted in developing DEFCs from both the fundamental understanding of the reaction to the prototype fuel cell design development. From fundamental perspectives, many analytical techniques have been extended towards in-situ identification and quantification of the reaction products. This is a significant advancement for they now provide the opportunity to visualize the progress of the reaction in real-time hence provides the much needed insights for understanding the reaction mechanism. A range of tools (electrochemical techniques, mass spectroscopy, surface enhanced Raman spectroscopy, sum frequency generation spectroscopy, X-ray absorption spectroscopy, chromatography, and nuclear magnetic resonance spectroscopy) and protocols for using them to probe electrocatalytic reactions in-situ are now available in the literature. Besides the electrochemical techniques, infrared spectroscopy, nuclear magnetic resonance spectroscopy, and X-ray absorption/photoemission spectroscopy are recommended as complementary techniques to capture complete details of the reaction mechanism. To complement these experimental tools is the use of first-principles calculations such as DFT for atomic insights to facilitate the screening of the best candidate catalysts for experimental testing. Combining the contributions of these various techniques for the past two decades has provided good understanding of EOR mechanism although it is very complex. A special credit goes to the application of NMR[155,286] which has disclosed intermediates such as $CH_3CH(OH)_2$, $CH_3CH(OH)OCH_3$, $CH_3CH(OH)OCH_2CH_3$, and $CH_3COOCH_2CH_3$ which were impossible to distinguish with the other techniques used so far.

When it comes to catalyst design, excellent progress has been made which allows tailoring the nanoparticle structures and morphology from the atomic level. Now it is possible to make nanoparticles with preferred facets (111, 100 etc.), dimensions (1D, 2D, 3D such as nano-sheets, nano-wires, nano-tubes, nano-cages, nano-boxes, nano-spheres etc.), and compositions (mono- or multi-metallic). All these possible structures provide great opportunities for structure-activity relationship studies which are yet to be optimized for EOR. These possibilities also present a great challenge for there are many to be optimized. In addition to these possibilities, there is

great consensus in literature that supports have a significant influence on the catalytic properties of the nanoparticles. Of particular interest are the metal-oxide supports such as SnO_2, CeO_2, NiO/foams, and TiO_2. In terms of selectivity towards cleaving the C–C bond, CeO_2 stands out as the best candidate support. On the other hand SnO_2, although it significantly improves the reaction kinetics, the selectivity for breaking the C–C bond is very poor. However, it presents the opportunity of considering running the EOR in DEFCs with the benefit of getting value added chemicals instead of CO_2. In designing the catalyst structures, it seems the efforts should be focused on 3D and/or mesoporous materials. This is because, from computational insights, ethanol is reported to preferentially adsorb with the oxygen lone pair of electrons which allows the activation of the alpha-carbon (α-C). Therefore, it would be interesting to confine ethanol molecule in thin-cavity catalysts which would allow the beta-carbon (β-C) to be activated too.

Five prototype DEFCs have been proposed and tested in literature to date. They are proton-exchange membrane fuel cells, anion-exchange membrane fuel cells, alkaline-anode acid-cathodes fuel cells, direct alkaline fuel cells without membranes, and solid oxide fuel cells. Each design has its own advantages and disadvantages which mean that there should be simultaneous development and optimization hence presents a great challenge. Nevertheless, these provide the opportunity to start identifying for what application each design is best suited for and the potential returns. Regardless of which prototype design is the best, the various components of the fuel cells still needs combined efforts of both scientists and engineers. These components include the development of membranes, ionomers, catalysts (anode and cathode), water transport and ethanol transport management, carbon dioxide management, and electrolyte formulations that favour the reaction selectivity towards complete oxidation. For the electrolyte formulations, there is need to use buffer solutions to mitigate the effect of the changing pH at electrolyte/electrode interfaces. The changing pH when working especially in alkaline conditions alters the reaction kinetics as reported in the literature. The other option would be to consider the use of ionic liquids with ions which would not block the catalyst active sites for ethanol oxidation. Overall, the development for DEFCs looks promising in the near future.

Chapter 3: Research methodologies

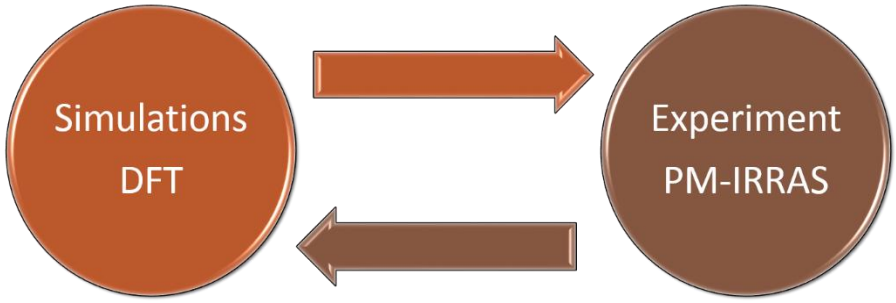

3.1 Introduction

The methodologies used to achieve the objectives set out in this project can be broadly grouped into two categories: i) Experimental methods, and ii) Computational approaches. The chapter merges all the experimental details from the other chapters published elsewhere in addition to some extra details specific to our lab which are not published and may vary from one laboratory to another.

3.2 Experimental details

3.2.1 Materials

The following materials: Palladium chloride ($PdCl_2$) anhydrous (*Fisher*), Ruthenium (III) chloride ($RuCl_3$) 99.99% anhydrous (*Alfa Aeser*), Ethylene glycol (EG) (*Fisher*), Potassium hydroxide (KOH) 85% (*EMD*), Sodium hydroxide (NaOH) ACS grade (*EM Science*), carbon black (C) Vulcan XC-72R (*Cabot*), Nitrogen gas (N_2) 99.9% (*Linde*), carbon monoxide (1000 ppm CO in He) (*Linde*), Nafion perfluorinated ion-exchange resin 5 wt.% solution in lower aliphatic alcohols/H_2O mix containing 15-20% water from (*Aldrich*), and Ethanol 99.9% (*Fisher*), $NaBH_4$ (*Acros Organics* 98+%), HCl (*Fisher* 36.5-38%), Tin oxide (*NanoArc* 99.5%), Titanium oxide (*Kronos* ≥ 96.5%, 2073), and Cerium oxide (*Alfa Aesar* 99.5%) were used as received.

3.2.2 Catalyst preparation – Polyol method

The Pd_xRu_{1-x}/C nanoparticles were prepared using a polyol method reported in literature.[1,2] In a typical synthesis, 0.25 g of the metal precursor salts ($PdCl_2$ and $RuCl_3$) were separately dissolved in 50 mL of EG. Then appropriate amounts of the two salt solutions were mixed to prepare Pd_xRu_{1-x} (x = 1, 0.99, 0.90, 0.95, 0.80, 0.50 and 0). The solution pH was adjusted to 8 by adding 0.06 M NaOH in EG. The mixture was homogenized by stirring for 30 minutes at room temperature before refluxed at 160° for 2 hours. To the resulting colloidal NPs, appropriate amount of carbon black was added to obtain supported catalysts of 20 wt. % loading. The mixture was stirred for 48 hours so as to achieve high dispersion and complete deposit of Pd-Ru nanoparticles. The supported catalysts were thoroughly washed and rinsed five times with de-ionized water (18 Ω cm) to remove EG and salt ions through vacuum filtration and dried in the oven at 100°C for 4 hours.

3.2.3 Catalyst preparation – $NaBH_4$ reduction method

The palladium nanoparticles were synthesized using $PdCl_2$ as precursor salt and was deposited in-situ on the support using $NaBH_4$ as a reducing agent. The $PdCl_2$ salt (67 mg) was dissolved in 5 mL of water and 100μL of HCl. The 50 wt.% of the supports; Vulcan carbon black, Tin oxide (SnO_2), Titanium oxide (TiO_2), and Cerium oxide (CeO_2) were each mixed in 5 mL of water. Then the aqueous solutions of $PdCl_2$ and that of each support were combined together and diluted to 50 mL using deionized water (Millipore Milli-Q 18 Ωcm). The solutions were stirred in the air environment for at least one hour or until were well homogenized. A 2 wt.% (36 mg) solution of $NaBH_4$ was prepared during the stirring in order to avoid the loss of hydrogen via evolution. The aqueous $NaBH_4$ was added dropwise, with a stoichiometric excess of 100%, to the reagents. The resulting colloidal solution was kept stirring for 15 minutes to ensure complete reduction of $PdCl_2$ and was then washed twice with deionized water and twice with ethanol before being dried in a freeze dryer.

3.2.4 Physical characterization techniques

3.2.4.1 Transmission Electron Microscopy (TEM)

TEM is a powerful microscopy technique for visualizing materials at atomic level. Its working principle is based on the transmission of a beam of electrons via an ultra-thin sample and forms

an image as a result of the interaction of the electrons transmitted through the sample. The image is then magnified and focused onto an imaging device for output. Scanning Transmission Electron Microscopy (STEM) is similar to TEM with the exception that a narrow beam of electrons is focused on the ultra-thin sample and scanned over in a raster. The average particle size from these techniques was estimated using ImageJ software by counting at least 300 particles per catalyst.

TEM measurements were performed on JEOL JEM-1230, 100 kV. The catalyst powders were dispersed in alcohol and water through ultrasonication. The appropriate amount of the catalyst powder solution was dropped onto the copper grid and air-dried for TEM measurements.

STEM measurements were performed on the FEI Titan3 80-300 microscope equipped with a CEOS aberration corrector for the probe forming lens and a monochromatic field-emission gun was used to acquire HAADF-STEM images of the nanoparticles supported on carbon samples. The HAADF-STEM was operated at 300 k eV. The specimens were prepared by sonicating the as-prepared catalyst powders in ethanol. One drop of the solution was then placed onto a 200 mesh TEM copper grid coated with a lacey carbon support film (Ted Pella) and dried in air.

3.2.4.2 **X-ray diffraction (XRD)**

XRD is a powerful technique for characterizing crystalline materials to reveal their bulk structure. It is based on the principle that when X-rays pass through a crystal, each atom in the structure scatters the waves uniformly in space. The interference of all these scattered waves in large crystals leads to destructive interference in most of the directions because for every wave scattered a second wave in the crystal exists with a phase shift of half-wave length. Constructive interference occurs only in certain directions which are related to the distances between atomic planes, i.e., the d values, and the angle θ at which the X-rays enter and leave a crystal.[3] Therefore, the diffraction patterns are used to construct the bulk crystal structure of a material.

X-ray diffraction patterns in this work were collected using a Rigaku Ultima IV diffractometer using a Cu Kα X-ray source (λ = 1.54183 A, 40 kV, 44 mA). The diffraction patterns were recorded in the focused beam geometry with a divergence slit of 2/3 °, a scan speed of 0.17 ° min^{-1} and a scan step of 0.06 ° between 30 ° and 75 °. The diffraction patterns from Pd_xRu_{1-x} colloids were collected with and without the carbon support for catalyst with lower Ru content and the key reflections were confirmed to be unchanged due to presence of carbon. However, for

samples with more than 10%Ru content, patterns from colloidal solutions were recorded to avoid the diminished peak intensities. The crystallite size of the nanoparticles was estimated using Scherrer equation based on the (111) peak of Pd and the full width at half maximum (FWHM) of the peak.

3.2.4.3 **X-ray photoelectron spectroscopy (XPS)**

XPS is a sensitive spectroscopic technique that measures the elemental composition of surfaces at the parts per thousand ranges. It provides useful information on the chemical state and electronic state of the elements that exist within a material. These information is extracted from the binding energies of the electrons ejected from the surface atoms of the materials.[4]

In this work, XPS measurements were performed in a KRATOS Axis Ultra DLD with a Hybrid lens mode at 140 W and pass energy of 20 eV using a monochromatic Al Kα. The appropriate amount of catalyst powder dispersed in ethanol was pipetted onto a piece of Si substrate and then dried for the XPS analysis. In all cases no Si2p peaks were observed showing that the substrate was covered with a relatively thick layer of catalyst. The Pd3d XPS core level spectra were analyzed using a fitting routine which decomposes each spectrum into individual mixed Gaussian-Lorentzian peaks using a Shirley background subtraction over the energy range of the fit using XPS PEAK 4.1 software. Their deconvolution was carried out using doublets with spin orbit splitting 5.3 eV and intensity ratio $Pd3d_{5/2}$:$Pd3d_{3/2}$ = 3/2,[5] while a peak asymmetry was used in the case of the Pd3d peak, which was attributed to the metallic state as reported by Hufner *et al.* [6] The peak asymmetry of the metallic state was defined by using the sample of pure Pd after reduction under H_2. Binding energy scale was corrected using the C1s peak at 284.6 eV as an internal standard. The accuracy of measurement of the binding energy is ± 0.1 eV while that of FWHM ± 0.05eV.

3.2.5 Electrochemical measurements

Two electrochemical measurement techniques were used in this study, i.e., cyclic voltammetry (CV) and chronoamperometry (CA) techniques, which are commonly used for the evaluation of electrocatalysts. CV is a potentiodynamic technique for acquiring qualitative information on heterogeneous electron-transfer reactions and redox processes such as locating the redox potentials of the electroactive species.[7] The technique consists of scanning linearly the potential of a stationary working electrode using a triangular potential waveform and measuring the

current resulting from the electrochemical reactions. CA on the other hand, involves applying a constant potential to the working electrode and monitoring the current response with time. It is used mostly to test the catalyst stability, to measure the diffusion coefficient of electroactive species or to measure the surface area of the electrode.[8]

The CV and CA measurements were performed using a BioLogic VSP potentiostat equipped with the EC-Lab software.[8] All experiments were conducted at room temperature in a customized Teflon cell. A glassy carbon (GC) electrode of 0.1962 cm^2 geometric surface area was used as the working electrode. In the earlier part of the project, the potentials were measured with respect to mercury-mercurous sulphate (Hg/Hg_2SO_4, K_2SO_4) electrode (MSE) but later was changed to Mercury-mercury oxide (Hg/HgO) from Koslow scientific. Therefore, some potentials are reported verses MSE, some verses Hg/HgO, and others verses RHE to maintain the conventions used during their respective publications. A large surface area Pt-gauze served as a counter electrode. 1M KOH was used as the electrolyte and was continuously purged with nitrogen gas. The GC-electrode was polished prior to each experiment using a solution of 6 μm ground alumina on a polishing cloth.

The CV measurements vs MSE were carried out between -1.4 V to -0.4 V at a scan rate of 20 mVs^{-1}.[9] The CVs vs Hg/HgO were done in the range of -0.65 V to 0.15 V. Ten cycles were performed using a scan rate of 25 mVs^{-1} and then five cycles at 5 mV s^{-1} were collected from which a representative cycle is reported. The chronoamperometry measurements were performed at different potentials for 1.5 hours. The CVs were recorded before and after each CA measurement to verify the stability of the catalyst. All current densities were normalized with respect to mass loading of Pd (mA mg^{-1}Pd) in order to compare the performance of the catalysts.

The catalyst inks were prepared by dissolving 6 mg of catalyst powders in 1 ml of de-ionized water, 200 μL of ethanol, and 100 μL of Nafion perfluorinated ion-exchange resin 5 wt.% solution in lower aliphatic alcohols/H_2O mix containing 15-20% water from (*Aldrich*). The mixture was sonicated for at least 10 min to form a homogeneous colloidal solution. The ink solution (5 μL) was deposited onto the GC-electrode surface and dried in air at room temperature for about 15 min and used as the working electrode.

The CO stripping experiments were used for two purposes: i) to determine the electrochemical active surface area (ECSA), ii) to characterize and compare the electrochemical surface activity of the catalysts. The CO stripping experiments were carried out in a solution of 1M KOH. First

nitrogen was bubbled through the solution for 30 minutes to remove any dissolved oxygen. Then ten CVs were done in order to have a stable and reproducible CV in 1M KOH. The potential was then held at -0.55 V/MMO (or -1.1 V/MSE) for 30 minutes, while bubbling CO for the first 20 minutes in order to saturate the Pd nanoparticles surface. Nitrogen was then bubbled through the solution for the remaining 10 minutes to remove excess dissolved CO. The potential was then cycled between -0.7 V and 0.2 V starting from the holding potential at a scan rate of 25 mVs^{-1}. For experimental and data processing details in lieu of spectroelectrochemical measurements are provided in chapter 4.

3.3 Computational approaches

DFT calculations were performed with the Vienna *Ab-initio* Simulation Package (VASP version 5.3.3).[10,11] The generalized gradient approximation of Perdew, Burke, and Erzenhorf (PBE)[12] was used to compute the exchange-correlation energy. The projected augmented wave (PAW) method [13,14] was employed to describe the core-electron interaction. A plane-wave basis set with an energy cut-off was set to 400 eV was used. The Pd surfaces were modelled by a periodic slab with a p(3x3) unit cell of five Pd layers and a vacuum regions of 10 Å. A 7 x 7 x 1 Monkhorst-Pack *k*-points mesh was employed for the Brillouin zone integration together with a second order Methfessel-Paxton smearing method [15] with a sigma of 0.2 eV.

The Pd slabs were cut from the optimized bulk unit cell with a lattice constant of a = 3.94 Å. All the other fcc metal slabs were generated from the optimized Pd (111) cell parameters and were scaled using the ratio of Pd:M lattice parameters (where M is the lattice parameter of the optimized unit cell of the metal). Similarly, for the hcp metals were generated from the optimized Ru(0001) with cell parameter (2.71 and 4.28 Å). In all geometry optimizations only the top-two monolayers were allowed to relax whereas the bottom three layers were kept fixed. All optimizations were carried out to forces below 0.02 eV/Å.

All energies are referenced to the bare Pd slab, ethanol, water and hydrogen in the gas phase. The latter two serve to introduce oxygen atoms and to account for the coupled proton-electron transfers, respectively. In particular, the reaction energies of electrochemical steps (i.e. steps where the number of protons in the system is changing) are computed according to the computational hydrogen electrode,[16] e.g. the reaction (equation 3.1):

$$CH_3CO + H_2O \rightarrow CH_3COOH + 2H^+ + 2e^- \quad (3.1)$$

is computed as (equation 3.2)

$$E_{rxn} = E_{(CH3COOH)} - (E_{(CH3CO)} + E_{(H2O)} + 0.5\ E_{(H2)}) - 2U \quad (3.2)$$

Where we have assumed U to be with respect to the pH insensitive RHE and a pH of 0. Note that at pH = 14, we write the same expression for the reaction energy, but formulate the reaction as

$$CH_3CO + OH^- \rightarrow CH_3COOH + e^- \quad (3.3)$$

Similarly, we write

$$CH_3CHO + OH^- \rightarrow CH_3CO + H_2O + e^- \quad (3.4)$$

in alkaline conditions and compute the reaction energy (E_{rxn}) as

$$E_{rxn} = E_{(CH3CO)} - (E_{(CH3CHO)} + 0.5*E_{(H2)}) - U \quad (3.5)$$

The transition states (TS) have been located as follows: the state with the C–C bond broken was constructed in analogy to the adsorption mode of the individual fragments. This co-adsorbed state was optimized in order to ensure that no significant lateral interactions were introduced. Then, a rough nudged-elastic band (NEB) [17] computation with 8 images between the initial and final state was performed, seeded by interpolations between the two states obtained by Opt'n Path code [18] which uses a combination of internal and Cartesian coordinates. After about 50 cycles of NEB, an improved guess for the transition state was obtained, which was refined by the dimer method [19] and verified to be a first order saddle point by a frequency analysis.

Infrared spectra of surface species were modelled following the same procedure, the intensities being evaluated using density functional perturbation theory.[20] Infrared spectra of solution species were computed using the same DFT functional (PBE) combined with a continuum model for the water solvent (PCM) [21] with a def2-TZVP basis set using the Gaussian09 version D.01 program.[22]

Chapter 4: Polarization Modulation Infrared Reflection Absorption Spectroscopy (PM-IRRAS) Utility in Surface and *In-situ* Studies: Experimental and Data Processing Details

Publication: E. A. Monyoncho, V. Zamlynny, T. K. Woo, and E. A. Baranova *xxx* 2017 – Analyst (submitted)

Abstract

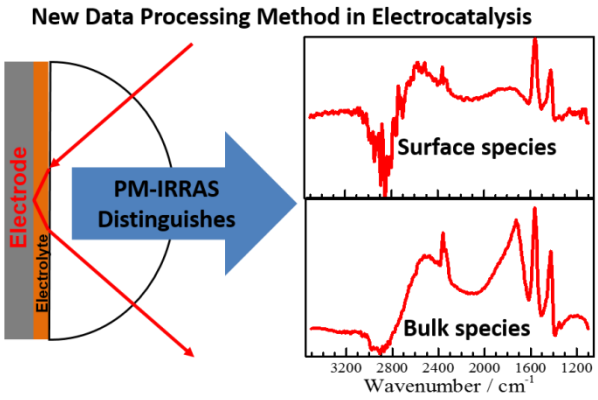

Infrared spectroscopy is a powerful non-destructive technique for identification and quantification of organic molecules widely used in macromolecular studies. For many years there have been efforts to adopt the technique for *in situ* monitoring of reactions. From these efforts polarization modulation infrared reflection absorption spectroscopy (PM-IRRAS) was developed three decades ago. Unfortunately, because of the poor signal to noise ratio (S/N) and the complexity in data processing and interpretation, PM-IRRAS had been avoided in lieu of the single potential alteration infrared (SPAIRS) and subtractively normalized interfacial Fourier transform infrared spectroscopy (SNIFTIR). In this work, we present a new approach for PM-IRRAS data processing which provides more insights than ever reported before and dramatically improves the S/N. In the new approach, we recommend three complementary equations (equation 4.7, 4.9, and 4.10) as the new standard protocol for presenting PM-IRRAS data. These equations are robust in visualising surface processes such as solid-liquid and solid-gas interphases. Equation 4.7 highlights the surface absorbed species with respect to isotropic background with or without the influence of the applied potential. Equation 4.9 highlights the

surface potential-driven changes between the sample and reference reflectance spectra, where the surface thickness is governed by the optical constants of the reflective surface, and is less than 1 μm for glassy carbon (Figure 4.7a). Equation 4.10 highlights bulk-phase potential-driven changes in both solution-phase and surface species between the sample and reference spectra (Figure 4.7b), hence can be used to track the production of volatile and non-volatile species which desorb from the surface as soon as they are formed. Examples of ethanol electrooxidation reaction data are provided to illustrate the new utility of the PM-IRRAS technique which is poised to modernise our understanding of surface process chemistry and physics.

Keywords: PM-IRRAS; Spectroelectrochemistry; Electrocatalysis, Experiment optimization; interfacial electrochemistry; ethanol electrooxidation

4.1 Introduction

Many surface sensitive spectroscopic techniques have been developed to aid in unraveling i) the identity of adsorbed and solution species that are formed during electrochemical perturbations such as redox processes at the electrode-liquid interfaces, ii) the surface bonding, intermolecular interactions, and the electric field-driven dynamics of adsorbates, and iii) in monitoring the potential-dependent concentrations of molecular and ionic species, both adsorbed and in solution.[1] Among these techniques are: infrared absorption (IR) spectroscopy,[2–6] surface-enhanced Raman spectroscopy (SERS),[7,8] sum frequency generation (SFG) spectroscopy,[9,10] etc. Infrared techniques are particularly of interest because they can provide information about the structure and geometric orientation of adsorbed molecules. The main sampling modes for IR spectroscopy are; transmission, diffuse reflectance infrared Fourier transform (DRIFT), attenuated total reflection infrared (ATR-IR) spectroscopy also called surface-enhanced infrared reflection absorption spectroscopy (SEIRAS), and infrared reflection absorption spectroscopy (IRRAS). The aim of this work is to showcase the development stages of IRRAS leading to polarization modulation infrared reflection absorption spectroscopy (PM-IRRAS) and the major break-through we have made in signal processing which is expected to significantly improve its utility in electrocatalysis and macromolecular (such as biomolecular) surface studies, especially when using electric potential perturbations.

The foundational principles of IRRAS were established by Greenler's theoretical and experimental work in the 1960s.[11,12] In these works, Greenler first used calculations to show that

a thin, moderately absorbing, organic layer on a metal surface has an absorption factor in the infrared which varies greatly with the angle of incidence and the state of polarization of the incident radiation.[11] Following these theoretical insights, he presented the requirements for a spectroscopic system under conditions of multiple reflections and described a method for obtaining many reflections between closely spaced mirrors, which he constructed and used to get a spectrum of a cellulose acetate layer on a silver mirror for illustration.[12] These works were seminal because they opened the field of IRRAS use for obtaining detailed molecular information about the chemical identity, geometry, and adsorption site of adsorbed species on surfaces. These molecular level insights are critical for understanding not only the reaction mechanisms but also the interaction between surfaces and adsorbates such as polymers and proteins.

Therefore, IRRAS is a powerful technique for studying thin-films, solid-liquid and solid-gas interfaces at the molecular level. However, in the external reflection geometry, which is amenable for *in-situ* studies, IRRAS suffers the challenge of strong IR absorption from the electrolyte for the case of solid-liquid interfaces. Traditionally, attenuated total reflectance (ATR) approach was preferred for *in-situ* measurements because it eliminated the solvent contribution. Unfortunately, ATR has poor sensitivity and limited choice of useful electrodes (only IR transparent electrodes can be studied).[1] To overcome these challenges, efforts were directed towards the development of suitable external reflection cells.[13–16] To improve the sensitivity to surface species, the development of external infrared reflection spectroscopy led to two modulation techniques. In the first approach, the potential was modulated. This approach led to the development of techniques known as "electrochemically modulated infrared spectroscopy EMIRS",[13,14] and "subtractively normalized interfacial Fourier transform infrared spectroscopy (SNIFTIRS)",[15] and "single potential alteration infrared spectroscopy (SPAIRS)".[16] The potential modulation approach has been extensively used for *in-situ* IR studies on the electro-oxidation of small organic molecules on electrode surfaces. EMIRS was the first attempt to develop *in situ* external infrared reflectance method from the internal infrared reflectance method just developed. EMIRS was analogous to the external reflectance method used in the UV-visible region and in Raman spectroscopy (SERS) method. Parallel with respect to the plane of incidence, p-polarized radiation was used for measurements since the perpendicularly (with respect to the plane of incidence) s-polarized component was known to be inactive at the metal

surface. Therefore, only vibrational modes producing dipole changes with a component perpendicular to the electrode surface were observable from the spectra of adsorbed species (*vide infra*).[17] The development of EMIRS was a significant shift which went against the established assumptions that the presence of an aqueous electrolyte would cause insurmountable problems to the development of *in situ* external IRRAS cell.[18]

One has to take into account during EMIRS data interpretation, that the modulation of potential yields the difference spectra between the species in solution near the electrode and the adsorbed species on the electrode surface. Such spectra often display bipolar features and look different compared to the complete spectra of the adsorbed molecules.[17] The extension of EMIRS from dispersive instruments to Fourier transform instrumentation is what is generally known as SNIFIRS. However, there were some minor additional improvements. In SNIFTIRS, the potential of the electrode was held at some reference potential E_1 and an IR reflectance spectrum was obtained several times and averaged as R_1.[15] Then the potential of the electrode was stepped to a second potential of interest E_2, and the procedure was repeated to obtain the averaged spectrum R_2. The base potential E_1 is normally chosen at a value where no Faradaic processes occur, so that R_1 is the reflectance spectrum of the solvent, electrolyte, substrate, and optics.[17] The potential is then stepped to a value E_2 where electron transfer at the substrate occurs. Therefore, R_2 spectrum recorded under same experimental conditions as R_1 additionally contains spectral information of the electro-generated product(s) and consumed reactant(s). The signal is calculated and reported as the difference spectrum between R_2 and R_1, normalized by the reference spectrum R_1, i.e. $\Delta R/R = (R_2-R_1)/R_1 = R_2/R_1 - 1$. In its original form, EMIRS was suitable for studying reversible potential-depended phenomena such as CO adsorption and oxidation. Therefore, in parallel to SNIFTIRS, SPAIRS was developed to mitigate the limitation of EMIRS that allows examining only reversible potential-depended phenomena by adapting this technique to examination of the potential-induced changes associated with chemically irreversible processes, such as electrooxidation of organic molecules.[16] The principle behind SPAIRS was that a single potential excursion was employed during the spectra acquisition, which allowed changes in the thin-layer solution composition as well as the interface itself to be monitored. The electro-generated products' signal was obtained by subtracting a spectrum acquired immediately prior to the application of potential from the signal acquired following the electrode potential excursion. Hence, SPAIRS and SNIFTIR are the same in principle and both

allow the quantitative determination of the potential-depended reaction products. They also both, require high signal-to-noise (S/N) ratio before these techniques can be used for quantitative determinations.

Alternatively, the radiation polarization can be modulated between the orthogonal states to achieve surface sensitivity. Such an approach is utilized in a technique known as polarization modulation infrared reflection absorption spectroscopy (PM-IRRAS).[19,20] PM-IRRAS (in some literature given as IRRAS), was developed as the most sensitive technique for species close to the reflecting surface. In PM-IRRAS, polarized IR radiation is modulated between the parallel (p-) and perpendicular (s-) states with a high-frequency modulator (such as photoelastic modulator, PEM). The physics of electromagnetic interaction with flat solid surfaces is now well understood.[11,12,18,35,36] The reflectivity of a material depends on its optical constants (*n, k*), angle of incidence (Θ), and polarization of incident radiation.[36] Figure 4.1 shows how the reflection of electromagnetic radiation takes place from reflective surfaces for s- and p-polarized radiation, respectively.[11]

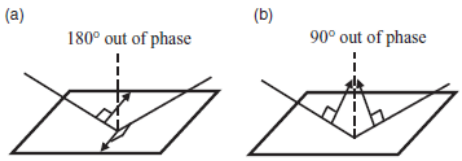

Figure 4.1: Greenler's original description of the interaction of polarised radiation with a mirror surface during IRRAS experiments.

While s-polarised radiation undergoes a 180^0 phase shift (Figure 4.1a) resulting in a nodal point (zero magnitude) in the corresponding electric field, p-polarised radiation has significant component which is normal to the surface (Figure 4.1b) and thus gets enhanced field that can approach almost 4x the initial mean squared electric field strength (MSEFS) at optimal angles.

The advantages of PM-IRRAS compared to the other techniques were highlighted by Faguy *et al*. who showed that besides superior S/N, the PM-IRRAS was almost insensitive to atmospheric water and carbon dioxide.[24,25] The main challenge limiting the universal utility of PM-IRRAS has been the broad-band background that is introduced to the spectra because PEM can be optimized for a monochromatic IR light while the polychromatic radiation is sent through the device in the Fourier transform instrument, complicating quantitative spectra interpretation.[26] Significant efforts have been directed towards removing these PEM artefacts through

normalization by reference spectrum [27] or by using a calibration spectra acquired in an independent experiment.[28] In this work, we provide a new approach for processing PM-IRRAS data to overcome this challenge.

It is important to note that most of the *in situ* infrared reflection absorption studies reported in literature is done using single crystal metallic electrodes. However, electrochemically inactive glassy carbon (GC) is considered the best conductive substrate for studying metal nanoparticles. Although, Datta *et al*.[29,30] have shown that the GC can be used as the reflective surface, studies using GC are scarce.[31] This restriction has been imposed by the established assumption that a shiny reflective surface was necessary to improve the S/N, hence limiting the application of the technique to nanoparticle electrodes. Interestingly, a look at Greenler's seminal work showed that the absorption factor (*A*) of the surface species "ignores the effects of reflection from the surface of the thin absorbing layer, the change in reflection conditions at the metal surface produced by the thin layer, multiple reflections within the layer, and other effects" but it is rather governed by the "standing wave electric field, into which the thin absorbing layer is introduced".[11] The standing wave electric field is produced due to the combination of incident and reflected light at the reflective metal surface and is dependent on the angle of incidence.[11] Note that the boundary between surface species and bulk gas or liquid phase is defined by the distance between the surface node and the adjacent antinode of the standing wave, which is between 6,000 and 25,000 Å in the mid-infrared (MIR).[11] Therefore, the surface roughness of 50 nm (500 Å) typical for metal nanoparticles should have minimal interference with the signal. It turns out that this standing wave electric field is highly depended on the nature of light polarization; for p-polarization (electric field parallel to the plane of incidence) the electric field is enhanced at the surface while for the s-polarization (electric field perpendicular to the plane of incidence) the electric field is cancelled because of the 180 º phase shift between the incident and reflected wave.[11,12,18,32,33] In this work we will demonstrate that excellent S/N can be obtained using GC with a paste of nanoparticles in aqueous electrolyte.

The aim of this work is to make available a new approach for processing and presenting PM-IRRAS data which provides additional insights on the reaction dynamics at the electrode-electrolyte interface. We demonstrate that the new approach significantly improves the S/N level to allow the monitoring electrochemical reactions employing nanoparticles deposited on GC as the working electrode in aqueous electrolyte. The use of PM-IRRAS in such extreme conditions

in this work means that it can be easily adopted for other surface analysis and in situ studies. The extension of PM-IRRAS application from the conventional single crystal reflective surface studies to nanoparticle surface studies even on GC opens the door to the huge field of nanoscience. Herein we provide experimental and theoretical details which were implemented hence leading to the excellent signal sensitivity enhancement achieved. The new approach simplifies PM-IRRAS data processing and allows direct interpretation of the spectra without the need for the extensive calibration procedures currently being used. We recommend three complementary equations as the new routine for reporting PM-IRRAS data. We envision that the new PM-IRRAS utility will enrich our understanding in many fields such as surface processes and in situ monitoring of reactions to unravel reaction mechanisms.

4.2 Experimental and theoretical approaches

4.2.1 Experimental details

PM-IRRAS experiments were performed using Bruker's Tensor 37 FTIR spectrometer equipped with a radiation polarisation modulator (PEM-100 controller with II/ZS50 ZnSe, 50 kHz optical head from *Hinds Instruments*, Hillsboro, OR), nitrogen cooled mercury cadmium telluride detector (LN-MCT Narrow PMA50, *Infrared Associates Inc*., Stuart, FL), electronic band pass filters (B.P.), and demodulator (Synchronous Sampling demodulator (SSD), *GWC Instruments*, Madison, WI). The optical details are similar to other set ups reported in literature [22,23,34] and is provided in the Figure 4.2

The non-polarized IR beam from the spectrometer is reflected by a flat mirror (a) at 45º to a parabolic mirror (b) which converges the radiation to its focal point (f = 160 mm) at electrode in the cell via the static metal grid polarizer (1-inch diameter ZnSe substrate, Bruker) and photoelastic modulator (PEM). The static polarizer generates p-polarized light which is then modulated by the PEM controller at 100 kHz to generate both p- and s-polarizations with respect to the electrode surface. The p- and s-radiations go through the cell (sample) and are reflected at a pre-determined optimum angle (*vide infra*) by the electrode via a focusing lens (1-inch diameter ZnSe, (d)) to the detector. The detected signal is amplified and split into two signals; the absolute difference signal $|J_2(R_p - R_s)|$ and the average signal $(R_p + R_s)/2$.

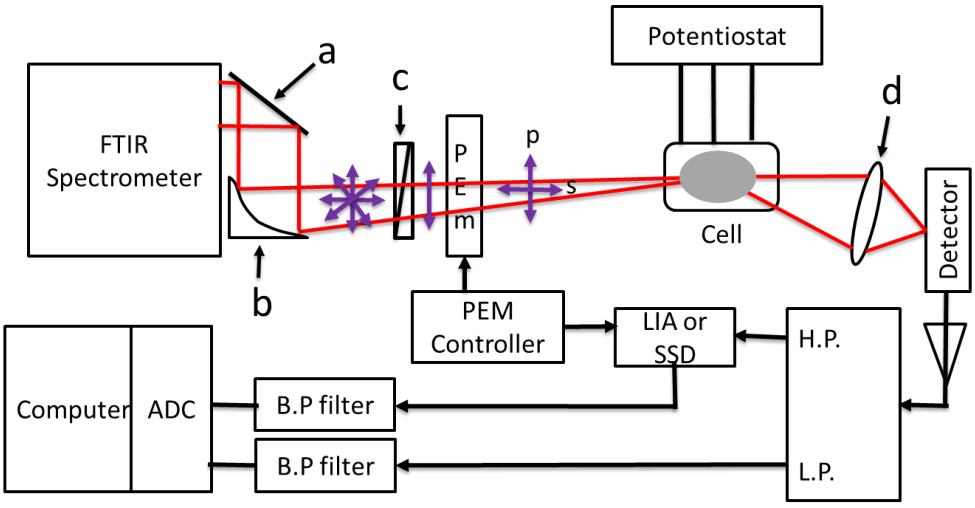

Figure 4.2: PM-IRRAS instrumentation schematic showing IR radiation optical path (red colour) the positions for the mirrors (flat (a) and parabolic (b)), static polarizer (c), photoelastic modulator (PEM), spectroelectrochemical cell, focusing lens (d), detector, and data processing electronics, i.e., High Pass (H.P.) filter and Low Pass (L.P.) filter, Band Pass (B.P) filter, and Analog to Digital Converters (ADC). The non-polarized IR radiation from the spectrometer is reflected by a flat mirror (a) to a parabolic mirror (b) which converges the radiation to its focal point at the cell electrode via the static polarizer (c) and PEM. The static polarizer generates p-polarized light which is modulated by the PEM controller at 100 kHz to generate s-polarization with respect to the electrode surface. The p- and s-radiation go through the cell, and then are focused with the lens (d) to the detector at a pre-determined optimum angle. The detected signal is amplified and split into two channels (see text for details).

The (absolute) difference signal goes through the H.P. filter into the demodulator (LIA or SSD) where a reference signal from the PEM controller is provided and then sent through the B.P. filter.[5] The average signal obtained at the L.P. and is passed directly into B.P. filter. The signals from the two channels are digitized and saved separately as interferograms for further processing by the user. The signal processing electronics, High Pass (H.P.) and (L.P.) filters, Band Pass (B.P.) filters, Analog to Digital Converter (ADC), and the computer are part of the Bruker setup. Electrode potential was controlled by a BioLogic VSP potentiostat equipped with the EC-Lab software (Bio-Logic Science Instruments SAS, Claix, France).

The spectroelectrochemical cell was designed and machined in-house following literature guidelines.[6,35–39] The main objective of the cell design was to minimize the background electrolyte absorption of infrared light by using a thin-layer configuration as shown in Figure 4.3.

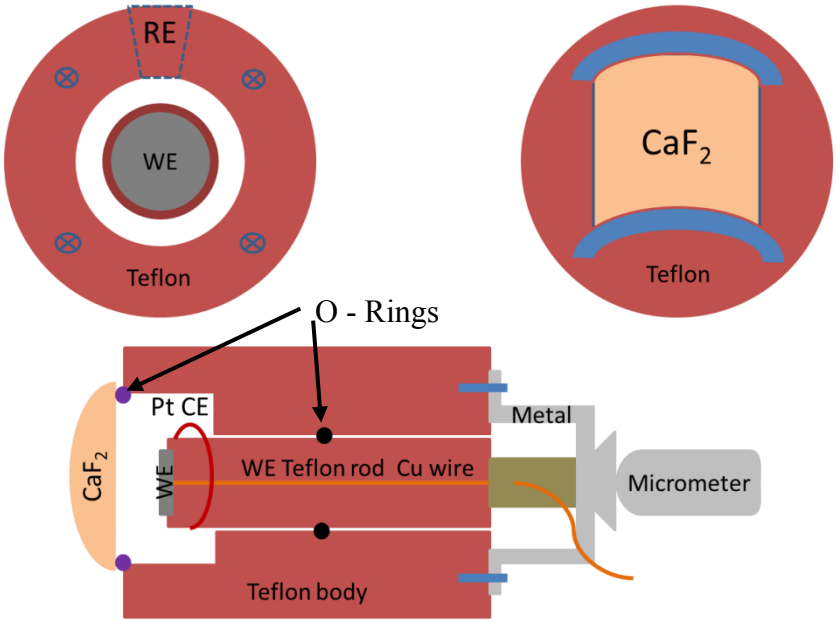

Figure 4.3: Spectroelectrochemical cell schematics (top left) Front view without the hemi-cylinder (CaF_2) window, (top right) Front view with the window, and (bottom) Top view cross-section of the cell. The glassy carbon pasted with nanoparticles was used as the working electrode (WE), Pt wire was used as the counter electrode (CE), and mercury-mercury oxide (Hg/HgO) was used as the reference electrode (RE). The body was made of Teflon.

The cell was machined of a Teflon body, then equipped with IR transparent window (CaF_2 hemi-cylinder 12.5 mm radius x 25 mm length, *New Era Spectro*, Vineland, NJ), and a micrometre screw (*Starret*, Athol, MA) for adjusting the thin-cavity thickness between the working electrode (WE) and the window to a few micrometres. A mirror polished glassy carbon (GC, 12.5 mm diameter, *Ted Pella, Inc*., Redding, CA) on a Teflon rod connected to a copper wire as the electrode current collector. The nanoparticle paste was applied on the GC and used as the working electrode. A platinum wire served as the counter electrode, it was wrapped around the WE Teflon rod to minimize solution resistance and provide uniform current distribution pattern to the working electrode. The mercury-mercury oxide (Hg/HgO) (5088B, *Koslow scientific*, Englewood, NJ) was inserted into the cell directly from the top opening as a reference electrode (RE). It is positioned on top of the cell close to the WE to minimize an uncompensated ohmic drop. The incident radiation passes through the window and electrolyte in the thin-layer cavity onto the GC-WE and is reflected back out of the cell and focused onto the detector as shown in Figure 4.2.

Various protocol(s) for PM-IRRAS data acquisition have been summarized by Christensen.[26] After the CVs to determine ethanol electrooxidation profile, Figure 4.4a, a combination of staircase and time-dependent protocols were employed as shown in Figure 4.4b. The reference spectra were acquired without applying any potential or current to the working electrode, i.e., at open circuit potential (OCP).

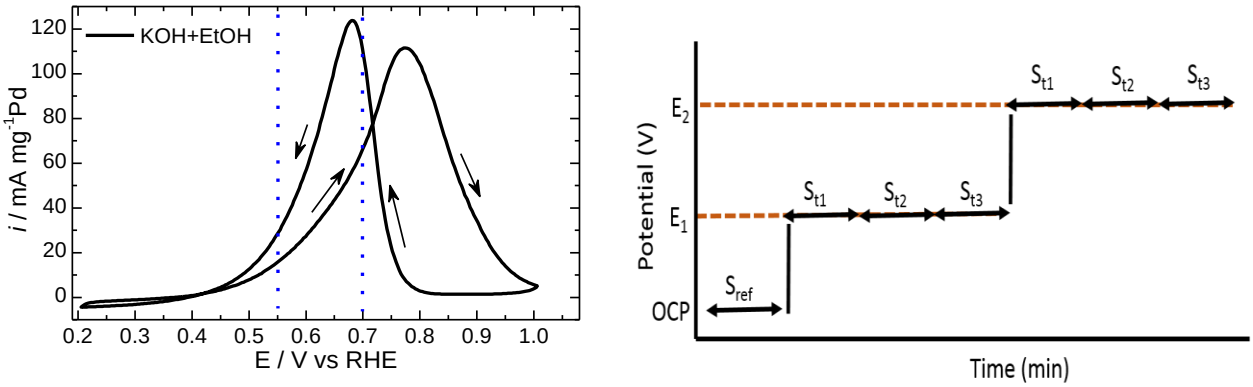

(a) (b)

Figure 4.4: (a) the CV to show ethanol electrooxidation profile and (b) the staircase and time-dependent data acquisition protocol. The reference spectrum (S_{ref}) was collected at open circuit potential (OCP) and sample spectra (S_t) were collected at potentials (E_1, E_2 … E_n) where faradaic activity took place. The time intervals were typically five minutes.

In a typical experiment, the electrolyte was introduced into the optically aligned cell and the CV was recorded to assure the quality of deposited nanoparticles on the GC. The chamber (PMA-50 XL) and the spectroelectrochemical cell were purged with nitrogen gas for 30 minutes to remove CO_2 from the system, then the electrode was pushed against the CaF_2 window (hemicylinder in shape) without stopping purging. To ensure a stable background was attained, background spectra were collected to track the level of CO_2 in the system at OCP. Typically, after two hours the reference spectrum was acquired at OCP followed by sample spectra at various oxidation potentials (E_1, E_2 …E_n) as shown in Figure 4.4. Sample spectra at each potential were acquired at five minutes increments for up to 30 minutes before stepping to the next potential. The potentials, E_1, E_2 …E_n, were selected from the CV profile. The reflectivity signal was acquired by the co-addition of 256 interferograms (128 forward and 128 backward scans) collected with a resolution of 8 cm^{-1}. The obtained interferograms were then Fourier transformed into reflectivity spectra using Bruker OPUS software.

The details for nanoparticle synthesis and characterization are already published elsewhere.[40–42] The Pd/C nanoparticles reported in Figures 4.6 and 4.7 were synthesized using the polyol method, while the Pd nanoparticles on four different supports reported in Figures 4.8-11 were prepared using $NaBH_4$ reduction method (the nanoparticles were synthesised by another student – see contribution statement for details).

4.2.2 **Theoretical approach details**

It is important to determine and optimize the experimental conditions that yield maximum MSEFS in order to achieve the best S/N for the surface adsorbed species. The key optimization parameters in the spectroelectrochemical model shown in Figure 4.5 are;[6,43] i) the mean square electric field strength (MSEFS), ii) the angle of incidence (Θ), and iii) the thin-cavity thickness between the electrode and IR window.

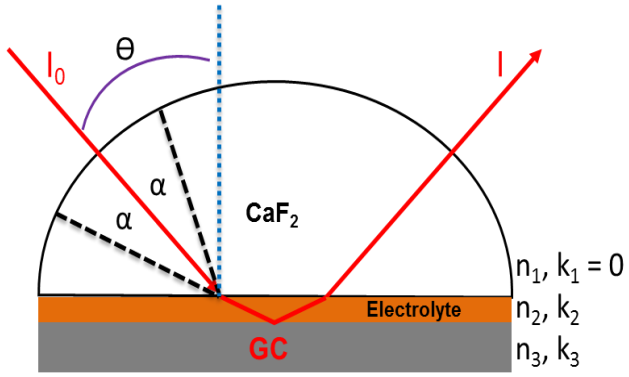

Figure 4.5: Model for external reflection IRRAS used in determining optimum experimental conditions. Θ is the angle of incidence; ± α is the convergence of the incidence beam; *n* and *k* represent the optical constants of each layer of a three-layer cell (modelled as a stratified medium).

The detected signal is dependent the MSEFS magnitude which is influenced by the angle of incidence and the thin-cavity thickness. The optimum values of these parameters are dependent on the optical constants (*n, k*) of the window, the electrolyte, and the working electrode used. The optimum angle of incidence and thin-cavity thickness which leads to maximum MSEFS were calculated using Fresnel1, in-house software, written by Zamlynny.[6,43] The software employs a stratified interfacial model and Fresnel equations in a matrix form to calculate the reflectivity and the MSEFS.[44]

The optimum experimental set up conditions were calculated scanning the angle of incidence from 0° to 90° with an increment of 0.1° and the thin-cavity thicknesses was allowed to vary

between 0 and 10 µm with an increment of 0.1 µm. Such conditions encompass all possible experimental conditions which can be applied to the experimental setup that employs CaF_2 windows. In a typical IR spectrometer, there is convergence of incident beam (shown as ±α in Figure 4.5) at each angle of incidence (Θ). This behaviour was simulated by varying the angle of convergence from -3° to +3° with respect to each angle of incidence using an increment of 0.1° and the average value of the MSEFS was then determined to represent the MSEFS of the convergent beam at each angle. Note that the angle of convergence of 3^0 was chosen to match the experimental beam configuration. All the angles are reported with respect to surface normal and the origin of the IR beam is considered to be within the CaF_2 hemisphere (i.e. the reflection losses at the window air interfaces are ignored). The thin cavity (gap thickness) is measured with respect to the metal surface. Figure 4.6 shows the typical 3D graph calculated from the model at each wavenumber (showing the graph for 2300 cm^{-1} for illustration).

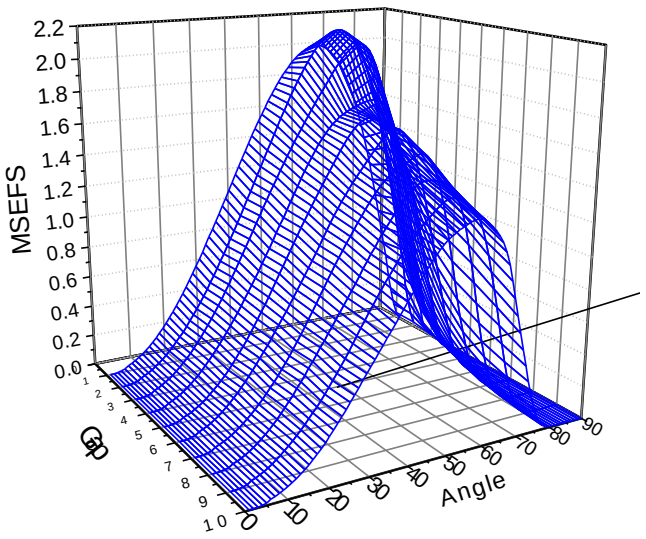

Figure 4.6: The MSEFS profile as a function of the angle of incidence and the thin-cavity (gap) thickness. Position of the global maximum of MSEFS = 2.21 is at the angle of incidence of 63 º and thin cavity of 1.4 µm. Calculations represent the CaF_2/H_2O/GC cell at a wave number of 2300 cm^{-1} with an incident beam convergence of ±3º

A global maximum of the three coordinates in Figure 4.6 was found to be (2.21, 63, 1.4) which corresponds to MSEFS, the angle of incidence, and the thin-cavity gap thickness, respectively. These values correspond to the optimal experimental parameters at wavenumber 2300 cm^{-1}.These three coordinates of the global maximum (MSEFS, angle of incidence, gap or thin-cavity thickness) were calculated for the entire mid infrared region from 1100 cm^{-1} to 4000 cm^{-1} with an

increment of 100 cm^{-1} (CaF_2 window is not transparent below 1100 cm^{-1}). The graphs showing how these three parameters vary between 1100 cm^{-1} and 4000 cm^{-1} are shown in Figure A1-1 (appendix section 1). From these calculations we established the best experimental set up conditions, the optimum angle of 63 degrees for the photoelastic modulator (PEM) setting at 2300 cm^{-1} was used. However, it was not possible to precisely adjust the gap thickness to 1.4 µm because the working electrode was not perfectly parallel with the window surface. Instead a wedge configuration was obtained, which was later found to be an advantage for signal sensitivity.[45]

Further calculations were done to determine the boundary between surface species and bulk-phase species for a glassy carbon electrode as shown in Figure 4.7.

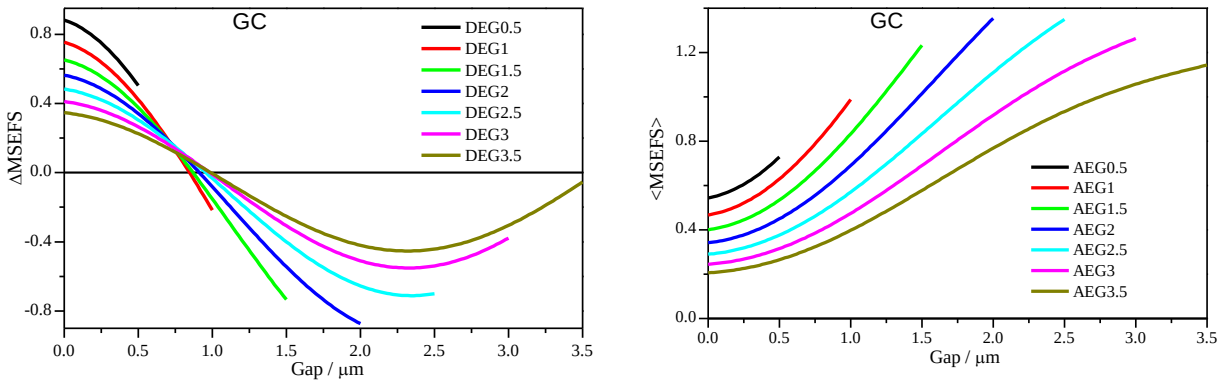

(a) (b)

Figure 4.7: The simulated MSEFS to show the expected interaction of infrared light with absorbing species at various thin cavity (gap) settings shown in the legend. The plots were made taking into account the optical constants of the GC, water as the electrolyte and CaF_2 as the window for (a) difference channel (|ΔR|) and (b) average channel (<R>). The angle of incidence was 63^0 and the beam convergence was $\pm 3^0$ (matching closely the experimental conditions).

Note that in this model we have assumed the optical properties of the nano-catalysts to be negligible for two reasons; i) the optical values for this nanoparticles are not known to us at the moment, ii) a monolayer of discrete nanoparticles were applied of the GC, hence more than 95% of the reflection was coming from the GC surface. Therefore, any contribution from the optical properties of the nanoparticles is not considered and is expected to be insignificant to the conclusions to be made in this work as mentioned in the introduction. Figure 4.7(a) shows that the boundary for surface species on the GC is at less than 1 µm due to the rapid decreasing of the MSEFS magnitude for the difference channel. The magnitudes of MSEFS show the degree to

which the species would absorb the IR radiation. It is evident that MSEFS in the average channel, Figure 4.7(b), increases with distance from the electrode indicating that the bulk-phase signal will be more sensitive to the locations further away from the electrode.

4.2.3 **PM-IRRAS Data processing protocols**

The detected PM-IRRAS intensity signal (I_d) has two components.[28,46] One component carries only the relatively low frequency modulation (I_{DC}) at frequencies ω_i introduced by the interferometer as shown in equation 4.1 and 4.2 depending on the *p*- or *s*-polarization setting of the static polarizer before the photoelastic modulator (PEM).

$$I_{DC} = C_{DC} I_0^p(\omega_i)[\tfrac{(R_p+R_s)}{2} + \tfrac{(R_p-R_s)}{2} J_0\varphi_0] \quad 4.1$$

Or

$$I_{DC} = C_{DC} I_0^s(\omega_i)[\left(\tfrac{R_p+R_s}{2}\right) - \left(\tfrac{R_p-R_s}{2}\right) J_0\varphi_0] \quad 4.2$$

The second component has a double modulation, one at the relatively low Fourier frequencies ω_i and another at the much higher frequency ω_m induced by the PEM as shown in equation 4.3.

$$I_{AC} = C_{AC} I_0^{p,s}(\omega_i)[(R_p - R_s).J_2(\varphi_0).\cos(2\omega_m t)] \quad 4.3$$

where $I_0^{p,s}(\omega_i)$ is the intensity of the *p*- or *s*-polarized infrared radiation of frequency ω_i at the output of the static polarizer before the PEM, R_p and R_s are the polarized reflectances of the substrate system, and J_2 and Jo are the second- and zero-order Bessel function of the maximum dephasing φ_0 introduced by the PEM. Therefore, the detected intensity can be written as shown in equation 4;[27]

$$I_d = C I_0(\omega_i)\left\{\tfrac{(R_p+R_s)}{2} - \tfrac{(R_p-R_s)}{2} J_2(\varphi_0) + (R_p - R_s) J_2(\varphi_0)\cos(2\omega_m t)\right\} \quad 4$$

where $I_0(\omega_i)$, is the light intensity after the static polarizer and the other constants as defined above. With the use of an electronic filter with high-pass output set at $2\omega_m$ and low-pass output set at least an order of magnitude below$2\omega_m$, respectively, as detailed in [27] the detected intensity I_d is easy to split into the two signals going to two different channels. One channel receiving the average signal (R_p + Rs)/2 and the other receiving the magnitude difference |(R_p - R_s)| interferograms (the latter contains the gradually sloping $|J_2(\varphi_o)|$ envelope as the background. For simplicity, herein the intensity from equation 4.1 or 4.2 is referred to as the Reflectivity *average signal*, ($R_{avg.}$) while signal given by the equation 4.3 is referred to as the Reflectivity *difference signal* ($R_{dif.}$) Both signals are obtained from the signal described by equation 4.4 after its

demodulation (by either the LIA or SSD). The ratio of these two components gives the so called "raw PM-IRRAS signal" as shown in equation 4.5

$$S(PM-IRRAS)(\text{Raw}) = \frac{R_{dif}(Raw)}{R_{avg}(Raw)} = \frac{C_{AC}|(R_p - R_s).J_2(\varphi_0)|}{\frac{C_{DC}(R_p+R_s)}{2} \pm \frac{1}{2}(R_p - R_s).J_0(\varphi_0)} \qquad 4.5$$

Note that in equation5, the term $\frac{1}{2}(R_p - R_s).J_0(\varphi_0)$ is usually much smaller than $\frac{C_{DC}(R_p+R_s)}{2}$, because the reflectivities are typically (at least for metal mirrors) close to each other and hence their differences are much smaller than their averages, and often is omitted/ignored for convenience. C_{DC} and C_{AC} are mostly representing the gain of signal in the respective channels. The first is typically equal to 1 and the second varies between 1 and 100 and must be taken into consideration when processing PM IRRAS spectra. After simplification and gain correction we have corrected PM IRRAS signal as shown in equation 4.6:

$$S(PM-IRRAS)(\text{Corrected}) = \frac{R_{dif}(Corrected)}{R_{avg}(Corrected)} = \frac{|(R_p - R_s)|.|J_2(\varphi_0)|}{\frac{(R_p+R_s)}{2}} \qquad 4.6$$

In the absence of $|J_2(\varphi_0)|$ envelope and other experimental artifacts that affect background, theoretical PM IRRAS signal should be given by the ratio of the absolute intensity difference $|\Delta R|$= absolute (R_p-R_s) and the signal average $\langle R \rangle = (R_s+R_p)/2$ according to equation 4.7:

$$S(PM-IRRAS) = \frac{|\Delta R|}{\langle R \rangle} \qquad 4.7$$

This signal is equivalent to the Absorbance calculated from transmittance measurements done in the course of conventional spectroscopy experiments.

4.2.4 **Commonly used signal processing approach**

The signal from equation 8 is relatively easy to interpret for the case of films deposited directly on metal substrates because the intensity of s-polarized light at the metal surface is zero and therefore the only significant artefact comes from the J_2 which can be removed by calibration procedures described elsewhere.[6,28] However, for the cases when the IR absorbing species such as water sub-phase is present in the vicinity of the metal substrates the cancellation of contribution of s-polarized component is incomplete and because of that, there is a significant frequency dependent contribution of this sub-phase to the detected signal which requires subtraction of the background spectrum to extract the very weak absorption bands of the deposited monolayer or electro-generated species.[46] Therefore, it is necessary in the latter case to collect the PM-IRRAS spectra with covered $S_{(d)}$ and uncovered $S_{(0)}$ substrates. For

electrooxidation reactions, this means collecting the reference spectra at open circuit potential (OCP) and sample spectra at an oxidation potential, both under the same experimental conditions. At these conditions, the two spectra superimpose quasi-perfectly and allow for successful removal of the aqueous electrolyte background by taking the difference as shown in equation 4.8.

$$\Delta S = (S_{(d)} - S_{(0)}) \qquad 4.8$$

$S_{(0)}$ signal can also be used to correct for the $J_2(\varphi_0)$ envelope if the difference signal (ΔS) is divided by $S_{(0)}$. Note that the division by $S_{(0)}$ removes $J_2(\varphi_0)$ but introduces the response of the aqueous background. Thus it is good for qualitative interpretation only (if sufficient quality spectra are available).

Equation 4.8 represents the commonly used approach to process the PM-IRRAS signals. Often PM IRRAS yields too weak absorption bands with equation 4.8, which are masked in random noise, hence creating the need to collect multiple spectra in order to see the difference signal between the sample and reference spectra. In addition, the need to normalize the signal with a reference spectrum like SNIFTIRS discourages the wide use of PM-IRRAS.[26] In response to this challenge, we have taken a simpler but yet more powerful approach to process the PM-IRRAS spectra as presented below. The approach yields excellent S/N enabling us to see weak absorption bands with a very few scans (≤ 256). The approach also allows direct interpretation of the spectra, and gives additional insights of the reaction mechanism such as solid-electrolyte dynamics.

4.2.5 **Proposed new signal processing approach**

The new approach is based on the effort to avoid equation 4.7, where the difference signal ($|\Delta R| = R_{\text{dif.}}$) is divided by the average signal ($(<R>) = R_{\text{avg}}$), because the two signals carry completely different information and so is their reflectivity features. The R_{avg} carries information of the surface, bulk-phase, and background while the R_{dif} carries primarily information of the surface species within micrometres (μm) from the reflecting surface. Therefore, the two sets of data, i.e., sample (R_{dif} and R_{avg}) and reference (R_{dif} and R_{avg}) are processed using equations 4.9 and 4.10 instead.

$$Surface\ reflectivity\ factor = \left(\frac{Sample\ (R_{dif})}{Reference\ (R_{dif})}\right) - 1 \qquad 4.9$$

$$Bulk\ reflectivity\ factor = \left(\frac{Sample\ (R_{avg})}{Reference\ (R_{avg})}\right) - 1 \qquad 4.10$$

where surface reflectivity factor ($R.F._{surf}$) and bulk reflectivity factor ($R.F._{bulk}$) corresponds to electro-generated changes between the sample and reference potentials at the surface and bulk-phase, respectively. By these definitions (equations 4.9 and 4.10), the positive and the negative peaks mean the presence and absence of absorbing species in the sample spectrum with respect to the reference spectrum. The two definitions have been termed "Reflectivity Factors" to emphasize the fact that they are different from the initial definition of Absorbance Factor as defined by Greenler but the interpretation of the spectra is similar. Therefore, reflectivity factor magnitude is proportional but not equal to absorbance and hence the species concentration as defined by Beer-Lambert's Law.

The advantages of equation 4.9 and 4.10 are; i) the cancellation of artefact constants such Bessel functions J and amplifier gains in each channel (R_{dif} or R_{avg}), hence allowing a direct interpretation of the resulting spectra, ii) additional physical insights are gained at the solid-liquid interface because we now have two spectra with complementary information, i.e., the surface and bulk-phase species compared to the one spectrum obtained if equation 4.8 was used according to the "established" approach.

Herein, we recommend the use of equations 4.7, 4.9, and 4.10 as the new protocol for reporting PM-IRRAS data. This is because equation 4.7, reports the absolute absorption (i.e. not the potential-driven adsorption changes) of the surface species with respect to the isotropic bulk background, which can be either liquid- or gas-phase. Note that equation 4.7 yields two sets of spectra, one for the reference and the other for the sample which are used to calculate ΔS in equation 4.8. Equation 4.9 ($R.F._{(surf)}$) highlights the difference information about the changes of adsorbed species at the electrode surface due to the applied potential. Hence, it captures information of volatile species which desorbs and moves away from the electrode surface as soon as they are formed. According to the Figure 4.7(b) such a behaviour should be best monitored by the average channel signal calculated according to Equation 4.10 ($R.F._{(bulk)}$). Therefore, a combination of these three equations (4.7, 4.9, and 4.10) provides a set of critical information to visualize and highlight solid-liquid processes and/or solid-gas processes in Electro- and Heterogeneous catalysis. This new approach can also be extended to the studies on thin films and macromolecular species such as proteins, enzymes, and surfactants. In the following section, we are going to present examples to illustrate the utility of the new protocol

using PM-IRRAS data from ethanol electrooxidation reaction on nanoparticles deposited on glassy carbon electrode.

4.3 **Results and discussion**

The detailed ethanol electrooxidation reaction mechanism are provided in chapter 6 and 7.[40–42] In this chapter, the focus is on PM-IRRAS data presentation and discussion on PM-IRRAS utility based on the proposed new data processing approach. First, we look at ethanol electrooxidation on Pd/C nanoparticles synthesized using the polyol method, then shift to a comparative study of ethanol electrooxidation on Pd nanoparticles on different supports. Figure 4.8 shows the typical CV profile for ethanol electrooxidation in alkaline media from which potentials for tracking the products were determined.

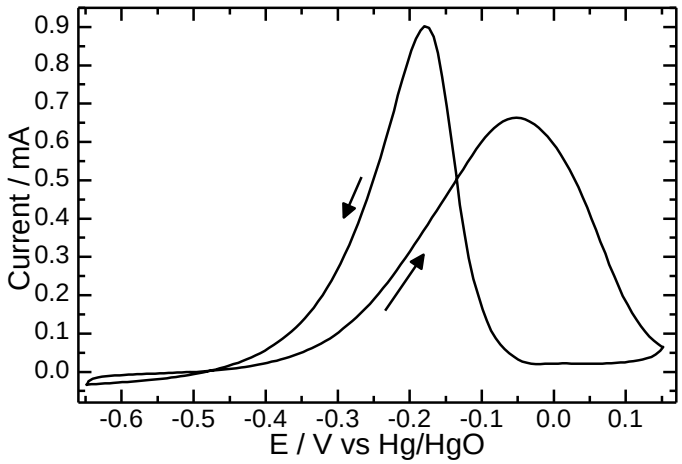

Figure 4.8: The cyclic voltammogram showing electrooxidation profile for 1M (EtOH + KOH)

Figure 4.9 shows the reflectance spectra corresponding to a reference channel (R_{dif} and R_{avg}) and the sample channel (R_{dif} and R_{avg}) for ethanol on Pd/C nanoparticles.

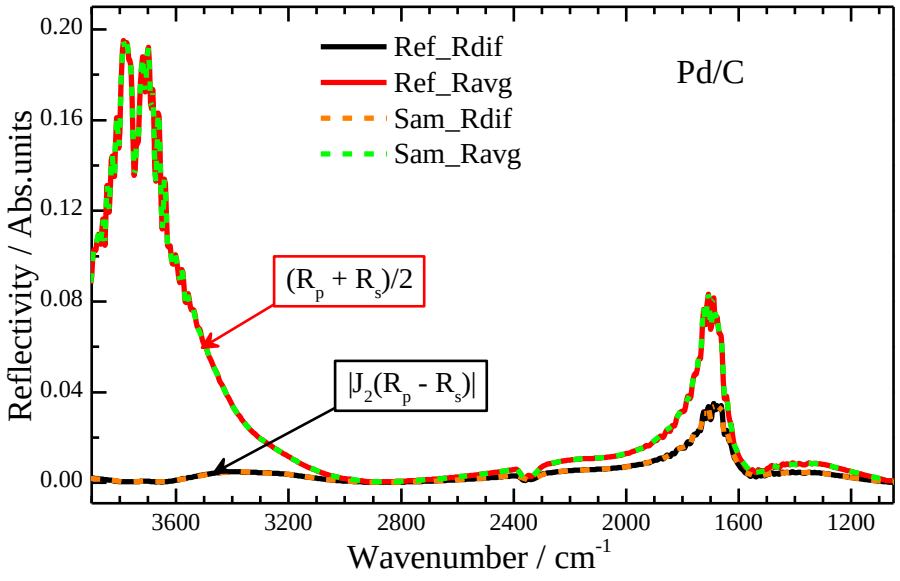

Figure 4.9: The typical reflectivity spectra for a reference at open circuit potential and sample at -0.30 V/ Hg/HgO after holding potential for 30 minutes.

The main features of these spectra are the residual water vibrations at 1700 cm^{-1} and 3700 cm^{-1}, and CO_2 vibrations at 2345 cm^{-1}. Notice that there are differences between R_{dif} and R_{avg} reflectivities but no differences between reference and sample channels for each reflectivity. These reflectivity spectra carry potential-dependent information but do not display it until processed further. Therefore, we are going to processes the spectra using equations 4.7, 4.8, 4.9, and 4.10.

Figure 4.10 shows the calculated spectra using equation 4.7 (Figure 4.10(a)), equation 4.8 (Figure 4.10(b)), equation 4.9 (Figure 4.10(c)), and equation 4.10 (Figure 4.10(d)). Equation 4.7 (Figure 4.10(a)) does not reveal any potential-driven changes between the sample and reference spectra.

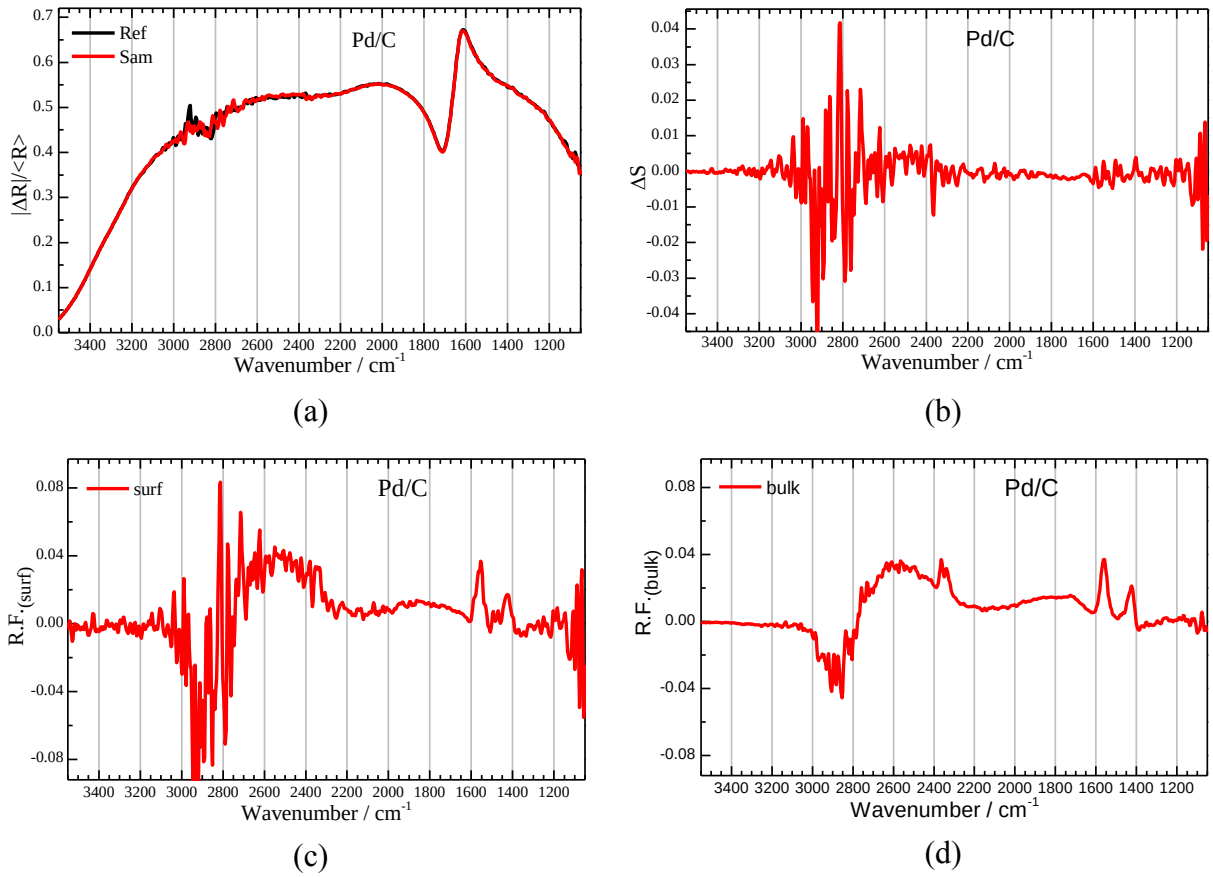

Figure 4.10: Processed data for 1M (KOH + Ethanol) electrooxidation on Pd/C nanoparticles; (a) the raw PM-IRRAS ($|\Delta R|/<R>$) signal for the reference and sample using equation 4.7, (b) the final PM-IRRAS (ΔS) signal using equation 4.8, (c) surface oxidation species ($R.F._{(surf)}$) signal using equation 4.9, and (d) the bulk/liquid-phase oxidation species ($R.F._{(bulk)}$) in the thin cavity using equation 4.10. Equation 4.9 and 4.10 shows potential-driven changes while equation 4.7 and 4.8 do not. The reflectivity spectra data shown in Figure 4.9 were used.

Note that the baseline for these spectra is not straight because of the Bessel functions contributions. Similarly, Equation 4.8 (Figure 4.10(b)) does not reveal the potential-driven changes although the Bessel functions contributions have been removed. Therefore, according to the established method, no changes took place between the reference and sample spectra. But when we process the same data with equations 4.9 and 4.10, the potential-driven changes are obvious as shown in Figure 4.10(c) and Figure 4.10(d), respectively. Note the excellent S/N ratio especially Figure 4.10(d) compared to the established method Figure 4.10(b).

From the comparisons in Figure 4.10, it is clear that equations 4.9 and 4.10, reveals not only the evidence of electro-generated products between the reference and sample potentials but also tells us the dynamics of the interface. The new proposed equations reveals the formation of acetate (peaks at 1560 cm^{-1} and 1423 cm^{-1}) and CO_2 (peak at 2343 cm^{-1}) while the established

method (equation 4.7 and 4.8) reveals no changes between reference and sample spectra. When it comes to the reaction dynamics, the new equations reveals that CO_2 once formed it immediately desorbs into the bulk-phase (Figure 4.10(d)), which is why it is not observed at or near the electrode surface (Figure 4.10(c)). The new equations also reveals the consumption of C–H vibrations based on negative peaks centered at 2900 cm^{-1} which is expected during ethanol electrooxidation. These observations provide us with convincing evidence that we are indeed able to capture more details of the reaction dynamics with this new approach.

The absence of the electro-generated products' features for the established method in Figure 4.10(b) is consistent with simulations of the system response via the use of Fresnel equations and can be attributed to the optical properties of GC which are distinctly different from that of metals. The metals are much more reflective and hence can have up to fourfold enhancement of the MSEFS at the surface while GC is expected to attenuate the MSEFS to the values of 0.4-0.8 depending on the window-electrode separation as shown in Figure 4.7. Even with metal electrodes, it had been the norm when using PM-IRRAS to make thousands of scans in order to improve the S/N enough to see the signal. But with the proposed equations, even as low as 16 scans are sufficient to distinguish the signal from the noise making the technique very inconvenient for in-situ kinetics studies.

With the established method, particularly Equation 4.7 can also be beneficial when comparing different systems. To illustrate its utility in complementary to equations 4.9 and 4.10, we are going to use PM-IRRAS reflectivity data from ethanol electrooxidation on Pd nanoparticles on CeO_2, SnO_2, TiO_2, and C supports. The reflectivity spectra for the reference and sample look similar to the ones shown in Figure 4.9 (see appendix Figure A1-2). Figure 4.11 shows the processed spectra using equation 4.7. It is important to mention that the features for equation 4.7 are somehow influenced by the size of the thin-cavity; hence precaution should be applied when interpreting the spectra.

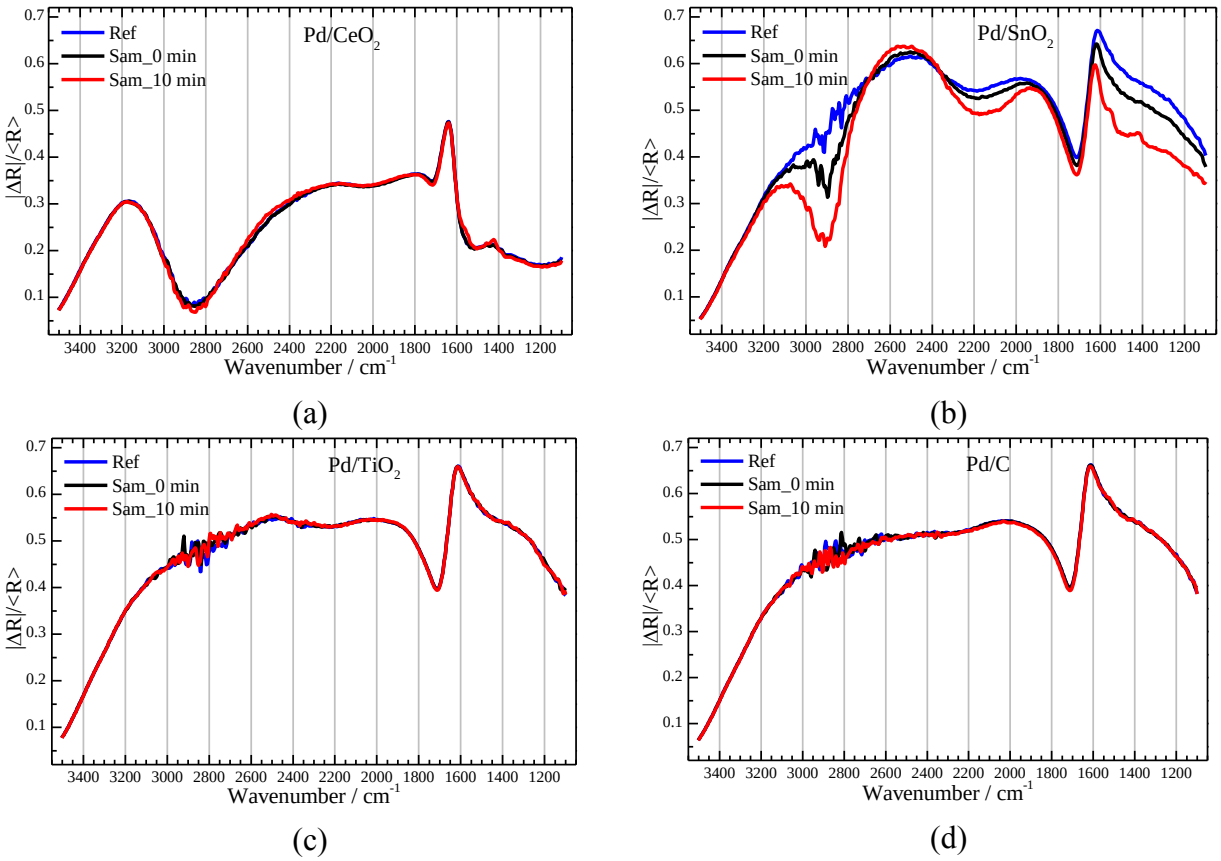

Figure 4.11: The calculated spectra using equation 4.7 for ethanol electrooxidation on Pd nanoparticles supported on; (a) CeO_2, (b) SnO_2, (c) TiO_2, and (d) C. The reference and sample spectra were collected at open circuit potential and at -0.30 V/ Hg/HgO, respectively. Only two time intervals (0 and 10 minutes) are reported for clarity.

Figure 4.12 shows the same data of Figure 4.11 processed using equation 4.9. Since the y-axis is directly proportional to the amount of the species generated on the surface, these spectra, particularly the acetate peaks (1423 cm^{-1} and 1560 cm^{-1}) and the unidentified product peak centered at 2700 cm^{-1} (likely from C – H, C = O, and O – H interaction), shows that Pd/SnO_2 is the most active catalyst system, in agreement with chronoamperometry data (Figure 7.10 chapter 7). Pd/SnO_2, also forms distinctively different products from the other catalysts (particularly the higher/stronger peak centered at 2700 cm^{-1}).

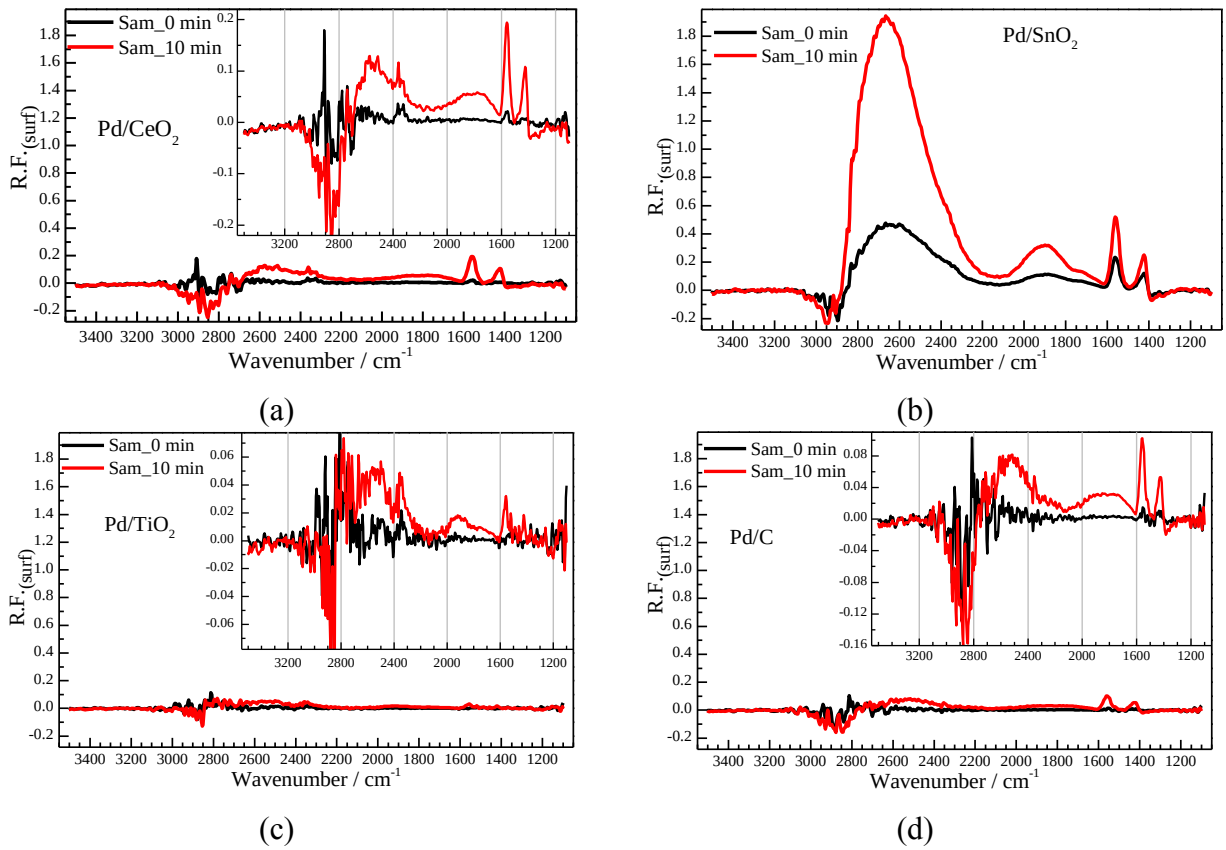

Figure 4.12: The surface reflectance factor ($R.F._{(surf)}$) spectra for ethanol electrooxidation on Pd nanoparticles supported on; (a) CeO_2, (b) SnO_2, (c) TiO_2, and (d) C. The spectra were processed using equation 4.9. Reference spectra were collected at open circuit potential and sample spectra were recorded at -0.15 V/ Hg/HgO, only two time intervals (0 and 10 minutes) are reported for clarity. The reaction was done in 1M (KOH+EtOH) electrolyte. (The graphs have same y-axis scale for comparison and the insert plots show the zoomed in graphs for spectra details. The reflectivity data used are the same as that used for Figure 4.11.

Unlike the acetate peaks (1423 and 1560cm^{-1}), the peak centered at 2700 cm^{-1} is greatly dependent on the ratio of KOH to EtOH as shown in Figure A1-3(c) and Figure A1-4(c). Changing the KOH : EtOH ratio from 1:1 to 5:1 (5:1 is the stoichiometric ratio for complete oxidation of ethanol to CO_2 and H_2O) reduced the peak at 2700 cm^{-1} by a factor of 9 while the acetate peak at 1560 cm^{-1} is only reduced by a factor of 2. Therefore, we ascribe the strong peak at 2700 cm^{-1} to the incomplete oxidation of ethanol due to insufficient amount of hydroxyl (OH^-) groups. Further studies are required to establish the origin of the peak. It does not seem to be acetaldehyde (CH_3CHO) since it does not correlate well with the C=O bond vibrations at 1724 cm^{-1}.

Figure 4.12(a) and (d) reveals that the activities of Pd/CeO_2 and Pd/C, respectively are very similar and acetate is the main product (1423 cm^{-1} and 1560 cm^{-1}), Pd/TiO_2 is the least active

catalyst which only shows the asymmetric acetate vibrations at 1560 cm^{-1}. However, Pd nanoparticles on CeO_2 and TiO_2 do show some evidence of C–C bond cleavage by the presence of the CO_2 peak at 2343 cm^{-1}. This surface specific information, is now readily accessible by using equation 4.9 is critical for the rational selection of catalyst supports.

On the other hand, applying equation 4.10 will now allow us to look at the products which desorb into the bulk-phase and the corresponding processed spectra are shown in Figure 4.13. Figure 4.13 reveals that the product distribution for ethanol electrooxidation on Pd NPs in alkaline media is greatly influenced by the catalyst support.

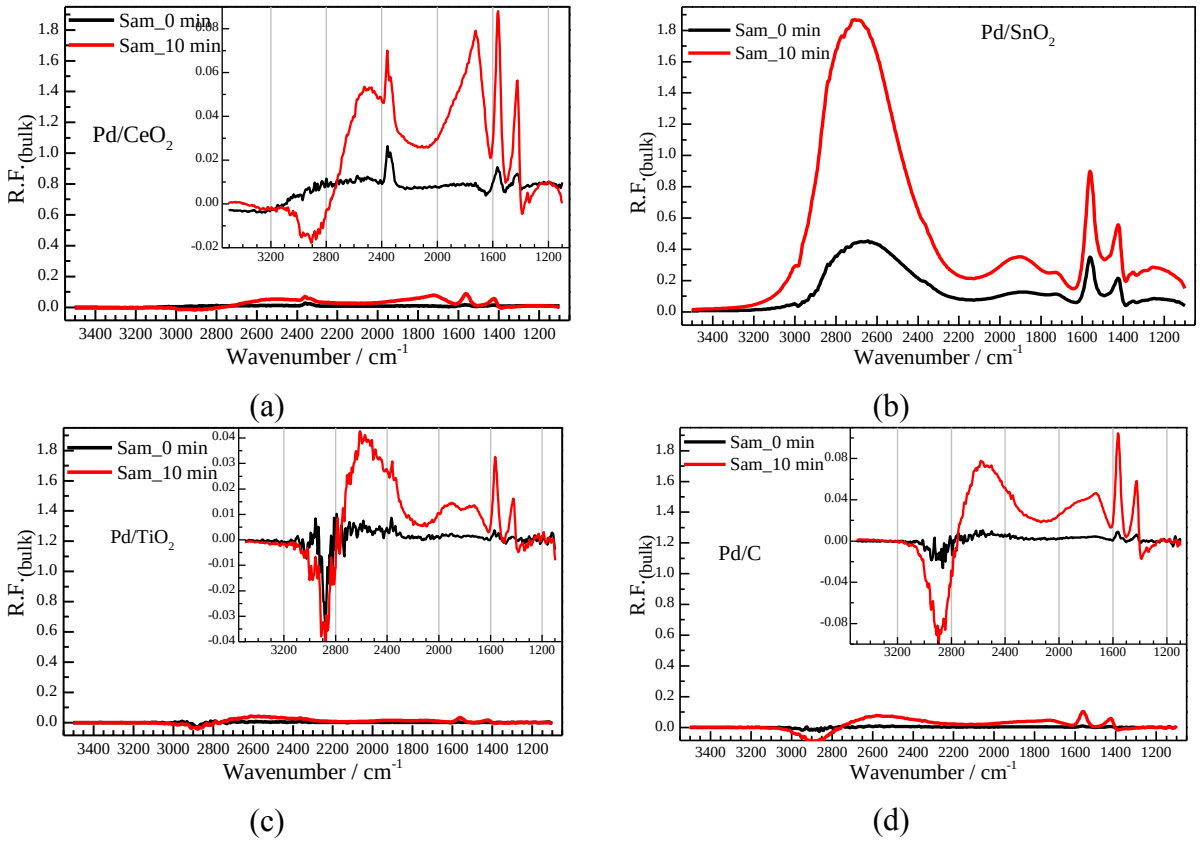

Figure 13: The bulk Absorbance Factor ($R.F._{(bulk)}$) spectra for ethanol electrooxidation on Pd NPs supported on; (a) CeO_2, (b) SnO_2, (c) TiO_2, and (d) C. The spectra were calculated using equation 4.10. Reference spectra were collected at open circuit potential and sample spectra were recorded at -0.15 V/ Hg/HgO, only two time intervals (0 and 10 minutes) are reported for clarity. The reaction was done in 1M (KOH+EtOH) electrolyte. The reflectivity data used is the same as that used for Figure 4.11.

Figure 4.13(a) reveals that CeO_2 improves the selectivity of Pd nanoparticles towards cleaving the C–C bond (peak at 2343 cm^{-1}) and the carbonyl (C=O) rich product (peak at 1724 cm^{-1}), while Figure 4.13(b) shows that SnO_2 favors incomplete oxidation products. TiO_2 and C are

almost similar in activity as shown in Figure 4.13(c) and (d), respectively. Equation 4.10 indeed reveals interesting product distribution features particularly the peaks between 1600–1800 cm^{-1} and 2800–3100 cm^{-1} which are dependent on the catalyst support. This insight needs further detailed investigation but is beyond the scope of this work which is to highlight the resourcefulness of PM-IRRAS when the new data processing protocol is followed.

For comparison with the established method, the data presented in Figures 4.12 and 4.13 was processed by equation 4.8 and resulting spectra are shown Figure 4.14.

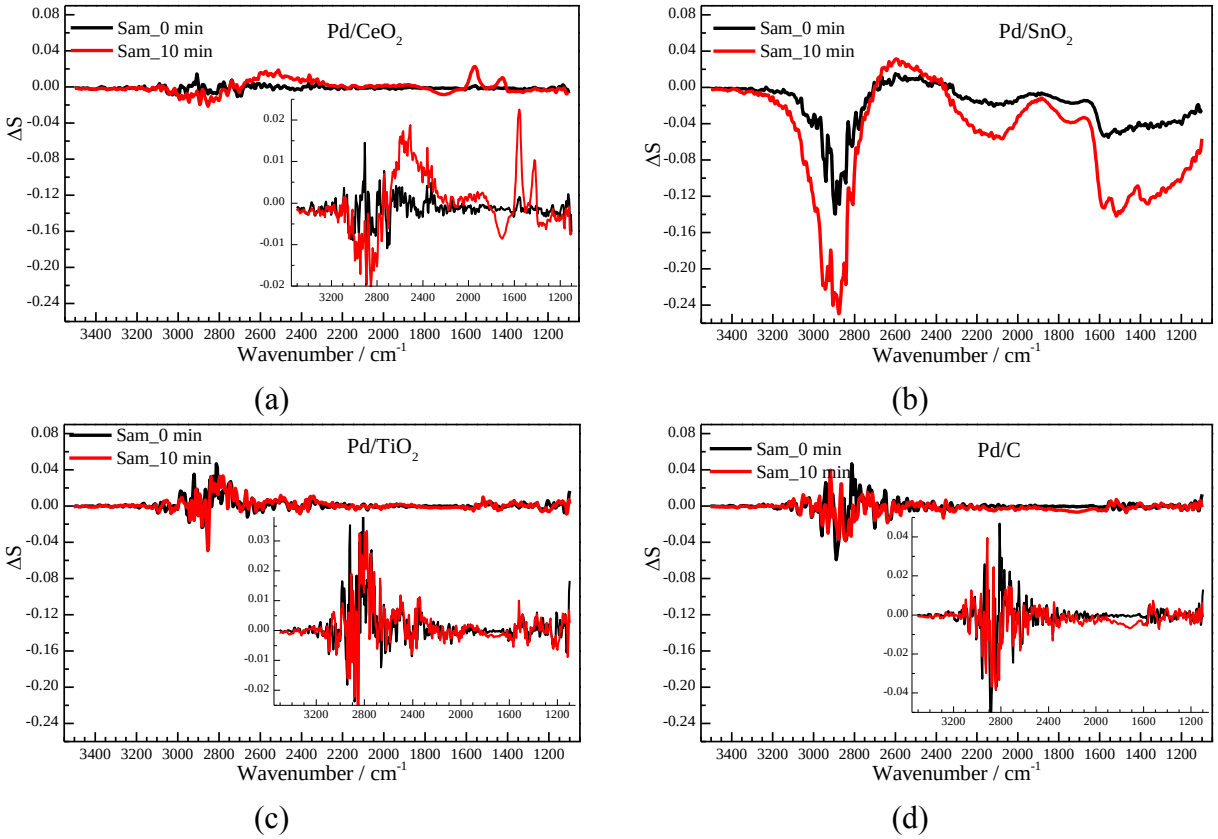

Figure 4.14: The ΔS spectra for ethanol electrooxidation on Pd NPs supported on; (a) CeO_2, (b) SnO_2, (c) TiO_2, and (d) C. Reference spectra were collected at open circuit potential and sample spectra were recorded at -0.15 V/ Hg/HgO, only two time intervals (0 and 10 minutes) are reported for clarity. The reaction was done in 1M (KOH+EtOH) electrolyte. Same data as in Figure 4.11 was used.

Figure 4.14 is convincing evidence that with the "established" Δ*S* approach; we not only have difficult highlighting the potential-dependent information but we also have the challenge to interpret the spectra obtained. Most likely this occurs because the surface and bulk changes are combined when taking a reflectivity ratio during the calculation of *S(PM-IRRAS)* according to equations 4.7, resulting in a partial cancellation of the signals from the electro-generated species

because it is present both at the surface and in the bulk-phase electrolyte. Thus, this approach appears to be inferior especially for GC system with respect to the new spectra processing methods described in this work

4.4 Conclusions

We have demonstrated a new approach for processing PM-IRRAS data which allows for direct interpretation of the spectra without the need for the tedious calibration procedures. To gain deeper insights for the system under investigation (surface processes or *in situ* reaction studies), we recommend three complementary equations (equation 4.7, 4.9, and 4.10) as the new protocol for presenting PM-IRRAS data. These equations are robust in visualising the reaction dynamics at the solid-liquid and solid-gas interphases. Equation 4.7, *S(PM-IRRAS)*, highlights the surface absorbed species with respect to isotropic background with or without the influence of the applied potential. Unfortunately it can have limited utility for GC and other weakly reflective electrode systems, especially if the surface species have relatively low contrast (little change) with respect to the bulk background as the result of applied potential. Equation 4.9 ($R.F._{(surf)}$), highlights the surface potential-driven changes between the sample and reference reflectance spectra. The observed surface thickness is governed by the optical constants of the reflective surface, which is less than 1 μm for GC (Figure 4.7(a)). Equation 4.10, $R.F._{(bulk)}$, highlights primarily the bulk potential-driven changes in both solution-phase and surface species between the sample and reference spectra (Figure 4.7(b)). Hence, $R.F._{(bulk)}$ can be used to track the production of volatile and non-volatile species which desorb from the surface as soon as they are formed, which is equivalent to combining regular IRRAS with either the differential electrochemical mass spectroscopy (DEMS) or chromatographic techniques (HPLC).

Using the new protocol presented in this work, PM-IRRAS provides more insights than ever reported before. The new approach will find wide application such as in heterogeneous catalysis, biomolecular and macromolecular surface studies, and in electrocatalysis. The new utility of the PM-IRRAS technique is poised to modernise our understanding of solid-liquid and solid-gas interphase chemistry and physics.

Supporting Information: Coordinates of the global maximum in the MSEFS for CaF_2/H_2O/GC system between 1100–4000 cm^{-1}, reference reflectivity for ethanol electrooxidation on Pd/CeO_2 and Pd/SnO_2 and processed spectra for ethanol electrooxidation on

Pd/SnO_2 to show reproducibility of spectra features reported herein are provided in appendix section 1.

Chapter 5: Ethanol Adsorption on Low-index Palladium Surfaces: Characterization of Geometries and Binding Energies via Density Functional Theory

Publication: E. A. Monyoncho, E. A. Baranova, and T. K. Woo. *J. Phys. Chem. C* – resubmission

Abstract

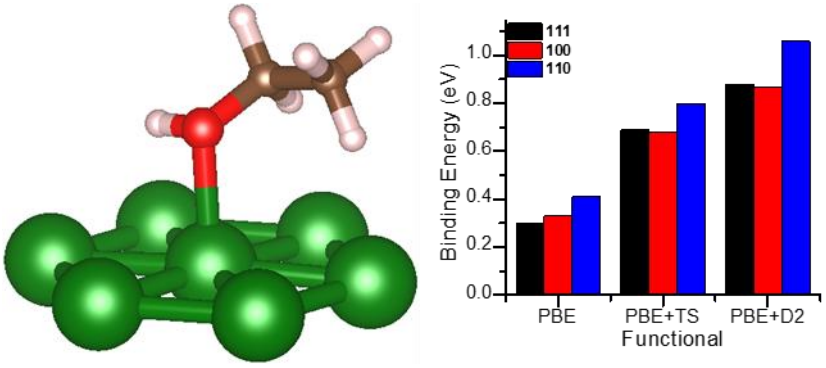

In modelling catalysts, geometric configurations and binding energies are key parameters for understanding catalyst-molecule interactions. The preferred adsorption sites, geometric configurations, and binding energies for ethanol on three low-index i.e. open (100), monoatomic (110) and close-packed (111) Pd surfaces were examined in the framework of Density functional theory (DFT). The effect of two van der Waals corrected-DFT functionals on these parameters are presented and compared to pure density functional by Perdew, Burke, and Erzenhorf (PBE). The two dispersion corrected functionals considered were the parameterized method (DFT-D2) by Grimme and the parameter-free method (DFT-TS) by Tkatchenko and Scheffler. Ethanol was found to bind the strongest on the (110) surface, whereas binding energies for (100) and (111) surfaces are similar and lower in strength in the three functionals as shown in the (TOC graphic). It was found that the inclusion of van der Waals interactions was fundamental in stabilizing the ethanol molecules on the Pd surfaces and in some cases significantly changes the binding geometries. The stabilization of ethanol molecule on Pd surfaces is attributed to the concentration of the charge density distribution at the Pd-O bond leading to shorter bond lengths and stronger binding energies. Analysis of the projected densities of states for the Pd-ethanol complexes showed that the C and O p_z-states and the Pd d-band electrons play a critical role in

stabilizing the adsorbate on the surface. These results are expected to simplify ethanol modeling on transition metals.

Keywords: Ethanol electro-oxidation, ethanol adsorption energies, palladium catalyst, DFT

5.1 Introduction

Palladium is considered to be among the best candidate catalysts for direct ethanol fuel cells (DEFCs).[1,2] While Pd shows no catalytic activity towards ethanol oxidation in acidic media, it has been found to be stable and suitable to enhance ethanol oxidation in alkaline medium.[3] There are many potential strategies of improving Pd-based DEFCs such as alloying Pd with other metals and using various supports as reviewed in chapter 2, to design stable electrocatalysts that promptly oxidize ethanol. These design strategies and others are expected to raise the fuel cell tolerance towards contaminants that can poison the anode by blocking the surface active/reactive sites rendering the fuel cell unusable.[5] However, to tap into these strategies, fundamental microscopic understanding on how ethanol interacts with different metal facets is critical. To date, several DFT studies have been pursued to characterize the surface chemistry of the ethanol-Pd system.[3,6–9]

With the help of two cluster models (Pd_5 and Pd_9), Cui *et al.* have looked into the dramatic increase of ethanol electro-oxidation induced by an alkaline media as compared to that of an acidic media.[3] Their DFT results concluded that adsorbed OH species on the Pd surface can ensure the continuous ethanol dehydrogenation required for efficient ethanol electro-oxidation. Additionally, DFT works by Li *et.al.*[7] and Guo *et.al.*[6] have found that the Pd(110) surface displays higher reactivity and different selectivity than the Pd(111) surface towards ethanol decomposition. They found that the most energetically-favorable ethanol-Pd configurations had binding energies of 0.51 eV (11.7 kcal/mol) on the Pd(111) surface while it was 0.52 eV (11.9 kcal/mol) for the Pd(110) case. However, such results must be regarded with care as the number of layers employed to build the surface models were different for both cases (three and six atomic layers respectively).

Ethanol decomposition on Pd surfaces has also been studied by Wang *et.al.* who reported binding energies in the range of 2.06 – 2.40 eV (47.5 – 55.3 kcal/mol) for adsorption of ethanol on Pd(100), (110) and (111) surfaces.[9] These values are significantly larger than those computed

by Li *et.al.* and Guo *et.al.* who found very similar binding energies on the order of 0.48 – 0.52 eV (11-12 kcal/mol).[6,7] Another striking difference between the work of Wang and the ones by Li and Guo, is that the former one finds ethanol binding on the Pd(110) surface to be more stable by as much as 0.35 eV (8 kcal/mol) as compared to the Pd(111) surface, while the latter works find the relative stability to be much lower, ~0.009 eV (0.2 kcal/mol). In all the previous works, ethanol adsorption on Pd was found to occur through the oxygen atom for all the three surfaces studied.

In addition to the large differences that turned out when comparing the binding energies between the DFT calculations from References [[6,7,9]], it is important to notice that van der Waals corrections were not considered within their computational approaches. Incorporation of van der Waals interactions can in some cases lead to much different binding energies and geometries for the ethanol–Pd surface system as recently shown by Tereshchuk and Da Silva.[8] In particular, these authors found that in the absence of van der Waals corrections, the ethanol C–C bond resulted oriented almost perpendicular to the metal surface in agreement with Refs[[6,7,9]]. Incorporation of DFT+D3 functional corrections in the calculations led to re-orientation of the ethanol C–C bond to an almost parallel (horizontal) alignment to the surface.

Our efforts to consistently survey the available literature found the existing *ab-initio* data on ethanol adsorption on Pd surfaces to be conflicting and incomplete. For example, to the best of our knowledge there is no available research that analyzes ethanol adsorption on Pd (001) and (110) surfaces which has included van der Waals corrections. Furthermore, only one orientation for the ethanol molecule on the Pd surface was investigated in all cited Refs[[6–9]]. Lastly, none of the available works considered *trans*-ethanol configurations when modeling the ethanol-Pd interactions, which is surprising given its abundant presence in the gas phase as shown by experimental data.[10]

The aim of this work is to remedy all the previous shortcomings by providing a more comprehensive investigation of the ethanol-Pd surface interactions to facilitate future modelling. To achieve such a goal we have performed a detailed investigation of possible ethanol adsorption sites on the three low-index Pd surfaces (100), (110), and (111). We have used three different computational approaches in order to ascertain how the final results are affected by various theoretical approximations. The models considered were pure DFT calculations in the generalized gradient approximation and two dispersion corrected DFT-functionals. The

correction functionals considered were the parameterized method DFT-D2 by Grimme and the parameter-free method DFT-TS by Tkatchenko and Scheffler.[11,12] The binding sites, optimized geometries, and adsorption energies are presented and discussed. The insights presented in this work are expected to facilitate modelling ethanol adsorption on transition metals by rapidly locating the global minimum energies and configurations.

5.2 Theoretical approaches and computational details

Two methods for implementing London forces resulting from dynamical correlations between fluctuating charge distribution of interacting molecules are used to add a dispersion correction term, E_{disp}, to the conventional Kohn-Sham DFT energy, E_{DFT}. One is an empirical van der Waals correction method proposed by S. Grimme (DFT-D2) and the other is a parameter free method proposed by A. Tkatchenko and M. Scheffler (DFT-TS).[11–13] The corrected total energy, $E_{DFT+(D2/TS)}$, is expressed as:

$$E_{DFT+(D2/TS)} = E_{DFT} + E_{disp} \quad 5.1$$

E_{disp} is the sum of the pairwise interatomic term computed by the equations (5.2) and (5.3) for DFT-D2 and DFT-TS, respectively.

$$E_{disp} = -s_6 \sum_{i=1}^{N_{at}-1} \sum_{j=i+1}^{N_{at}} \frac{C_6^{ij}}{R_{ij}^6} f_{damp}(R_{ij}) \quad 5.2$$

$$E_{disp} = -\frac{1}{2} \sum_{ij} \frac{C_6^{ij}}{R_{ij}^6} f_{damp}\left(R_{ij}, R_i^0, R_j^0\right) \quad 5.3$$

Where N_{at} is the number of atoms in the system, R_{ij} is the distance between atoms i and j, C_6^{ij} is the corresponding dispersion coefficient, s_6 is a global scaling factor that only depends on the density functional used, R_i^0 and R_j^0 are the van der Waals radii, f_{damp} is the damping function to avoid near singularities for small distances. The important difference between the two methods is that in DFT-TS the dispersion coefficients and damping function are charge-density dependent. Therefore, the DFT-TS method is able to take into account variations in van der Waals contributions of atoms due to their local chemical environment.

To assess the role van der Waals interactions play on ethanol adsorption on Pd surfaces and to compare the approximation accuracy of the two proposed approaches, three sets of calculations were performed. The first set did not include any corrections of van der Waals-type but pure density functional, PBE, while the other two sets of calculations incorporated the two alternative

descriptions for modeling the van der Waals interactions. Both approaches were performed as implemented in Vienna *Ab-initio* Simulation Package (VASP version 5.3.3) and described in detail in chapter 3.[14,15]

The Pd surfaces were modelled with the help of periodic slab geometries generated from (3x3) surface unit cells which extended a depth of five Pd monolayers with vacuum regions of 10 Å. Three different geometries were considered: an open (100) surface, a monatomic step (110) surface and a closed-packed (111) surface all of which are shown in Figure 5.1

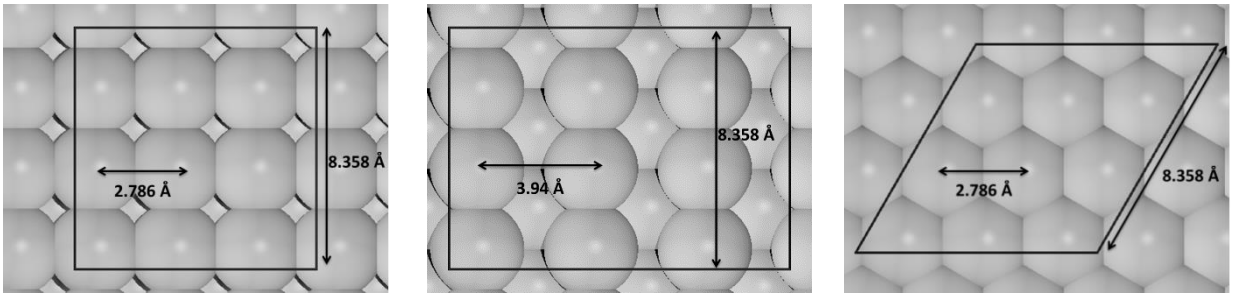

(a) (b) (c)

Figure 5.1: Top view of the surface unit cells used for generating the different slabs: (a) Pd(100), (b) Pd(110) and (c) Pd(111).

Slabs were cut from the optimized Pd bulk unit cell with a lattice constant of a = 3.94 Å which overestimates the experimental value of 3.89 Å by 1%. In all geometry optimizations only the top-two Pd monolayers were allowed to relax whereas the bottom three monolayers were kept fixed. We employed a force stopping criterion for all optimizations with tolerance set to 0.02 eV/Å. Such an approach rendered small changes in energies and geometries as compared to allowing full relaxation of all atoms in the slabs (energy changes of less than 0.03 eV (6.9 kcal/mol) and distance variations between Pd atoms in the top monolayers less than 0.002 Å). This is not surprising since the slabs were cut out from the optimized bulk unit cell.

In addition to the different slabs, three different initial configurations for the ethanol molecule resting on each surface were considered. Shown in Figure 5.2 (a), (b) and (c) are the cited configurations labelled by us as “horizontal”, “oxygen down” and “oxygen up”.

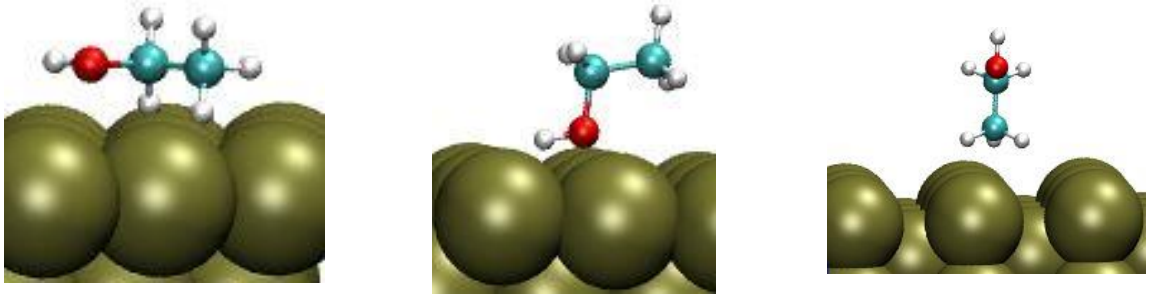

(a) (b) (c)

Figure 5.2: The three starting configurations of ethanol on the Pd surfaces: (d) horizontal (e) oxygen down and (f) oxygen up.

Ethanol is known to possess two stable conformers in the gas-phase: the *cis*-conformation in which the O–H bond is almost perpendicular to the C–C bond (Figure 5.3 a) and the *trans*-conformation in which the O–H bond is parallel to the C–C bond (Figure 5.3 b).

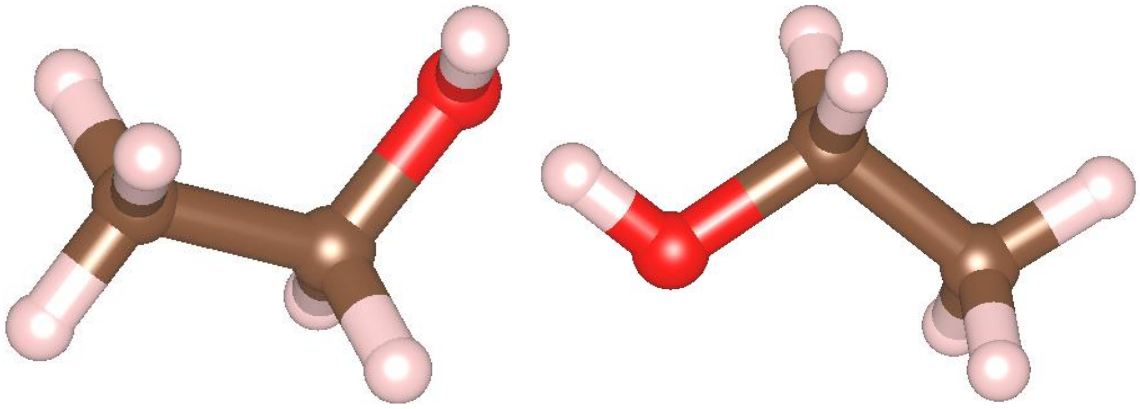

(a) (b)

Figure 5.3: The two possible conformations of ethanol in the gas phase: (a) cis-Ethanol, (b) trans-Ethanol.

The energies for these two isomers are almost identical differing by just 0.01 eV (0.2 kcal/mol). In principle, local energy minima of surface-adsorbed ethanol must differ depending on which of the two ethanol isomers initially approaches the Pd surface. For instance, the *cis* isomer tends to prefer a conformation in which the C–C bond is somewhat perpendicular to the surface as reported in the previous literature while the *trans* isomer prefers a conformation with the C–C bond parallel to the surface as will be discussed below. The fact that experimental data [10] supports the prevalence of the *trans*-conformation in the gas phase, our calculations will focus on this geometry. However, an example will be given for the *cis*-conformation to compare our energy values to those reported in the literature. For the *trans*-ethanol geometry optimization we

gathered the initial atomic coordinates from the Computational Chemistry Comparison and Benchmark Database (CCCBDB).[16] Next, a single molecule was allowed to relax in a large cubic periodic box with side length of 15.0 Å.

Optimizations of the hybrid systems were started by placing the ethanol molecule over the corresponding optimized Pd slab at about 2 Å away from the surface in the three different positions described in Figure 5.2. Upon optimization, the adsorption energy (E_{ads}) for the ethanol-Pd slab was calculated using equation (5.4).

$$E = E_{EtOH+Pd} - (E_{EtOH} + E_{Pd}) \qquad 5.4$$

where $E_{(EtOH+Pd)}$, $E_{(EtOH)}$, and $E_{(Pd)}$ are the total energies of the full system, the isolated ethanol molecule and the clean Pd surface accordingly. To gauge the stability of adsorbed ethanol molecules on the aforementioned Pd surfaces, bader charge density distribution and local projected density of states (LDOS) calculations using an 11 x 11 x 1 *k*-point mesh were conducted. Lastly, system visualizations were performed using the Visual Molecular Dynamics (VMD),[17] Materials Studio packages[18] and Visualization for Electronic Structure Analysis (VESTA).[19]

5.3 Results and Discussion

To facilitate comparison among the different systems and models we have split the presentation of our results into two parts. Part one, comprise results corresponding to the "horizontal" and "oxygen down" ethanol configurations on three different Pd surfaces with values shown in Table 5.1. Part two encompasses data corresponding to the "oxygen up" case as covered with values shown in Table 5.2. The results were grouped in such a manner based on the similarities displayed by the final equilibrated structures of the ethanol molecule. After optimization, "horizontal" and "oxygen down" systems rendered very similar final structures as opposed to "oxygen up", which had different configuration. The "horizontal" ethanol configuration is characterized by initially having the C–C–O plane aligned parallel to the Pd surfaces (Figure 5.2a). Conversely, in the "oxygen down" configuration the C–C bond was initially aligned parallel to the surface and oxygen atom being closer to the surface (Figure 5.2b). The key parameters distinguishing between optimized "horizontal" and "oxygen down" geometries are the angle formed between Pd–O–C bonds and O–Pd bond distances as

summarized in Table 5.1. The "oxygen up" arrangement had the C–C bond oriented perpendicular to the surface and the oxygen atom facing away from it (Figure 5.2c).

Table 5.1: Adsorption energies E_{ads} in eV and (kcal/mol), the angle ϴ between palladium-oxygen-carbon (Pd-O-C) bonds and oxygen-palladium (O-Pd) bond distances (Å) of ethanol on Pd obtained after geometry optimizations using PBE, PBE+D2 and PBE+TS. The data corresponds to optimizations performed on "horizontal" (h) and "oxygen down" (Od) initial configurations.

Initial geometry guess	**PBE**			**PBE+D2**			**PBE+TS**		
	Θ_{Pd-O-C}	**O-Pd**	**E_{ads}**	**Θ_{Pd-O-C}**	**O-Pd**	**E_{ads}**	**Θ_{Pd-O-C}**	**O-Pd**	**E_{ads}**
Pd100+EtOH-h	121.2	2.35	-0.33(7.6)	114.4	2.30	-0.87(20.1)	121.4	2.33	-0.68(15.7)
Pd100+EtOH-Od	133.0	2.42	-0.28(6.4)	120.4	2.36	-0.79(18.2)	125.3	2.36	-0.59(13.6)
Pd110+EtOH-h	117.4	2.33	-0.41(9.4)	110.7	2.30	-1.06(24.4)	115.6	2.31	-0.80(18.4)
Pd110+EtOH-Od	122.5	2.32	-0.38(8.8)	114.1	2.25	-0.91(21.0)	116.7	2.25	-0.78(18.0)
Pd111+EtOH-h	119.1	2.40	-0.30(6.9)	116.2	2.32	-0.88(20.3)	118.4	2.37	-0.69(15.9)
Pd111+EtOH-Od	123.5	2.37	-0.30(6.9)	119.4	2.27	-0.83(19.1)	121.8	2.34	-0.68(15.7)

Table 5.2: Equilibrium adsorption energies in eV and (kcal/mol) and C–Pd & H–Pd (the closest H) bond lengths (in Å) of *trans*-ethanol corresponding to 'oxygen up' configurations.

Oxygen up configuration	PBE			PBE+D2			PBE+TS		
	C-Pd	H-Pd	E_{ads}	C-Pd	H-Pd	E_{ads}	C-Pd	H-Pd	E_{ads}
Pd100+EtOH	3.41	2.64	-0.03(0.7)	3.25	2.23	-0.33(7.6)	3.37	2.56	-0.23(5.3)
Pd110+EtOH	3.38	2.64	-0.05(1.1)	n/a	n/a	n/a	3.18	2.22	-0.31(7.1)
Pd111+EtOH	3.64	2.73	-0.03(0.7)	3.15	2.53	-0.32(7.4)	3.37	2.46	-0.25(5.8)

5.3.1 Surface characterization for "horizontal" and "oxygen down" initial configurations

EtOH on the Pd(111) surface: Figure 5.4, shows the low energy equilibrium configurations for adsorbed *trans*-ethanol on the Pd(111) surfaces.

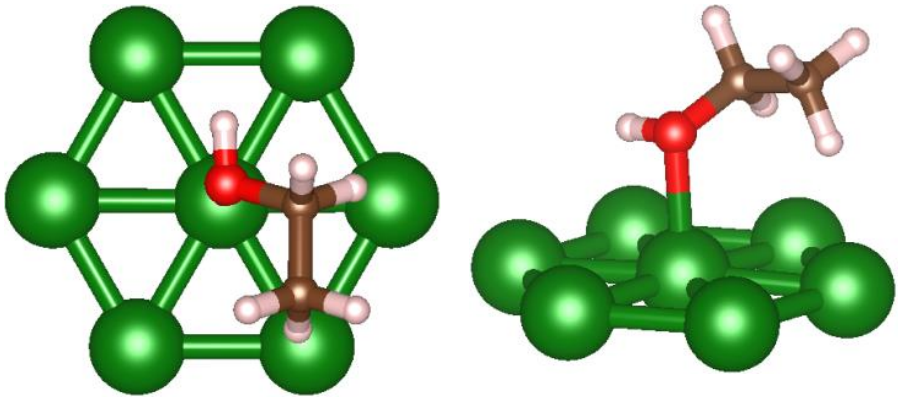

Figure 5.4: Top and side views of final optimized geometry of the *trans*-ethanol molecule on low index Pd surfaces (111). Only one set is shown because the configurations for "horizontal" and "oxygen down" were similar.

The geometry configuration to favoured 'on top' arrangements (the oxygen atom rests over a Pd surface atom) for all three approaches considered herein (PBE, PBE+D2, and PBE+TS). Such equilibrium geometries point out to an adsorption process mediated by the oxygen atom, with ethanol equilibrium morphologies in which the O–H and C–C bonds resulted in almost parallel alignment to the Pd surface. The "horizontal" and "oxygen down" configurations turned out to be almost isoenergetic, with maximum energy differences of 0.04 eV (1 kcal/mol) for all three approaches used. The inclusion of van der Waals corrections within the computations proved to strongly enhance ethanol stability on the surfaces. The strength of the binding energetics increased from, approximately, -0.30 eV (-6.9 kcal/mol) in PBE to -0.68 eV (-15.7 kcal/mol) and -0.85 eV (-19.6 kcal/mol) in the case of PBE+TS and PBE+D2, respectively (see Table 5.1). This stabilization is in qualitative agreement with the recent work of Tereshchuk and Da Silva who have reported that the adsorption energy of ethanol on the Pd (111) surface increased from 6 kcal/mol to 17 kcal/mol upon inclusion of PBE+D3 corrections.[8]

To establish if the *trans*-ethanol has dominance in the overall adsorption process, we performed a set of geometry relaxation with *cis*-ethanol at the surface location corresponding to the global minima identified by us for *trans*-ethanol. Such an exercise yielded binding energies of -0.28 eV (6.4 kcal/mol) and -0.75 eV (17.3 kcal/mol) for the PBE and PBE+D2 functionals. Therefore, from these results we have established that the binding of *trans*-ethanol is more favorable (-0.88 eV) than that of *cis*-ethanol (-0.75 eV) which would facilitate future modelling studies.

EtOH on the Pd(100) surface: In the case of the Pd(100) surface, two minor possible ethanol adsorption sites were identified but the geometric configurations were the same as shown in Figure 5.5.

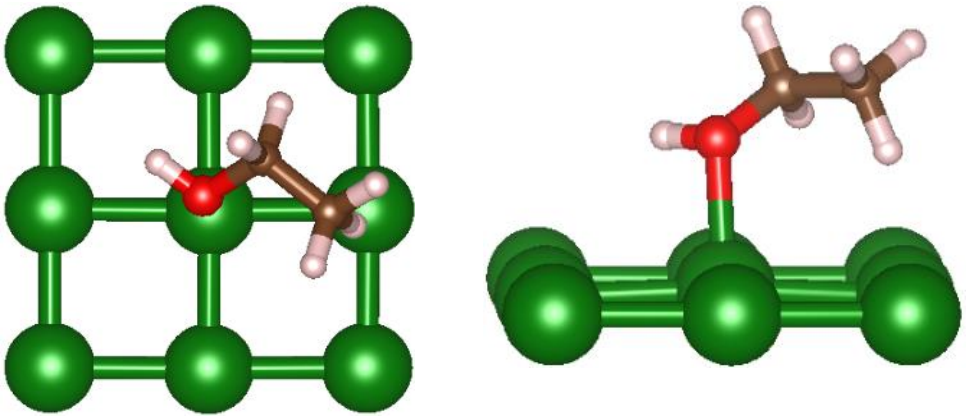

Figure 5.5: Top and side views of final optimized geometry of the *trans*-ethanol molecule on low index Pd surfaces (100). There were minor adsorption site differences between "horizontal" and "oxygen down" as explained in the text.

The first adsorption site was found to have the oxygen atom occupying an 'on-top' configuration, Figure 5.5. The 'on-top' binding sites were obtained in computations initialized from "horizontal" initial configurations employing PBE and PBE+TS functionals and from "oxygen down" initial configurations in combination with the PBE+TS functional. In the second adsorption site, the oxygen atom was found to display a 'bridge' placement (the oxygen atom lies over the bond formed by two Pd atoms. This binding site resulted from calculations using PBE+D2 functional on "oxygen down" initial configuration. Conversely, PBE+D2 acting on "horizontal" initial configuration produced final ethanol geometry where the oxygen atom was slightly off from displaying 'on top' final configurations.

We found the 'on-top' binding site to be slightly more energetically-preferable than the 'bridge' by about 0.09 eV (2 kcal/mol). Similar to Pd(111) surface, 'on-top' ethanol adsorption on Pd(100) was found to take place through the oxygen atom with both the O–H and C–C bonds showing parallel alignment to the surface and the inclusion of van der Waals corrections enhanced stabilization of ethanol on the surface. The binding energy trend displayed the following order: -0.31 eV (7.1 kcal/mol), -0.64 eV (14.7 kcal/mol) and -0.83 eV (19.1 kcal/mol) for PBE, PBE+TS and PBE+D2, respectively (see Table 5.1).

EtOH on the Pd(110) surface: Like in the past two surface cases, here we found ethanol adsorption to occur again via the oxygen atom as shown in Figure 5.6.

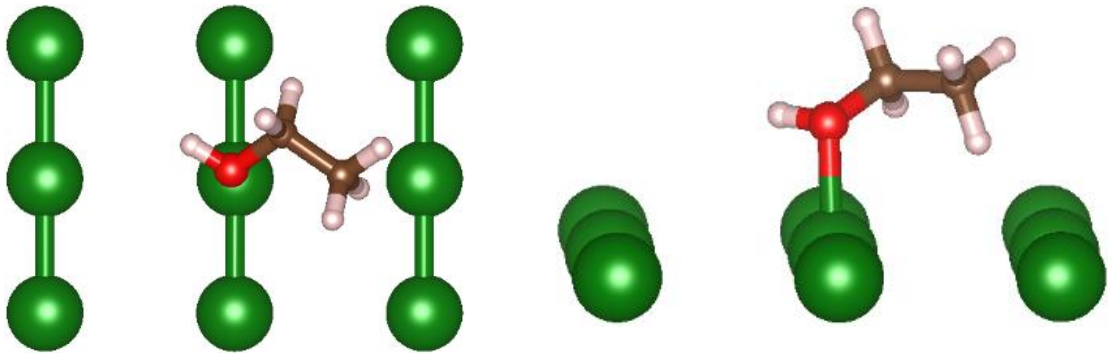

Figure 5.6: Top and side views of final optimized geometry of the *trans*-ethanol molecule on low index Pd surfaces (110).

Only one binding site was identified for Pd(110) slabs; the 'on-top' configuration with O–H and C–C bonds parallel-oriented with respect to the surface. Computed binding energies turned out to be: -0.39 eV (9.0 kcal/mol), -0.79 eV (18.2 kcal/mol) and -0.98 eV (22.6 kcal/mol) for PBE, PBE+TS and PBE+D2, respectively as covered in Table 5.1. Note that our data for the current 'on-top' binding site was found to be in good agreement with the data reported by Guo *et al*.[6]

5.3.2 Surface characterization for "oxygen up" initial configurations

In general, adsorption calculations performed on "oxygen up" configurations did not render significant variations between the outcomes from different surfaces. In figure 5.7 we show top and side views of optimized geometries on Pd(111), (100) and (110) slabs for PBE+TS stable geometries. The final geometries obtained with the other two methods (PBE and PBE+D2) were qualitatively similar to the results shown on Figure 5.7 with one exception. The "oxygen up" configuration for ethanol on the Pd(110) using the PBE+D2 functional did not remain stable in terms of the molecule orientation with respect to the slab. Upon optimization, this assembly led to "horizontal" ethanol geometry similar to the one portrait in Figure 5.6. Adsorption energies and bond lengths (C–Pd and H–Pd) for all final equilibrated geometries are summarized in Table 5.2.

Generally, optimization of "oxygen up" configurations rendered molecular structures with the β-C closer to the Pd surface. We found low values for the binding energy in the order 0.04 – 0.09 eV (1-2 kcal/mol) in the absence of van der Waals correction terms. Inclusion of such terms via PBE+TS or PBE+D2 methods stabilized the ethanol on the surface by an extra of 0.22 – 0.35 eV (5-8 kcal/mol). Overall, equilibrium sites obtained from "oxygen up" configurations employing

corrected-functionals displayed much weaker binding energies than 'on top' calculations modelled with the pure PBE functional covered in the past section (about 6.9 kcal/mol difference). As earlier, it was found that the binding on the Pd(110) surface is slightly more favorable than that on the (100) and (111).

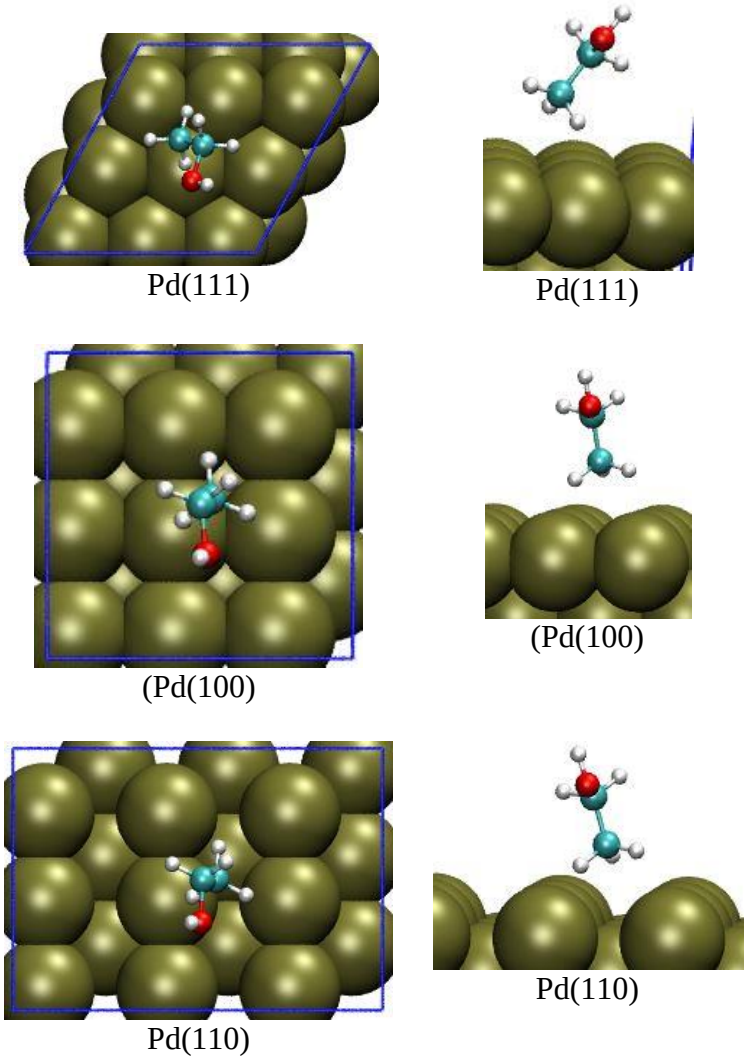

Figure 5.7: Optimized geometries of trans-ethanol on low index (111), (100), and (110) Pd surfaces for 'oxygen up' configurations.

5.3.3 Electronic structure of ethanol adsorption on palladium surfaces

Adsorption characteristics of a system can be extended beyond geometry and binding energies, using electronic structure configurations to rationalize in more detail the differences between adsorbed structures. To gain further insight into the nature of the ethanol-Pd surface interactions we performed bader charge distribution analysis and projected local density of states (LDOS) analysis to study the variations that appeared in the system's electronic structure as a

consequence of the adsorption process. The LDOS is a descriptor that accounts for how much the total density of states around the vicinity of an atom (or group of atoms) contributes to a certain orbital. Such a descriptor displays large peak intensities at energies where there is a significant contribution in eigenstates. It can also show large intensities at energy intervals with a large number of states. Such analysis was conducted on each individual system: an isolated ethanol molecule, clean Pd slabs corresponding to each surface studied and the final configurations of all ethanol-Pd surface complexes. Since ethanol with "oxygen up" configurations did not lead to any significant interaction with Pd surfaces and due to the similarities between "horizontal" and "oxygen down" configurations the following discussion will focus on the most stable configurations with emphasis in the effect of van der Waals corrections.

First, we analyzed the charge distribution and the nature of the energy levels of the ethanol molecule in gas phase as shown in Figure 5.8. For the case of energy levels, a convention where the z-direction was chosen perpendicular to the *xy* plane (defined by C–C–O atoms) was adopted. Following such a convention, the iso-surfaces of the three top-most occupied molecular orbitals of ethanol in vacuum were calculated are shown in Figure 5.8. The HOMO for ethanol has π^* anti-bonding character and is composed from combining p_z atomic orbitals from the oxygen atom and α-C atom as well as the *s* atomic orbitals from the hydrogens. The second occupied orbital (HOMO-1) is made up by p_x and p_y atomic orbitals from both the two carbon atoms and oxygen atom with an additional contribution from the *s* atomic orbitals on the hydrogens. The third occupied orbital (HOMO-2) shows mostly anti-bonding character and is made up of a combination of p_z atomic orbitals from the two carbons. There is a small bonding character associated to the HOMO-2 which stems from associating the p_z atomic orbitals on the oxygen and the α-C. The next two following orbitals (not shown) HOMO-3 (-3.11 eV) and HOMO-4 (-3.63 eV) are made up of in-plane p_x and p_y atomic orbitals respectively. We would like to point out that ethanol has a relatively large HOMO-LUMO gap as computed from density functional calculations via the PBE functional (~ 6.34 eV).

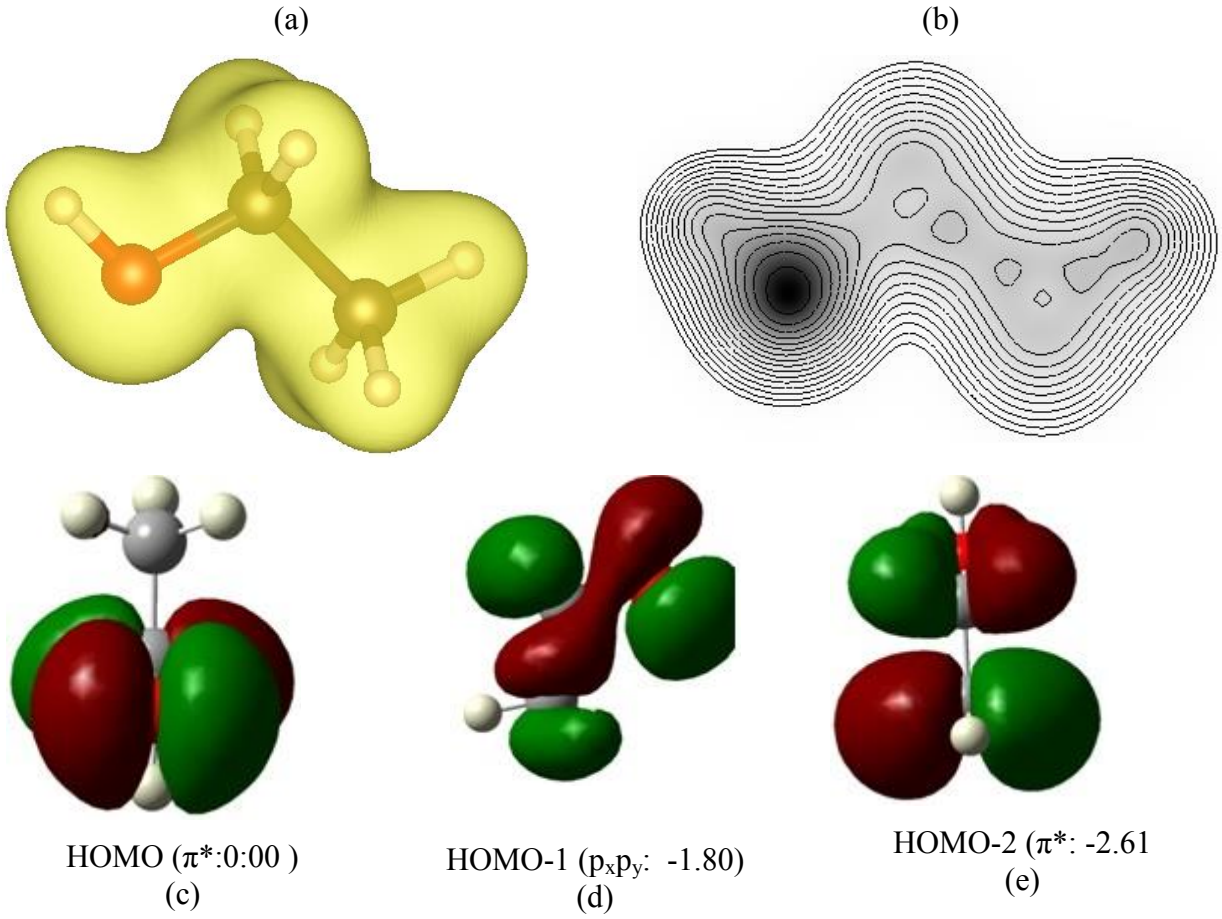

Figure 5.8: (a) Shows the charge distribution isosurface for ethanol and (b) shows a slice at the C–C–O bond. The bottom row shows the molecular orbitals isosurfaces at relative energies (in eV) of the orbitals of (c) 0.00 eV, (d) -1.80 eV, and (e) -2.61 eV. The zero energy corresponds to the highest occupied molecular orbital (HOMO).

Ethanol interacts with Pd metal surfaces through oxygen atoms' lone pair of electrons. A representative charge distribution for the three functionals tested (PBE, PBE+TS and PBE+D2), sliced at C–O–Pd bonds for ethanol-Pd systems is shown in Figure 5.9.

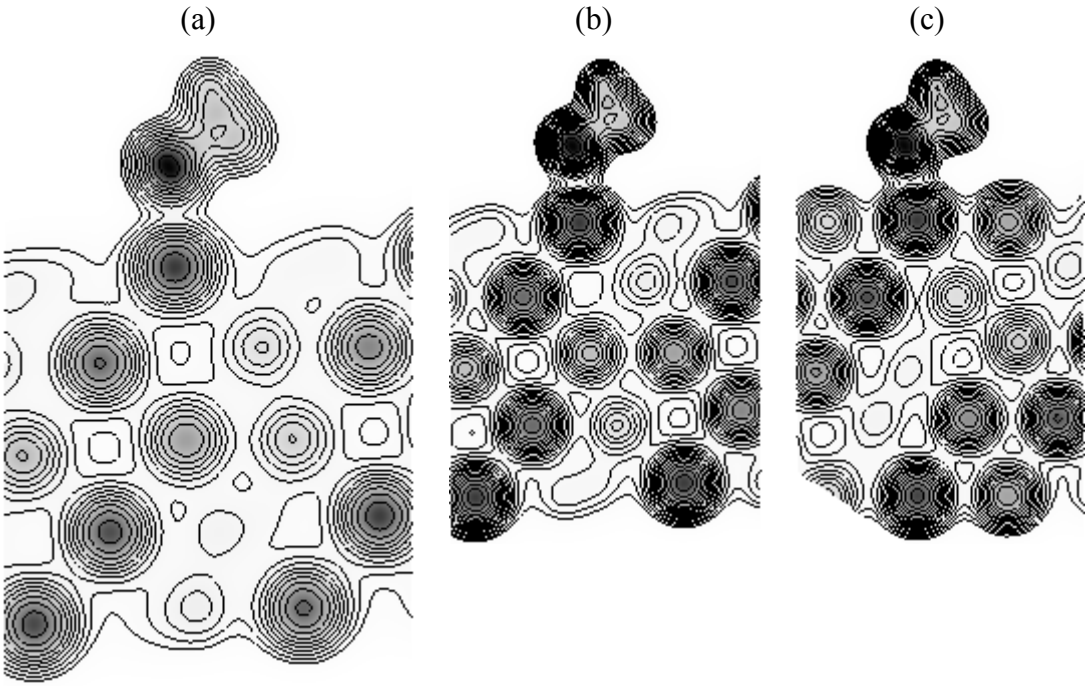

Figure 5.9: Charge density distribution showing the slice through C–O–Pd bond for PBE (a) PBE+TS (b) and PBE+D2 (c). The charge distribution shown is from the most stable structure of ethanol-Pd(100) surface. The systems were plotted on the same scale for comparison. The van der Waals corrections tend to concentrate the charge distribution closer to the atoms hence holding them tight together.

The corresponding net charge distribution (the difference between neutral atom and adatom) are summarized in Table 5.3.

Table 5.3: Bader charges of atoms for molecularly adsorbed ethanol on (100) surface with an adatom present and for gas phase ethanol

Geometry	E_{ads}/eV	Pd_{ads}/e	O/e	C_α/e	C_β/e	alcohol H/e	H_α/e
Pd100 PBE	-0.33	0.105	-1.100	0.333	-0.154	0.622	0.068
PBE+TS	-0.68	0.109	-1.151	0.355	-0.140	0.662	0.065
PBE+D2	-0.87	0.112	-1.073	0.334	-0.111	0.595	0.073
Ethanol	-	-	-1.120	0.466	-0.118	0.610	0.010

The charge distribution slices shown in Figure 5.9 were graphed on the same scale and the difference between pure PBE functional and dispersion corrected functionals is revealed. For weaker binding energies, obtained from PBE functional, the atoms are well relaxed with a higher cell volume. Consequently, the charge distribution is well spread out. Inclusion of van der Waals corrections on the other hand, tends to concentrate the charge distribution closer to the atoms

hence holding them tight together. It is evident from Figure 5.9 that dispersion corrected models (PBE+TS and PBE+D2) show high charge density between the Pd–O bonds leading to the observed strong binding energies. For the strongest binding energies, PBE+D2, the oxygen atom is in closer proximity to more surface Pd atoms as shown in Figure 5.9(c). This closer proximity of oxygen atoms with Pd atoms allows electronic hybridization in the boundary leading to stronger bonds. The charge distribution shows that bonding Pd is positively polarized while the oxygen atom is negatively polarized (Table 5.3 column 3 and 4). The polarization of Pd atom bonding to oxygen atom was found to increase with the increasing binding energy due to dispersion corrections.

LDOS analysis of atoms provided us with further means to differentiate between weak and strong adsorption sites. Analysis of the LDOS on ethanol revealed a molecular HOMO which strongly hybridized with the surface states. This fact was better supported after comparing atomic LDOS for carbon and oxygen for the three functionals tested. Figure 5.10 is a representative LDOS analysis that was performed uniquely on the carbon and oxygen atoms at the three levels of theory employed in the calculations. Only the p-orbitals are shown for clarity.

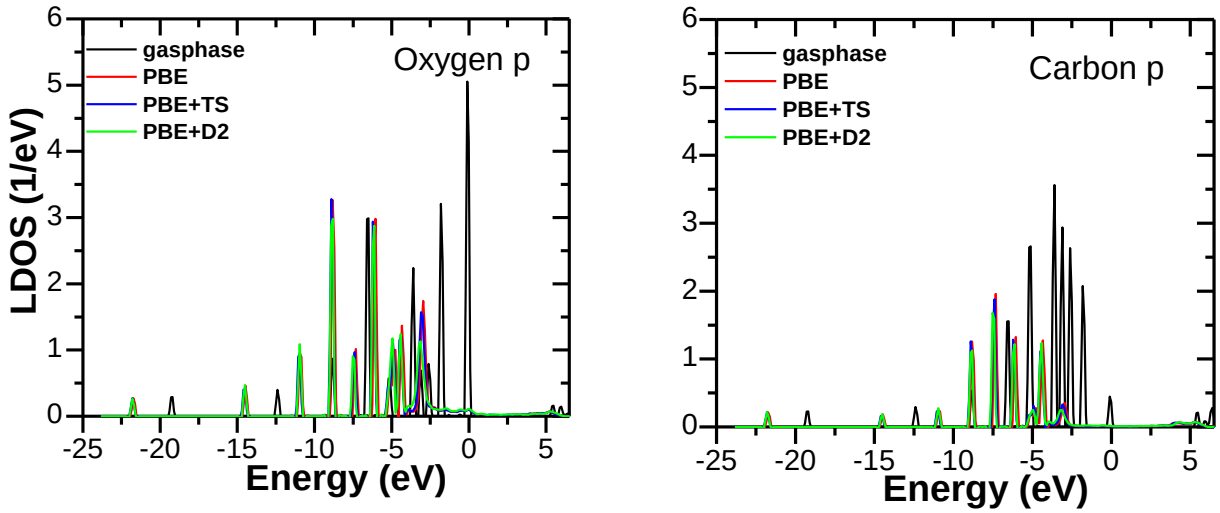

(a) (b)

Figure 5.10: Representative p-orbital LDOS for oxygen and carbon atoms from most stable ethanol-Pd(100) surface "horizontal" configuration with and without dispersion corrections.

The carbon and oxygen 2p-states were found to fall within the Pd d-band region, i.e., the Pd d-band extended down to -5 eV below the Fermi energy as depicted in Figure 5.10. We found that the carbon and oxygen p_z-states (0 eV p-states) hybridized with the surface Pd atoms and cannot be associated with carbon or oxygen after bonding. All other states (peaks) were found to shift

towards lower energies. The HOMO-1, HOMO-2, and HOMO-3 levels located within the Pd d-band increased their widths to the extent that the overlap between the HOMO-2 and HOMO-3 made them hardly distinguishable from one another. Depopulation of p_z-states from carbon and oxygen atoms upon adsorption indicates a charge transfer in agreement to bader charge distribution analysis for the case of PBE and PBE+D2 shown in Table 5.3. For the two cases, the net charge for oxygen decreased from -1.12 in gas phase to -1.10 and -1.07 in adsorbed phase for PBE and PBE+D2, respectively.

The results show that inclusion of van der Waals interactions enhanced the broadening of carbon pz-states which found their tails extended above the Fermi level similar to other existing reports.[8] It is important to note that such polarization effects were only recorded when binding between the oxygen atoms and the surfaces took place. LDOS for Hydrogen and Pd atoms did not show any significant differences. However, we would like to comment on some unique observations for the case of Pd LDOS.

The LDOS corresponding to projections on only Pd slab atoms are shown in Figure 5.11. Three independent groups of calculations were conducted which comprised of projecting the electronic density i) on the top Pd surface atoms, ii) in the bulk Pd (middle) atoms, and iii) the bonding Pd atom. The intensities (y-axis) were normalized to generate mono-atomic responses (i.e. eV/atom) for each case to ensure meaningful comparisons. The LDOS for Pd atoms revealed a strong d-character in the region extending down to -5 eV below the Fermi level which compares well with previous data reported in the literature.[8] Such a d-band turned out to be almost fully occupied with a shape dependent on the surface geometry (100, 110 or 111) and volumetric features (surface only or bulk slab).

The graphs for the "average" LDOS of the slabs (not shown) were characterized by the presence of sharp peaks near the Fermi level which resulted mainly from contributions due to bulk Pd atoms shown in Figure 5.11 (A–C) curves 'b'. In addition, note the similarities displayed in Figure 5.11 between the "bulk" LDOS for the (100) and (111) cases. In those plots three major peaks were identified, one centered slightly below the Fermi level (-0.1 eV) and a second one located approximately in the middle of the d-band -2.5 eV below the Fermi energy and a less pronounced third peak located at approximately -4.0 eV below the Fermi level.

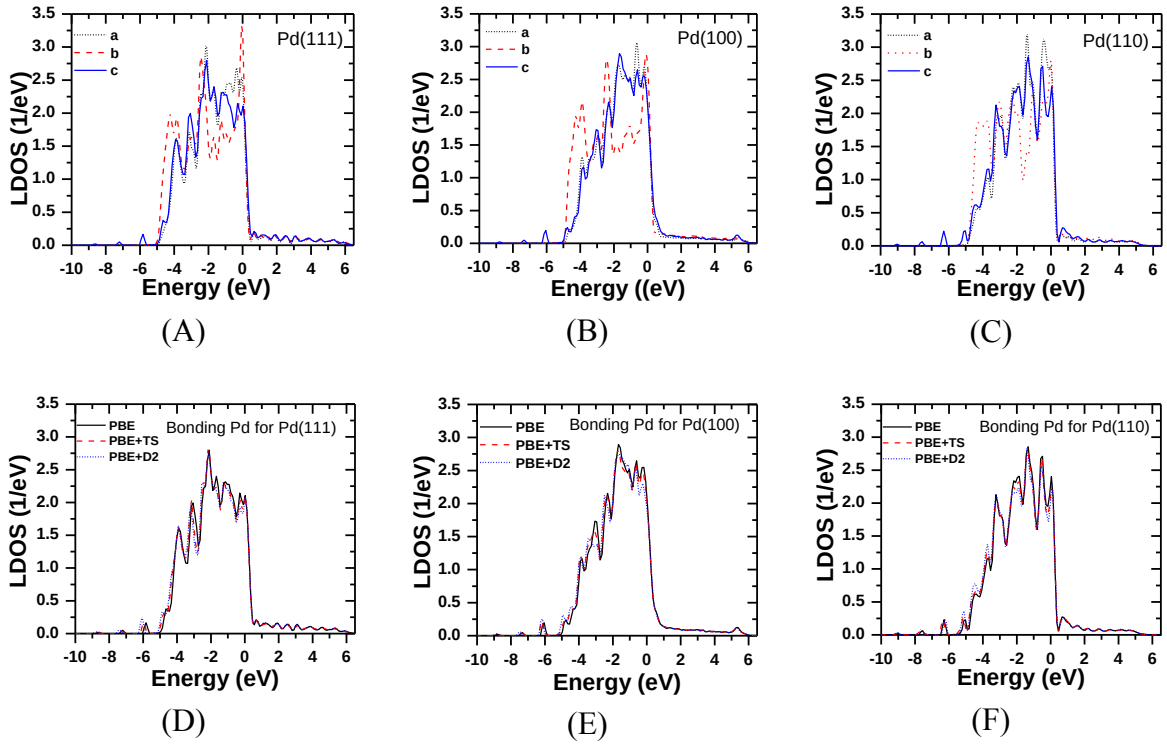

Figure 5.11: Graphs (A), (B), and (C) show the LDOS plots for (a) surface Pd atoms, (b) bulk middle Pd atoms, and (c) the bonding Pd atoms at PBE level. Graphs (D), (E), and (F) show the LDOS plots for bonding Pd atoms at PBE, PBE+TS and PBE+D2. (A) and (D), (B) and (E), and (C) and (F) represents (111), (100), and (110) Pd surfaces, respectively. The LDOS for Pd atoms revealed a strong d-character in the region extending down to -5 eV below the Fermi level.

When comparing the LDOS of only surface atoms in the absence of the adsorbent Figure 5.11 (A–C) curves 'a' or in the presence of the adsorbent curves 'c', we found that with or without van der Waals corrections, the states remained almost unchanged. This could be due to the potential mismatch between the high 3d-states of the Pd and the low p-states of ethanol. Therefore, LDOS computations involving projections on surface atoms did not prove useful to identify the most stable configuration of the adsorbate on the surface compared to charge distribution analysis.

In summary, charge density distribution analysis and LDOS calculations proved to be a suitable tool to characterize the nature of the adsorbed state of the ethanol molecule on Pd surfaces. Charge analysis turned out to be more effective in explaining the difference between weak and strong binding sites which in extension explains the effect of van der Waals interactions. The charge density in the Pd–O bond increased for dispersion corrected calculations leading to stronger binding energies. The minimal changes encountered in the LDOS between the gas phase and adsorbed states of ethanol initialized from "oxygen up" configurations

revealed no overall binding features. Although the inclusion of dispersion corrections stabilized the adsorbate for the "oxygen up" configuration, variations in the LDOS projected onto the adsorbate remained negligible. On the contrary, strong orbital hybridization encountered in "horizontal" configurations lead to stronger adsorbate/surface interactions which ultimately resulted in chemical bonding.

5.4 Conclusions

In this work we conducted first-principles calculations to study ethanol adsorption on three low-index palladium surfaces (111,110 and 100). We have showcased the significant role of two van der Waals correction functionals (PBE+D2 and PBE+TS) in the electronic configuration of ethanol adsorption on Pd and their effects on the adsorption energy values. Compared to pure PBE calculations, inclusion of dispersion corrections turned out to significantly increase the binding energies by as much as 0.56 eV (13 kcal/mol). It was found that inclusion of such corrections improves ethanol adsorption stability compared to pure DFT functionals hence would be critical in establishing adsorption trends of closed shell molecules on transition metals.

We found ethanol to bind the strongest onto the Pd(110) surface and the PBE+D2 computational approach to yield the strongest binding energy. These results contradict the data reported by Wang *et al*.[9] where ethanol was shown to bind the strongest on the Pd(100) surface. Our final geometry for adsorbed *trans*-ethanol is in qualitative agreement with previous results presented in the literature where ethanol-Pd surface binding was reported to be mediated by 'on top' configurations.[6–9]

Stronger binding energies upon inclusion of dispersion corrections were attributed to the increasing charge density distribution between Pd–O bonds leading to enhanced interactions. In particular, the projected local density of states calculations revealed that the carbon and oxygen p_z-states and the Pd d-band electrons play a critical role in stabilizing the adsorbate on the surface. Such reinforcement in the interactions ultimately led to a reduction in the Pd–O and Pd–C bond lengths.

Three different initial geometry configurations were tested to ensure a comprehensive search was done to mitigate inaccuracies due to wrong geometry or energy minimal structures which are not the global minimum. In this work, we show that *trans*-ethanol configuration is the most stable geometry that should be used in the simulations and not the *cis*-ethanol configuration

presented in the previous reports. We report that the most energetically-stable geometry configuration for ethanol corresponds to when the C–C bond is almost parallel to the surface plane with the oxygen atom somewhat closer to the surface and located right on top of a Pd atom. This kind of configuration is referred to as “horizontal” in this work. Ethanol was found to be more stable on (110), followed by (100) then (111).

Chapter 6: Synergetic effect of Palladium-Ruthenium Nanostructures for Ethanol Electrooxidation in Alkaline Media

Publication: E. A. Monyoncho, S. Ntais, F. Soares, T. K. Woo, and E. A. Baranova *Journal of Power Sources,* 287 (**2015**) 139-149, DOI: 10.1016/j.jpowsour.2015.03.186

Abstract

Palladium-ruthenium nanoparticles supported on carbon Pd_xRu_{1-x}/C (x = 1, 0.99, 0.95, 0.90, 0.80, 0.50) were prepared using a modified polyol method for ethanol electrooxidation in alkaline media. The resulting bimetallic catalysts were found to be primarily a mix of Pd metal, Ru oxides and Pd oxides. Their electrocatalytic activity towards ethanol oxidation reaction (EOR) in 1M KOH was studied using cyclic voltammetry and chronoamperometry techniques. Addition of 1 to 20 at.% Ru to Pd not only lowers the onset oxidation potential for EOR but also produces higher current densities at lower potentials compared to Pd by itself. Thus, $Pd_{90}Ru_{10}/C$ and $Pd_{95}Ru_5/C$ provide the current densities of up to four times those of Pd/C at -0.96 V and -0.67 V vs MSE, respectively. The current density at different potentials was found to be dependent on the surface composition of Pd_xRu_{1-x}/C nanostructures. $Pd_{90}Ru_{10}/C$ catalyst with more surface oxides was found to be active at lower potential compared to $Pd_{95}Ru_5/C$ with less surface oxides, which is active at higher potentials. The steady-state current densities of the two best catalysts, $Pd_{90}Ru_{10}/C$ and $Pd_{95}Ru_5/C$, showed minimal surface deactivation from EOR intermediates/products during chronoamperometry.

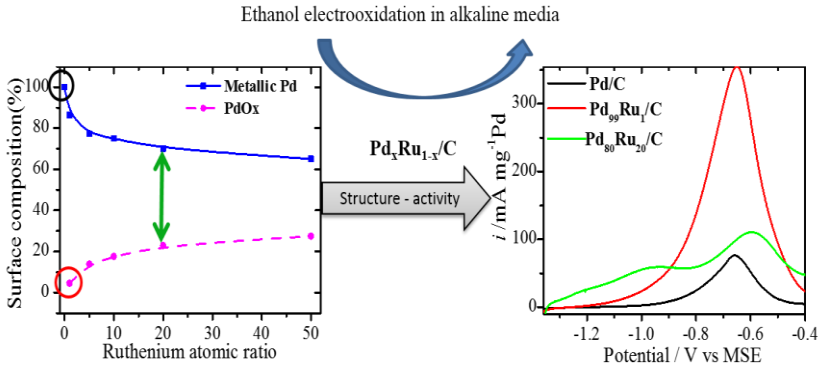

Keywords: Ethanol electrooxidation, Palladium, Ruthenium, nanoparticles, alkaline solution, direct alcohol fuel cells

6.1 Introduction

Palladium has been shown as a promising electrocatalyst for ethanol oxidation in alkaline media.[1] Efforts in combining Pd with a second metal that can be either noble, e.g., Ru, Au, Rh or non-noble metals such as Fe, Co, Ni, Cu and Mo have been shown to improve not only the catalytic activity but also reduce the cost of the *membrane electrode assemblies* (MEAs).[2–6] Ruthenium is known as a good promoter for alcohol oxidation and was recently reported to enhance ethanol oxidation on Pt in alkaline media yielding CO_2 as the major final product.[7] Recently, the interest for bimetallic Pd-Ru catalyst systems for ethanol oxidation reaction (EOR) in alkaline media has attracted the attention of various research groups.[8–13]

Chen *et al.* and Sun *et al.* have compared the performance of Pd-Ru and Pt-Ru and showed that Pd-Ru in alkaline media is almost four times better for EOR than Pt-Ru.[8,14] Yi *et al.* studied porous Pd-Ru nanoparticles supported on titanium prepared by hydrothermal method.[9] They reported that $Pd_{87}Ru_{13}$ showed the best catalytic activity towards EOR in alkaline media in means of current density and onset potentials. They suggested that the "bifunctional mechanism" and the large surface area of $Pd_{87}Ru_{13}$ are playing a critical role in the overall catalytic performance. Anindita *et al.* investigated nanostructured Pd-Ru nanoparticles supported on carbon synthesized using sodium borohydride reduction method.[10] They prepared Pd-0.5wt% C and Pd-0.5wt%C-x wt. % Ru where x was 1, 5, 10, 20, and 50. They found that when the ruthenium content is 20 wt.% electrocatalytic activity for EOR in alkaline media increases considerably. Bagchi *et al.* studied the electrocatalytic activity of an electrodeposited Pd-Ru catalyst supported on nickel for EOR in alkaline media.[11,13] They observed that the amount of loading and the composition of the catalyst have a superimposed effect on ethanol electrocatalytic activity. The thinner the electrodeposit film, the greater was the peak current per unit mass of deposit due to greater roughness factor arising from small size of the crystallites. Correia *et al*. studied EOR using Pd-Ru bimetallic complexes.[12] Although, they found increased current density at high potentials, no improvement was observed on onset potential for the reaction. In the recent work by Liang Ma *et al*.,[15] authors reported EOR on Pd-Ru supported on carbon prepared by impregnation method with Ru content ranging between 20 and 50%. Liang

Ma *et al*. showed that Pd-Ru system not only performs well in half-cell tests but also gave 1.8 times higher power density compared to Pd/C in prototype fuel cell assemblies. They showed that the best performing catalyst has composition of 25% Ru and that the PdRu/C catalysts are promising materials for ethanol oxidation in alkaline environment.

Despite all these studies on Pd-Ru catalyst system for EOR in alkaline media and the observed promotional effect of Ru on Pd electrocatalytic activity, several key points still remain to be understood and clarified. Among them, the role and fate of Ru both bulk and surface content. Similarly, the effects of surface structure modifications on the catalytic activity of bimetallic Pd-Ru nanoparticles for EOR in alkaline media are not yet fully understood.

In the current work, we show the correlation of the surface-structure-composition-activity of Pd_xRu_{1-x} (where x = 1, 0.99, 0.95, 0.90, 0.80 and 0.50) for ethanol electrooxidation in alkaline media. The nanoparticles were prepared using a polyol method and then supported on carbon. The NPs were characterized by scanning transmission electron micro-spectroscopy, X-ray diffraction techniques and X-ray photoelectron spectroscopy. The electrocatalytic activity was investigated using cyclic voltammetry and chronoamperometry techniques.

6.2 Results and discussion

6.2.1 Scanning Transmission Electron Microscopy (STEM)

The size distribution and surface morphologies of the nanoparticles were determined using HAADF-STEM. Figure 6.1 shows a representative HAADF-STEM micrograph of $Pd_{95}Ru_5/C$ and $Pd_{90}Ru_{10}/C$ catalysts with the corresponding histograms.

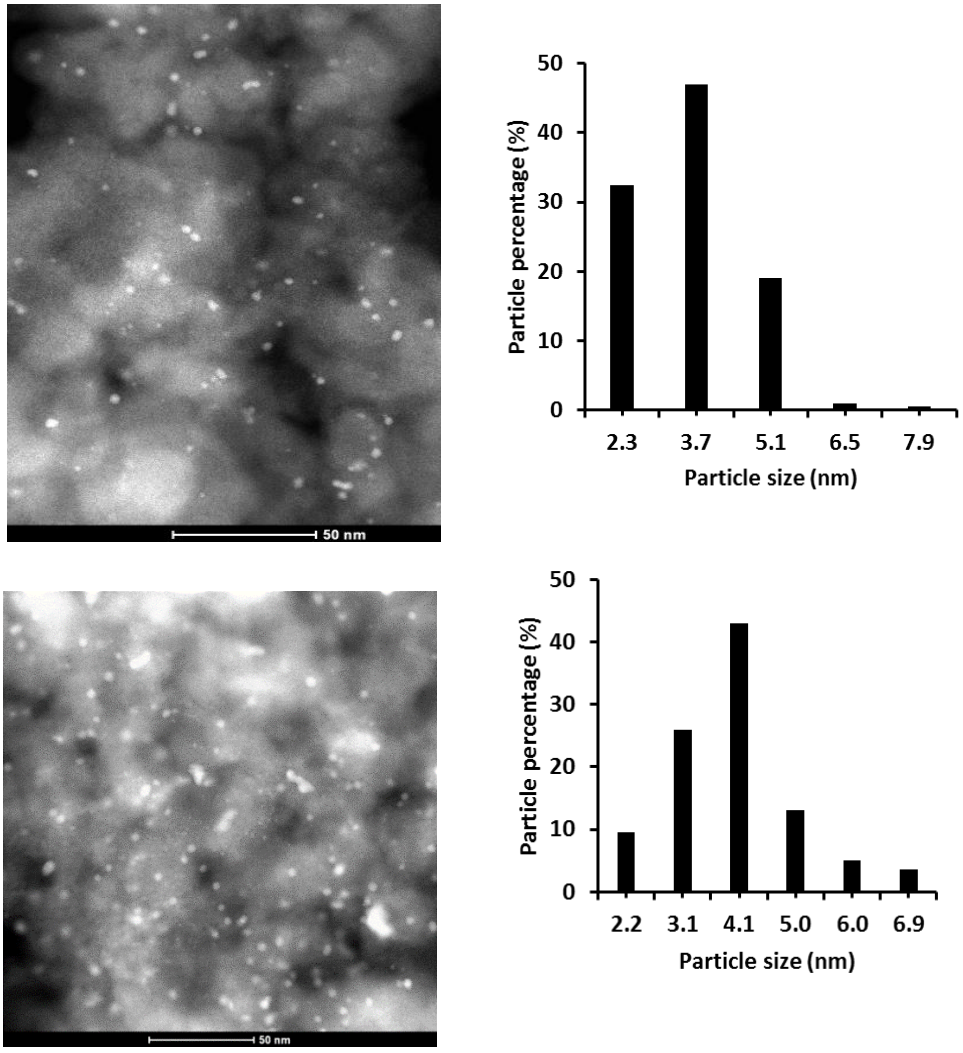

Figure 6.1: STEM images and their corresponding particle size distribution histogram for $Pd_{95}Ru_5/C$ (top) and $Pd_{90}Ru_{10}/C$ (bottom)

The nanoparticles were found to have a narrow size distribution between 2 nm and 5 nm. Figure 6.2 shows the micrographs of Pd/C, Pd99Ru1/C, Pd80Ru20/C and Pd50Ru50/C. The samples with ≤ 5%Ru content showed poor dispersion while those with ≥ 5%Ru showed better dispersion of the nanoparticles

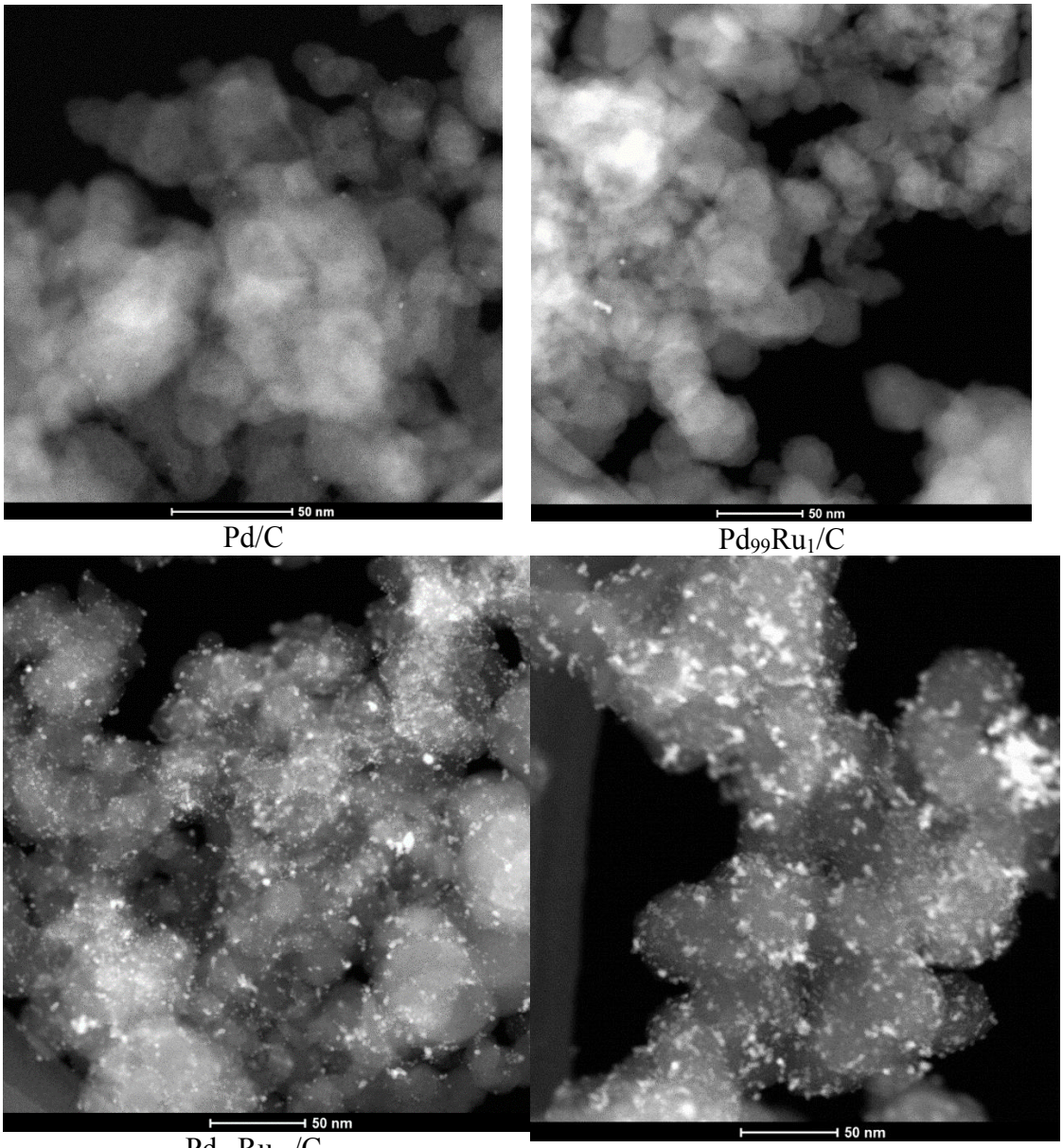

Pd/C $Pd_{99}Ru_1/C$

$Pd_{80}Ru_{20}/C$ $Pd_{50}Ru_{50}/C$

Figure 6.2: STEM image of Pd/C, $Pd_{99}Ru_1/C$, $Pd_{80}Ru_{20}/C$ and $Pd_{50}Ru_{50}/C$

The surface morphology of the nanoparticles was found to be rough as shown in Figure A2-1 (appendix section 2), which increases the surface area of the catalyst and improves the interaction of the adsorbate with the catalyst.

6.2.2 **X-Ray Diffraction Patterns (XRD)**

The X-ray diffraction patterns (XRD) of the nanoparticle are shown in Figure 6.3. The diffraction patterns are composed of face-centered-cubic (fcc) structure signature peaks at 40, 46 and 68° 2θ correspond to (111), (200) and (220) reflections, respectively. The fcc diffraction

patterns confirm that the bulk structure of Pd was retained in the nanoparticles. As can be seen from Table 6.1, the 2θ position of Pd(111) peak for Pd-Ru catalysts is very close to pure Pd, indicating that Pd and Ru do not form an alloy.

Table 6.1: Summary of *fcc* Pd(111) characteristics and crystallite sizes for Pd_xRu_{1-x} catalysts

Catalyst	***2θ max***	***Intensity (cps)***	***FWHM °2θ***	***Crystallite size(nm)***
Pd/C	40.06	890	0.55	15.4
$Pd_{99}Ru_1/C$	40.08	286	1.22	6.9
$Pd_{95}Ru_5/C$	40.09	66	1.27	6.7
$Pd_{90}Ru_{10}$	40.09	98	1.21	7.0
$Pd_{80}Ru_{20}$	40.05	80	1.08	7.8
$Pd_{50}Ru_{50}$	40.05	64	1.95	4.3

The interlayer spacing (d) for the (111) planes for Pd and Pd-Ru catalysts was found to be similar i.e., 2.25 Å which confirms no alloy formation between Pd and Ru. These results are in agreement with the XPS data (*vide infra*) and other experimental [16] and theoretical [17] reports. Therefore, Pd_xRu_{1-x}/C nanoparticles formed a bi-phase catalyst system. A peak shift of at least 0.2 degree on a 2Θ scale is required to have a lattice parameter value change by 0.01 which would be reasonable in order to conclude that an alloy is formed. In this work, the peak shifts were within < 0.1 2θ °. Since there was no diffraction peaks corresponding crystalline Ru nor did we detect any metallic Ru atoms by XPS, it is appropriate to conclude that Ru exist in an amorphous phase, in the form of oxides. The average crystallite size was estimated from peak positions and the full width at half maximum (FWHM) of the Pd(111) reflection peak using Scherrer equation. The maximum peak intensity position (°2θ max) was determined from a second order polynomial fit to the top 20% of the experimental intensities around 40° 2θ. The FWHM were determined using the minimum intensity measured at around 55 ° 2θ as the zero height. The Pd(111) peak 2θ max, its FWHM and the calculated crystallite sizes for the catalysts are shown in Table 6.1. The crystallite size was found to decrease with increasing Ru content but not in a linear trend.

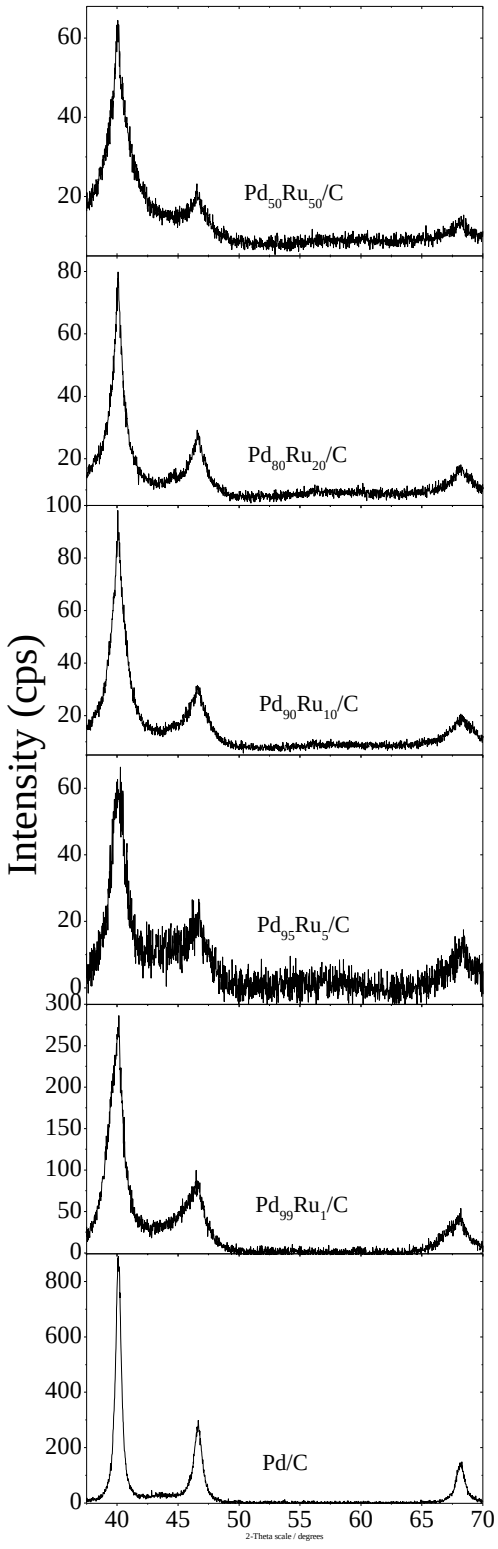

Figure 6.3: X-ray diffraction patterns of Pd_xRu_{1-x} nanoparticles.

6.2.3 **X-Ray Photoemission Spectroscopy (XPS)**

XPS was used to determine the elemental surface composition and structure of the catalysts. Figure 6.4 presents the deconvoluted Pd3d and the corresponding Ru3p peaks for all samples and Table 6.2 summarizes the peak positions binding energies (BE), FWHM and the relative intensities of each component and their assignments. The deconvolution of the Pd3d peak shows the existence of peaks at around 335.5(Pd^{I}), 336.6 (Pd^{II}), 337.7 (Pd^{III}) and 338.6 eV (Pd^{IV}), which are attributed to palladium atoms in four different chemical environments. The Pd^{I} is attributed to Pd in the metallic state, while the Pd^{II} is due to Pd^{2+} in PdO.[18,19] The Pd^{III} is characteristic of Pd atoms in 4+ oxidation state and more specifically in PdO_2.[20] Finally, the position of peak detected at higher BEs (Pd^{IV}) has been ascribed before to PdO_3 [20] though its origin can be assigned to $PdCl_2$. This last component is present in all samples implying that small traces of unreacted $PdCl_2$ exist in each sample. However its relative intensity contribution does not represent more than 9% of the surface Pd detected using XPS (see further discussion on chlorine content in the supporting information).

Due to the overlap of the Ru3d peak and the C1s peak, the Ru3p spectra were recorded and they are presented in Figure 6.4 B. The Ru3p peak is relatively wide (3.8-4 eV, for the Ru3p3/2) and asymmetric even if it represents an oxide [21] and for its deconvolution more studies using reference samples are necessary. The position though of the recorded peaks can give important qualitative information concerning the chemical environment of Ru atoms. For the Ru/C and the Pd_xRu_{1-x}/C samples with relatively high Ru content (10-50%) the obtained spectra are centered at around 463.5 eV. This energy is characteristic of Ru^{4+}, e.g., in RuO_2.[22] The rather high FWHM of peaks implies the existence of Ru atoms in more than one oxidation state which is a well-known phenomenon in literature.[23] For example, Francisco Colom in reference [23] reports that in alkaline environment (the conditions used in our synthesis) all the Ru atoms assume oxidation state (IV) and (VI) by spontaneous oxidation or reduction reactions.

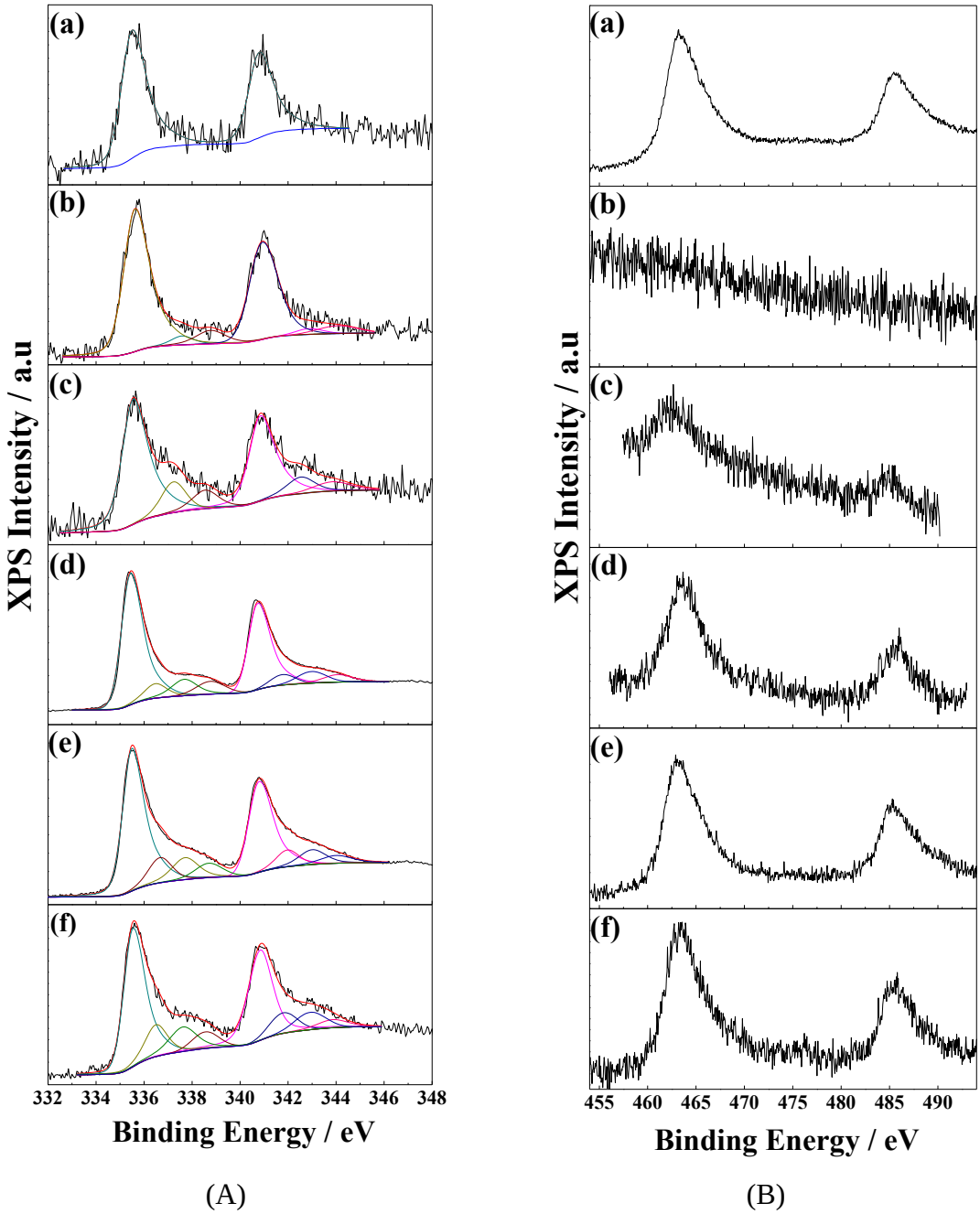

Figure 6.4: XPS spectra A) Pd_3d of Pd/C (a), $Pd_{99}Ru_1$ (b), $Pd_{95}Ru_5$ (c), $Pd_{90}Ru_{10}$ (d), $Pd_{80}Ru_{20}$ (e), $Pd_{49}Ru_{51}$ (f) and B) Ru_3p of Ru/C (a), $Pd_{99}Ru_1$ (b), $Pd_{95}Ru_5$ (c), $Pd_{90}Ru_{10}$ (d), $Pd_{80}Ru_{20}$ (e), Pd49Ru51 (f)

Therefore, Ru exists mainly in oxidized form such as the hydrated Ru^{4+} ($RuO_2.nH_2O$) species or as the $RuCl_x$ species.[23] In the case of the Pd-Ru samples with low content of Ru (99:1 and 99:5) the Ru signal is low. Thus for the 99:1 no Ru3p signal could be obtained (Figure 6.4 B, spectrum b), whereas the spectrum for 95:5 catalyst was recorded after prolonged acquisition

which means that during the measurement the X-ray beam have caused the partial reduction of the sample. The center of the $Ru3p_{3/2}$ peak is shifted 1.3 eV to lower BEs and could be attributed to Ru in lower oxidation state. Though, this energy shift is considered as a result of the prolonged X-ray irradiation in order to increase the signal to noise ratio of this sample that caused a partial reduction and consequently the shift of the center of the peak.

To summarize, Ru in all cases is mainly in the form of $RuO_2.nH_2O$ without excluding the existence of other oxygenated and/or chlorinated species in low percentage.[24] Using the intensity of the Pd3d and the $Ru3p_{3/2}$ and their sensitivity factors [25] the Pd/Ru atomic ratios were calculated and the values are shown in Table 6.2. The obtained values are lower compared to the experimental nominal values calculated from atomic ratios. This observation indicates that surface composition is different from the bulk one.

From this XPS results several interesting observations can be drawn out. As was reported earlier for PtIr nanoparticles prepared by polyol method [26] that in the case of PtIr alloys the $Pt4f_{7/2}$ and the $Ir4f_{7/2}$ peaks are expected to shift to higher and lower BEs, respectively compared to the peak positions of the pure metals. This is because of the difference in the electrochemical potential of electrons in two metals that form an alloy, accompanied by re-hybridization of the d-band as well as the sp-band. [26] According to our present results for Pd-Ru systems, no significant shift of the peaks attributed to the metallic state was observed. This may indicate that Pd and Ru do not form an alloy in agreement with XRD patterns.

For the samples with high Ru content, both PdO and PdO_2 are detected as shown in Figure 6.4. However, at low Ru content Pd exists only in one oxide form. More specifically, for the $Pd_{99}Ru_1/C$ the deconvolution of the Pd3d shows the presence of PdO_2 only while for $Pd_{95}Ru_5/C$ sample the less oxygenated species PdO was detected. This observation maybe explained by the complex oxidation states of Ru and their stability/or reduction potentials vs those of Pd. Pd is known to exist mainly in oxidation state (II) and (IV) in compounds with other elements, while Ru can exist in oxidation states ranging from (0) for metal carbonyls to (VIII), and because of the capacity of its ions to form polynuclear complexes apparent fractional oxidation states are also known.[23]

Table 6.2: Summary of the binding energies (BE), FWHM and the relative intensities of each of the peak components and their assignments.

Catalyst	$Pd3d_{5/2}$				$Ru3p_{3/2}$	Pd/Ru Atomic ratio[a]
	B.E. (eV)	FWHM (eV)	% Relative intensities	Assignment	BE (eV)	
Pd on C	335.5	1	95.5	Metallic Pd	-	-
$Pd_{99}Ru_1/C$	335.6 337.6 338.7	1 1.2 1.4	86.4 4.6 9	Metallic Pd PdO_2 $PdCl_2$	-	-
$Pd_{95}Ru_5/C$	335.5 336.7 338.5	1 1.2 1.4	77.2 13.9 8.9	Metallic Pd PdO $PdCl_2$	462.3	5.4 (19)
$Pd_{90}Ru_{10}/C$	335.4 336.5 337.7 338.7	0.9 1.1 1.3 1.4	75 7.6 10 7.4	Metallic Pd PdO PdO_2 $PdCl_2$	463.6	4.8 (9)
$Pd_{80}Ru_{20}/C$	335. 5 336.7 337.7 338.7	0.9 1.15 1.3 1.4	70 11.5 11.4 7.1	Metallic Pd PdO PdO_2 $PdCl_2$	463.3	1.2 (4)
$Pd_{50}Ru_{50}/C$	335. 5 336.6 337.6 338.5	0.9 1.15 1.3 1.4	65 14 13.4 7.6	Metallic Pd PdO PdO_2 $PdCl_2$	463.5	0.4 (0.96)
Ru on C	-	-	-	-	463.45	-

[a] The values in parenthesis shows the experimental nominal values.

Therefore, with very small amounts of Ru content in $Pd_{99}Ru_1/C$, in the alkaline synthetic conditions used, all the Ru atoms exists in higher oxidation states, which are unstable and tends to get charge from Pd atoms/ions hence oxidizing it to Pd^{4+} As the Ru content is increased other intermediate oxidation states of Ru could be formed, which can easily be oxidized and hence reduce Pd^{4+} to Pd^{2+}. It is interesting to note that as the amount of Ru was increased, the mixture of Pd oxide species (PdO and PdO_2) was formed, which reflects the dynamic nature of the reaction intermediates. Consequently, as the surface oxide species increased the surface metallic Pd species decreased. The total Pd oxide species increased from 4.5% for Pd/C to 4.6%, 13.9%, 17.6%, 22.9%, and 27.4% for $Pd_{99}Ru_1/C$, $Pd_{95}Ru_5/C$, $Pd_{90}Ru_{10}/C$, $Pd_{80}Ru_{20}/C$, and $Pd_{50}Ru_{50}/C$, respectively (see Table 2 for the percentage distribution of each oxide species). This observation strongly indicates that the presence of Ru affects the surface oxidation state of Pd.

6.2.4 **Energy-dispersive X-ray spectroscopy (EDX)**

Energy-dispersive X-ray spectroscopy was used qualitatively to confirm individual elemental composition of the nanoparticles. Figure 6.5 shows the representative zoomed in micrographs and their corresponding EDX analysis of the catalysts, i.e., $Pd_{99}Ru_1/C$, $Pd_{80}Ru_{20}/C$ and $Pd_{50}Ru_{50}/C$. Please note Cu and Mo counts are artefacts from the sample grid and holder,

respectively. Ru was not detected for $Pd_{99}Ru_1/C$ which was expected because of the small concentration. All the other samples did show that the Pd nanoparticles are enriched with Ru.

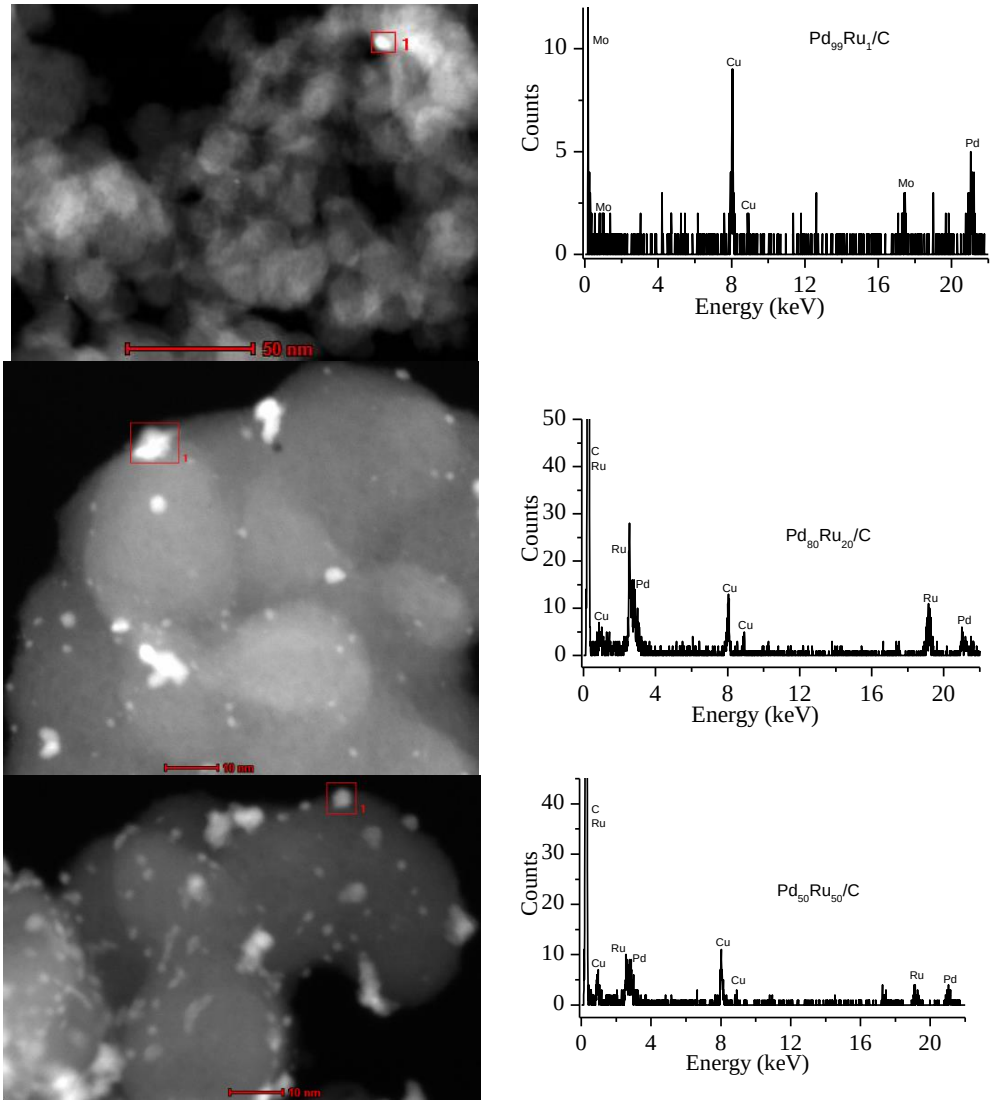

Figure 6.5: EDX spectra (right) and their corresponding micrographs (left) for $Pd_{99}Ru_1/C$ (top), $Pd_{80}Ru_{20}/C$ (middle) and $Pd_{50}Ru_{20}/C$. Cu and Mo counts are artefacts from the sample grid and holder, respectively.

6.2.5 **Electrochemical studies**

6.2.5.1 **CO stripping voltammetry**

The catalyst surface activities were characterized by carbon monoxide oxidation voltammograms. CO is a major poisoning intermediate during alcohol electrooxidation reaction.

Therefore, this study highlights the tolerance of the catalysts against CO deactivation challenge. Figure 6.6 shows the CO stripping voltammograms in 1M KOH at room temperature.

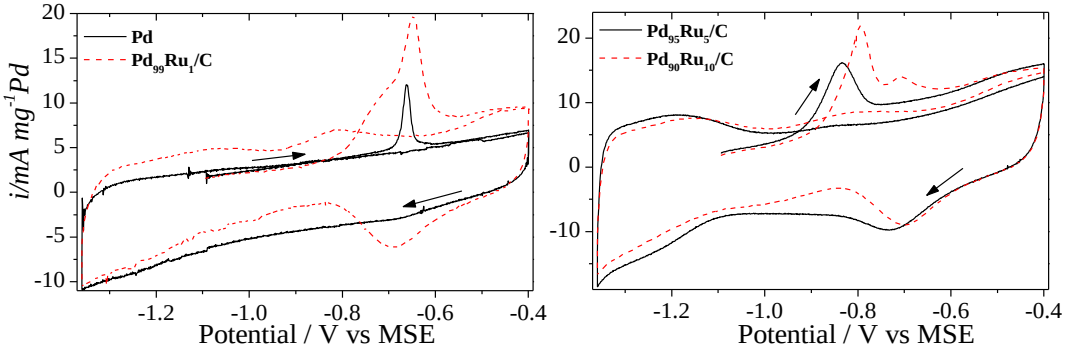

(a)

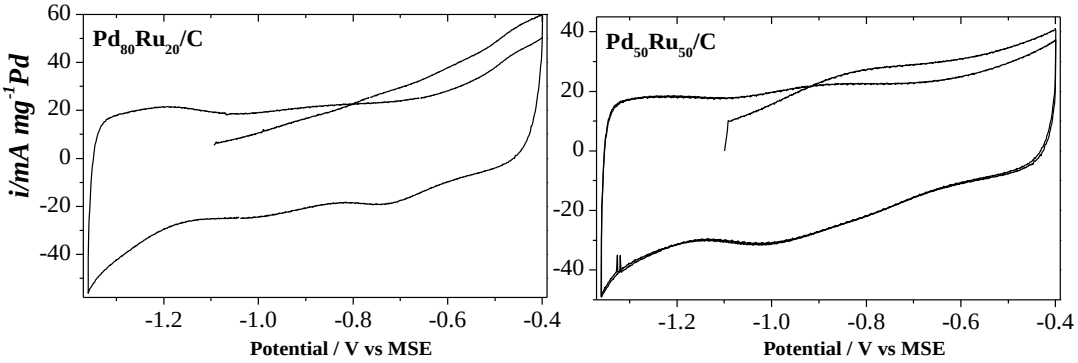

(b)

Figure 6.6: Polarization curves of the electrocatalytic oxidation of CO on Pd_xRu_{1-x}/C nanoparticles recorded in 1.0 M KOH at scan rate of 25 mVs^{-1}. The potential was held at E = -1.1 V for 20 minutes during CO adsorption then excess CO was removed from the solution by bubbling N_2 gas for another 20 minutes before recording the CVs. Current densities are normalized with respect to mass loading of Pd on the glassy carbon (GC).

The 1st CV cycle of the CO stripping for Pd_xRu_{1-x}/C catalyst with ≤10% Ru content showed distinct peaks (Figure 6.6 a) while catalysts with higher Ru loading had no peaks (Figure 6.6 b). The 2nd cycle shows no CO oxidation peak indicating a complete removal of CO from the catalyst surface during the 1st cycle. The CO oxidation peak for Pd/C and $Pd_{99}Ru_1/C$ is at the same potential (≈ -0.66 V vs MSE) suggesting similar active sites which can be attributed to metallic Pd which is the abundant species based on XPS data (Figure 6.4 and Table 6.2). However, the presence of a shoulder (pre-peak) and higher charge density for $Pd_{99}Ru_1/C$ indicates the effect of surface structure-activity modification due to the presence of small amounts of Ru. The pre-peak shoulder shows that the presence of Ru ions lowers CO oxidation

potential while increasing the current density. The effect of Ru promotional activity is amplified with the increasing Ru content which shows the CO oxidation peak shift to more negative potentials. For $Pd_{95}Ru_5$/C ratio a single almost symmetrical shaped CO oxidation peak was observed at ≈ -0.83 V while for $Pd_{90}Ru_{10}$/C ratio two overlapping peaks at ≈ -0.79 V and ≈ -0.71 V were obtained. This finding re-enforces literature reports that the presence of Ru mitigates CO poisoning in Pt catalysts.[27] The absence of CO oxidation peaks for $Pd_{80}Ru_{20}$/C and $Pd_{50}Ru_{50}$/C would be attributed to the presence of higher Ru-oxides, which readily oxidizes CO at a lower potential than the adsorption potential of -1.1 V used in this study hence leading to no CO adlayer on the catalyst surfaces. We suggest the mechanism to involve RuOx because metallic Ru is unstable in high pHs. It has also been reported that in alkaline conditions RuO_4^- ions readily oxidize water molecules liberating oxygen [23] which would then react with adsorbed CO molecules to form CO_2. Fisher *et al*. had attributed the shifting of CO oxidation peak to lower potentials to the segregation of Ru on Pd, however this was done in acidic solution, where metallic Ru is stable for CO adsorption.[28] The insights from CO oxidation graphs (shape and position of the peaks) would help in describing surface structure-activity of the catalysts. For example, in [29–31] it was used to identify the active sites and mechanism for CO oxidation on Pt-based electrodes.

Figure 6.6 also reveals significant differences for Pd_xRu_{1-x} catalyst based on their PdO_x reduction peaks centered at ≈-0.7 V. Pd/C did not form significant PdO_x due to lower anodic potential limit of -0.4 V we used leading to weak reduction peak during the reverse scan. As the surface Pd-oxides increase due to addition of Ru, the PdO_x reduction peaks becomes stronger as shown by catalysts $Pd_{99}Ru_1$/C, $Pd_{95}Ru_5$/C and $Pd_{90}Ru_{10}$/C. Further increase of Ru content encapsulates the nanoparticle which prevents easy reduction/oxidation of Pd leading to the diminished PdO_x reduction peaks for $Pd_{80}Ru_{20}$/C and $Pd_{50}Ru_{50}$/C.

6.2.5.2 **Cyclic voltammetry (CV)**

Cyclic voltammetry was used to study ethanol oxidation behaviour on Pd_xRu_{1-x}/C. Figure 6.7 shows the CVs in 1M KOH with and without ethanol.

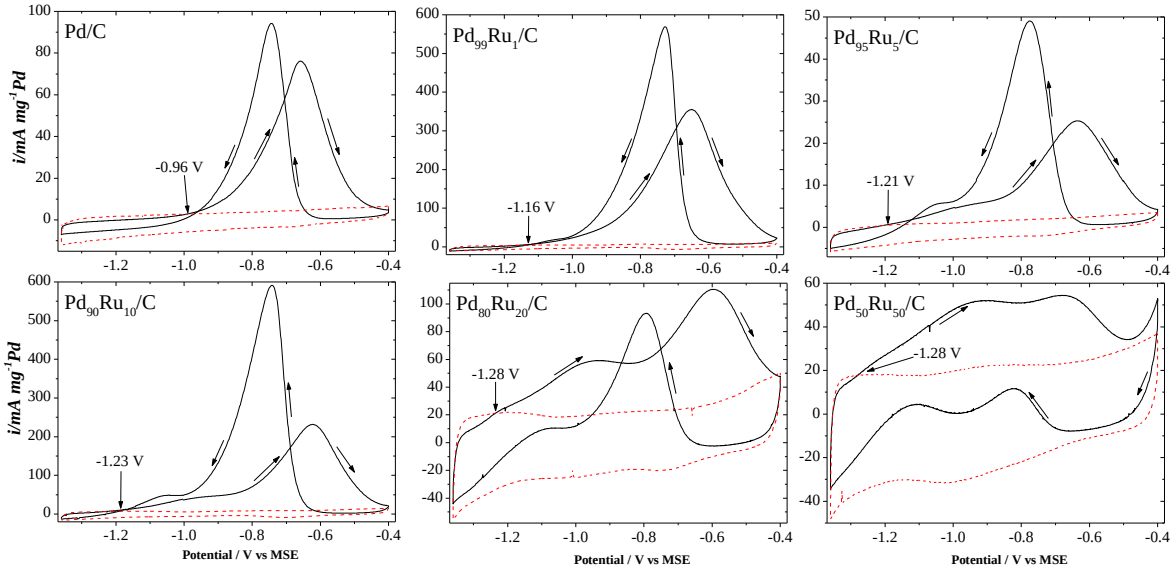

Figure 6.7: Polarization curves of the electrocatalytic ethanol oxidation reaction on Pd_xRu_{1-x}/C recorded in 1.0 M KOH + 1.0 M C_2H_5OH (solid line) and in 1.0 M KOH (dotted line) at a scanning rate of 20 mVs^{-1}. Current densities are normalized with respect to mass loading of Pd on the glassy carbon

During the forward scan, currents starts to increase at ~ -0.99 V for Pd/C due to ethanol oxidation, reaches a maximum at ~ -0.66 V, followed by current decrease due to the surface deactivation by Pd oxide coverage and/or ethanol oxidation intermediates. Addition of 1%Ru lowered onset oxidation potential to ≈ - 1.16V and significantly increased the current density by more than 400% (see the differences of the y-scale on Figure 6.7). Increasing the amount of Ru shifted further the ethanol oxidation onset potential to lower values. The onset oxidation potentials and current densities for all samples are summarized in Table 6.3. It was found that increasing Ru content on Pd nanoparticles lowered the onset potentials for ethanol oxidation up to a maximum shift of 290 mV for $Pd_{50}Ru_{50}/C$ as shown in Figure 6.7 and Table 6.3. A higher shift was achieved in this work compared to 150 mV reported by Chen *et al.* [8] In the reverse scan, the catalyst remains deactivated up to ~ -0.65 V then current rises sharply as more ethanol is oxidized on the reduced surface. As shown in Figure 6.6, the surface oxide reduction starts at ~ -0.60 V and reaches a minimum at ~ -0.70 V.

Table 6.3: Summary of CVs oxidation potentials and CAs steady-state current densities after 2000 s for Pd_xRu_{1-x}/C catalysts.

Catalyst	*Pd loading (mg)*	*Anodic E (V)*		*i (mA mg^{-1} Pd)*	
		E_{onset}	*E* at i_{max}	*E* = -0.96 V	E=-0.67
Pd/C	0.0046	-0.99	-0.66	0.00	5.79
$Pd_{99}Ru_1/C$	0.0046	-1.16	-0.65	2.40	38.14
$Pd_{95}Ru_5/C$	0.0044	-1.21	-0.64	0.86	28.87
$Pd_{90}Ru_{10}/C$	0.0050	-1.23	-0.63	6.67	15.33
$Pd_{80}Ru_{20}/C$	0.0039	-1.24	-0.60	4.05	6.21
$Pd_{50}Ru_{50}/C$	0.0024	-1.28	-0.68	6.17	0.94

Ethanol electrooxidation peak on Pd/C and $Pd_{99}Ru_1/C$ have similar shape and they occur at the same potential (Figure 6.7) implying similar surface structure active sites, which correlates well with CO stripping CVs (Figure 6.6). For $Pd_{95}Ru_5/C$ to $Pd_{50}Ru_{50}/C$, an oxidation shoulder was observed at a lower potential at ~ -0.95V. The shoulder gets more pronounced with increasing Ru content. This shoulder was attributed to the synergetic effect between surface oxides (PdO_x and RuO_x) and Pd nanoparticles as discussed in section 6.2.6.

Figure 6.8 compares the forward scans of EOR on Pd_xRu_{1-x}/C catalysts. The current densities were found to vary non-linearly as a function of increasing Ru content within the voltage window covered (-1.4 V to -0.4 V).

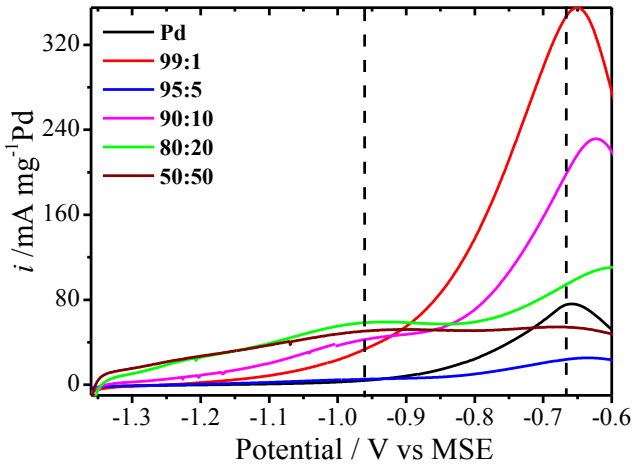

Figure 6.8: Forward scans of polarization curves of the electrocatalytic ethanol oxidation reaction on Pd_xRu_{1-x}/C electrocatalysts recorded in 1.0 M KOH + 1.0 M C_2H_5OH at a scanning rate of 20 mVs^{-1}. Current densities are normalized with respect to mass loading of Pd on the glassy carbon. The vertical dashed lines marks the potential of the chronoamperometry experiments in Figure 6.9

The current densities below -0.9 V showed different trends to the current densities above -0.9 V. The current densities at lower potentials are of great interest for fuel cell applications.

Therefore, we have tabulated the current densities at -0.96 V in Table 6.3 to show the effect of Ru on the catalytic activity of Pd nanoparticles. At lower voltage (-0.96 V) the current density from Pd/C is zero and it increases non-linearly with the increasing amount of Ru to a maximum of 6.67 mA mg^{-1}Pd for $Pd_{90}Ru_{10}$/C.

6.2.5.3 **Chronoamperometry (CA)**

Chronoamperometry was used to investigate the steady-state performance of the catalysts. CA measurements were carried out at onset and peak potentials for EOR on Pd/C catalyst, i.e., -0.96 V and -0.67 V, respectively. The behaviour of Pd_xRu_{1-x}/C catalysts at these potentials provides insights into the effect of adding Ru to Pd surface at lower and higher potentials. The steady-state current density is zero at onset oxidation potential (-0.96 V) for Pd/C while it is at maximum at the peak oxidation potential (-0.67 V). The resulting *i-t* curves at -0.96 V and at -0.67 V are shown in Figure 6.9.

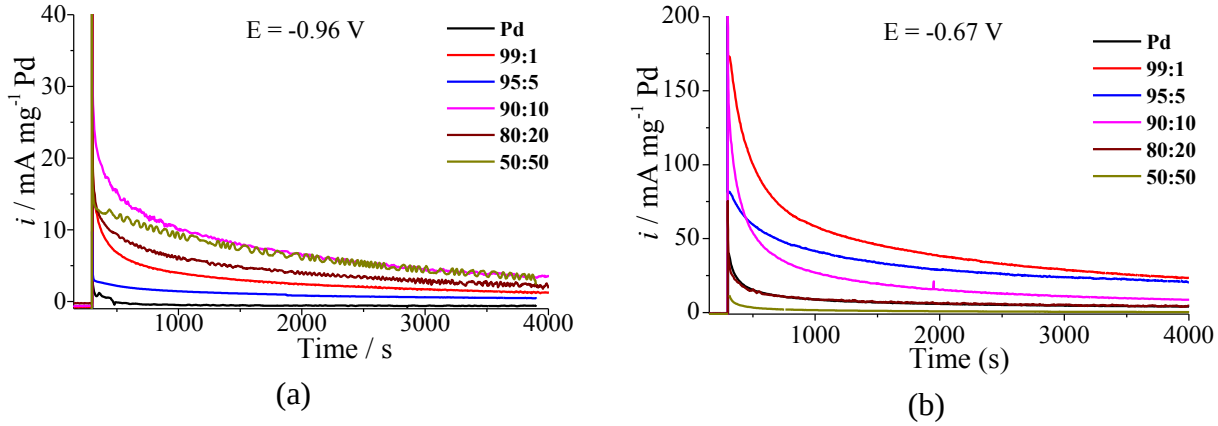

Figure 6.9: Potentiostatic chronoamperometry of Pd_xRu_{1-x}/C electroctalysts at (a) E = -0.96 V and (b) E = -0.67 V vs MSE recorded in 1.0 M KOH + 1.0 M C_2H_5OH. Current densities are normalized with respect to mass loading of Pd on the glassy carbon.

The steady-state current densities after 2000s from the two figures are tabulated in Table 6.3. The *i-t* curves show initial high currents, after stepping the voltage, due to EOR which rapidly decreases until a steady-state is established. The rapid decrease in current at the beginning is attributed to surface coverage by partially oxidized species which block the surface active sites of the catalyst. Therefore, the initial slopes of the *i-t* curves are good indicators of the catalyst surface reaction kinetics and the extend of the catalyst surface poisoning due to adsorbed oxidized intermediates and or products. The steeper the slope of the *i-t* curves the higher the deactivation of the catalyst active sites.

6.2.6 **Surface composition structure-activity correlations**

We have shown that combining Pd with Ru improves the catalytic activity towards EOR in alkaline media. Now let us take a deeper look at what is influencing the catalytic activity of the nanoparticles tested at the relevant electrode process level, i.e., the surface composition and morphology of the catalysts. Figure 6.10 shows the surface atomic composition of the catalysts in terms of metallic Pd and PdO_x as a function of Ru content and the corresponding steady-state current densities after 2000s at -0.96 V and -0.67 V vs MSE. The atomic composition is from XPS data in Table 6.2 and the corresponding CA current densities are from Table 6.3.

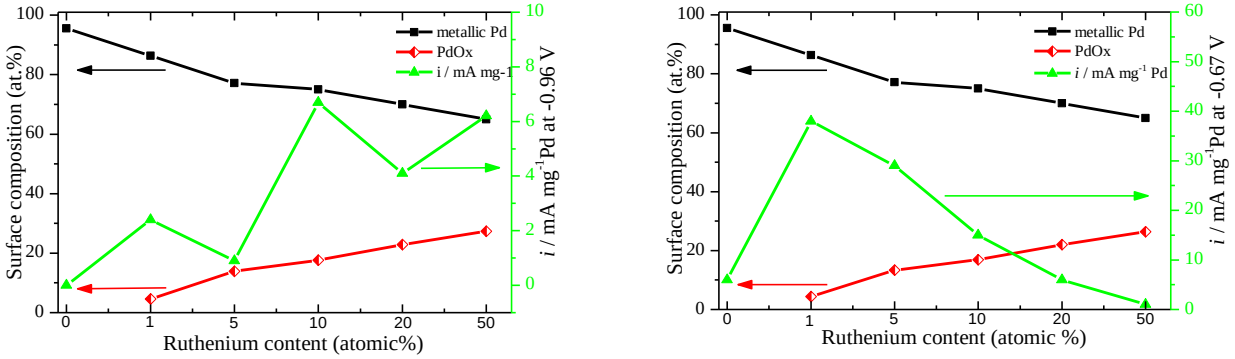

Figure 6.10: Surface atomic composition of Pd_xR_{1-x}/C from XPS data (black squares and red triangles – left axis) and the corresponding steady-state current density at E = -0.96 V (panel a) and at E = -0.67 V (panel b) vs MSE (green triangles - right axis). Original data from Table 6.2 and Table 6.3.

The surface Pd metallic species decreases as the coverage with surface oxide species increases as expected. Figure 6.10 provides evidence that there exists a correlation between surface composition and Ru content. Increasing the amount of Ru increases the Pd-oxide species on the nanoparticle surfaces. Since Ru was found to exist mainly in the oxidized state based on XPS data and discussion above, it is logical to assume that the amount of Ru oxides on the surface increased too as the Ru content was increased.

From the CVs (Figure 6.7 and 6.8), a correlation would be made from the single EOR peak at -0.67 V, which is almost symmetric, for $Pd_{99}Ru_1/C$ and Pd/C suggesting that their electrocatalytic activity occurred on similar surface active sites. Figure 6.10 shows that the surface composition for Pd/C and $Pd_{99}Ru_1/C$ catalyst to be ≈ 95.5% and ≈86.4% in metallic Pd state, respectively. Hence, the increased EOR current density for $Pd_{99}Ru_1/C$ is due to presence of Ru ions in vicinity to metallic Pd. However, recent theoretical studies have shown that it is the adsorbed OH on Pd

surface rather than Pd atoms which is the active center for the EOR [32] Therefore, EOR peak at -0.67 V, which is present in all samples, would be assigned to surface metallic Pd active sites. Increasing the amount of Ru in the nanoparticles was found to diminish this maximum current peak, i_{max}, by up to > 55% for catalyst with more than 5%Ru content, a trend consistent with the decreasing amount of surface metallic Pd shown in Figure 6.10. Traces of Ru at 1% were found to enhance ethanol electrooxidation leading to more than 400% i_{max} compared to Pd/C (see Figure 6.7 and note the y-scale difference). Increasing Ru content further decreased surface metallic Pd species from 86% in $Pd_{99}Ru_1$/C to 65% in $Pd_{50}Ru_{50}$/C. Consequently, the steady-state current densities decreased at -0.67 V as shown in Figure 6.10b. It is important to note that $Pd_{90}Ru_{10}$/C showed highest mass activity at -0.96 V (6.67 mA mg^{-1}Pd) while $Pd_{99}Ru_1$/C showed highest mass activity at -0.67 V (38.14 mA mg^{-1} Pd) after 2000s which highlights the differences in extrinsic and intrinsic properties of the catalysts.

The forward scans on Figure 6.8 shows that Ru content between 1 to 20% improves Pd activity towards EOR at lower potential (-0.96 V) which is further supported by CA analysis as shown in Figure 6.10 a. Figure 6.10 demonstrates that at lower potentials the current densities have an increasing trend as Ru content is increased and vice versa at higher potentials with a limiting activity at 20% Ru content. This limiting surface composition ratio is in good agreement with values reported in literature.[9,10] For example, Yi *et al.* reported an optimal ratio of 13% Ru for Pd-Ru nanoparticles prepared by hydrothermal method.[9] Anindita *et al.* reported the optimum ratio of 20% Ru for Pd-Ru nanoparticles synthesized via sodium borohydride reduction method.[11] Interestingly, Chen *et al.* reported a higher optimum ratio of 50% Ru for Pd-Ru catalysts prepared by impregnation and reduction method.[8] However, Ma *et al*. using Pd-Ru nanoparticles prepared by impregnation and sodium borohydride reduction method reported that catalysts with 25% Ru performed well.[33] But we have shown in this work that the promotional effect of Ru on EOR on Pd is greatly depended on the oxidation potential. It is important to note that these ratios are based on the nominal values and not the actual surface composition of the catalyst.

The appearance of EOR shoulder at lower potentials shown in Figures 6.7 and 6.8 would be attributed to the synergetic effect between the surface oxide species (Ru-oxides and Pd-oxides) and metallic Pd species. Although Ru-oxide species, particularly hydrous Ru oxide ($RuO_x.nH_2O$), had been reported to be the active site for methanol oxidation,[34] it is not the only

contributing factor in the current case. This is because Ru/C catalyst with 100% Ru-oxides surface composition was found to be a poor catalyst for EOR as shown in appendix Figure A2-2 (appendix section 2). The current densities for EOR showed increasing trend at lower potentials (Figure 6.10 a) as the surface oxides were increased and plateaus at 20 % Ru which is the limiting composition for a better performing catalyst at lower potential. At ≥ 20%Ru content, Pd nanoparticles are completely covered with Ru oxides which are poor EOR catalyst alone. Therefore, we propose that the synergetic effect is better expressed when the boundaries between surface oxides and metallic Pd form an interface with the electrolyte solution during electrooxidation reaction.

6.3 Conclusions

In conclusion, we have shown that Pd_xRu_{1-x}/C nanoparticles synthesized by a polyol method form a bi-phase catalyst system. No alloying between Pd and Ru atoms as revealed by XPS and XRD. The nanoparticle size distribution was found to range between 2–5 nm and the catalysts have a rough topology as show from STEM micrographs. The bulk nanoparticles were found to have an fcc structure indicating that they were mainly composed of Pd metal from XRD patterns. XPS and EDX analysis shows that the nanoparticle surfaces are composed of different percentages of metallic Pd species, Pd-oxide species, and Ru-oxide species. The Pd-oxide species were found to increase while the metallic Pd species decreased with the increasing amount of Ru content, a phenomenon attributed the complex oxidation states of Ru which ranges from (0) to (VII).

We report that the synergetic effect between surface oxide species (PdO_x and RuO_x) on Pd nanoparticles lowers EOR potential and 20%Ru is the limiting Pd_xRu_{1-x}/C composition for good performance at lower potential. The $Pd_{90}Ru_{10}$/C and $Pd_{99}Ru_1$/C were found to be the best catalyst systems which produced more than four times higher mass activity (current density per mass of Pd) compared to pure Pd at -0.96 V and -0.67 V vs MSE, respectively. The *i-t* curve slopes show that the two catalysts have lower surface deactivation from EOR intermediates/products. This work shows that Ru improves ethanol oxidation on Pd nanoparticles in alkaline media and the current densities are depended on the oxidation potential. CO stripping studies show that Pd-Ru combination mitigates CO poisoning in alkaline media which is a major challenge in acidic

media. Therefore, Pd-Ru is a promising bimetallic combination that can be optimized for use in ambient conditions DAFCs.

Supporting information: A representative HAADF-STEM micrograph with a zoomed in 3D nanoparticle surfaces and the CVs for Ru/C catalyst in 1M KOH with and without ethanol are provided in appendix section 2.

Chapter 7: The Role of Metal Oxide Support on Catalytic Activity of Pd Nanoparticles for Ethanol Electrooxidation in Alkaline Media

Publication: E. A.Monyoncho, S. Ntais, N. Brazeau, J-J. Wu, C-L. Sun, E. A. Baranova

ChemElectroChem, 3 (**2016**) 218-227, DOI: 10.1002/celc.201500432

Abstract:

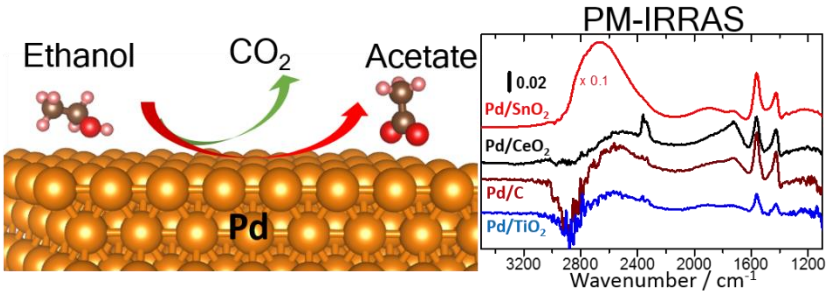

The promotional role of oxide supports (CeO_2, SnO_2, TiO_2) on ethanol electrooxidation in alkaline media over Pd nanoparticles (NPs) is presented and compared to Pd on carbon. The XPS revealed a shift to lower binding energy of the Pd3d peak when Pd NPs are deposited on metal oxides, implying a charge transfer from the oxides to Pd. The catalytic activity of the supported NPs for ethanol electrooxidation was assessed using cyclic voltammetry and chronoamperometry. The electrooxidation products were monitored in-situ using polarization modulation infrared reflection absorption spectroscopy (PM-IRRAS), which revealed that the supports influence the selectivity of reactions on Pd. The Pd/CeO_2 has superior selectivity towards breaking the C–C bond to produce CO_2 compared to other three supports. Acetate product was evident on all the catalysts but at different ratios. Pd supported on metal oxides showed higher activity; in particular CeO_2 and SnO_2 stand out as the best supports.

***Keywords*:** Ethanol electrooxidation, Palladium, Supported catalysts, Nanocatalyst, IR spectroscopy

7.1 Introduction

Palladium and Pd-based electrocatalysts have been identified as promising alternative to Pt-based catalysts for EOR in alkaline media owing to their high reaction kinetics.[9,13] There are several variables that can be modified to increase the electrocatalytic activity of Pd such as the size and shape of Pd nanoparticles,[14,15] the use of bimetallic nanoparticles,[16] and the use of active catalyst supports.[17–19] The support can have a pronounced effect on the activity of the catalyst by affecting its morphology, i.e., better particle dispersion and stability and in some cases electronic properties of the catalyst through the metal-support interaction (MSI) effect.[20–22] The most common catalyst support used in fuel cells is carbon black, which has a low corrosion resistance in proton or anion exchange membrane,[23] for this reason other catalyst supports such as TiO_2, SnO_2 and CeO_2 oxide have been considered for alcohol oxidation reactions.[24–37] These metal oxides have better chemical stability and most of the time enhances catalytic activity of the metals compared to commercial carbon. The catalytic promotional role of these supports are attributed to their reducibility as mixed ionic-electronic conductors and their ability to generate oxygen vacancies (absence of O^{2-}) in their crystal structures.[22] The vacancies can be generated in many different ways such as the dehydration of the surface hydroxyl species (OH^-) and the reduction of accessible metal cations in the oxides by chemical means.

The catalytic promotional properties of oxide supports in electrocatalysis has attracted the interest of many researchers, for instance TiO_2,[28,30–32] SnO_2,[10,24,26,37,38] and CeO_2 [25,33,34] have been extensively investigated. Focusing our attention to Pd-based catalysts on these supports for ethanol electrooxidation, Hu *et al*. prepared Pd nanoparticles on carbonized TiO_2 nanotubes for ethanol electrooxidation in alkaline media and reported that electrocatalyst with 1:1 mass ratio of Pd to TiO_2C for Pd/TiO_2/C gave the best performance compared to Pd/C and Pd/TiO_2.[32] Mao *et al*. used impregnation reduction method to prepare carbon supported PdSn/SnO_2 and showed that it had higher current density for ethanol electrooxidation in alkaline media compared to Pd/C, SnO_2/C, and PdSn/C.[37] They showed that SnO_2 improved Pd particle distribution. Bambagioni *et al*. have shown that the addition of CeO_2 as a co-support to carbon for Pd nanoparticles (Pd/C/CeO_2) improved the power density of the direct alkaline ethanol fuel cell by a factor of two compared to Pd/C.[25] Uhm *et al*. synthesized well-ordered arrays of free-standing Pd-CeO_2 nanobundles and reported that the catalysts had an increased number of oxygen species on the surface resulting in significant increase of their catalytic activity for the EOR in KOH.[33] Shen

and co-workers conducted a comparative study of ethanol electrooxidation on Pt/C and Pd/C catalysts promoted by CeO_2 in alkaline media and reported that CeO_2 significantly improved catalyst activity and poison tolerance.[39,40] Although, this promotional effect of these oxide supports is evident in these studies, no direct comparison for ethanol electrooxidation reaction on Pd nanoparticles supported on TiO_2, CeO_2, SnO_2, and C exists. Furthermore, there are several other questions regarding the role of the support such as the supports influence on nanoparticle size and elemental surface composition (e.g. surface oxides) also on Pd catalytic activity still remain to be elucidated.

In this work we conduct a comparative study of Pd nanoparticles (NPs) supported on TiO_2, SnO_2, CeO_2, and conventional carbon support, where the Pd NPs are prepared using the same synthesis procedure, and same metal loading. This approach allows us to evaluate the role/effect of the support on a number of properties of Pd NPs: i) the influence of support on the particle and crystallite sizes – TEM and XRD data, ii) the effect of support on surface composition (oxidation states of Pd) and electronic effect–XPS data, iii) the effect of support on chemisorption and dispersion properties –CO stripping data, and iv) the effect of support on electrocatalytic properties of Pd NPs for ethanol oxidation in alkaline media – cyclic voltammetry, chronoamperometry, and polarization modulation infrared reflection absorption spectroscopy (PM-IRRAS) data. To this end, Pd NPs supported on CeO_2, SnO_2, TiO_2 and carbon were prepared using sodium borohydride as a reducing agent in an aqueous medium. Ethanol electrooxidation reaction was studied in 1M ($KOH + C_2H_5OH$) using cyclic voltammetry and chronoamperometry. The chronoamperometry was coupled with in-situ identification of products using PM-IRRAS. A discussion is provided to correlate the first three properties (i - iii), to the electrocatalytic activity of Pd NPs induced by metal-support interactions.

7.2 Results and Discussion

7.2.1 Physicochemical characterization of supported Pd nanoparticles

The morphology and nanoparticle size distribution of the four catalysts were determined using TEM and the resulting micrographs and histograms, respectively are shown in Figure 7.1. The micrographs show that Pd nanoparticles were relatively well dispersed in all the four supports tested with some degree of agglomeration, which is more evident on SnO_2 support. The histograms show the particle size distribution of the Pd nanoparticles for each catalyst

synthesized. The average sizes of the nanoparticles were 10.4, 12.3, 12.6 and 14.2 nm for Pd NPs on SnO_2, CeO_2, carbon and TiO_2, respectively. It is interesting to note that Pd NPs had the smallest size on SnO_2 and largest size on TiO_2 support, while the size was comparable between C and CeO_2. The small specific surface area of TiO_2 (Table 7.1) may be responsible for the larger size of Pd clusters.

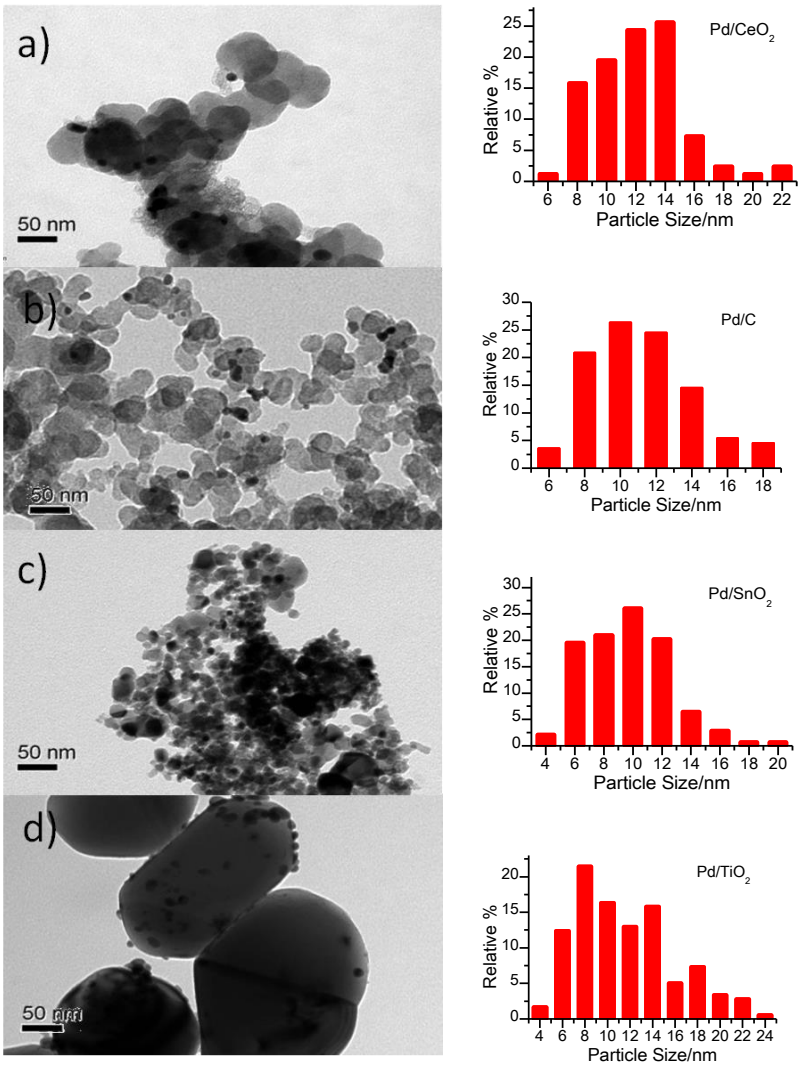

Figure 7.1: TEM micrographs of Pd nanoparticles supported on a) CeO_2; b) Carbon; c) SnO_2; d) TiO_2. The corresponding histograms on the right show the nanoparticle size distribution.

The crystal structure of the nanoparticles was determined using X-ray diffraction patterns as presented in Figure 7.2. The diffraction pattern shows that Pd NPs retained the bulk face centered cubic (fcc) structure, the symbol (*) shows the signature peaks for fcc. The signature fcc peaks were detected at 40.08 º, 46.5 º, and 68.2 º on 2θ scale for all the samples which

corresponds to (111), (200), and (220) planes, respectively. All the other extra peaks on the diffraction patterns correspond to the respective oxide support as shown in the diffraction patterns of the pure supports in Figure A3-1 (appendix section 3). The crystallite size of Pd nanoparticles was estimated using the Scherrer equation which yields the crystallite size of the nanoparticles.[41] The crystallite size was estimated using the Pd(111) peak, which was confirmed to have no significant overlap with the support peaks as shown in the Figures A3-1. The crystallite sizes of the particles were calculated to be 10.8, 7.5, 9.5, and 15.2 nm for Pd NPs supported on carbon, SnO_2, CeO_2, and TiO_2, respectively. The crystallite size trends are in a good agreement with the particle size diameters found from TEM micrographs as shown in Table 7.1. The lower crystallite values compared to particle sizes for Pd/CeO_2 and Pd/SnO_2 indicate the agglomeration of crystals in those supports. Therefore, the broader Pd peaks for CeO_2 and SnO_2 (Figure 7.2) is evidence to the smaller crystallite sizes of the nanoparticles but which agglomerates together to form the larger grains detected by the TEM.[42]

Table 7.1. Characteristics of Pd supported catalysts: crystallite size, average particle size, support particle size, electrochemical active surface area (ECSA) of Pd, and specific surface area (a_s) of the supports.

Catalyst	Crystallite size (nm)[a]	Average Pd particles size (nm) [b]	Support particle size (nm)	ECSA[c] (cm^2)	a_s m^2g^{-1}[d]
Pd/C	10.8	12.6	50	0.86	237
Pd/SnO_2	7.5	10.4	22-43	0.92	20-40
Pd/TiO_2	15.2	14.2	200	0.66	<20
Pd/CeO_2	9.5	12.3	60-100	0.85	35-50

[a] XRD measurements, [b] TEM measurements, [c] CO stripping CVs, and
[d] Manufacturer label

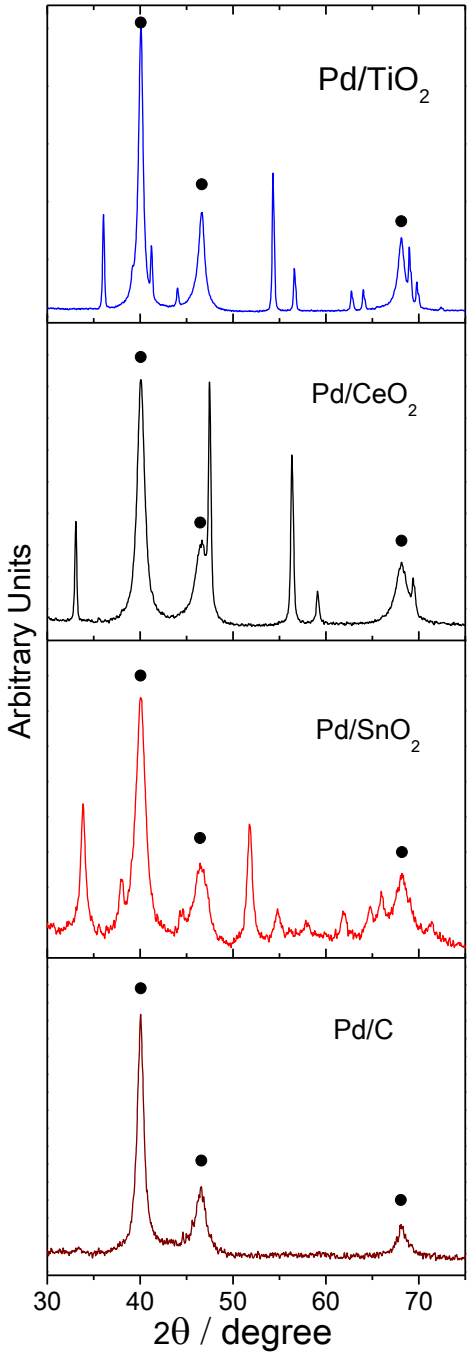

Figure 7.2: XRD patterns of supported Pd nanoparticles on various supports as shown. The symbol (•) correspond to face-centred cubic (fcc) structure diffractions for Pd.

The surface composition of the supported Pd nanoparticles on the different oxide supports was determined using XPS. Figure 7.3 shows the high resolution Pd3d XPS peaks for all four samples. Table 7.2 summarizes the XPS peak positions, the full width at half maximum (FWHM), the atomic percentage of each component, and the chemical environment assignment of the peaks. The deconvolution of the Pd3d peaks reveals the existence of Pd only in the metallic state for SnO_2 and TiO_2 supports. However, in the case of nanoparticles supported on carbon and CeO_2, the deconvolution reveals the existence of Pd atoms in higher oxidation states as well. In the case of Pd/C, the deconvolution revealed the existence of four peaks at 335.4, 336.4, 337.5 and 338.4 eV that are attributed to metallic Pd, PdO, PdO_2 and $PdCl_x$, respectively.[43–46] In the case of the Pd/CeO_2 the deconvoluted components are at 334.6 eV, 336.1, 337.4 and 338.4 eV, respectively. The existence of the peak at 338.4eV and its assignment to PdClx species is further supported by the detected Cl2p peaks (not shown here) for the Pd/C and Pd/CeO_2 catalyst. By using the intensities of the Cl2p and of the corresponding Pd3d component it was found that the Cl/Pd atomic ratio is 1.2 and 1.35 for the carbon and ceria supported catalyst, respectively. The existence of PdClx species on the surface of Pd prepared by chlorinated precursors has been reported before and seems that their presence can be affected by the nature of the support.[47,48] The removal of chlorine can take place by a drying-reduction pre-treatment but still a small amount may remain in the catalyst.[48]

Table 7.2. XPS Pd3d peak data of Pd nanoparticles on various supports

Catalyst	Pd3d (eV)	FWHM	Relative content (%)	Assignment
Pd/C	335.4	1.10	71.0	Metallic Pd
	336.4	1.25	13.5	PdO
	337.5	1.35	09.0	PdO_2
	338.4	1.40	06.5	$PdCl_2$
Pd/SnO_2	335.2	1.15	100	Metallic Pd
Pd/TiO_2	334.8	1.20	100	Metallic Pd
Pd/CeO_2	334.6	1.10	67.4	Metallic Pd
	336.1	1.20	09.1	PdO
	337.4	1.25	14.3	PdO_2
	338.4	1.35	09.2	$PdCl_2$

Our XPS results show that for Pd nanoparticles supported on oxides (CeO_2, SnO_2, and TiO_2), the peak, attributed to the metallic state, shows a shift to lower binding energies compared to the corresponding peak in the case of carbon-supported nanoparticles (Pd/C). For Pd/SnO_2, the peak

was detected at 335.2 eV, whereas in the case of Pd/TiO_2 and Pd/CeO_2, the metallic state (Pd^0) peak is shifted by 0.6 and 0.8 eV lower, respectively. Similar shifts of the Pd3d peak have been reported before for Pd supported on these oxides.[49] The observed shift of the Pd3d peaks to lower binding energy for Pd nanoparticles supported on oxides is attributed to a metal-support interaction, where the charge is transferred from the supports to Pd nanoparticles.[50,51] Upon contact of two metal atoms with different electronegativity, the charge will be transferred from the atoms with the lower electronegativity to the atoms with higher electronegativity until the energy level of the electrons at the interface is equilibrated. The electronegativity for the atoms involved here are; in increasing order of 1.12, 1.54, 1.96, 2.20, and 2.55 for Ce, Ti, Sn, Pd, and C, respectively.[52]

It is interesting to note that Pd was 100% reduced on SnO_2 and TiO_2 but only 67% reduced on CeO_2 as shown by XPS data in Table 7.2, which would seem to contradict the electronegativity difference trends. However, the observed difference would be explained based on the crystal structure of the supports. The CeO_2 has a fluorite-type structure and SnO_2 and TiO_2 have a rutile-type crystal structure. First, it is important to mention that the shift of the metallic peak follows the electronegativity trend as expected, i.e., highest shift for Pd NPs supported on CeO_2 because of its lowest electronegativity value and vice versa to nanoparticles on SnO_2. It follows then that the structure of the supports would be responsible for the lower percentage (67%) reduction of Pd atoms on CeO_2 since the samples were prepared using same protocol and conditions. It is well known that CeO_2 due to its non-stoichiometry has the ability to undergo conversion between Ce^{4+} and Ce^{3+} quite easily,[53] which can explain the presence of Pd oxides in Pd/CeO_2 catalyst.

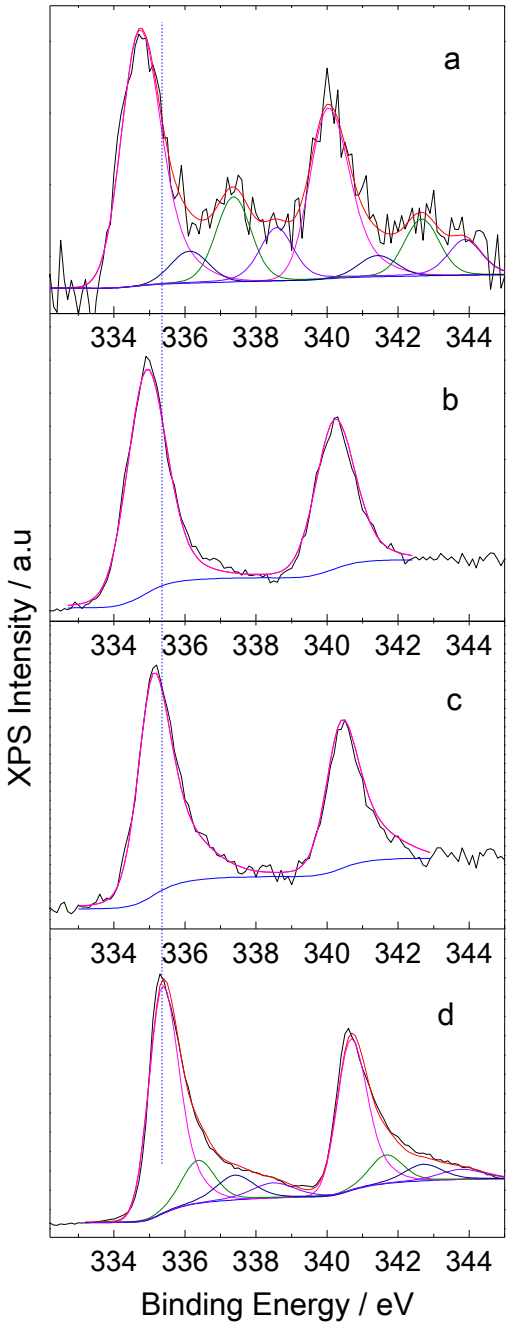

Figure 7.3. Pd3d XPS peak of Pd supported on (a) cerium dioxide (CeO_2), (b) titanium dioxide (TiO_2), (c) tin dioxide (SnO_2), and (d) carbon. The shifting of binding energy for Pd^0 (335.4 eV, vertical line) to lower values indicates the level of Pd-MO_2 (M=Sn, Ti, and Ce) interactions.

Figure 7.4 presents the XPS spectra of Ce3d for Pd/CeO_2 (a), Ti2p for Pd/TiO_2 (b), and Sn3d for Pd/SnO_2 (c) characteristic peaks of the supports. The Ce3d XPS spectrum is rather complex due to the electron correlation phenomena. In general, six peaks are characteristic of Ce^{4+} whereas four are characteristic of Ce^{3+}.

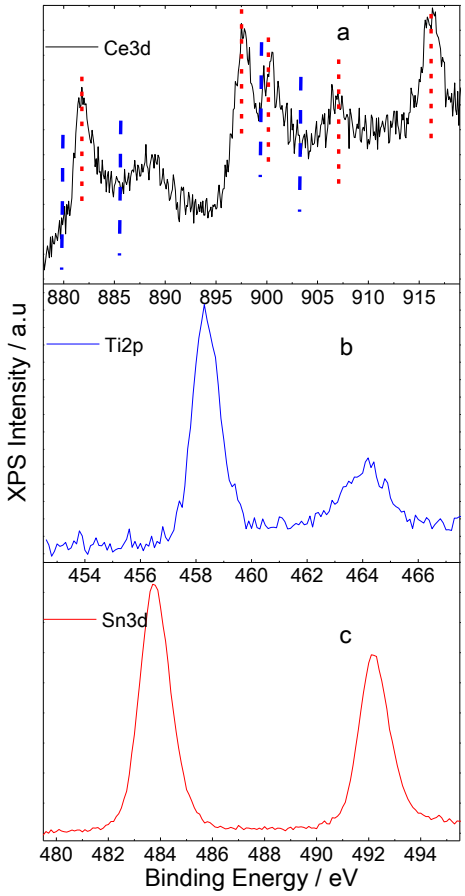

Figure 7.4. XPS peak of Ce3d for Pd/CeO_2 (A), Ti2p for Pd/TiO_2 (B), and Sn3d for Pd/SnO_2 (C).

On the one hand, the Ce3d5/2 peaks at 882, 888.7 and 897.8 eV and their corresponding Ce3d3/2 components at 900.7, 906.9 and 916.1 eV (dotted lines on Fig. 4a) are due to cerium atoms in CeO_2. On the other hand, the Ce3d5/2 at 880.3 and at 899.1 eV with their corresponding 3d3/2 lines at 885.8 and 903.5 eV (dashed lines on Fig. 4a) reveals the existence of cerium atoms in Ce^{3+} oxidation state and more specifically in Ce_2O_3.[54] For other two samples, Ti2p3/2 and Sn3d5/2 peaks are detected at 458.4 eV and 486.8 eV, respectively and are characteristic of Ti and Sn atoms in the 4+ oxidation state.[55,56] Though, the relatively large FWHM of the two peaks (~1.5 eV) implies the existence of Ti and Sn atoms in more than one chemical environment but more studies are necessary to confirm.

7.2.2 **CO stripping voltammetry**

The CO stripping charge was used to determine the electrochemical active surface area (ECSA) of the four catalysts using the protocol reported in literature.[57] Figure A3-2 (appendix

section 3) shows the first and second cycle of the CO stripping CVs for the four catalyst. The area between the two cycles from the potential of -0.17 V to 0.15 V and monolayer stripping charge of 420 μC cm^{-2} were used to determine the ECSA.[57] The ECSA values are shown in Table 7.1. The oxidation peak potential for CO was found to be -0.11 V for all samples. However, there is significant charge distribution depending on the support which indicates the differences in nanoparticles dispersion and CO binding on the surfaces. Pd NPs on SnO_2 were found to be the smallest (crystallite size = 7.5 nm, particle size = 10.4 nm) and hence leading to the highest ECSA of 0.92 cm^2. Interestingly this is the same value (0.93 cm^2) predicted as the real surface area of a polycrystalline Pd electrodes (taking the average of experimental values of (111), (100), and (110) surfaces) by CO stripping on Pd in electrochemical environment.[58] Note that Pd was 100% metallic on SnO_2 and TiO_2, hence not surprising to have such perfect polycrystalline nanoparticles. However, one may wonder how come we do not have similar real surface area for Pd NPs on TiO_2. First, Pd NPs on TiO_2 are the largest (crystallite size = 15.2 nm, particle size = 14.2 nm). Second, TiO_2 is a poor conductor hence will insulate some parts of the nanoparticles. The Pd nanoparticles supported on CeO_2 and C have similar ECSA, but lower than that of Pd/SnO_2, which is consistent with their approximately same percentage of metallic Pd based on XPS data in Table 7.2.

7.2.3 **Ethanol electrooxidation**

First, we present the CVs of the nanoparticles in 1M KOH then CVs in 1M (KOH + C_2H_5OH) solutions. The characteristic CVs of the four catalysts in 1M KOH at a scan rate of 25 mVs^{-1} are shown in Figure 7.5. The CVs show similar features as expected being in the same electrolyte, but with different current densities due to variations between the nanoparticle-support interactions, which in turn alters the catalytic activity at the interfaces. Figure 7.5 shows that in the anodic scan there are peaks below -0.4V (labelled as I) which are attributed to the oxidation of adsorbed and absorbed hydrogen on Pd nanoparticles. The anodic peaks labelled II observed between -0.35 V and -0.25 V are generally attributed to the adsorption of hydroxyl groups on the surface of Pd,[14,59] whereas the peaks labelled III situated at potentials higher than -0.25V corresponds to the transformation of adsorbed hydroxyl groups to higher valence oxides (PdO_x).

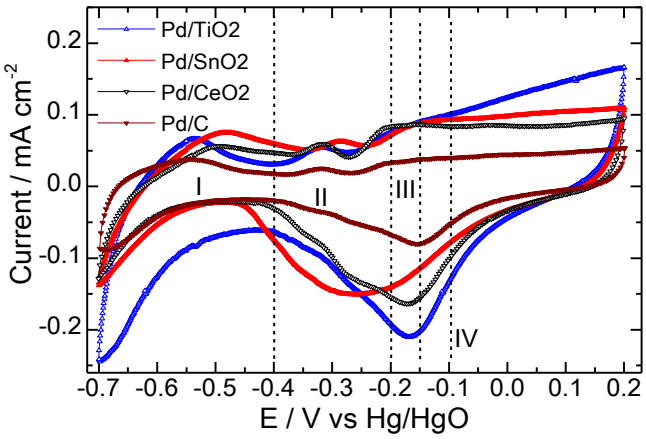

Figure 7.5. Cyclic voltammograms of Pd nanoparticles deposited on carbon, CeO_2, SnO_2 and TiO_2 in 1M KOH at v = 25 mVs^{-1}. The vertical lines show the potentials in which the CA experiments and in situ monitoring of products by PM-IRRAS were conducted during ethanol electrooxidation (*vide infra*).

PdO_x oxide formation is suggested to follow the reaction pathways shown in equations 7.1 to 7.3:[9]

$$Pd + OH^- \rightarrow Pd\text{-}OH_{ads} + e^- \qquad 7.1$$

$$Pd\text{-}OH_{ads} + Pd\text{-}OH_{ads} \rightarrow Pd\text{-}O_{ads} + H_2O \qquad 7.2$$

$$Pd\text{-}OH_{ads} + OH^- \rightarrow Pd\text{-}O_{ads} + H_2O + e^- \qquad 7.3$$

In the cathodic scan, the peaks labelled IV with its minimum situated at ~ -0.15 V (except for Pd/SnO_2 at ~-0.25 V) are attributed to the reduction of the PdO_x formed during the anodic scan. The shoulders seen on peak IV for Pd/CeO_2 can be attributed to the reduction of different oxidation states of Pd atoms on various Pd crystalline planes and on low coordination sites. For Pd/SnO_2, the reduction peak IV is broad and shifted to lower potentials indicating that the reduction process is thermodynamically unfavorable. When the applied potential is lower than -0.45 V the cathodic current decreases due to a combination of three overlapping phenomena: i) the adsorption of H on Pd surface, ii) the diffusion of H into the lattices of Pd, allowing more H atoms to be adsorbed on the surface, iii) the evolution of H_2 starts to take place as the potential lowered further.

The CVs for ethanol electrooxidation on the four catalysts in 1M (KOH + C_2H_5OH) are shown in Figure 7.6. The CVs were collected by scanning the potential from an initial open circuit voltage towards the anodic direction up to a maximum potential at 0.15 V, then in the cathodic

direction up to a minimum potential at -0.65 V at a rate of 5 mVs^{-1}. The measured open circuit potential of four catalysts was found to increases in the order of Pd/TiO_2 < Pd/C < Pd/SnO_2 < Pd/CeO_2 with values of -0.43 V, -0.52 V, -0.57 V, and -0.62 V, respectively. The CVs of the supports in 1M (KOH + C_2H_5OH) provided in appendix Figure A3-3, confirms that the supports have no catalytic activity for ethanol electrooxidation in alkaline media.

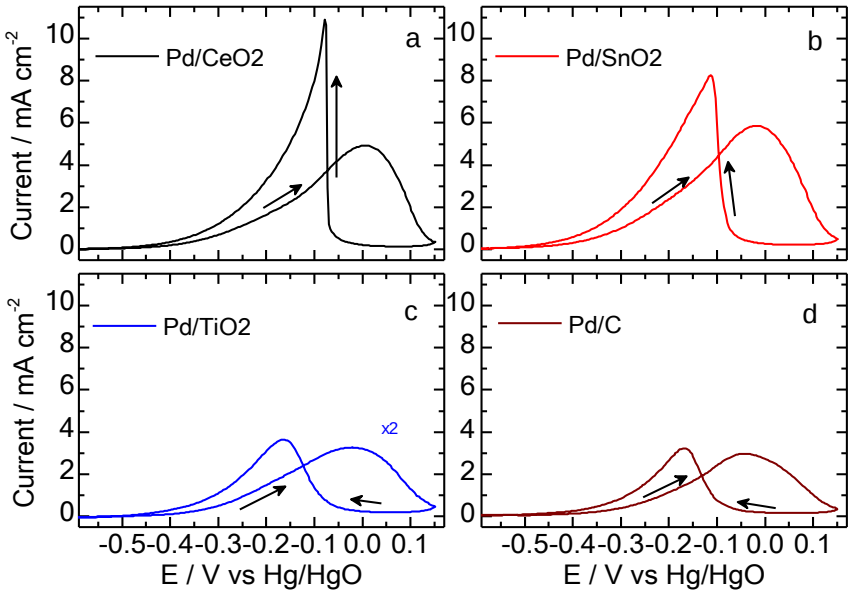

Figure 7.6: Cyclic voltammograms of Pd nanoparticles supported on CeO_2 (a), on SnO_2 (b), TiO_2 (c), and carbon (d) in 1M (KOH + C_2H_5OH) at ν = 5 mV s^{-1}. The current densities are given per the ECSA determined via CO stripping method.

Figure 7.7 compares the linear sweep voltammetry of the four catalysts in 1M (KOH + C_2H_5OH). It shows that for Pd NPs supported on TiO_2 and C, the onset potential (start of positive current) is around -0.33 V, while for nanoparticles supported on SnO_2 and CeO_2 it is shifted to lower value of -0.45 V. The trend of the anodic current magnitude is consisted with that of the ECSA and maximum anodic current densities (Ia, max) of the catalyst.

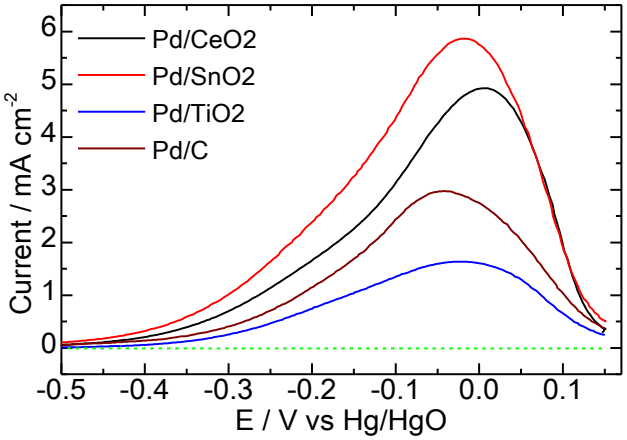

Figure 7.7: Linear sweep voltammetry of the four catalysts in 1M (KOH + C_2H_5OH) at v = 5 mVs^{-1}. The current densities *idem*.

At Ia max, the catalyst is deactivated due to formation of surface oxides and adsorbed oxidized species. Therefore, it is interesting to see the role of the supports in influencing the potential at which this phenomenon occurs. It was found that Pd NPs on C support are easily deactivated at the potential of -0.04 V (2.97 mA cm^{-2}), those on SnO_2 and TiO_2 deactivated at the same potential of -0.02 V (5.86 mA cm^{-2} and 1.63 mA cm^{-2} , respectively). But the nanoparticles on CeO_2 were very resistant, deactivating at 0.01 V (4.92 mA cm^{-2}). This observation indicates that CeO_2 is capable to accommodating more surface oxides (O^{2-}) than the other supports (*vide infra*).

During the reverse scan (Figure 7.6), the potential of the working electrode is gradually lowered allowing the transfer of electrons into the catalysts (reduction process). During the reverse scan, a positive current was obtained starting at around -0.05 V and rapidly increasing (unlike the gradual increase in anodic scan) to a maximum current (I_r, max), which depended on the nanoparticle support, then gradually decays to zero at lower potential. The differences observed in the reverse current peak shapes (see Figure 7.6) has to do with the ability of the oxidized species to diffuse into the bulk solution hence allowing fresh ethanol to access the catalyst surface. For instance, Pd/CeO_2 showed sharp current increase at -0.09 V during the backward scan, which can be explained by the known CeO_2 phenomenon that it releases lattice oxygen (O^{2-}) when reduced.[60] Therefore, the released oxygen species could help to push oxidized intermediates from the surface hence allowing rapid access by the fresh species for oxidation. As can be seen, CeO_2 and SnO_2 stand out as the best performers. CeO_2 is particularly of great interest based on the CVs in Figure 7.6a.

7.2.4 **In-situ identification of ethanol electro-oxidation products**

Chronoamperometry technique coupled with in-situ polarization modulation infrared reflection absorption spectroscopy (PM-IRRAS) was used to investigate ethanol electrooxidation products. The PM-IRRAS allows us to distinguish between the oxidation species on the electrode surface (the difference of p- and s-polarized reflection absorption spectra) and the oxidation species in the bulk electrolyte within the thin-cavity between the CaF_2 window and the electrode (the average of p- and s-polarized reflection absorption spectra) at each potential. Therefore, the spectra for the species on the electrode surface and spectra of the average species in the thin-cavity will be labelled as "surface" and "bulk", respectively.

The PM-IRRAS spectra for ethanol electrooxidation products are shown in Figure 7.8. The left and right figures show respectively the surface and bulk species of the four catalysts after holding potential at -0.3 V for 10 minutes. The presence of peaks at 1560 cm^{-1} and 1423 cm^{-1} on the surface and bulk spectra are evidence for the acetate ($CH3COO^-$) produced in the four catalysts. However, the amount of acetate varied from one support to another, where Pd NPs supported on TiO_2 were the least active while the Pd NPs on SnO_2 were the most active.

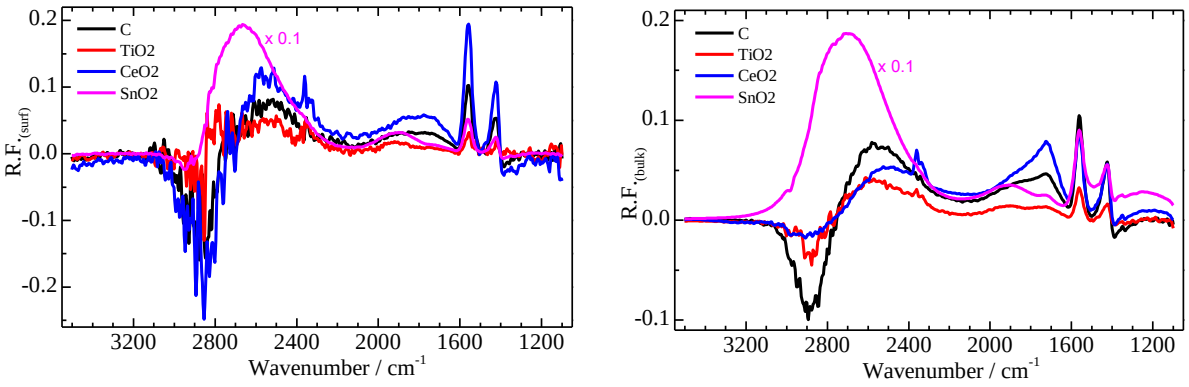

Figure 7.8: PM-IRRAS spectra generated during ethanol electrooxidation on Pd NPs supported on, SnO_2, CeO_2, C, and TiO_2 after holding potential at -0.3 V vs Hg/HgO for 10 minutes in 1M ($KOH + C_2H_5OH$).

Further spectra of the most active catalysts were collected at lower potentials close to the onset potential for EOR at -0.5 V and -0.4 V for Pd/CeO_2 and Pd/SnO_2, respectively are provided in Figure 7.9. The evidence for the C–C bond cleavage is shown by the CO_2 peak at 2345 cm^{-1}. The spectra demonstrate that the oxide supports have a significant influence on the selectivity of the electrooxidation species, in particular those species with absorption peaks centered on 1724

cm^{-1}, 1919 cm^{-1}, 2345 cm^{-1}, and 2700 cm^{-1}. Of top interest, is the selectivity towards breaking Pd/CeO_2 showed superior selectivity in breaking the C–C bond. In this regard, the utility of PM-IRRAS came into play in distinguishing that the produced CO_2 desorbs/diffuses from the surface into the bulk. The desorption of CO_2 into the bulk is confirmed by the higher intensity of the peak at 2345 cm^{-1} compared to that of the surface as shown in Figure 7.9 (a and b).

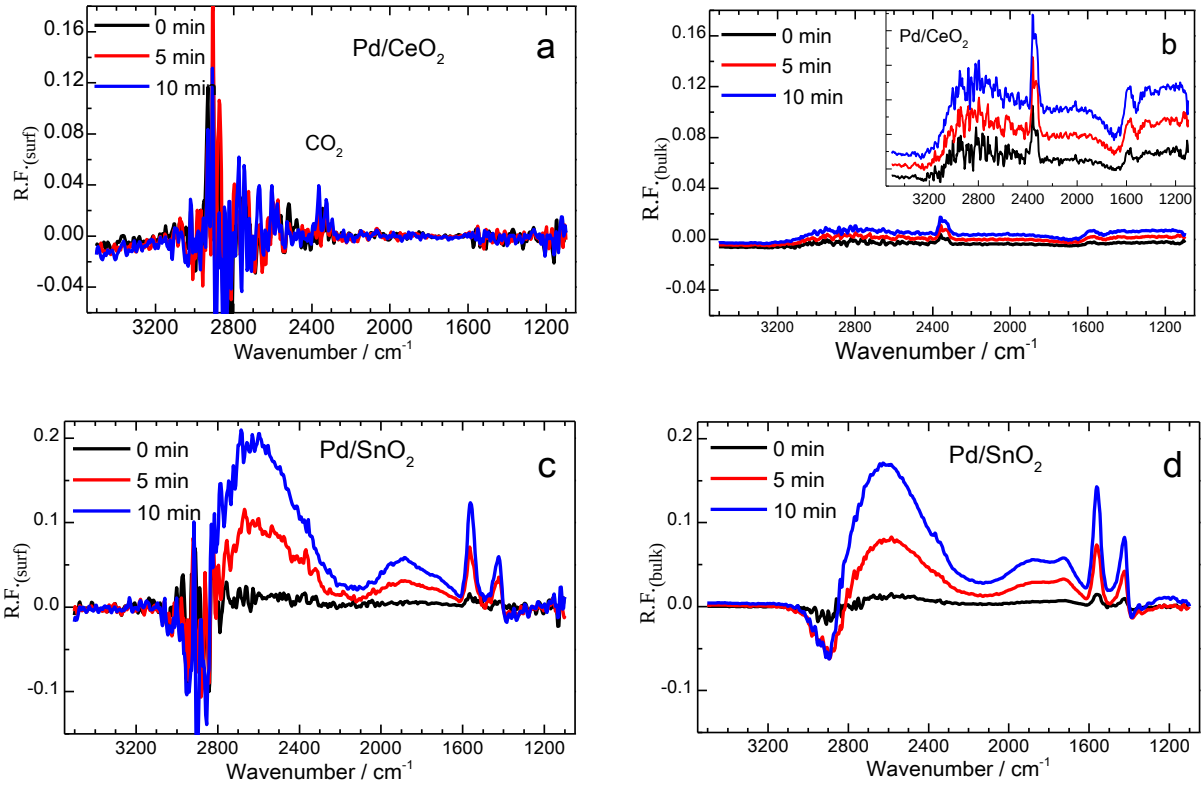

Figure 7.9: PM-IRRAS spectra generated during ethanol electrooxidation on Pd/CeO_2 at -0.5 V at increments of 5 minutes (upper panel) and on Pd/SnO_2 at -0.4 V at increments of 5 minutes (lower panel) in 1M (KOH + C_2H_5OH). The graphs shows the surface adsorbed species (a and c) and bulk-phase species (b and d).

With time and at higher potentials, the competition between the breaking of the C–C bond and the formation of acetate and the species at 1724 cm^{-1} increases for the Pd/CeO_2 NPs. The origin of the species absorbing at 1724 cm^{-1}, 1919 cm^{-1}, and 2700 cm^{-1} is currently being investigated. Pd/SnO_2 did not show any evidence of breaking the C–C bond; instead it showed high selectivity and high reaction kinetics towards the production of the species absorbing at 2700 cm^{-1}. Even at low potential (-0.4 V), acetate and the species at 2700 cm^{-1} were the main products as shown Figure 7.9 (c and d). This observation highlights the promotional catalytic effect of metal oxide

supports compared to the commonly used carbon.It is important to note the difference between the spectra of the surface and bulk species between 1600 cm^{-1} and 2000 cm^{-1}. The bulk spectra have a broad peak centered at 1724 cm^{-1}, which is well shaped for Pd/CeO_2, but it is missing on the surface spectra. Similarly, the surface spectra have a broad peak around 1919 cm^{-1}, which is well pronounced on Pd/SnO_2. The peak at 1724 cm^{-1}, maybe attributed to the C=O vibrations from acetaldehyde (CH_3CHO) or from the aldol product ($CH_3CH(OH)CH_2CHO$) formed from the desorbed acetaldehyde but it's subject to further investigation. This suggestion is based on the fact that on the surface the carbonyl double bond character is absent, because of the molecules interactions with the surface and due to its polarization from the applied potential.

The CAs of ethanol oxidation over the four Pd catalysts recorded at -0.40 V, -0.2 V, -0.15 V, and -0.09 V are shown in Figure 7.10. The current densities of Pd/TiO_2 and Pd/C are much lower compared to Pd/CeO_2 and Pd/SnO_2. In general the Pd NPs supported on metal oxides have a higher activity for ethanol electrooxidation than Pd/C catalyst, consistent with the amount of acetate produced. The significant difference in the current densities obtained, implies that the reaction kinetics at the interface is different on each support in agreement with the reaction selectivity demonstrated by the PM-IRRAS spectra.

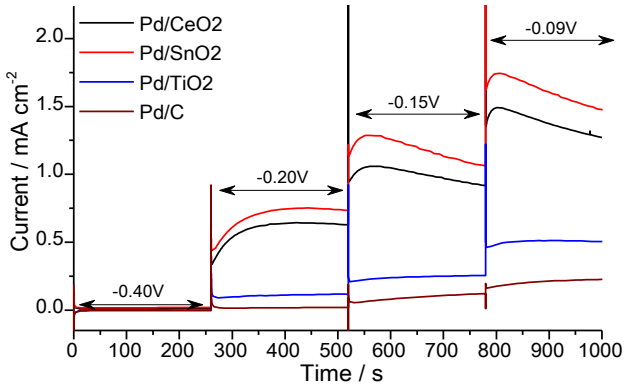

Figure 7.10: Chronoamperograms of Pd on different supports in 1M (KOH + C_2H_5OH) at various applied potentials vs Hg/HgO. The current densities are given per the ECSA determined via CO stripping method. Pd/SnO_2 gave the highest current density while Pd/C had the least.

The CAs reveals further important features of the reaction kinetics at the electrolyte-nanoparticles interface based on the current density traces. For Pd NPs on CeO_2 and SnO_2, the currents showed increasing trends as soon as the potential was changed/stepped and then decreased gradually. The initial increasing current densities (Figure 7.10) shows that the

nanoparticles on CeO_2 and SnO_2 are very active, which is in agreement with CV and PM-IRRAS results.

The high catalytic activity of Pd NPs on ceria and tin oxide could be correlated to metal support interaction (MSI) generated between Pd and oxides; however the particle size effect could also play a role. The smaller the nanoparticles the larger active surface area is available for the reaction as well as stronger MSI, because of the shorter charge transfer distances between two solids. A clear trend is observed between the crystallite sizes (Table 7.1) and the current densities (Figures 7.7 and 7.10). The smaller the crystallite size the higher the current density obtained which explains the higher catalytic activity for Pd/SnO_2 and Pd/CeO_2, respectively. The poor performance of Pd/TiO_2 would be attributed to their large crystallite/particle sizes and perhaps weaker MSI.

The origin of MSI in Pd NPs supported on oxides could be due to: (i) the higher availability of hydroxyl ions or oxygenated species ($O^{\delta-}$) from the support lattice which accelerates the oxidation rate of adsorbed ethanol intermediates especially on CeO_2, and SnO_2: (ii) The change in the so-called Volta potential difference [60–62] between the support and Pd NPs, which will alter the Fermi level of electrons in Pd leading to the modification of its catalytic properties. The Volta potential difference between Pd and carbon black is 0.23 eV and is the lowest among all the catalysts investigated in the present work. The values for Pd/SnO_2, Pd/CeO_2 and Pd/TiO_2 are 0.37, 0.43 and 0.92 eV, respectively,[63–65] however the catalytic activity of Pd for the EOR does not follow the same trend, which indicates that larger particle size of Pd/TiO_2 catalysts and presence of Pd agglomerates negates the expected support effect. According to XPS measurements, Pd3d peak position is shifted to lower binding energies confirming a charge transfer from the oxide support to Pd, which points out that metal-support interaction between Pd and metal oxide supports contributes to the enhanced ethanol electrooxidation reaction.

7.3 **Conclusions**

The results presented in this study showed that the metal oxide supports have a promoting effect on the electrocatalytic activity of Pd nanoparticles for EOR in alkaline media. A simple synthesis method was used to prepare Pd NPs, which were deposited in-situ on the surface of different reducible metal oxide (CeO_2, TiO_2 and SnO_2) and on conventional carbon support. XRD showed that the synthesized Pd NPs have fcc structure similar to bulk Pd. The XPS spectra

revealed a shift to lower binding energy of the Pd3d peaks for Pd NPs deposited on oxides due to the charge transfer from the oxide support, which result in a higher electron density on the NPs.

The PM-IRRAS spectra demonstrated the influence of the support on the selectivity of EOR on Pd NPs. Pd/CeO_2 nanoparticles showed superior selectivity for breaking the C–C bond, while Pd/SnO_2 did not show any evidence for breaking the C–C bond in spite of its highest reaction kinetics. Instead Pd/SnO_2 showed high selectivity towards the species with vibrations around 2700 cm^{-1} whose nature is currently under investigation. The current densities for ethanol electrooxidation on Pd deposited on CeO_2 and SnO_2 were significantly higher than those on Pd/TiO_2 and Pd/C. The increased current densities of Pd/CeO_2 and Pd/SnO_2 are proposed to be caused by a joined effects of hydroxyl (OH^-) adsorption, the oxygen ions ($O^{\delta-}$) supply from the support to Pd active surface sites, and the modification of the Fermi level of Pd electrons caused by a larger contact potential difference between Pd NPs and oxide supports than between Pd and carbon. Acetate, CO_2, and three other species with vibrations at 1724 cm^{-1}, 1919 cm^{-1} and 2700 cm^{-1}, whose origin is not clear at this time [but speculated to be the aldol product, $CH_3CH(OH)CH_2CHO$] were identified as the EOR products on Pd on the four supports in alkaline media.

This work identifies CeO_2 as the promising support candidate for breaking the C–C bond and highlights the importance of selecting the catalyst support to promote Pd nanoparticles for EOR.

Supporting Information: CO stripping voltammograms of the four catalysts and the CVs of the supports in 1M KOH and in 1M (KOH + EtOH) are provided in appendix section 3.

Chapter 8: Ethanol Electrooxidation on Palladium Revisited using PM-IRRAS and DFT: Why is it difficult to break the C–C bond?

Publication: E. A. Monyoncho, S. N. Steinmann, C. Michel, E. A. Baranova, T. K. Woo, and P. Sautet. *ACS Catalysis*, 6 (2016) 4894-4906, DOI: 10.1021/acscatal.6b00289

Abstract

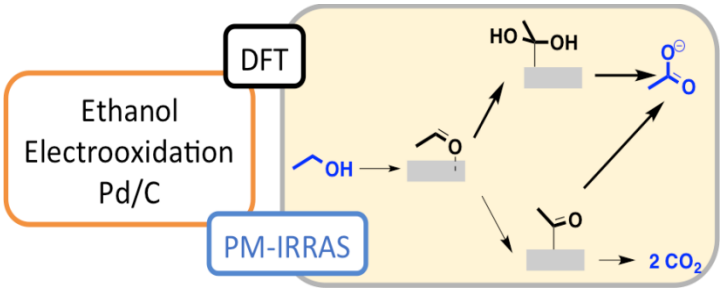

Insights into ethanol electrooxidation reaction mechanism on palladium in alkaline media are presented combining polarization modulation infrared reflection absorption spectroscopy (PM-IRRAS) and density functional theory (DFT) calculations. The synergy between PM-IRRAS and DFT calculations helps to explain why the C–C bond is not broken during ethanol electrooxidation, and the reaction stops at acetate. Coupling chronoamperometry (CA) with *in-situ* PM-IRRAS enabled us to simultaneously identify ethanol electrooxidation products on the catalyst surface and in the bulk solution. We show that at lower potential it is possible to break the C–C bond on Pd/C in alkaline media to form CO_2. However, the selectivity is poor due to competition towards the formation of acetate and other side products, which gets worse at higher potentials. DFT calculations were used to complete the picture using the computational hydrogen electrode approach. The calculations highlight the pivotal role of the CH_3CO intermediate that can either undergo a C–C bond scission yielding CO and then CO_2 or that can be oxidized towards CH_3COO^-. The latter is a dead end in the reaction scheme towards CO_2 production, since it cannot be easily oxidized nor broken into C_1 fragments. CH_3CO is however not the most favoured intermediate formed from ethanol electrooxidation on Pd, hence limiting the production of CO_2.

Keywords: Ethanol electrooxidation, Palladium, Spectroelectrochemistry, direct ethanol fuel cells, DFT, computational hydrogen electrode

8.1 Introduction

The development of alkaline fuel cells has mainly been hampered by the lack of stable and efficient anion exchange membranes. However, this challenge has been well tackled in recent years,[8,9] allowing the development of alkaline fuel cells (AFCs) which are of particular technological interest due to their simple designs and ability to operate at low temperatures (25-100 °C). In alkaline conditions, the kinetic of both the cathodic oxygen reduction and the anodic ethanol oxidation is facilitated. Furthermore, the expensive Pt catalyst can be replaced by the lower-cost and more active transition metals, for instance Pd.[10–14]

Therefore, to overcome the limitation of incomplete oxidation of ethanol to CO_2, several studies have attempted to provide a better understanding of the ethanol oxidation on Pd-based catalysts using the previous extensive work on the ethanol oxidation on Pt-based catalysts in acidic conditions as a starting point. Although the detailed understanding of ethanol electrooxidation mechanism is complex and controversial, there is a general consensus on Pt-based catalysts in acidic conditions that the reaction exhibits the so-called "dual pathway mechanism"[15,16] or "consecutive-parallel mechanism".[17] According to this dual path reaction scheme, two major pathways are in competition. In the C_2 pathway, the C–C bond does not break and ethanol is oxidized successively to acetaldehyde and then to acetic acid (acetate in alkaline). In the C_1 pathway, the C–C bond is broken, thus generating C_1 fragments. These fragments are oxidized into CO and eventually CO_2. When shifting to alkaline conditions, very few studies provide detailed molecular information.[18–23] Christensen *et al*. have shown in several studies that the interfacial pH drops at higher potentials due to the OH^- consumption that is not completely counterbalanced by the OH^- diffusion from the bulk to the interfacial region.[15–17] This phenomenon leads to a transition from alkaline to effectively acidic conditions. The transition potential varies with the diffusion rate of OH^-, i.e., working temperature, flow-rate and so on. They report that during electrooxidation reaction, ethanol is converted to acetate in alkaline pH while above the transition potential, i.e., in pseudo-acidic conditions, it yields acetic acid and trace amounts of CO_2 as a result of the slow C–C bond splitting.[25] This is in agreement with the

results from online mass-spectrometry, evidencing CO_2 production over Pt and Pd in 0.01 M NaOH, where acetic acid formation is almost absent.[26]

On Pd-based electrocatalysts, ethanol oxidation reactivity differs compared to Pt, which is illustrated most clearly in acidic conditions, where Pt yields mainly acetic acid and even some CO_2, while Pd is completely inactive.[27] In alkaline conditions, Pd is more active and it is generally proposed that ethanol is dehydrogenated into adsorbed acetyl (CH_3CO) (sometimes erroneously called ethoxy) which is further oxidized to acetate by the hydroxyl (OH^-) species.[28] This mechanism has received further credence using *in-situ* attenuated total reflection surface-enhanced infrared absorption spectroscopy (ATR-SEIRAS) measurements.[19] Yang *et al*. reported that ethanol oxidation starts with the α-C–H bond scission yielding adsorbed CH_3CO as a pivotal intermediate, which may be further oxidized into acetate or, given enough time, would fragment into C_1 adsorbed intermediates (due to observation of adsorbed CO).[19] These observations can be rationalized by recalling that the oxidation of acetyl to acetate is an electrochemical step, and therefore favoured by oxidative potentials, while the C–C bond cleavage is expected to be only weakly affected by the potential, assuming that this process is not coupled with an electrochemical step such as the C–OH bond formation.

To complement the experimental insights, modeling studies are also being reported. However, the complexity of the Pd/alkaline electrochemical interface not only challenges experiments but also the atomistic modeling of the underlying mechanism.[29] The main ingredients are the electrolyte and its pH, both influencing the reactivity directly (state of the electrode surface) and indirectly (modifying the environment). The electrochemical potential and the inclusion of well-established equilibria, such as the reactivity of acetaldehyde (e.g., enol and aldol formation) or of CO, which can be hydrated to yield formic acid adds to the complexity of the reaction network. It is currently impossible to consider all these aspects on a consistent level in one, exhaustive, study. Furthermore, the size of the "straight forward" reaction network for ethanol oxidation already includes 128 potential C_2 and 21 C_1 intermediates.

The influence of co-adsorbed species and of explicit water molecules has intrigued several groups. In particular, Neurock and co-workers have modelled ethanol oxidation by O_2 in alkaline conditions by including the aqueous media explicitly and adsorbed hydroxyl on the Pd surface.[30] They have shown that most of the C–H and O–H scissions of the ethanol oxidation network towards acetic acid/acetate have lower barriers when assisted by co-adsorbed hydroxyl on

Pd(111) compared with the bare metal. According to their results, acetaldehyde is a first intermediate towards acetic acid. Then, two possibilities exist: (i) the geminal diol, which can be formed by hydration of the acetaldehyde in solution, leads straightforwardly to acetic acid (ii) acetaldehyde is either oxidized by the direct formation of a C–OH bond, or the α-C–H bond is broken, leading to acetyl CH_3CO. In a more recent study, Hu and co-workers revisited this mechanism in the electrochemical context, but without accounting for the electrochemical potential. Their conclusions are in line with the ones of Neurock regarding the oxidation by oxygen using a more advanced description of the structure of the water solvent.[31] It should be noted that under electrochemical conditions, surface OH is also formed in acidic conditions, provided the electrochemical potential is sufficiently positive.[32] As a consequence, these simulations can be applied to both alkaline and acidic conditions.

In order to complement these studies, one should include the effect of the electrochemical potential. The electrochemical potential can be included at various levels of sophistication. The most important effects are due to a change in thermodynamics when electrons and protons are exchanged. This effect can be easily obtained as *a posteriori* correction to *ab initio* energies (typically periodic DFT) as originally proposed by Norskov, known as the computational hydrogen electrode.[7] This approach has been used successfully for MeOH oxidation on a large range of metals[33–35] and includes the thermodynamic driving force of the (H^+, OH^-) recombination into H_2O. Several groups have also proposed strategies to include the influence of the potential in the electronic structure computations.[36–41] Although more accurate, these approaches are also computationally more costly since they require the inclusion of the electrolyte to mimic adequately the capacitance of the interface, either with a continuum model,[42] a Poisson-Boltzmann theory,[40,43] or an explicit, but static description.[44] These approaches have been used for the study of small reaction path networks such as the CO_2 hydrogenation to formic acid [45] in combination with continuum models for the solvent or methanol and CO oxidation at a Pt catalyst.[46,47]

The aim of this work is to provide insights as to why the C–C bond is not broken during ethanol electrooxidation and to propose a detailed mechanistic schematic, which can be applied in understanding experimental observations. Ethanol oxidation potentials were determined by cyclic voltammetry. Chronoamperometry, coupled with *in-situ* PM-IRRAS, was used to identify the oxidation products both on the catalyst surface and in the bulk solution. Density functional

theory calculations are exploited to explore all possible intermediates including the electrochemical potential using the computational hydrogen electrode at an alkaline pH of 14. This setup allows us to include the thermodynamic effect of the involvement of hydroxide ions in the reaction mechanism without explicitly co-adsorbing OH on the catalyst surface. The potential energy profiles of the reactions were used to determine the most likely reaction pathway towards acetate on two different facets, Pd(111) and Pd(100). On the most active facet, a complete study of the C_2 and C_1 intermediates was done on the full range of the 12 electron oxidation (from ethanol to CO_2) to select the key intermediates for the C–C bond breaking. Besides, for the first time to the best of our knowledge, we assess the C–C bond breaking from these key intermediates in the context of electro-oxidation. The energy barriers provide general strategies for improving the catalyst towards C–C bond scission.

8.2 Results and discussion

8.2.1 Pd/C Nanoparticles characterization and electrochemical performance

The physical, structural, and chemical characterizations of Pd/C are provided in chapter 6 and in appendix Figure A4-1 (appendix section 4).[49] In summary, the supported particle size was determined to be on average 4 ± 2 nm. The XRD pattern showed that the nanoparticles retained the fcc structure of bulk Pd with peaks at 40, 46 and 68° 2θ corresponding to (111), (200) and (220) reflections, respectively.

Cyclic voltammetry was used to determine ethanol oxidation current/potential profiles for Pd/C nanoparticles in alkaline conditions as shown in Figure 8.1(a). Figure 8.1(a) shows a representative CV of Pd/C nanoparticles in 1M (KOH + CH_3CH_2OH) and 1M (KOH + CH_3COOH) solutions at 5 mV s^{-1}. The slow scanning rate helps to capture the oxidation profile with current densities close to a steady-state condition. For ethanol profile, during the *anodic* scan, a positive current starts at 0.39 V and increases *gradually* to a maximum current density at 0.77 V, and then decreases to zero at 1.00 V. During the *cathodic* scan, a positive current was obtained starting at 0.76 V, which increases *rapidly* to a maximum at 0.66 V, and then decreases to zero at 0.39 V. The CV profile for acetic acid did not show any oxidation current densities, proving that the resulting acetate (KOH + CH_3COOH) is the dead end during ethanol electrooxidation reaction.

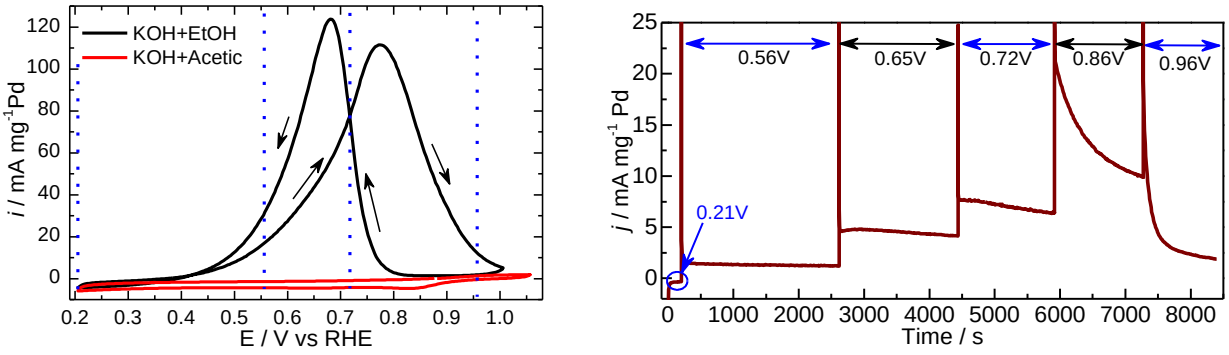

(a) (b)

Figure 8.1: The CV profile for Pd/C nanoparticles in 1M (KOH + EtOH) and 1M (KOH + Acetic) at v = 5 mV s^{-1}(a), and the CA profile of Pd/C nanoparticles in 1M (KOH + EtOH) at various potentials as indicated by the double arrows (b). The vertical lines and double arrows (coloured blue) shows the potentials whose PM-IRRAS spectra are discussed in the text.

This ethanol electrooxidation profile in Figure 8.1(a), is typical for alcohols and is generally interpreted as a signature of species blocking the electrocatalyst surface at higher potential that can be removed while scanning back to lower potentials hence allowing oxidation of fresh ethanol molecules.[19,64,65] To gain insights of the processes taking place at different potentials of the CV profile, CA coupled with PM-IRRAS were used and the resulting data is discussed in the following section.

8.2.2 Products identification during ethanol electrooxidation on Pd/C

Figure 8.1(b) shows the CA profile in which the potential was stepped up from 0.21 V/RHE to 0.96 V/RHE while collecting spectra at each potential in increments of 5 minutes up to 30 minutes. The spectra collected at 0.21, 0.56, 0.72, and 0.96 V/RH are shown in Figure 8.2(a)-(h). As presented above and in chapter 4, the PM-IRRAS unlike the regular IRRAS technique allows us to distinguish between the oxidation species on/near the electrode surface (using the difference absorption intensities of p- and s-polarized reflection) and the oxidation species in the bulk/liquid-phase electrolyte within the thin-cavity between the CaF_2 window and the electrode (using the average absorption intensities of p- and s-polarized reflection). Herein, the spectra for the species on the electrode surface and spectra of the sum species in the thin-cavity will be referred to as "surface" and "bulk solution" species, respectively.[66]

Prior to the measurement of ethanol electrooxidation species spectra, it is important to ensure that there is no atmospheric CO_2 and water vapour in the optical path which would not only decrease the IR intensity but also would contribute to observed spectra features. Especially the

presence of CO_2 is critical because it is one of the anticipated ethanol oxidation products. This objective was accomplished by purging the electrolyte and the cell chamber (PMA 50) with nitrogen gas and the level of CO_2 in the system was tracked by collecting a series of background PM-IRRAS spectra at open circuit potential, i.e., no applied potential. Figure A4-2 (appendix section 4) shows the background surface and bulk species spectra collected at various time intervals. The first spectrum (Figure A4-2 curve(s) (a)) was collected at the beginning of the experiment, i.e., 2.5 hours before actual measurements were started. Two other spectra were collected at 30 minutes Figure A4-2 curve (b) and at 3 minutes Figure A4-2 curve (c) before the actual measurements were done. In summary, it was determined that after 2.5 hours there was no significant background contribution to interfere with any spectra features as confirmed by the straight line of Figure A4-2 curve(s) c). Now we shift our attention to the spectra features obtained at the various potentials as shown in Figure 8.2. The potentials reported were selected from the different regions of the CV profile in Figure 8.1(a) and are meant to shed more insights of the reaction dynamics and/or intermediates/products at those regions.

Figure 8.2 (a) and (b), shows the PM-IRRAS spectra at 0.21 V/RHE where there is no ethanol electrooxidation according to CV and CA (Figure 8.1). At this potential we see a negative peak centered around 2908 cm^{-1} which is due to breaking of the C–H bond. There are also two positive peaks centered on 2819 cm^{-1} and 3668 cm^{-1} which corresponds to C–H and H_2O vibrations, respectively. These observations tell us that there is some form of re-organization of the electrolyte molecules on the electrode surface. On the other hand, we do not see any significant structural changes features in bulk solution as shown by the straight line in Figure 8.2(b). This is expected at this low potential.

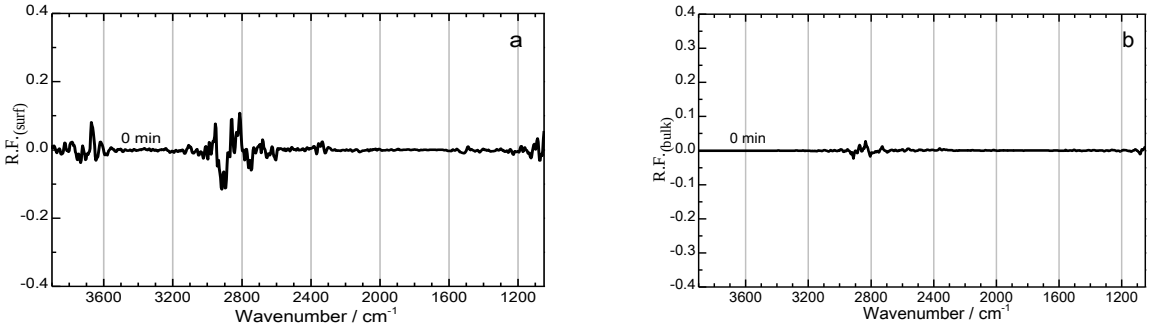

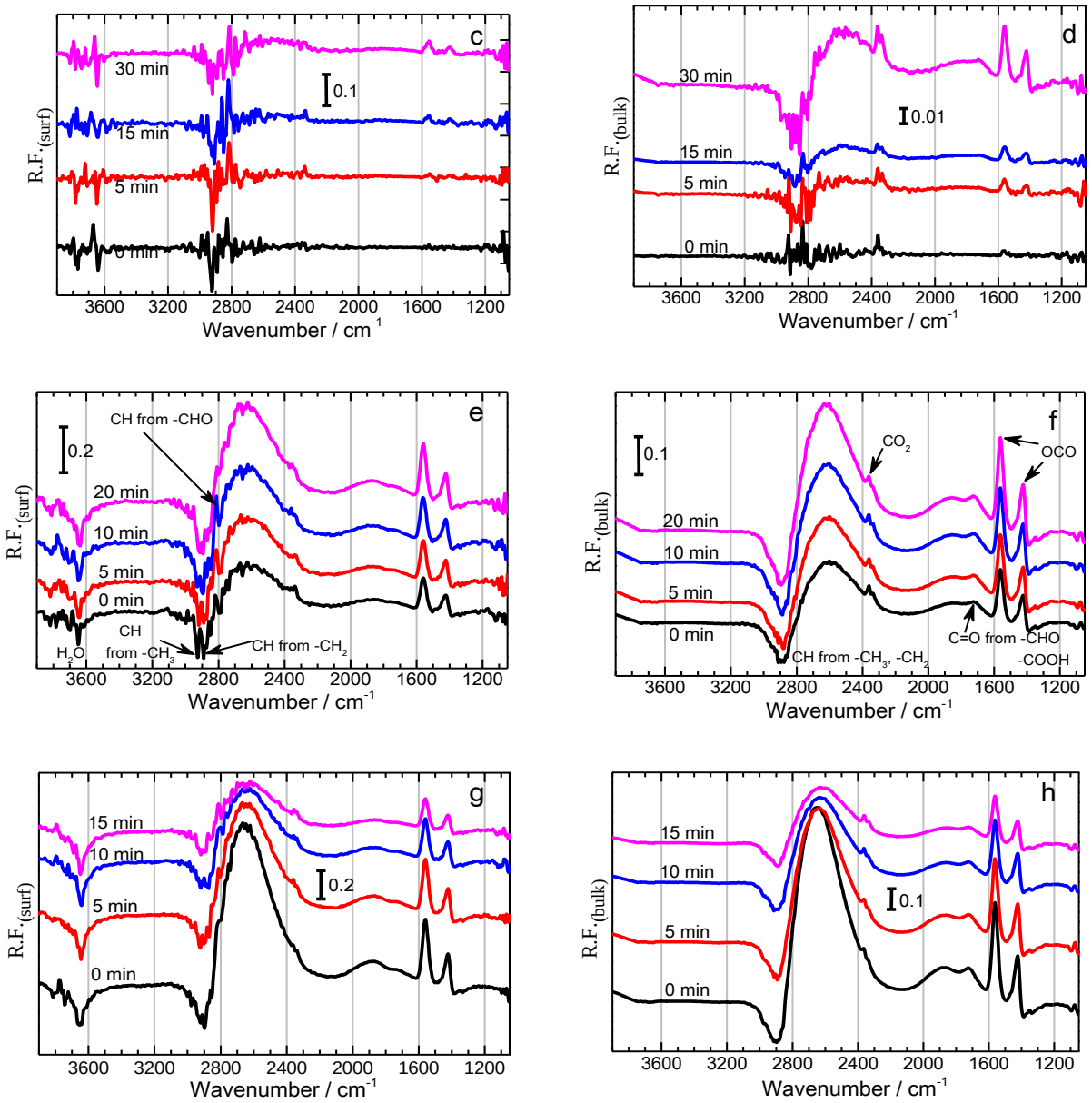

Figure 8.2: PM-IRRAS spectra for ethanol electrooxidation products on Pd/C nanoparticles in 1M (KOH + C_2H_5OH) at 0.21 V (a, b), 0.56 V (c, d), 0.72 (e, f), and 0.96 V (g, h) vs RHE. The left panels show oxidation species on the surface and the right panels show oxidation species in the thin-cavity/bulk solution. The spectra were processed using equation 3 and the reference spectrum was collected at the open circuit potential, see SI for details. At each potential (row), the y-scale was made the same for easy/direct comparison between surface and bulk species.

Figure 8.2 (c) and (d), shows the surface and bulk solution species at 0.56 V/RHE, which is closer to the onset potential for ethanol electrooxidation. The surface species spectra look very noise compared with the bulk solution spectra. This phenomenon can be attributed to the dynamic activities taking place on the electrode surface at this potential. Of top interest at this

potential, is the evidence of the C–C bond cleavage to form CO_2 due to the positive peak at 2353 cm^{-1}. With the PM-IRRAS we were even able to distinguish that the produced CO_2 quickly desorbs/diffuses into the bulk solution as shown by the intensity of the peak. The conversion of CO_2 into carbonate was not evident (see Figure A4-3) in this work probably due to the changing pH conditions within the thin-cavity from alkaline to neutral/acidic.[67] One can notice that while the amount of CO_2 increases clearly with time at lower potential (0.56V), its accumulation is hampered or overshadowed by other species at higher potential. Although, the formation of CO during EOR on Pd in alkaline has been reported,[21] we do not have evidence to support that argument in our spectra even after SNIFTIR treatment of our data as claimed in ref 21. Our data collaborates well with other similar work in literature where CO was not observed.[12] Therefore, the formation of CO during C–C bond cleavage maybe regarded to be a very fast process as it is directly converted to observed CO_2 at the lower potentials.

The presence of positive peaks at 1560 cm^{-1}(strong), 1423 cm^{-1} (medium), and 1350 cm^{-1}(weak) on the surface and bulk solution spectra in Figure 8.2(c) to (h), corresponds to the asymmetric, symmetric, and C–H bending vibrations from the acetate (CH_3COO^-) produced during ethanol electrooxidation in agreement with other literature reports.[19,21,68] These peak assignments were confirmed with transmission infrared spectroscopy as shown in Figure A4-3 and the use DFT simulations as reported in Table 8.2. The simulated spectra in solution (continuum model) show the same three peaks (1558 cm^{-1}; 1410 cm^{-1}; 1334 cm^{-1}). The strongest peak is also the one at 1558 cm^{-1} and corresponds to the asymmetric COO^- vibrations. The corresponding symmetric mode vibrates at 1334 cm^{-1} and has the second highest intensity. Finally, the peak around 1410 cm^{-1} corresponds to bending modes of the CH_3 group and features only a weak intensity. The relative positioning of the weak C–H bending and strong COO^- symmetric stretch are inverted in the DFT computations compared to experiment. This has already been reported in the literature.[69] Depending on the functional,[70] the C–H bending and symmetric COO stretching frequencies are more or less mixed, leading to intensity redistributions between the C–H and COO modes, suggesting that anharmonicity should be accounted for. Due to the very high computational cost of such a treatment, this is, however, beyond the scope of this paper. The COO^- symmetric stretch is red-shifted in our computations by about 100 cm^{-1}.

Table 8.1: Normal modes (in cm^{-1}) for acetate in the region 1200-1600 cm^{-1} (i) as obtained experimentally (see Figure A4-4) (ii) as computed as a function of the number of water molecules that solvate the COO^- moiety in solution (iii) as computed for CH_3COO adsorbed on a Pd(100) slab.

	Species	COO^-_{Sym}	CH	CH	COO^-_{Asym}	Splitting/cm^{-1}
(i)	**CH_3COO,** exp	1423	1346		1560	137
(ii)	CH_3COO	1334	1400	1417	1558	224
(ii)	CH_3COO, H_2O	1337	1403	1417	1541	204
(ii)	CH_3COO, $2H_2O$	1353	1402	1418	1534	181
(ii)	CH_3COO, $3H_2O$	1353	1398	1416	1524	171
(iii)	CH_3COO@Pd(100)	1360	1408	1430	1477	117

The inclusion of explicit water (see Table 8.1) mainly affects the COO^- stretch vibrations, with the asymmetric and symmetric mode being red- and blue-shifted by 30 and 20 cm^{-1}, respectively. This improves the mode splitting from 224 to 171 cm^{-1} compared to the experimental 137 cm^{-1}. From Table 8.1, it is noticeable that the infrared spectrum of CH_3COO adsorbed on a Pd(100), the asymmetric vibration is also red-shifted by 80 cm^{-1} compared to the one of CH_3COO using a continuum model for the water solvent. In addition, the two other peaks are much weaker than in solution. Thus, the comparison of the DFT simulations and the PM-IRRAS spectra shows that the "surface" species signal obtained experimentally corresponds mainly to solvated species in the interfacial water zone.

There is a remarkable difference between surface species and bulk solution species in the regions 1620 – 2000 cm^{-1}, and 3648 cm^{-1} which also highlights the utility of PM-IRRAS technique. It is evident that the species absorbing at 1726 cm^{-1} is mainly available in the bulk solution but not on/or near the electrode surface. This peak corresponds to C=O stretching vibrations of an aldehyde/ketone or acetic acid. Our DFT simulations for acetaldehyde show a strong peak at 1720 cm^{-1} (C=O) but also two weak peaks between 1300-1400 cm^{-1} (C–H bending), overlapping with the weaker peaks of acetate and one strong peak at 2812 cm^{-1} (C–H stretch), overlapping also with a broad band centered around 2600 cm^{-1}. The origin of the broad peak at 2600 cm^{-1} would be due to accumulation of combination of various intermediates (ethoxy, acetaldehyde & its hydrate form, and acetic acid) in the thin-cavity as shown in Figure A4-4. Figure A4-4a shows the simulated spectra for ethoxy (CH_3CH_2O), acetaldehyde (CH_3CHO), hydrated acetaldehyde (CH_3CHOOH), and acetic acid (CH_3COOH), which confirms that ethoxy and hydrated acetaldehyde have bands near 2600 cm^{-1}. Although, the simulated

spectrum for acetic acid [Figure A4-4(a)] does not show any peak between 2400 cm^{-1} and 2700 cm^{-1}, the experimental spectrum [Figure A4-4(b)] shows that acetic acid has three overlapping peaks within the region. Therefore, the potential candidates for the broad peak at 2400 – 2700 cm^{-1} would be ascribed to a combination of ethoxy, geminal-diol, and acetic acid as a result of the changing pH during the electrooxidation. Further studies are underway to confirm the true origin of this broad peak centered on 2600 cm^{-1}. The absence of the peak at 1726 cm^{-1} on the surface spectra is probably due to the low concentration of acetaldehyde and/or its interaction with the electrode surface. The negative peak at 3648 cm^{-1} on the surface species spectra is the evidence for the consumed water molecules at the electrode surface. Note that at higher potential, i.e., 0.96 V, where the catalyst surface is deactivated, the products accumulation decreases with time but no evidence for the formation of CO_2. This observation proves that acetate is indeed the dead end for EOR in agreement with the acetate CV in Figure 8.1 (a). Therefore, the cleavage of C–C bond is only possible at lower potentials.

To sum up, the PM-IRRAS spectra show that at lower potential it is possible to break the C–C bond of ethanol on Pd/C in alkaline media to form CO_2. However, the selectivity is poor due to competition towards the formation of acetate, which gets worse at higher potentials. In addition, traces of acetaldehyde are found in the bulk solution. Based on these experimental insights, we now explore the most likely intermediates involved in the reaction path using DFT calculations as presented in the next sections.

8.3 Reaction mechanism

The reaction network involved in ethanol electro-oxidation is quite complex as presented above, even after simplifying it by considering only proton coupled electron transfers as electrochemical steps. There are 12 electrons to be recovered through 9 proton abstractions and 3 OH additions. Our simulations do not include explicitly the influence of the water-based electrolyte on the intermediates structures. However, the main determining factor is the role of OH^- as a proton acceptor on the thermochemistry, and this is included in the computational hydrogen electrode approach.

Furthermore, the reaction only proceeds to completion if the C–C bond can be broken. Hence, we need at least to consider the following elementary reaction steps, with specific examples given for illustration in equations 8.1 – 8.4:

C–H scission:	$CH_3CH_2OH@Pd + OH^- \rightarrow CH_3CHOH@Pd + e^- + H_2O$	8.1
O–H scission:	$CH_3CH_2OH@Pd + OH^- \rightarrow CH_3CH_2O@Pd + e^- + H_2O$	8.2
C–OH formation:	$CH_3CHOH@Pd + OH^- \rightarrow CH_3CH(OH)_2@Pd + e^-$	8.3
C–C scission:	$CH_3CH_2OH@Pd + Pd \rightarrow CH_3@Pd + CH_2OH@Pd$	8.4

To break up the complexity into smaller manageable parts, we proceed as follows: PM-IRRAS data demonstrates that the electrooxidation of ethanol over Pd leads to identifiable acetate and traces of CO_2. Therefore, for simplicity, we start by studying the intermediates that lead to acetate on the dominant Pd(111) and the more reactive and still sufficiently abundant Pd(100) surface. A brief description of the geometric features can be found in appendix B, we discuss here their relative energies and the most likely reaction pathway until acetate. Then, in order to obtain a "complete" picture, we have searched the most stable C_1 and C_2 intermediates at each oxidation state until CO_2. Based on this overview, we shed more light on the reason why the reaction stops at the acetate level and why the selective cleavage of the C–C bond is difficult.

8.3.1 From ethanol to acetate

Pd(111): In appendix Figure A4-5 shows the adsorption structures of the most important intermediates involved in ethanol electrooxidation on Pd(111). The structures are in line with the literature [71] and thus we focus here on the relative energies of the intermediates at a given oxidation state and their involvement in the oxidation path towards acetic acid. Figure 8.3(a) shows the reaction energy profile for ethanol oxidation on Pd(111) at a potential of 0.26 V, based on the computational hydrogen electrode.[7] This potential corresponds to the thermodynamic equilibrium potential for the oxidation of ethanol to CO_2. In reality, over-potentials are necessarily observed but with only 0.4 V, Pd is rather promising in terms of onset potentials. Each column in the reaction coordinate corresponds to intermediates at a given oxidation state. Intermediates below and above the dotted line are due to exothermic and endothermic processes, respectively. The ethoxy (CH_3CH_2O) species is higher in energy than the α-dehydrogenated intermediate CH_3CHOH in agreement with previous reports.[71] However, Hibbits and Neurok [30] have modelled the oxidation of EtOH by O_2 in which the catalyst surface was pre-covered with O and O–H species and have shown that the formation of ethoxy has the lowest activation barrier in these conditions, proving that it is an important intermediate. The CH_2CH_2OH is intermediate in energy.

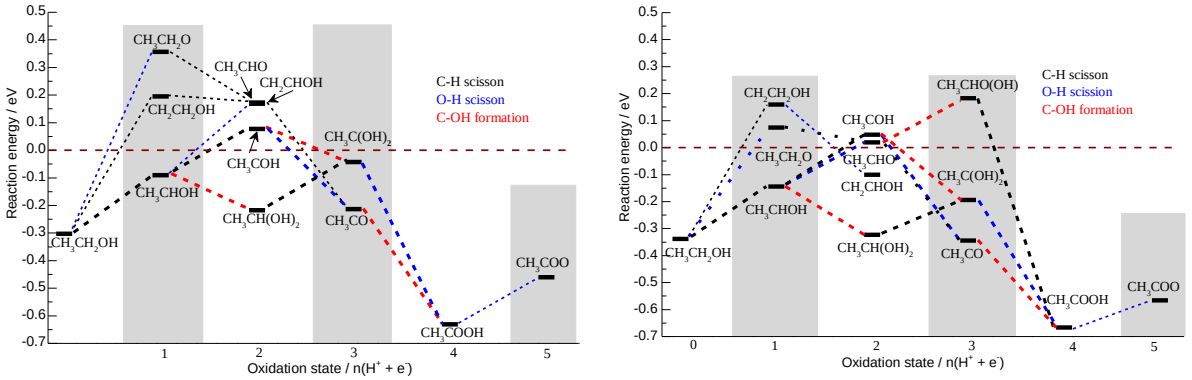

(a) Pd(111) (b) Pd(100)

Figure 8.3: Reaction energy profile for ethanol oxidation on (a) Pd(111) surface and (b) Pd(100) surface at a potential of 0.26 V vs RHE. Only the most important (and low lying) intermediates are shown. The dotted line connecting the intermediates are color coded according to the reaction process taking place, black and blue correspond to C–H and O–H bond scission, respectively while red corresponds to C–O bond formation

A second proton coupled electron transfer leads to an oxidation state which is particularly challenging to describe realistically: three adsorbed intermediates are connected through well-known solution equilibria: acetaldehyde, its hydrate (the geminal diol) and the enol; the forth intermediate considered (CH_3COH) is strongly bound to the metal surface and can only indirectly participate in the equilibrium.

On the surface, acetaldehyde and its enol are almost iso-energetic. Since the CH_2C_x intermediates at the following oxidation states are significantly higher in energy than the CH_3C_x intermediates, we consider the enol to be a dead end, i.e., it just participates in the equilibria if formed. In fact, it is rather the hydrate which is the dominant intermediate: it is the lowest energy intermediate is connected to the previous lowest energy intermediate and can form either in solution through acetaldehyde or on the surface by a surface O–H assisted process.

The oxidation of the hydrate does not lead to the lowest energy intermediate at oxidation state +3. The lowest energy intermediate at oxidation state +3 is the acetyl (CH_3CO) and it is only accessible from higher energy intermediates of the previous oxidation state +2. Oxidation of CH_3CO or $CH_3C(OH)_2$ invariably yields acetic acid, through a O–H addition and a dehydrogenation, respectively. Acetic acid is by far the lowest energy intermediate on the surface at oxidation state +4 (the second lowest fragment is CH_2CO at 0.86 eV higher in energy), and can desorb easily into solution. Then, in alkaline solution the formation of CH_3COO^- is straightforward. This reaction network explains satisfactorily the observed formation of acetic acid (or acetate at high pH values). After a quick comparison of the acetic acid formation on the

Pd(100) surface, the following sections investigate the prospects to split the C–C bond in ethanol.

Pd(100): Figure A4-6 (appendix) shows the adsorption structures of the most important intermediates involved in ethanol electrooxidation on Pd(100). The geometry of the adsorbates is very similar to that on Pd(111) and is therefore not discussed any further. Figure 8.3(b) shows the reaction energy profile for ethanol electrooxidation on Pd(100) surface at a potential of 0.26 V. Here we highlight the differences between Pd(100) surface and Pd(111). One difference is that the reaction energies are shifted to lower energies by ca. 0.1 – 0.2 eV, meaning that the (100) surface is more reactive than the (111) surface in agreement with previous reports.[72–74] The second difference is that the relative stability of acetaldehyde (CH_3CHO) and 1-hydroxyethylidene (CH_3COH) is reversed: on the 100 surface, CH_3CHO is 0.02 eV more stable than CH_3COH. However, it is doubtful that these very small energy differences are representative of the situation under electro-catalytic conditions where the solvent and the potential may easily change the relative energies by more than this difference. In any case, the geminal-diol is the lowest intermediate at this oxidation state for both surfaces. Therefore, we can conclude that investigating the Pd(100) or Pd(111) surface is qualitatively the same. Nevertheless, since the (100) surface is more active for bond formation and splitting reactions,[74] and these reactions are key and highly activated on this surface (*vide infra*), we report only the results for Pd(100) in the remainder of this article. Based on our DFT results, we can also predict the over-potential to produce CH_3COOH from EtOH on Pd catalysts and this over-potential is in agreement with the onset potential observed experimentally.

The lowest energy path is represented at various potentials in Figure 8.4. It starts with the generation of CH_3CHOH, an endothermic step at 0.26 V. It yields the gem-diol $CH_3CH(OH)_2$ at the degree of oxidation +3 that is further dehydrogenated into $CH_3C(OH)_2$, a step that is also endothermic at this potential. The last step is strongly exothermic and gives CH_3COOH. At 0.45 V, all the steps along the most stable path to CH_3COO^- are predicted being endothermic. At that potential, even the generation of acetaldehyde starts to be exothermic. Those potentials are in line with our experimental results (CV in Figure 8.1 and the PM-IRRAS spectra in Figure 8.2) where the reaction starts at around 0.45 V and where traces of acetaldehyde are identified at 0.65 V/RHE and more intense at 0.72 V.

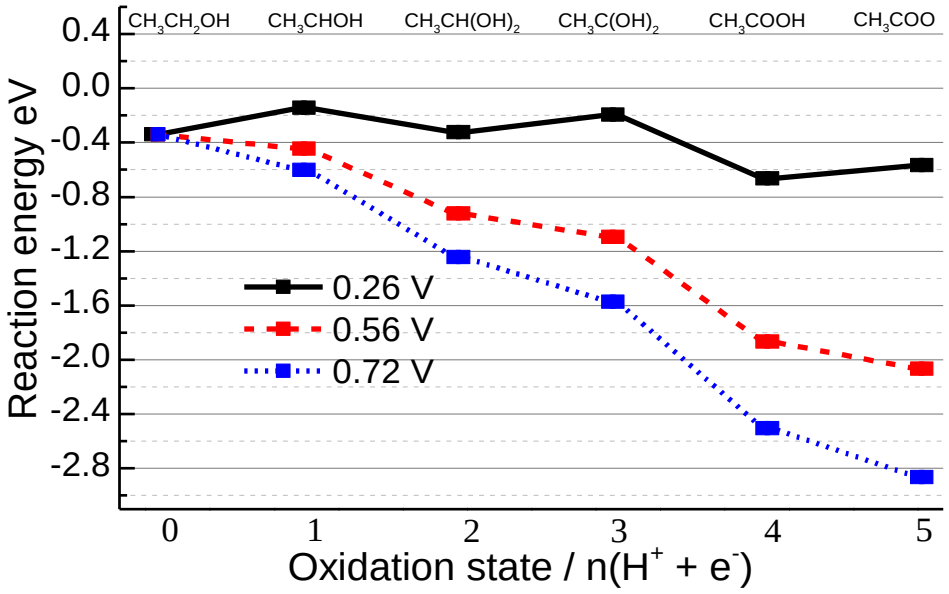

Figure 8.4: Reaction energy profiles for ethanol electrooxidation on Pd(100) surface showing the effect of the electrochemical potential (0.26 V, 0.56 V, and 0.72 V vs RHE) for the most likely C2 reaction path.

8.3.2 Intermediates beyond Acetate and Breaking the C–C bond

The chemical viability of DEFCs relies on two related aspects. First, the fuel needs to be completely oxidized in order to obtain a realistically useful energy and current density. In other words, catalysts oxidizing ethanol to acetate (acetic acid in acidic media) are not useful in practice, as they would liberate only 4 out of 12 possible electrons. Second, the kinetics needs to be efficient at a reasonably low over-potential. According to the Butler-Volmer equation, a proton coupled electron transfer is directly accelerated by the over-potential. Furthermore, the barriers for formal dehydrogenation reactions are fairly small on Pd (in the order of 0.7 eV). While the C–OH formation could be somewhat more activated, it can equally be considered an electrochemical step and therefore its barrier is likely to be heavily lowered by the over-potential and the presence of surface hydroxyls. If the C–C dissociation were coupled with the formation of the C–OH bond, in a concerted mechanism with the hydroxide anion attacking from the solvent, this dissociation would also strongly depend on the electrochemical potential. However, modeling such a process would require a full description of the solvent and a complete inclusion of the electrochemical potential, which is out of the scope of this study. The direct C–C bond splitting, in contrast, is a chemical step and thus hardly affected by the electrochemical potential as extrapolated from our findings for the electro-carboxylation of ethene.[75] Hence, investigating

the feasibility of C–C bond splitting is key in order to understand both, incomplete oxidation and sluggish kinetics and this can be done without the inclusion of the electrochemical potential.

Let us start by addressing the first question: which is the most likely possible path that would lead from ethanol to CO_2 instead of acetic acid based on thermodynamics? Figure 8.5 summarizes our effort to identify the lowest energy intermediates at each of the 12 oxidation states, accounting for C–H, O–H and C–C bond activations as well as C–OH bond formation. The intermediates below the zero horizontal dashed line in Figure 8.5 are due to an exothermic process while those above the line are due to an endothermic process at the potential of 0.26 V, i.e., the minimum potential for which ethanol oxidation is energetically feasible in terms of free energy.

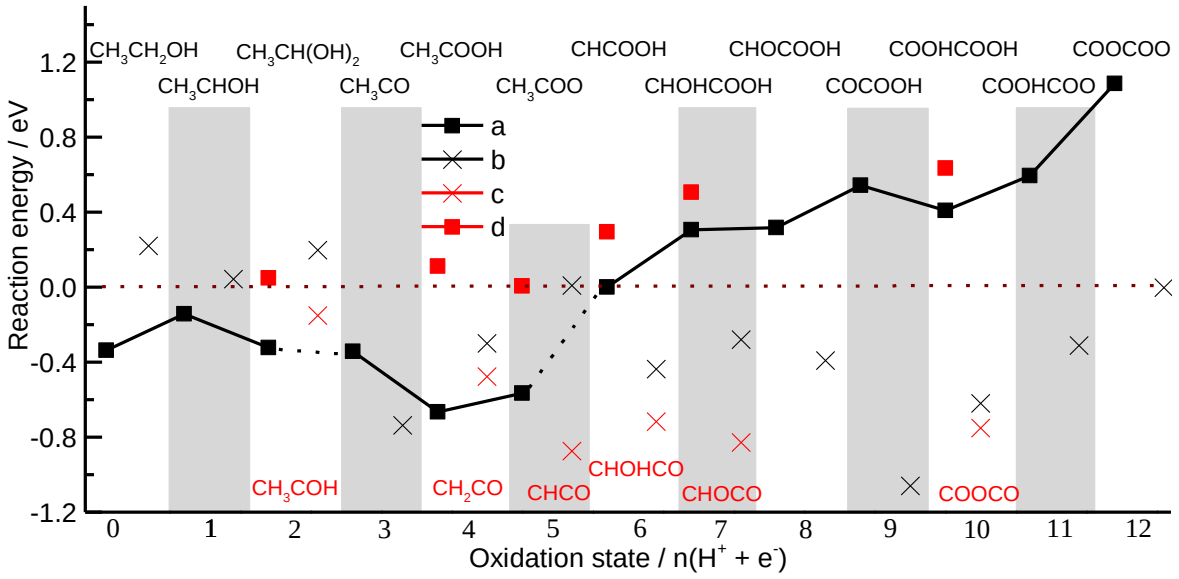

Figure 8.5: Global reaction energy profile of the most stable intermediates during ethanol electrooxidation process on Pd(100) at 0.26 V/RHE. The black squares show the most stable C2 intermediates at each oxidation state (C_2 path) whose intermediates are indicated at the top. To guide the eyes, a line has been added, in solid (resp. dotted) when the intermediates are connected (resp. not) from one oxidation state to the next. Legend: (a) Most stable C2 species, (b) C1 fragments generated from the most stable C2, (c) Most stable C1 fragments, and (d) Parent C2 species of the most stable C1 fragments which are shown at the bottom.

At each oxidation state we indicate the most stable C_2 intermediate and the energy of its C–C bond broken C_1 analogue. Of course, at any given oxidation step, the lowest intermediate before the C–C bond breaking does not need to yield the lowest two C_1 fragments at that oxidation step, which is indicated by the presence of open circles on Figure 8.5. Note that we did not consider

additional "pure" chemical steps which further complicate the reaction network, e.g. by introducing formic acid (HCOOH) at the same oxidation state as CO. Similarly, the lowest energy intermediate at each oxidation state “n” is not necessarily directly related to the intermediate of oxidation state “n+1” (e.g., $CH_3CH_2(OH)_2$ is the most stable intermediate at oxidation state +2, but at +3, it is CH_3CO), which is indicated by broken black lines instead of the full lines.

As mentioned in the introduction, ethanol electrooxidation mechanism is best presented in a “dual path mechanism scheme”. The C_2 path does not involve the breaking of the C–C bond while in the C_1 the C–C bond yielding C_1 fragments. In agreement with previous reports,[31] we found a reasonably well-connected C_2 pathway up to CH_3COO (+5). However, from +5 to +6, the lowest energy intermediate changes dramatically from CH_3COO to CHCOOH. Furthermore, the process is endothermic by 0.6 eV at the thermodynamic equilibrium potential for the overall reaction. This implies that a potential of at least 0.6 V would be necessary to drive the oxidation beyond acetate (acetic acid). The fact that these intermediates are not connected would mean a further increase of the over-potential. This is in agreement with the cyclic voltammetry experiments demonstrating that acetic acid is inert for further oxidation, i.e., no current transfer was observed in the CVs with 1M ($KOH+CH_3COOH$) solution as shown in Figure 8.1(a). To conclude, Figure 8.5 indicates that it would be ideal to split the C–C bond before reaching acetate (acetic acid in acid media), which is the dead end of the reaction with the current catalysts. On the other hand, on thermodynamic grounds, the C–C bond splitting is "constantly" beneficial from oxidation state +6 onwards and, in general, passing to the C_1 pathway is more likely when the C_2 fragment can be split through a de-carbonylation, generating a highly stable CO moiety.

Turning to the second limitation, i.e., the sluggish kinetics, we investigate the reasons for which the C–C bond is not split before reaching acetic acid. Both for ethanol and for the first oxidative intermediate, the C–C bond breaking is highly unlikely as the thermodynamics are fairly unfavourable. However, at oxidation state +2 and +3 the breaking of the C–C bond could occur based on thermodynamic grounds. So why is it barely observed experimentally? To answer this question, we have identified transition states for breaking the C–C bond in the key intermediates at oxidation state +2 and +3 (Figure 8.6).

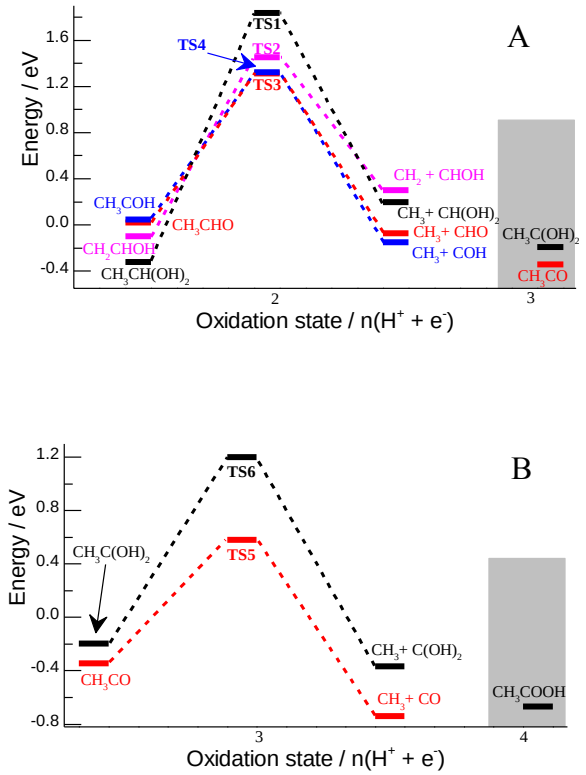

Figure 8.6: Energy profile for breaking the C–C bond on Pd(100) for species at oxidation state two (A) and at oxidation state three (B), both at 0.26 V vs RHE.

The first, general observation is that the activation energies are quite high with about 1.3 eV, even on the Pd(100) surface which is more active than the Pd(111) surface. There are two barriers that differ significantly from this number. First, is the highest activation barrier for breaking the C–C of the hydrate, $CH_3CH(OH)_2$ (oxidation state +2) ($E^{\ddagger}$ = 2.1 eV). This large barrier is probably due to the fact that the carbons of the reactant are not interacting with the catalyst surface, hence they are not activated. Besides, the steric crowding which destabilizes both the transition state and the product, barely affects the reactant, which does not adsorb through a carbon atom but rather through the two lone-pair of electrons of the oxygen atoms. In support of this argument, we find that the energy barrier for the dehydrogenated geminal diol is significantly lower (1.4 eV).

In this case, the steric crowding in the reactant and product is similar, as both adsorb through the unsaturated carbon atom hence benefiting from less destabilization. Second, the lowest barrier for breaking C–C bond is found for acetyl (CH_3CO) with activation energy of "only" 0.9 eV, which is attributed to the very stable CO product on Pd surface. Note, however, that this is

still a significant barrier at room temperature that cannot be lowered by the application of potential. Furthermore, the C–C splitting is in competition with the thermodynamically favorable C–OH bond formation that yields acetic acid. Playing on the structure of the catalyst, one may favor the C–C bond splitting since this is a structure-sensitive reaction that is favoured on low-coordinated facets: the C–C bond splitting in CH_3CO drops from 1.4 eV on Pd(111) [76] to 0.9 eV on Pd(100) and 0.7 eV on Pd(110).[77]

The reaction selectivity towards acetic acid is better understood from the aforementioned reaction energy profiles, keeping in mind the C–H and O–H bond breaking in ethanol catalyzed by Pd have a barrier lower than 0.8 eV.[78] These steps can be even further activated by the presence of surface hydroxyls as shown in previous DFT studies.[30,31] The thermodynamic impact of the recombination of H^+ and OH^- is, however, also included in our present study through the use of the computational hydrogen electrode. At oxidation state +2 the most stable intermediate (the gem-diol $CH_3CH(OH)_2$) does not undergo C–C splitting ($E^‡$ = 2.1 eV) and also higher lying intermediates only react slowly towards C_1 products and face a strong competition with C–OH bond formation. Hence, the hydrate gets oxidized, despite the fact that this does not lead to the lowest energy intermediate at oxidation state +3. At oxidation state +3, there are three processes in competition. In one process, the $CH_3C(OH)_2$ is quickly oxidized to acetic acid ($E^‡ < 0.8$ eV) and the C–C bond remains intact. In the second process, the most stable but kinetically less accessible intermediate CH_3CO, can undergo slow C–C bond splitting ($E^‡$ = 0.9 eV) and the fragments eventually be oxidized to CO/CO_2. In the third process, CH_3CO can be oxidized to acetic acid as explained above, which is an electrochemical process that is favoured by oxidative potentials. In other words, the necessary potentials and the unfavourable "connection" between the most stable intermediates lead to the dominance of acetic acid as a product and to the small probability of splitting the C–C bond at an early stage of the oxidation process. These results show how challenging and complex it is to design a catalyst for complete electrooxidation of ethanol to CO_2.

8.3.3 Proposed ethanol electrooxidation mechanism

In this section, we summarize the reaction scheme that results from our joint experimental and theoretical study as shown in Figure 8.7. Ethanol is converted to acetaldehyde by oxidative dehydrogenation on Pd. This is a two-step processes that has been studied in details by DFT

simulations including co-adsorbed species and water solvent [30] To be able to screen a much larger part of the reaction network of ethanol electrooxidation into CO_2, we had to simplify our model to a Pd/vacuum interface.

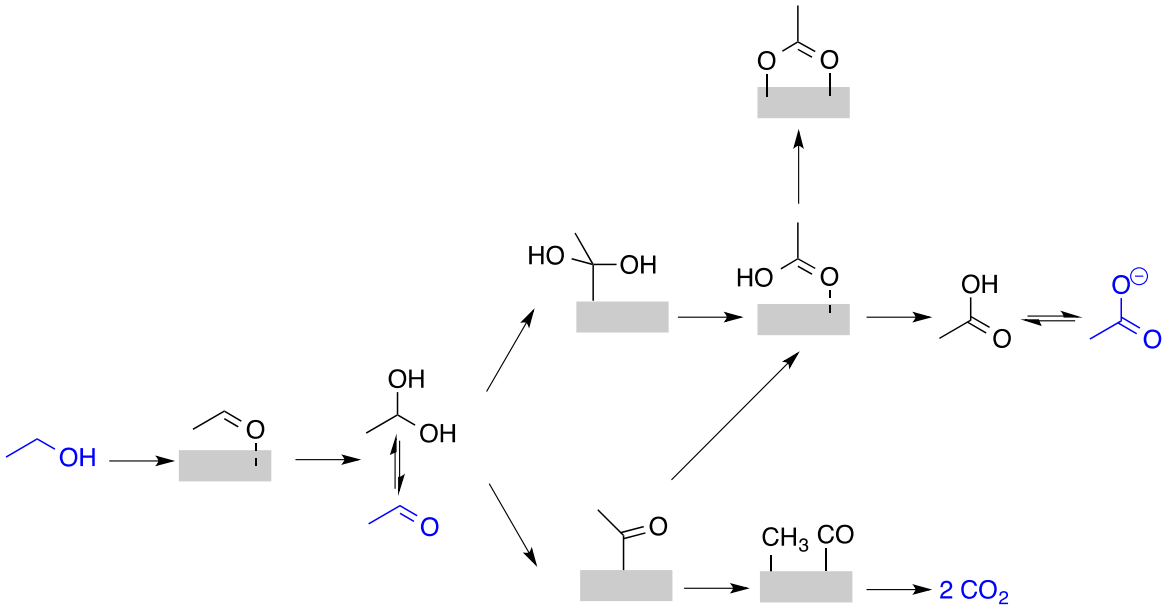

Figure 8.7: General Reaction Scheme based on our results. In blue, the experimental evidences. In black are the intermediates as suggested by our DFT simulations. Most of the steps are catalyzed by the Pd electrode (single arrows) while others are solution equilibria (two one-sided arrows).

The effect of the co-adsorption of water are not included but expected to be negligible on the relative energies.[79,80] Indeed, even if the details differ, our study leads to the same conclusion at oxidation state +2: acetaldehyde is in equilibrium with its hydrate, the gem-diol. And acetaldehyde is seen in the bulk solution by PM-IRRAS. Then, two routes are in competition. First, the gem-diol is the most stable adsorbed species at its degree of oxidation. The α-C–H bond breaking is particularly facilitated in electrochemical conditions and leads to $CH_3C(OH)_2$ that easily yields acetic acid. In the second route, acetaldehyde is dehydrogenated into acetyl, CH_3CO. Since acetaldehyde is less stable on the surface than its gem-diol, this route is disfavoured. However, the acetyl is a pivotal intermediate. Its degree of oxidation is the first along the path where the key C–C bond scission can occur exothermically from the most stable C_2 fragment. Moreover among all the intermediates of degree +2 and +3, it is the one that exhibits the lowest activation barrier for the C–C bond scission (0.9 eV). Hence, even though a chemical step, CH_3CO decarbonylation could compete with the C–H, O–H and C–OH

rearrangements that are facilitated by the electrochemical potential. Thus, the CO_2 traces we have observed experimentally at low potentials by PM-IRRAS are probably generated from adsorbed acetyl. This is in line with the ATR-SEIRAS experiments of Yang *et al*.[19] However, the acetyl can also easily lead to acetic acid by the formation of a C–OH bond, a process that is accelerated by oxidative potentials. This explains the experimental observation that the selectivity towards CO_2 decreases at higher potential.

In summary, the C–C bond scission that is essential to open the route to a full oxidation of ethanol can occur at the degree of oxidation +3. However, it is a slow process and in competition with the faster oxidation to acetic acid. For degree of oxidation > +5, the C–C bond splitting is exothermic, opening the road to the C_1 pathway. However, there is a strong disconnection on the C_2 pathway between the most stable species at degree +5 (CH_3COO) and the most stable species at degree +6 (CHCOOH) that hinders the oxidation of acetate (Figure 8.5), in line with the experimentally observed impossibility to oxidize acetic acid in KOH under our conditions (Figure 8.1).

8.4 Conclusion

We have presented a comprehensive study of the reaction mechanism of ethanol electrooxidation over Pd surfaces, combining cyclic voltammetry, chronoamperometry, PM-IRRAS, and DFT calculations. The PM-IRRAS information (identification of surface and bulk solution species) simplified the number of possible intermediates considered in the DFT modelling, while DFT insights provided invaluable information of the elementary reaction intermediates and kinetic parameters, which was not accessible experimentally. This strategy can be easily extended to other alcohols or organic molecules on other metal surfaces.

In this work, we have solved two of the long debated puzzles: the path leading to the formation of acetate, the product obtained over a Pd catalyst in alkaline conditions and the most likely intermediates where the C–C bond can be broken. For the formation of acetic acid, we have identified two converging paths: the most stable path, going through the gem-diol (hydrate of acetaldehyde), and the second most stable path going through the acetyl (CH_3CO). Unfortunately, acetate cannot be oxidized further over Pd according to our CV and DFT results, closing the door to the C_1 path and thus the complete oxidation of ethanol. Hence, to contribute to the second debate, we have determined the most likely intermediates where the C–C bond can

be broken before reaching acetate. We have demonstrated that acetyl (at oxidation state three) has by far (>0.3 eV) the lowest activation energy for the C–C bond breaking ($E^{\ddagger}$ = 0.9 eV). However, the over-potentials required for reasonable current densities are strongly accelerating the electrochemical oxidation process. This favours the C–OH formation over the C–C splitting reaction. Therefore, CH_3CO is quickly oxidized to acetic acid, thereby suppressing the C–C bond breaking, explaining the negligible amount of CO_2 detected at higher potentials. In other words, CH_3CO plays a pivotal role since it can either undergo a C–C bond splitting, eventually yielding CO_2, or be oxidized towards CH_3COOH, a dead end in the reaction scheme. Through this analysis, our work has determined the conditions for a better selectivity towards CO_2: destabilize the gem-diol, stabilize the acetyl and facilitate its splitting into CH_3 and CO. A large descriptor-based search of catalysts is being started to find *in silico* alloy formulations that would obey to these conditions.

Supporting Information: The PM-IRRAS background/references, FTIR transmission spectra for KOH and KOH+ (acetic acid, sodium acetate, sodium carbonate, and ethanol), and most stable geometric ethanol oxidation intermediates structures are provided in appendix section 4.

Chapter 9: Computational Screening for Selective Catalysts: Cleaving the C–C bond during Ethanol Electrooxidation Reaction

Publication: E.A. Monyoncho, S. N. Steinmann, C. Michel, E. A. Baranova, T. K. Woo, and P. Sautet. – to be submitted

Abstract

Efforts towards rational design of efficient catalysts, requires the identification of activity and selectivity trends. In this work, we use DFT calculations to screen for the activity and selectivity trends for ethanol electrooxidation reaction (EOR) on 21 close-packed surfaces transition metals (Ag, Au, Cu, Cd, Co, Ni, Ir, Pd, Pt, Pb, Rh, Hf, Os, Re, Ru, Sc, Ti, Tl, Y, and Zn). In a previous study (ACS Catalysis 2016), we established that acetyl and acetate were the critical intermediate and product, respectively during ethanol electrooxidation on Pd/C in alkaline media. Therefore, herein we have generated a precedence list of metals for consideration in designing EOR catalysts based on adsorption and reaction energy descriptors (Table 1). From the screening descriptors it is evident that rational design of EOR catalysts requires the use of multi-metallic formulations such as bimetallic. We recommend a strategy which combines metals with high selectivity for acetyl formation (Ti, Hf, and Pt) with those favouring the C–C cleavage (Pd, Ni, Rh, Sc, Ir, Os, Ru, and Co). Note that these trends are based on the assumptions that the metals are in the metallic state and the electrolyte has no significant contributions. Therefore, it is necessary that in experimental testing the surface elemental composition and oxidation state of the catalysts is known to facilitate trends comparison with theoretical predictions. The insights presented in this work are expected to facilitate the rational design of catalyst beyond that of EOR.

Keywords: Catalyst design, ethanol electrooxidation, DFT, transition metals, reaction energies

9.1 Introduction

Ethanol is considered to be an ideal molecule for fundamental mechanistic studies for a number of reasons: i) the potential application as a carbon neutral fuel source for direct ethanol fuel cells,[1,2] ii) the potential use as a feedstock for value-added chemicals such as hydrogen through oxidation or steam reforming,[3] iii) it is a model molecule for the study of larger biomass-derived compounds such as glycerol and sugars.[4] Therefore, the catalytic activation of ethanol continues to be the subject of active experimental and theoretical study. Density functional theory (DFT) has been well used to for the study of ethanol decomposition on transition metals (TM).[5–12] These theoretical studies are mainly looking at ethanol decomposition mechanism either from steam reformation or electrooxidation perspectives. In steam reformation, ethanol is reacted with steam at high temperatures to produce hydrogen and other products while in electrooxidation, ethanol is reacted at an over-potential to generate electricity. Herein we are going to focus on the electrooxidation process. Before getting into the details of our study, we would like to highlight a few of the theoretical studies available in literature, which are closely related to our study.

Sutton *et al*. studied ethanol activation on seven close-packed metal surfaces (Co, Ni, Pd, Pt, Rh, and Ru) and focused on three aspects:[6] i) they used DFT calculations to identify common features and qualitative differences in the energetically most favourable decomposition pathways, ii) they examined the trends in the minimum adsorption and activation energies to identify qualitative descriptors for activity and selectivity, and iii) they developed BEP correlations that can be used for high-throughput kinetic models for ethanol activation on transition metals.

Tereshchuk *et al*. investigated ethanol and water adsorption on 12 close-packed TM surfaces (Fe, Co, Ni, Cu, Ru, Rh, Pd, Ag, Os, Ir, Pt, and Au) using DFT with van der Waals Correction.[7] They reported the adsorption properties of ethanol on these metals with and without van der Waals corrections but no reaction pathways were explored. Wang *et al*. modelled ethanol decomposition mechanism on 9 close-packed metals (Co, Ni, Cu, Rh, Pd, Ag, Ir, Pt, and Au) but from the reforming perspective.[8] However, they strangely modelled Co as fcc instead of the hcp structure.

Ferrin *et al*. used two scaling relations to map out the potential energy surface (PES) for ethanol decomposition, i.e., C–O and C–C bond breaking on ten close-packed metal surfaces

(Cu, Pt, Pd, Ni, Ir, Rh, Co, Os, Ru, and Re).[12] They used a simplified kinetic model to qualitatively predict trends in ethanol decomposition activity and selectivity on six of the metals (Cu, Pt, Pd, Ir, Rh, and Ru) which they compared with gas-phase heterogeneous experiments, which showed that Ru was the best for splitting the C–C bond among the metals they investigated. The authors predicted that the C–C bond cleavage happens on CH_2CO intermediate.

In our previous work, we have mapped out a detailed reaction mechanism for ethanol decomposition during electrooxidation at an applied potential of 0.26 V/RHE.[5] We combined experimental (polarization modulated infrared reflection absorption spectroscopy (PM-IRRAS)) and DFT insights to explain why it is very difficult to break the C–C bond during ethanol electrooxidation. We showed that acetyl is a critical intermediate from which the C–C bond can be activated. However, the strong electrochemical competition for acetyl oxidation to acetic acid (acetate in alkaline media) greatly limits the amount of CO_2 generated to less than 1% in favor of acetate formation for the case of Pd nanoparticles in alkaline media we looked at.

The aim of the current work is to use computations to screen for the best candidate transition metals for ethanol electrooxidation with emphasis on the selectivity towards breaking the C–C bond. The study focuses on acetyl and acetate, the key intermediate and product, respectively generated during ethanol electrooxidation in alkaline media. We identify the trends for cleaving the C–C bond on 21 close-packed TM surfaces (Ag, Au, Cu, Cd, Co, Ni, Ir, Pd, Pt, Pb, Rh, Hf, Os, Re, Ru, Sc, Ti, Tl, Y, and Zn). DFT computations for six adsorbates (C, O, CO, CH_3, CH_3CO, and CH_3COO) were done on all the 21 transition metals. This study is expected to facilitate the rational design of ethanol electrooxidation catalysts as well as provide the basis for explaining experimental observations.

9.2 Results and discussion

Recently, we mapped out the reaction paths for ethanol electrooxidation on Pd as shown in Figure 9.1, which presents the potential energy profile of the key intermediates involved at different oxidation stages.[5]

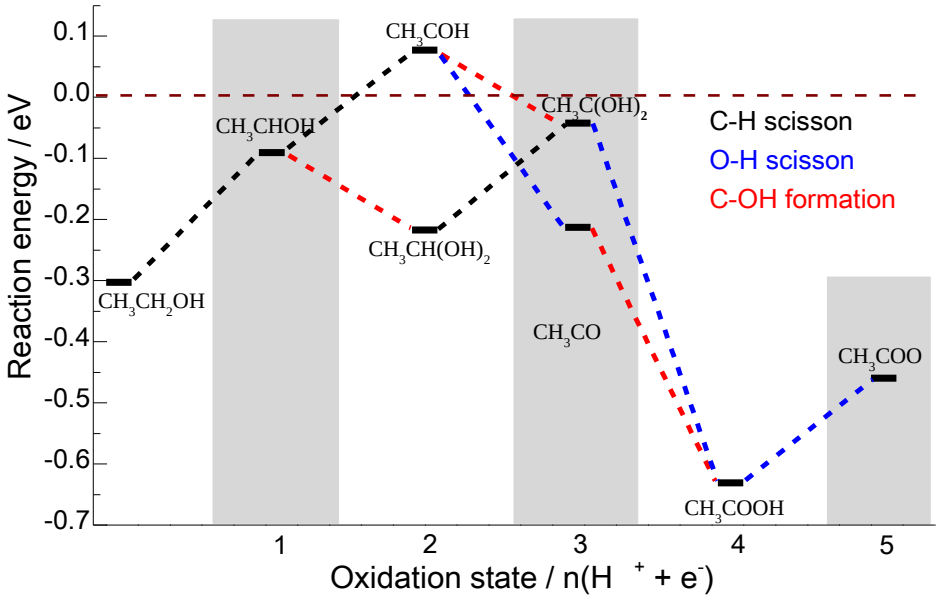

Figure 9.1: DFT Reaction energy profile for ethanol electrooxidation on Pd(111) at 0.26 V/RHE showing the intermediates involved at different oxidation states. Adapted from reference[5]

Two paths leading to the formation of acetic acid (acetate in alkaline media) are identified in Figure 9.1 at oxidation state 3. One pathway is via the acetyl group (CH_3CO) and the other is via the geminal diol ($CH_3C(OH)_2$). The most stable states are not connected between oxidation states 2 and 3. $CH_3CH(OH)_2$ cannot be turned into the acetyl in one single elementary step. This disconnection slows the reaction down and makes it challenging to elucidate the (competitive) reaction pathways. However, to break the C–C bond, we determined that the reaction selectivity has to be steered through the acetyl pathway, otherwise the reaction is stopped once acetate is formed, i.e., no effective catalysts for electro-oxidation of acetic acid in alkaline medium are known to us.[5]

In summary, the most important reaction intermediates/products and the key steps involved for ethanol electrooxidation on Pd(111) in Figure 9.1, can be condensed to a simple schematic shown in Figure 9.2.

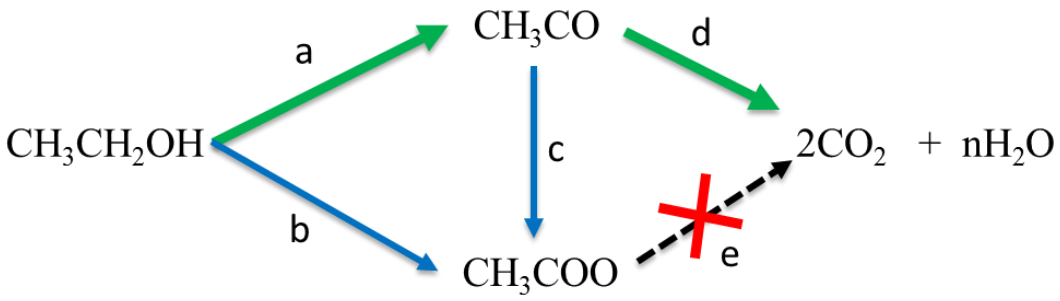

Figure 9.2: The simplified schematic of the most important intermediates and reaction paths for ethanol electrooxidation mechanism. The desired reaction paths are "a" and "d" but the acetate paths (b and c) are dominant which leads to a dead end. Path "e" is not possible with the current catalysts.

Our experimental data from PM-IRRAS revealed that acetate (paths b, and a → c) is dominant during ethanol electrooxidation on Pd/C nanoparticles but it leads to a dead end, hence no further oxidation to CO_2 and H_2O (path e).[5] Therefore, the CO_2 observed during ethanol electrooxidation experiments stems exclusively from the acetyl path "a → d". Unfortunately, acetyl is not energetically favorable on Pd surfaces (see Figure 9.1) and if formed it is readily oxidized to acetate, hence only a limited percentage can be fully oxidized to CO_2 and H_2O. Therefore, we would like to establish how acetate and acetyl interacts with other transition metal surfaces to determine which can better stabilize acetyl while destabilizing acetate during ethanol electrooxidation. Stabilizing acetyl on metal surfaces is expected to improve the reaction selectivity towards the path where the C–C bond can be broken.

9.2.1 Geometry and adsorption trends of Acetate and acetyl on transition metals

Figure 9.3 shows the binding mode geometries for acetate and acetyl on transition metal surfaces. The stable geometric configurations for acetate showed identical configuration on all the 21 metals, while acetyl showed three binding mode configurations depending on the metal surface (see Table A5-1 in appendix).

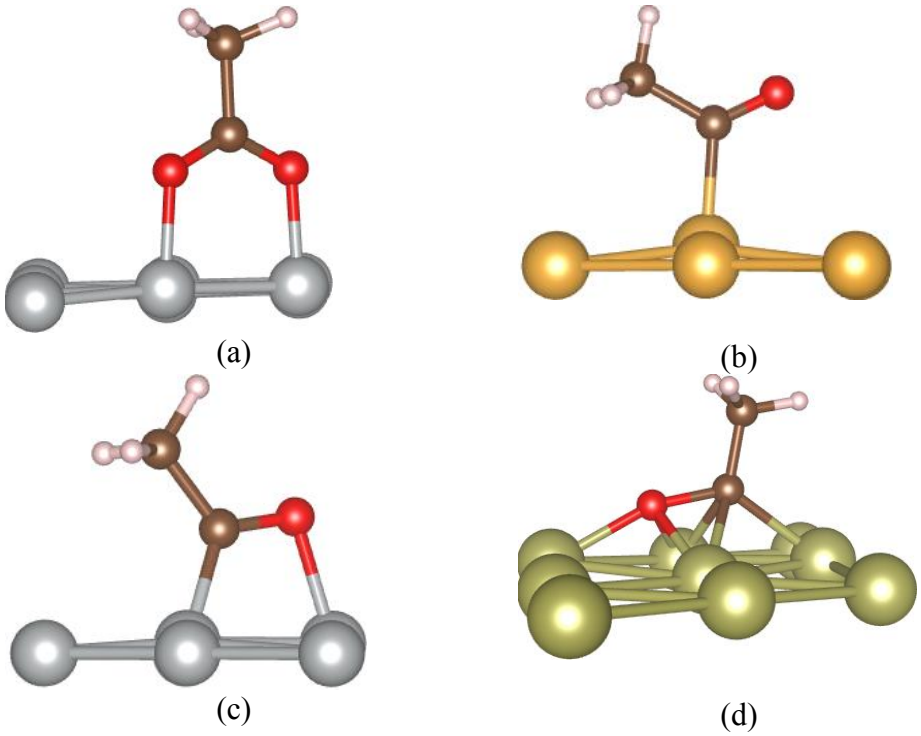

Figure 9.3: Geometry side views for (a) acetate. Acetate had same configuration on all metals. Acetyl had three different configurations depending on the metal surface such as (b) on Au, (c) on Ni, and (d) on Hf (See Table S1 and S2 for details).

Acetate was found to adsorb on metal surfaces exclusively via O atoms (Figure 9.3(a)), hence O binding energy was used as descriptor to screen for metals that can destabilize acetate. The results of the screening are shown in Figure 9.4. There exist a linear relation between acetate and O binding energies on all 21 transition metals. Au and Ag are predicted as the best metals to destabilize acetate because of their weak binding energies. On the other hand, acetyl was found to have three distinct adsorption modes depending on the metal as shown in Figure 9.3(c – d). Therefore, acetyl can bind with either C or both C and O. On most metal surfaces, acetyl binds via C as shown in Table A5-1 (appendix). Figure 9.5 shows the linear correlations observed for acetyl vs C binding energies on selected metal surfaces. Metals which showed strong interaction with acetyl such as Hf (Figure 9.4(d)) are not included in Figure 9.5 to allow comparisons of structures with similar binding modes.

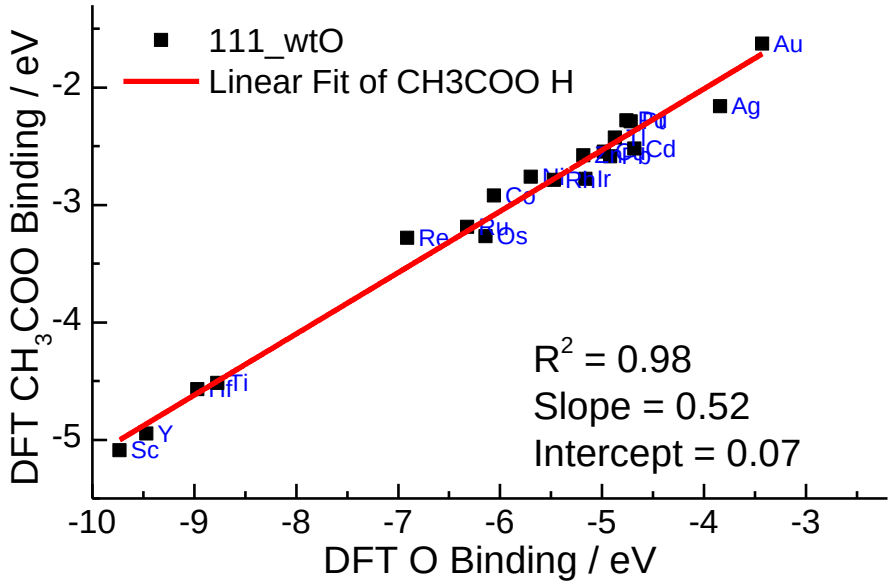

Figure 9.4: The linear relation between CH_3COO and O binding energies on metals. The weakly binding metals Au and Ag are predicted to be the best candidates to destabilize acetate.

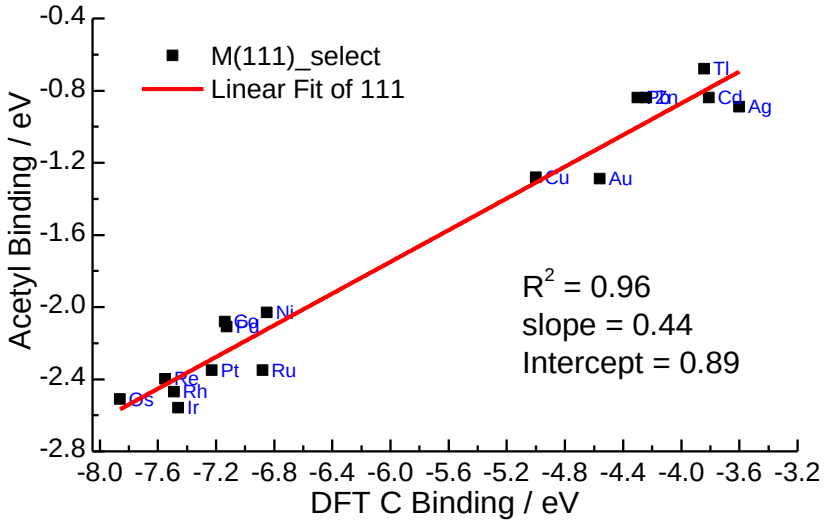

Figure 9.5: The linear relation between CH_3CO and C binding energies for selected metals with similar acetyl binding mode geometry configuration. Metals are divided into two main groups, i.e., stabilizing (bottom left corner) and less stabilizing (top right corner)

Figure 9.5, groups the transition metals into two categories; i) the bottom left corner metals (Os, Ir, Rh, Re, Pt, Ru, Pd, Co, and Ni) which favor acetyl stabilization, and ii) the top right corner metals (Cu, Au, Zn, Pb, Tl, Cd, and Ag) which are less favorable for acetyl stabilization.

From the adsorption energy trends we have identified that Os, Ir, Rh, Re, Pt, Ru, Pd, Co, and Ni favor acetyl stabilization while Au and Ag are ideal for acetate destabilization. Therefore, based on binding energy descriptors we have two sets of metals which can be combined in the rational design of catalyst. Now we would like to turn into reaction energy descriptor for further details.

9.2.2 **Ethanol reaction to acetyl and acetate trends on transition metals**

Figure 9.6 shows the reaction energies for the formation of acetyl and acetate from ethanol (equations (9.1) and (9.3), respectively) at an applied potential of 0.26 V/RHE for a series of metals.

$$CH_3CH_2OH + H_2O + M \rightarrow CH_3COO@M + 5\,H^+ + 5\,e^- \qquad 9.3$$

Because of the overlapping labels in Figure 9.6, the energy values are provided in Table A5-3 (appendix). Red lines are used in Figure 9.6 to group the metals into various groups for easy comparisons; i) the horizontal line divides the metals into those which are energetically "favorable" and "unfavourable" for acetate formation based on whether they are "below" or "above" the line, respectively. All the metals were found to be below the line with the exception of Au, meaning they favor acetate formation. ii) the vertical line splits the metals into those which are energetically "favorable" and "unfavourable" for acetyl formation based on whether they are on the "left side" or "right side" of the line, respectively. On this criterion, metals are grouped into three, i.e., most favorable (far left side), favorable (middle), and unfavourable (right side). iii) the diagonal line (y=x) compares the preference of the metals to form acetate or acetyl, metals below/right side favor acetate formation and vice versa. Using this criterion, only Ti and Hf favours acetyl formation while all the other metals favor acetate formation.

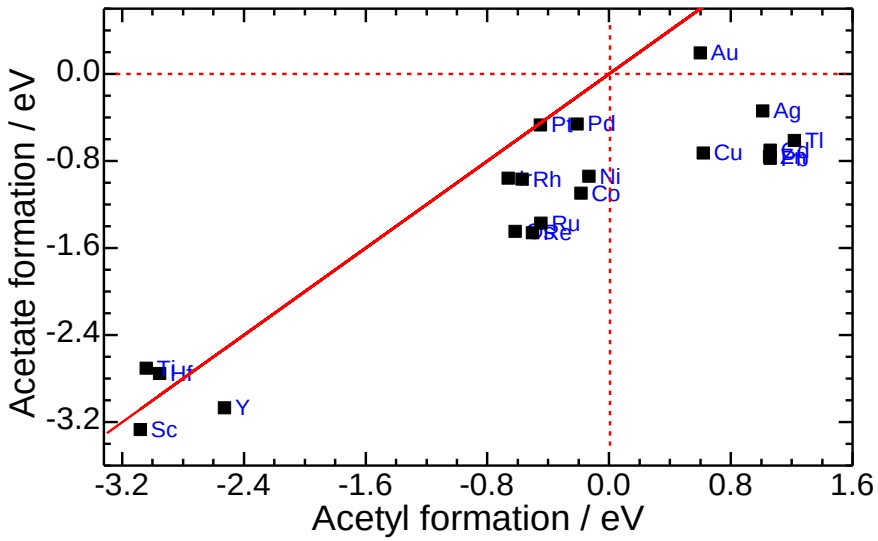

Figure 9.6: The reaction energies for the formation of Acetate and Acetyl from ethanol at 0.26 V/RHE. The positive slope relationship means the formation energy trends on the 21 close-packed transition metal surfaces are similar but acetate formation is more favourable than acetyl as shown in the graph.

This observation tells us that with the exception of Ti and Hf, no other metal can be used as the catalyst for ethanol electrooxidation by itself to favor acetyl reaction pathway. This is rather interesting because as mentioned above there are a number of metals which are capable of stabilizing acetyl on the metal surfaces. However, this finding helps to explain that the challenge of breaking the C–C bond is the selectivity of the reaction towards acetyl and not its stability on the metal surface.

The unfavourable situation for the stability of acetyl with respect to acetate is clearly illustrated when presenting the selectivity as a ratio between the reaction leading to acetyl and the one to acetate. Ideally, acetyl should be stabilized with respect to acetate in order to avoid the thermodynamic driving force towards this dead end. Therefore, we have decided to plot this ratio as a function of the C and O binding energies (E_C, E_O) as shown in Figure 9.7. $K_{rel} = \exp(-\Delta\Delta G/RT)$, where $\Delta\Delta G = \Delta G_{CH3CO} - \Delta G_{CH3COO} = 0.44\ E_C - 0.52\ E_O - 0.9$.

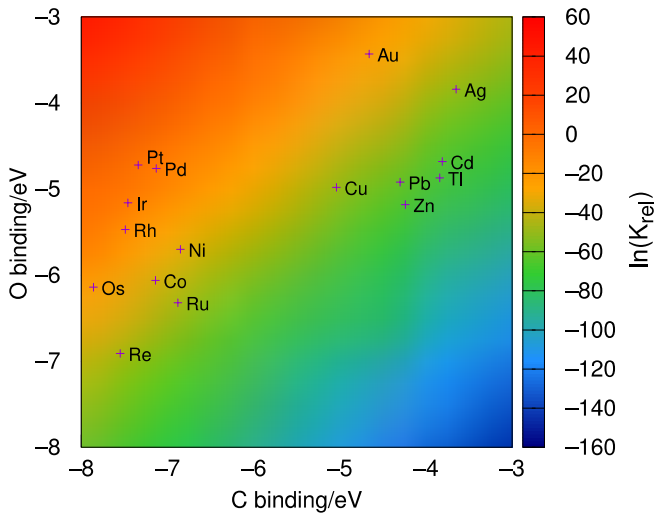

Figure 9.7: Selectivity between CH_3COO and CH_3CO, which are the preferred species for negative and positive values, respectively. The points for the investigated metals are indicated by crosses, based on their DFT computed C and O binding energies.

From Figure 9.7, we can say that the order of the best metal catalyst is Pt, Pd, Ir, Rh, Os, and Au. Similarly, the worst metals are Tl, Cd, Zn, and Pb.

9.2.3 Acetyl reaction selectivity towards acetate and C–C bond cleavage trends on transition metals

In this section, we zoom into the two main competing reactions which consume acetyl species during ethanol electrooxidation. Understandably, it is possible that acetyl would be forming other side products such as reacting with ethoxy species to form $CH_3CH(OH)OCH_2CH_3$, but we do not have experimental evidence of these other products in our previous work on ethanol electrooxidation on Pd/C in alkaline media.[5] Therefore, we are focusing on acetate formation and C–C bond cleavage reactions as shown in equations (9.4) and (9.5), respectively.

$$CH_3CO@M + H_2O \rightarrow CH_3COO@M + 2H^+ + 2e^- \quad 9.4$$

$$CH_3CO@M \rightarrow CH_3@M + CO@M \quad 9.5$$

Figure 9.8 shows the reaction energies for the two reactions at 0.26 V/RHE and the TS energies for breaking the C–C bond in (a) and (b), respectively. Figure 9.8(a) has red lines which divide metal activities into three major categories; i) metals below the horizontal line favor acetate formation from acetyl while those above do not. By this grouping we find that all metals are predicted to favor acetate formation with the exception of Ti and Hf. Interestingly, the same

metals were predicted to favor acetyl formation from ethanol compared to acetate. ii) metals on the left side of the vertical line favor C–C bond cleavage while those on the right do not.

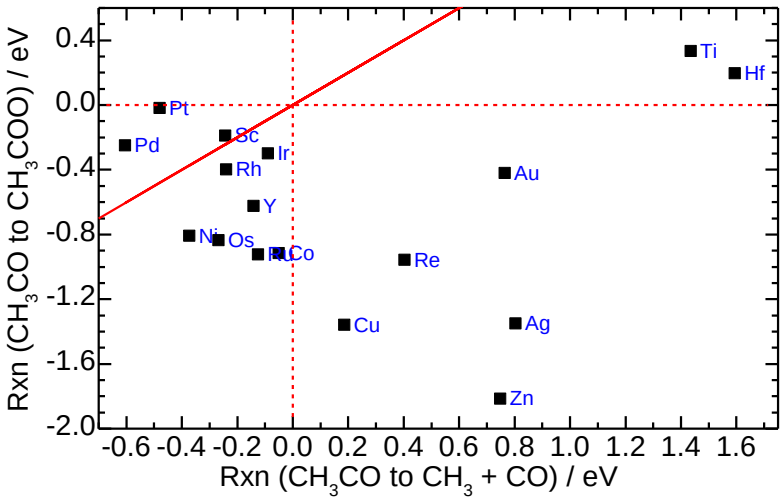

(a)

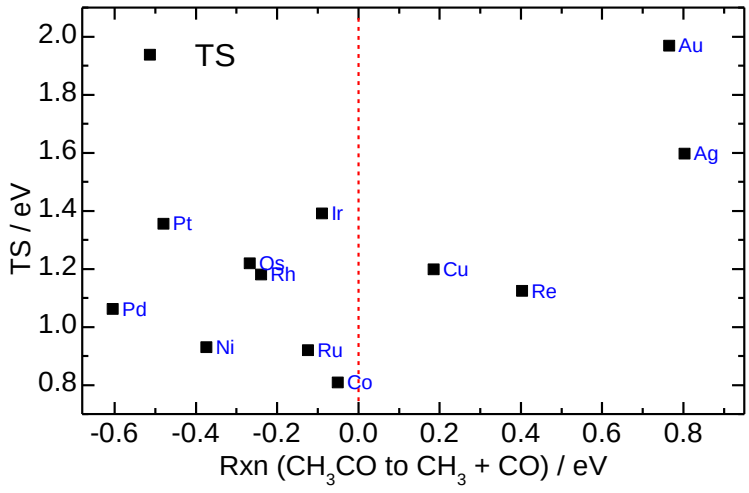

(b)

Figure 9.8: Graphs showing the correlation between (a) reaction energies for splitting the C–C and acetate formation from acetyl intermediate at 0.26 V/RHE, (b) TS and C–C splitting energies from acetyl for commonly used transition metals. The vertical line separates exothermic and endothermic C–C split metals on left and right side, respectively. Co has the lowest activation energy while Au has the highest.

By this criterion we have Pd, Pt, Ni, Sc, Rh, Os, Ir, Y, Ru, and Co as favorable metals for breaking the C–C bond and in that order. iii) the diagonal line reveals the metal selectivity in oxidizing acetyl towards acetate or C–C bond cleavage, those above/left favor C–C cleavage and vice versa .Therefore, the best catalysts for cleaving the C–C bond and in that order from Figure

9.8(a) are Pd, Pt, and Sc followed by Rh, Ir, Y, Ni, Os, Ru and Co. The ideal catalyst(s) would have been in the top left corner of Figure 9.8(a) which is not surprisingly empty. Interestingly, of the four metals (Hf, Ti, Sc, Y) which were found to be very active for acetyl and acetate formation (Figure 9.6), Sc and Y are predicted to be favorable for breaking the C–C bond while Hf and Ti are excluded. The reason for this trend is not clear to us at the moment. However, this switch between selectivity and activity means careful consideration is required in the catalyst design strategies to be discussed below. Nevertheless, Figure 9.8(a) has not only predicted the best candidate metals but also has put them in a precedence order list.

Figure 9.8(b) shows the correlation between the C–C bond cleavage energy and their corresponding energy barriers. From the plot the best catalyst are to be located at the bottom left corner, i.e., metals on which the cleavage of the C–C bond is both exothermic and has the lowest activation energy. Based on this criterion, Co, Ni, Ru and Pd stand out as the best metals. It is nteresting to note that Pt is predicted to have much higher activation energy than Ni, although Pt was identified to be the best in favouring the C–C cleavage over acetate formation compared to Ni. This kind of counter interplay between the various aspects of the reaction mechanism could explain why it is challenging to design efficient catalyst for ethanol electrooxidation.

9.2.4 **Rational catalyst design strategies and considerations**

To rationally propose strategies for designing catalyst for ethanol electrooxidation, we summarize the trends insights presented above in Table 9.1. Table 9.1 reveals that designing an efficient catalyst for ethanol electrooxidation is a daunting challenge because of the complexity of the switching of the metal activities for the intermediates involved in the reaction. For example, i) the strategy of destabilizing acetate and stabilizing acetyl calls for combining Au and Os, but neither of the two is good for cleaving the C–C bond. ii) the strategy of selecting metals which can selectively cleave the C–C bond with lowest energy barrier calls for Pd, but Pd has very poor selectivity for acetyl formation and stabilization. iii) Ti and Hf have good selectivity for acetyl formation, but they are the worst when it comes to C–C bond cleavage.

Notwithstanding all the challenges mentioned above, one emerging strategies for designing bimetallic catalyst from Table 9.1 is to combine metals with high selectivity for acetyl formation (Ti, Hf, Pt) with those which have high selectivity for breaking the C–C bond (Pd, Ni, Sc, Rh, Ir, Y, Os, Ru, and Co). From this strategy, only Pt-based, i.e., PtM(M = Pd, Ru, Ni, Rh, Ir) have

been extensively studied. Unfortunately, we currently do not have systematic studies of ethanol electrooxidation on Ti and Hf to validate this prediction.

Table 9.1: Summary of the identified activity and selectivity trends for ethanol electrooxidation on 21 transition metals. The screening is based on adsorption and reaction energy descriptors.

Data	Description	Best predicted metals in precedence order
Figure 4	Destabilizing acetate	Au, Ag
Figure 5	Stabilizing acetyl	Os, Ir, Rh, Re, Pt, Ru, Pd, Co, Ni
Figure 6	Selectivity for acetyl formation	Ti, Hf, Pt
Figure 7	Selectivity for acetyl (C vs O)	Pt, Pd, Ir, Rh, Os, Au
Figure 8(a)	C–C cleavage	Pd, Pt, Sc, Rh, Ir, Y, Ni, Os, Ru, Co
Figure 8(b)	TS C–C cleavage	Co, Ni, Ru, Pd

It is important to note that the metal activity predictions presented above assumes that the metals are in their metallic states (oxidation state zero). Therefore, for any comparisons between the predicted trends and experimental observations should be evaluated with this background in mind. This requirement is important because the effect of the surface compositions such as oxides or alloying are not taken into account in the model but would be of significant contribution to the observed experimental activity. Therefore, surface elemental composition of the catalyst will be critical in rationalizing the observed experimental performance of the catalysts. Here are some examples to illustrate this point. Gralec *et al*. studied the role of the Keggin-type phosphomolybdate ($PMo_{12}O_{40}^{3-}$) ions adsorbed on C-supported PtRu and PtRu/C for EOR.[28] They showed with XPS data that modification of PtRu/C nanoparticles with phosphomolybdate ions lead to the suppression of the formation of surface Ru oxides which resulted into more than 40% activity increase for EOR at potentials > 700 mV/RHE.[28] Similarly, Calderon-Cardenas *et al*. studied the effect of the composition and thermal treatment in H_2 of Pt-Rh/C materials with atomic ratios of Pt:Rh 3:1, 1:1 and 1:3 and metal loading of 40 wt.% for EOR in alkaline media.[29] They reported that thermally treated Pt-Rh catalysts in a hydrogen atmosphere showed greater stability and higher current densities and suggested the necessity of exploring the effects of thermal treatments of the catalysts for EOR. These two examples basically mean that when metals are mainly in their metallic state they have higher activity. Hence to compare the performance of two metals for a given reaction it is important to ensure they are in the same state.

9.3 **Conclusions**

In summary, we have used computational methods to search for the best mono-metallic catalyst for efficient and complete ethanol electrooxidation. We found that all of the 21 transition metals modelled favor acetate over acetyl formation, with the exception of Ti and Hf, which calls for the need to design catalyst formulation with two or more metals. Nevertheless, we have generated the list in order of their activity and selectivity using the first-principle insights. We found a special category of metals (Hf, Ti, Sc, and Y) which are predicted to be very active because of their strong binding energies which are worth for further investigations experimentally. Co is a strong competitor to Ru in breaking the C–C bond, however, it is scarcely used as catalyst promoter for EOR.

The trends identified in this work provides basis to compare or explain the performance of various catalysts and the rational for designing them. The major assumptions in the model used to generate the trends presented herein are: i) the metals are assumed to be in the metallic state, ii) the electrolyte is assumed to have no effect on the selectivity and activity of the catalyst. In reality, the surface oxidation state of the metal catalysts will vary depending on the electrolyte used and the applied potential. Therefore, to compare experimental trends with the trends in this work care should be taken to ensure the metals are in the same oxidation state. Future work should consider including these assumptions in the model.

Supporting Information: Tables with i) adsorption energies of C, O, CO, CH_3, CH_3CO and CH_3COO, ii) bond distances for CH_3CO on metal surfaces, and iii) reaction energies for acetyl, acetate, and C–C bond cleavage are provided in appendix section 5 .

Chapter 10: Conclusions and Recommendations

10.1 Conclusions

A new approach for processing PM-IRRAS data which allows for direct interpretation of the spectra without the need for the tedious calibration procedures is proposed in chapter 4. In the new approach, three complementary equations (equation 4.8, 4.14, and 4.15) are recommended for presenting PM-IRRAS data which provide more insights than ever reported before. These equations are robust in visualising the reaction dynamics at the solid-liquid and solid-gas interphase for liquid and gas phase reactions, respectively. Equation 4.8 highlights the surface absorbed species with respect to isotropic background with or without the influence of the applied potential. Unfortunately, it may have limited utility for GC and other weakly reflective electrode systems, especially if the surface species have relatively low contrast (little change) with respect to the bulk background as the result of applied potential. Equation 4.14 highlights the surface potential-driven changes between the sample and reference reflectance spectra. The observed surface thickness is governed by the optical constants of the reflective surface, which is less than 1 μm for GC (Figure 4.9a). Equation 4.15 highlights primarily the bulk potential-driven changes in both solution-phase and surface species between the sample and reference spectra (Figure 4.9b). Hence, it can be used to track the production of volatile and non-volatile species which desorb from the surface as soon as they are formed, which is equivalent to combining regular IRRAS with either the differential electrochemical mass spectroscopy (DEMS) or chromatographic techniques (HPLC).

In chapter 5, the significant role of two van der Waals correction functionals (PBE+D2 and PBE+TS) in the electronic configuration of ethanol adsorption on Pd and their effects on the adsorption energy values is showcased. Stronger binding energies upon inclusion of dispersion corrections are attributed to the increasing charge density distribution between Pd–O bonds leading to enhanced interactions. In particular, the projected local density of states revealed that carbon and oxygen p_z-states and the Pd d-band electrons play a critical role in stabilizing the

adsorbate on the surface. Such reinforcement in the interactions ultimately led to a reduction in the Pd–O and Pd–C bond lengths.

In chapter 6, it is shown that Ru indeed improves ethanol electrooxidation on Pd nanoparticles in alkaline media and the current densities obtained are depended on the applied potential. The CO stripping studies showed that Pd-Ru catalysts mitigate the CO poisoning in alkaline media which is a major challenge in acidic media. Therefore, Pd-Ru is a promising bimetallic combination that can be optimized further for ambient alkaline DEFCs. The improved catalytic activity was attributed to the synergetic effect between surface oxide species (PdO_x and RuO_x) and metallic Pd. The best composition formulation for good performance especially at lower potential was found to below 20% Ru. The $Pd_{90}Ru_{10}$/C and $Pd_{99}Ru_1$/C were found to be the best catalyst systems which produced more than four times higher mass activity (current density per mass of Pd) compared to pure Pd at -0.96 V and -0.67 V vs MSE, respectively.

In chapter 7, it is shown that the metal oxide supports have a promoting effect on the electrocatalytic activity of Pd nanoparticles for EOR in alkaline media. Of the supports tested (C, TiO_2, CeO_2 and SnO_2) nanoparticles supported on CeO_2 showed superior selectivity for breaking the C–C bond, while nanoparticles supported on SnO_2 did not show any evidence for breaking the C–C bond in spite of their highest reaction kinetics.

In chapter 8, the combination of in-situ experimental studies and computation chemistry calculations were successfully used to provide mechanistic understanding of ethanol electrooxidation reaction. The synergy between the two methodologies was critical in explaining as to why it is very challenging to break the C–C bond during ethanol electrooxidation, hence achieving the first objective set out in chapter 1. The identification of surface and bulk solution species by PM-IRRAS technique, simplified the number of possible intermediates considered in the DFT modelling. On the other hand, DFT insights provided invaluable information of the elementary reaction steps and kinetic parameters which were not accessible experimentally.

The work in chapter 8, solved two of the long debated puzzles in literature were: i) the path leading to the formation of acetate, which is the main product during ethanol electrooxidation in alkaline conditions. ii) the most likely intermediate(s) where the C–C bond can be broken. For the formation of acetate (acetic acid) two converging paths were identified. The most likely path goes through the gem-diol (hydrate of acetaldehyde), and the second path goes through the acetyl (CH_3CO) intermediate (Figure 8.3). Unfortunately, acetate cannot be oxidized any further as

confirmed by CV (Figure 8.1) and DFT insights (Figure 8.5), hence closing the door for complete oxidation of ethanol.

To the second debate, acetyl was identified as the most likely intermediate where the C–C bond can be broken before reaching acetate. This fact is demonstrated in Figure 8.6 where acetyl, an intermediate at oxidation state three, has by far the lowest activation energy for the C–C bond breaking ($E^{\ddagger}$ = 0.9 eV) while all the other intermediates have activation energy of greater than 1.3 eV. Unfortunately, the over-potentials required for the reasonable current densities strongly accelerate the electrochemical oxidation process which favours the C–OH formation over the C–C splitting reaction. Therefore, CH_3CO is quickly oxidized to acetic acid, thereby suppressing the C–C bond breaking which explains the negligible amount of CO_2 detected especially at higher potentials. Therefore, the conditions for a better selectivity towards CO_2 are to destabilize the gem-diol, stabilize the acetyl in order to facilitate the C–C cleavage.

Chapter 9, presents an effort made towards a rational strategy for designing catalysts with selectivity for breaking the C–C bond and highlights the top candidate transition metals for consideration in those endeavours. Based on computational insights, the emerging strategy for designing bimetallic catalysts was to combine metals with high selectivity for acetyl formation (Ti, Hf, Pt) with those which have high selectivity for breaking the C–C bond (Pd, Ni, Sc, Rh, Ir, Y, Os, Ru, and Co) as shown in Table 9.1. However, when evaluating catalysts based on these predictions, one must remember the assumptions made in the model. The major assumptions in the model used to generate the trends are: i) the metals are assumed to be in the metallic state, ii) the electrolyte is assumed to have no effect on the selectivity and activity of the catalyst. In reality, these factors will have a significant impact on the trends. For example, the surface oxidation state of the metal catalysts will vary depending on the electrolyte used and the applied potential.

10.2 Recommendations for further work

Based on the conclusions presented above on the achievements attained so far for ethanol electrooxidation reaction, there are many opportunities for further studies to make the commercialization of DEFCs a reality. The new and deeper mechanistic understanding of the reaction provided in this work opens the door for the rational design of the catalysts in order to achieve the second objective set out in chapter 1. Similarly, the opportunities to optimize the

reaction conditions such as looking for the best electrolyte formulations and the reaction temperature can now be readily investigated with more clarity in the details, thanks to the analytical tools now available.

I recommend that in the designing of the catalyst and selection of supports, special consideration be given to 3D and/or mesoporous materials such zeolites and metal-organic-frameworks (MOFs) and metal oxides. This recommendation is based on computational insights which showed that ethanol preferentially adsorb with the oxygen lone pair of electrons which allows the activation of the alpha-carbon (α-C). Therefore, confining the molecule within a thin-cavity catalyst would allow the activation of the beta-carbon (β-C). With this approach, even if the C–C bond is not broken, the current density is expected to be greatly improved because ethanol will be oxidized to oxalate (OOCCOO) instead of acetate (CH_3COO). Among the supports tested in this work, CeO_2 showed superior selectivity for breaking the C–C bond hence follow-up studies on this support will be highly welcomed.

I recommend that consideration be given to the use of buffer solutions and use of ionic liquids instead of the two extremes currently used, i.e., acidic or basic conditions. The use of buffer solutions is expected to solve the issue of the changing pH in the double layer during ethanol electrooxidation. This is important because ethanol electrooxidation reaction kinetics are sensitive to pH as revealed in the literature review (chapter 2). The consideration for ionic liquids is expected to mitigate the issue of carbonate precipitation which occurs as the result of the reaction between CO_2 and KOH. Ionic liquids may also improve the reaction selectivity by stabilizing the acetyl intermediate species which we found in this work to be critical for cleaving the C–C bond.

I recommend that the DFT calculations reported in chapter 9, i.e., screening for the best candidate metals, be revisited with van der Waals correction functionals (PBE+D2/D3 and PBE+TS) reported in Chapter 5. This study would be important to verify if these corrections have any effect on the screening trends observed for the best candidate metals for EOR so that comparisons with experimental observations will be based on solid foundation of first-principle predictions. The next steps should also include computational screening for alloys, surface oxides, and the influence of electrolytes.

I recommend infrared spectroscopy (especially PM-IRRAS), nuclear magnetic resonance (NMR) spectroscopy, and X-ray absorption/photoemission spectroscopy (XAS/XPS) to be the

standard complementary techniques in the future studies, for they can help to capture the complete details of the reaction mechanism. From the literature review, it is evident that a range of analytical tools (electrochemical techniques, mass spectroscopy, surface enhanced Raman spectroscopy, sum frequency generation spectroscopy, XPS, chromatography, and NMR) and protocols for using them to probe electrocatalytic reactions in-situ are now available. The synergy between experimental data from these techniques and computational chemistry is needed solve the reaction mechanism puzzles.

References

(1) Heinzel, A.; Cappadonia, M.; Stimming, U.; Kordesch, K. V.; de Oliveira, J. C. T. In *Ullmann's Encyclopedia of Industrial Chemistry*; Wiley-VCH Verlag GmbH & Co. KGaA, Ed.; Wiley-VCH Verlag GmbH & Co. KGaA: Weinheim, Germany, 2010.
(2) Jiang, S. P.; Wang, X. In *Solid State Electrochemistry II*; Kharton, V. V., Ed.; Wiley-VCH Verlag GmbH & Co. KGaA: Weinheim, Germany, 2011; pp 179–264.
(3) Steele, B. C. H.; Heinzel, A. *Nat. Lond. U K* **2001**, *414* (6861), 345–352.
(4) Zhang, S.; Shao, Y.; Yin, G.; Lin, Y. *J. Mater. Chem. A* **2013**, *1* (15), 4631.
(5) An, L.; Zhao, T. S.; Li, Y. S. *Renew. Sustain. Energy Rev.* **2015**, *50*, 1462–1468.
(6) Goldemberg, J. *Science* **2007**, *315* (5813), 808–810.
(7) Grove, W. R. *J. Frankl. Inst.* **1843**, *35* (4), 277–280.
(8) Akhairi, M. A. F.; Kamarudin, S. K. *Int J Hydrog. Energy* **2016**, *41* (7), 4214–4228.
(9) Sharaf, O. Z.; Orhan, M. F. *Renew. Sustain. Energy Rev.* **2014**, *32*, 810–853.
(10) Kamarudin, M. Z. F.; Kamarudin, S. K.; Masdar, M. S.; Daud, W. R. W. *Int J Hydrog. Energy* **2013**, *38* (22), 9438–9453.
(11) Brouzgou, A.; Podias, A.; Tsiakaras, P. *J. Appl. Electrochem.* **2013**, *43*, 119–136.
(12) Yu, E. H.; Wang, X.; Krewer, U.; Li, L.; Scott, K. *Energy Environ. Sci.* **2012**, *5* (2), 5668–5680.
(13) Rabis, A.; Rodriguez, P.; Schmidt, T. J. *ACS Catal.* **2012**, *2* (5), 864–890.
(14) Antolini, E.; Gonzalez, E. R. *J Power Sources* **2010**, *195* (11), 3431–3450.
(15) Lamy, C.; Lima, A.; LeRhun, V.; Delime, F.; Coutanceau, C.; Léger, J.-M. *J. Power Sources* **2002**, *105* (2), 283–296.
(16) Almeida, T. D. S.; De Andrade, A. R. In *New and Future Developments in Catalysis: Batteries, Hydrogen storage and Fuel Cells*; Elsevier, 2013; pp 429–452.
(17) Lamy, C.; Coutanceau, C.; Leger, J.-M. In *Catal. Sustainable Energy Prod.*; Barbaro, P., Bianchin, C., Eds.; Wiley-VCH Verlag GmbH & Co. KGaA, 2009; pp 3–46.
(18) Koper, M. T.; Lai, S. C.; Herrero, E. In *Fuel Cell Catalysis*; John Wiley & Sons, Inc., 2008; pp 159–207.
(19) Varcoe, J. R.; Slade, R. C. T. *Fuel Cells* **2005**, *5* (2), 187–200.
(20) Tsivadze, A. Y.; Tarasevich, M. R.; Andreev, V. N.; Bogdanovskaya, V. A. *Russ. J. Gen. Chem.* **2007**, *77* (4), 783–789.
(21) Nørskov, J. K.; Rossmeisl, J.; Logadottir, A.; Lindqvist, L.; Kitchin, J. R.; Bligaard, T.; Jónsson, H. *J. Phys. Chem. B* **2004**, *108* (46), 17886–17892.
(22) McLean, G. F.; Niet, T.; Prince-Richard, S.; Djilali, N. *Int J Hydrog. Energy* **2002**, *27* (5), 507–526.
(23) Ogumi, Z.; Matsuoka, K.; Chiba, S.; Matsuoka, M.; Iriyama, Y.; Abe, T.; Inaba, M. *Electrochem. Tokyo Jpn* **2002**, *70* (12), 980–983.
(24) Varcoe, J. R.; Slade, R. C. T.; Yee, E. L. H. *Chem Commun Camb. U K* **2006**, No. 13, 1428–1429.
(25) Zeng, R.; Varcoe, J. R. *Recent Pat Chem Eng* **2011**, *4* (2), 93–115.
(26) Bidault, F.; Brett, D. J. L.; Middleton, P. H.; Brandon, N. P. *J. Power Sources* **2009**, *187* (1), 39–48.
(27) Zhao, T. S.; Li, Y. S.; Shen, S. Y. *Front. Energy Power Eng. China* **2010**, *4* (4), 443–458.
(28) Singh, R. N.; Madhu; Awasthi, R. In *New and Future Developments in Catalysis: Batteries, Hydrogen Storage Fuel Cells*; Elsevier B.V., 2013; pp 453–478.
(29) Rao, L.; Jiang, Y.; Zhang, B.; You, L.; Li, Z.; Sun, S. *Huaxue Jinzhan* **2014**, *26* (5), 727–736.
(30) Wang, Y.; Zou, S.; Cai, W.-B. *Catalysts* **2015**, *5* (3), 1507–1534.
(31) Badwal, S. P. S.; Giddey, S.; Kulkarni, A.; Goel, J.; Basu, S. *Appl. Energy* **2015**, *145*, 80–103.
(32) An, L.; Zhao, T. S.; Chen, R.; Wu, Q. X. *J. Power Sources* **2011**, *196* (15), 6219–6222.
(33) Agel, E.; Bouet, J.; Fauvarque, J. F. *J Power Sources* **2001**, *101* (2), 267–274.
(34) An, L.; Zhao, T. S.; Xu, J. B. *Int. J. Hydrog. Energy* **2011**, *36* (20), 13089–13095.
(35) An, L.; Zhao, T. S.; Zeng, L.; Yan, X. H. *Int. J. Hydrog. Energy* **2014**, *39* (5), 2320–2324.
(36) Verma, A.; Basu, S. *J. Power Sources* **2007**, *174* (1), 180–185.

(37) Gaurava, D.; Verma, A.; Sharma, D. K.; Basu, S. *Fuel Cells* **2010**, *10* (4), 591–596.
(38) Verma, A.; Basu, S. *J. Power Sources* **2005**, *145* (2), 282–285.
(39) Verma, A.; Jha, A. K.; Basu, S. *J. Fuel Cell Sci. Technol.* **2005**, *2* (4), 234.
(40) Lee, K. T.; Gore, C. M.; Wachsman, E. D. *J. Mater. Chem.* **2012**, *22* (42), 22405–22408.
(41) Cimenti, M.; Hill, M. J. *Energies* **2009**, *2* (2), 377–410.
(42) Cuenya, B. R. *Thin Solid Films* **2010**, *518* (12), 3127–3150.
(43) Yin, Z.; Lin, L.; Ma, D. *Catal Sci Technol* **2014**, *4* (12), 4116–4128.
(44) Bron, M.; Roth, C. In *New and Future Developments in Catalysis*; Elsevier: Amsterdam, 2013; pp 271–305.
(45) Bandarenka, A. S.; Koper, M. T. M. *J. Catal.* **2013**, *308*, 11–24.
(46) Calle-Vallejo, F.; Koper, M. T. M.; Bandarenka, A. S. *Chem Soc Rev* **2013**, *42* (12), 5210–5230.
(47) Bandarenka, A. S.; Varela, A. S.; Karamad, M.; Calle-Vallejo, F.; Bech, L.; Perez-Alonso, F. J.; Rossmeisl, J.; Stephens, I. E. L.; Chorkendorff, I. *Angew Chem Int Ed* **2012**, *51* (47), 11845–11848.
(48) Calle-Vallejo, F.; Tymoczko, J.; Colic, V.; Vu, Q. H.; Pohl, M. D.; Morgenstern, K.; Loffreda, D.; Sautet, P.; Schuhmann, W.; Bandarenka, A. S. *Science* **2015**, *350* (6257), 185–189.
(49) Yu, Y.; Zhang, Q.; Liu, B.; Lee, J. Y. *J. Am. Chem. Soc.* **2010**, *132* (51), 18258–18265.
(50) Guzmán-Blas, R.; Menéndez, C. L.; Vélez, C. A.; Fachini, E. R.; Johnston-Peck, A.; Senanayake, S. D.; Stacchiola, D.; Sasaki, K.; Cabrera, C. R. *Smart Grid Renew. Energy* **2013**, *4* (7), 1–9.
(51) Wang, H.-F.; Ariga, H.; Dowler, R.; Sterrer, M.; Freund, H.-J. *J. Catal.* **2012**, *286*, 1–5.
(52) Speder, J.; Altmann, L.; Roefzaad, M.; Baumer, M.; Kirkensgaard, J.; Mortensen, K.; Arenz, M. *Phys Chem Chem Phys* **2013**, *15* (10), 3602–3608.
(53) Figueiredo, M. C.; Solla-Gullón, J.; Vidal-Iglesias, F. J.; Nisula, M.; Feliu, J. M.; Kallio, T. *Electrochem. Commun.* **2015**, *55*, 47–50.
(54) Martinez-Rodriguez, R. A.; Vidal-Iglesias, F. J.; Solla-Gullon, J.; Cabrera, C. R.; Feliu, J. M. *ChemPhysChem* **2014**, *15* (10), 1997–2001.
(55) Liu, Z.; Lee, J. Y.; Han, M.; Chen, W.; Gan, L. M. *J. Mater. Chem.* **2002**, *12* (8), 2453–2458.
(56) Suffredini, H. B.; Salazar-Banda, G. R.; Avaca, L. A. *J. Power Sources* **2007**, *171* (2), 355–362.
(57) Zhang, Z.; Liu, J.; Gu, J.; Su, L.; Cheng, L. *Energy Environ. Sci.* **2014**, *7* (8), 2535.
(58) Hayden, B. E. *Acc. Chem. Res.* **2013**, *46* (8), 1858–1866.
(59) Yu, E. H.; Wang, X.; Liu, X. T.; Li, L. *RSC Energy Env. Ser* **2012**, *6* (Catalysts for Alcohol-Fuelled Direct Oxidation Fuel Cells), 227–249.
(60) Dicks, A. L. *J. Power Sources* **2006**, *156* (2), 128–141.
(61) Antolini, E. *Appl. Catal. B Environ.* **2009**, *88* (1–2), 1–24.
(62) Bambagioni, V.; Bianchini, C.; Marchionni, A.; Filippi, J.; Vizza, F.; Teddy, J.; Serp, P.; Zhiani, M. *J. Power Sources* **2009**, *190* (2), 241–251.
(63) Singh, R. N.; Awasthi, R. *Catal. Sci. Technol.* **2011**, *1* (5), 778.
(64) Monyoncho, E. A.; Ntais, S.; Brazeau, N.; Wu, J.-J.; Sun, C.-L.; Baranova, E. A. *ChemElectroChem* **2016**, *3* (2), 218–227.
(65) Katayama, Y.; Okanishi, T.; Muroyama, H.; Matsui, T.; Eguchi, K. *ACS Catal* **2016**, *6* (3), 2026–2034.
(66) Godoi, D. R. M.; Villullas, H. M.; Zhu, F.-C.; Jiang, Y.-X.; Sun, S.-G.; Guo, J.; Sun, L.; Chen, R. *J. Power Sources* **2016**, *311*, 81–90.
(67) Maache, R.; Brahmi, R.; Pirault-Roy, L.; Ojala, S.; Bensitel, M. *Top Catal* **2013**, *56* (9–10), 658–661.
(68) Bambagioni, V.; Bianchini, C.; Chen, Y.; Filippi, J.; Fornasiero, P.; Innocenti, M.; Lavacchi, A.; Marchionni, A.; Oberhauser, W.; Vizza, F. *ChemSusChem* **2012**, *5* (7), 1266–1273.
(69) Wei, Y.-C.; Liu, C.-W.; Kang, W.-D.; Lai, C.-M.; Tsai, L.-D.; Wang, K.-W. *J. Electroanal. Chem.* **2011**, *660* (1), 64–70.
(70) Uhm, S.; Yi, Y.; Lee, J. *Catal. Lett.* **2010**, *138* (1–2), 46–49.
(71) Neto, A. O.; Linardi, M.; Anjos, D. M. dos; Tremiliosi-Filho, G.; Spinacé, E. V. *J. Appl. Electrochem.* **2009**, *39* (7), 1153–1156.

(72) Xu, C.; Tian, Z.; Shen, P.; Jiang, S. P. *Electrochim Acta* **2008**, *53* (5), 2610–2618.
(73) Shen, P. K.; Xu, C. *Electrochem. Commun.* **2006**, *8* (1), 184–188.
(74) Xu, C.; Zeng, R.; Shen, P. K.; Wei, Z. *Electrochimica Acta* **2005**, *51* (6), 1031–1035.
(75) Xu, C.; Shen, P. K. *J Power Sources* **2005**, *142* (1–2), 27–29.
(76) Martinez, U.; Serov, A.; Padilla, M.; Atanassov, P. *ChemSusChem* **2014**, *7* (8), 2351–2357.
(77) Mao, H.; Wang, L.; Zhu, P.; Xu, Q.; Li, Q. *Int. J. Hydrog. Energy* **2014**, *39* (31), 17583–17588.
(78) Russo, P. A.; Ahn, M.; Pinna, N.; Sung, Y.-E. *RSC Adv* **2013**, *3* (19), 7001–7008.
(79) An, H.; Pan, L.; Cui, H.; Li, B.; Zhou, D.; Zhai, J.; Li, Q. *Electrochimica Acta* **2013**, *102*, 79–87.
(80) Moghaddam, R. B.; Pickup, P. G. *Electrochimica Acta* **2012**, *65*, 210–215.
(81) Takeguchi, T.; Anzai, Y.; Kikuchi, R.; Eguchi, K.; Ueda, W. *J. Electrochem. Soc.* **2007**, *154* (11), 1132.
(82) Jiang, L.; Colmenares, L.; Jusys, Z.; Sun, G. Q.; Behm, R. J. *ELECTROCATALYSIS THEORY Ind. Appl. Sel. Pap. 5th Int. Conf. ECS06 10-14 Sept. 2006 Kotor MontenegroELECTROCHEMICAL MICRO Nanosyst. Technol. Sel. Pap. 6th Int. Symp. EMNT 2006 22-25 August 2006 Bonn Ger.* **2007**, *53* (2), 377–389.
(83) Okanishi, T.; Matsui, T.; Takeguchi, T.; Kikuchi, R.; Eguchi, K. *Appl. Catal. Gen.* **2006**, *298*, 181–187.
(84) Batzill, M.; Diebold, U. *Prog. Surf. Sci.* **2005**, *79* (2–4), 47–154.
(85) Silva, J. C. M.; Buzzo, G. S.; De Souza, R. F. B.; Spinacé, E. V.; Neto, A. O.; Assumpção, M. H. M. T. *Electrocatalysis* **2015**, *6* (1), 86–91.
(86) De Souza, R. F. B.; Buzzo, G. S.; Silva, J. C. M.; Spinacé, E. V.; Neto, A. O.; Assumpção, M. H. M. T. *Electrocatalysis* **2014**, *5* (2), 213–219.
(87) Nguyen, S. T.; Yang, Y.; Wang, X. *Appl. Catal. B Environ.* **2012**, *113–114*, 261–270.
(88) Hu, F.; Ding, F.; Song, S.; Shen, P. K. *J. Power Sources* **2006**, *163* (1), 415–419.
(89) Liu, Q.; Jiang, K.; Fan, J.; Lin, Y.; Min, Y.; Xu, Q.; Cai, W.-B. *Electrochim Acta* **2016**, *203*, 91–98.
(90) Lewera, A.; Timperman, L.; Roguska, A.; Alonso-Vante, N. *J. Phys. Chem. C* **2011**, *115* (41), 20153–20159.
(91) Lim, E. J.; Kim, H. J.; Kim, W. B. *Catal. Commun.* **2012**, *25*, 74–77.
(92) Bai, Y.; Wu, J.; Xi, J.; Wang, J.; Zhu, W.; Chen, L.; Qiu, X. *Electrochem. Commun.* **2005**, *7* (11), 1087–1090.
(93) Chen, H.; Huang, Y.; Tang, D.; Zhang, T.; Wang, Y. *Electrochimica Acta* **2015**, *158*, 18–23.
(94) Li, N.; Zeng, Y.-X.; Chen, S.; Xu, C.-W.; Shen, P.-K. *Int. J. Hydrog. Energy* **2014**, *39* (28), 16015–16019.
(95) Xu, C.; Shen, P. K.; Ji, X.; Zeng, R.; Liu, Y. *Electrochem. Commun.* **2005**, *7* (12), 1305–1308.
(96) Modibedi, R. M.; Louw, E. K.; Mathe, M. K.; Ozoemena, K. I. *ECS Trans* **2013**, *50* (21, Electrochemical Atomic Layer Epitaxy and Quantum Confinement), 9-18, 10 .
(97) Xu, C.; Shen, P. kang; Liu, Y. *J. Power Sources* **2007**, *164* (2), 527–531.
(98) Hu, F.; Chen, C.; Wang, Z.; Wei, G.; Shen, P. K. *Electrochim Acta* **2006**, *52* (3), 1087–1091.
(99) Tauster, S. *J. Catal.* **1978**, *55* (1), 29–35.
(100) Tauster, S. J.; Fung, S. C.; Garten, R. L. *J. Am. Chem. Soc.* **1978**, *100* (1), 170–175.
(101) Sanchez, M. *J. Catal.* **1987**, *104* (1), 120–135.
(102) Katayama, Y.; Okanishi, T.; Muroyama, H.; Matsui, T.; Eguchi, K. *ACS Catal.* **2016**, *6* (3), 2026–2034.
(103) Figueiredo, M. C.; Arán-Ais, R. M.; Climent, V.; Kallio, T.; Feliu, J. M. *ChemElectroChem* **2015**, *2* (9), 1254–1258.
(104) Lai, S. C. S.; Kleijn, S. E. F.; Öztürk, F. T. Z.; van Rees Vellinga, V. C.; Koning, J.; Rodriguez, P.; Koper, M. T. M. *Catal. Today* **2010**, *154* (1–2), 92–104.
(105) Cremers, C.; Bayer, D.; Kintzel, B.; Joos, M.; Jung, F.; Krausa, M.; Tübke, J. *ECS Trans.* **2008**, *16*, 1263–1273.
(106) Rao, V.; Hariyanto; Cremers, C.; Stimming, U. *Fuel Cells* **2007**, *7* (5), 417–423.
(107) Takahashi, H.; Sagihara, M.; Taguchi, M. *Int. J. Hydrog. Energy* **2014**, *39* (32), 18424–18432.

(108) Bayer, D.; Berenger, S.; Cremers, C.; Tübke, J. *ECS Trans.* **2010**, 95–103.
(109) Bayer, D.; Berenger, S.; Joos, M.; Cremers, C.; Tübke, J. *Int. J. Hydrog. Energy* **2010**, *35* (22), 12660–12667.
(110) Busó-Rogero, C.; Herrero, E.; Feliu, J. M. *ChemPhysChem* **2014**, *15* (10), 2019–2028.
(111) Lai, S. C. S.; Koper, M. T. M. *Phys. Chem. Chem. Phys.* **2009**, *11* (44), 10446–10456.
(112) Tripković, A. V.; Popović, K. D.; Lović, J. D. *Electrochimica Acta* **2001**, *46* (20–21), 3163–3173.
(113) Busó-Rogero, C.; Solla-Gullón, J.; Vidal-Iglesias, F. J.; Herrero, E.; Feliu, J. M. *J. Solid State Electrochem.* **2016**, *20* (4), 1095–1106.
(114) Sun, C.-L.; Tang, J.-S.; Brazeau, N.; Wu, J.-J.; Ntais, S.; Yin, C.-W.; Chou, H.-L.; Baranova, E. A. *Electrochimica Acta* **2015**, *162*, 282–289.
(115) Kumar, A.; Buttry, D. A. *Electrocatalysis* **2016**, *7* (3), 201–206.
(116) Modibedi, R. M.; Mehlo, T.; Ozoemena, K. I.; Mathe, M. K. *Int. J. Hydrog. Energy* **2015**, *40* (45), 15605–15612.
(117) Carrera-Cerritos, R.; Fuentes-Ramírez, R.; Cuevas-Muñiz, F. M.; Ledesma-García, J.; Arriaga, L. G. *J. Power Sources* **2014**, *269*, 370–378.
(118) Wang, L.; Bevilacqua, M.; Chen, Y.-X.; Filippi, J.; Innocenti, M.; Lavacchi, A.; Marchionni, A.; Miller, H.; Vizza, F. *J. Power Sources* **2013**, *242*, 872–876.
(119) Assaud, L.; Brazeau, N.; Barr, M. K. S.; Hanbücken, M.; Ntais, S.; Baranova, E. A.; Santinacci, L. *ACS Appl. Mater. Interfaces* **2015**, *7* (44), 24533–24542.
(120) Rohwer, M. B.; Modibedi, R. M.; Ozoemena, K. I. *Electroanalysis* **2015**, *27* (4), 957–963.
(121) Cerritos, R. C.; Guerra-Balcázar, M.; Ramírez, R. F.; Ledesma-García, J.; Arriaga, L. G. *Materials* **2012**, *5* (12), 1686–1697.
(122) Cherevko, S.; Kulyk, N.; Chung, C.-H. *Nanoscale* **2012**, *4* (1), 103–105.
(123) Safavi, A.; Abbaspour, A.; Sorouri, M.; Mohammadi, A. *ChemElectroChem* **2016**, *3* (4), 558–564.
(124) Zhiani, M.; Majidi, S.; Rostami, H.; Taghiabadi, M. M. *Int. J. Hydrog. Energy* **2015**, *40* (1), 568–576.
(125) Chen, Y.; Bellini, M.; Bevilacqua, M.; Fornasiero, P.; Lavacchi, A.; Miller, H. A.; Wang, L.; Vizza, F. *ChemSusChem* **2015**, *8* (3), 524–533.
(126) Serov, A.; Andersen, N. I.; Kabir, S. A.; Roy, A.; Asset, T.; Chatenet, M.; Maillard, F.; Atanassov, P. *J. Electrochem. Soc.* **2015**, *162* (12), F1305–F1309.
(127) Li, Y.; Xu, Q.; Li, Q.-Y.; Wang, H.; Huang, Y.; Xu, C. *Electrochimica Acta* **2014**, *147*, 151–156.
(128) Chu, D.; Wang, J.; Wang, S.; Zha, L.; He, J.; Hou, Y.; Yan, Y.; Lin, H.; Tian, Z. *Catal. Commun.* **2009**, *10* (6), 955–958.
(129) Ma, L.; Chu, D.; Chen, R. *Int. J. Hydrog. Energy* **2012**, *37* (15), 11185–11194.
(130) Cherevko, S.; Xing, X.; Chung, C.-H. *Electrochimica Acta* **2011**, *56* (16), 5771–5775.
(131) Bayer, D.; Cremers, C.; Baltruschat, H.; Tübke, J. *ECS Trans.* **2011**, *41* (1), 1669–1680.
(132) Xu, C.; Cheng, L.; Shen, P.; Liu, Y. *Electrochem. Commun.* **2007**, *9* (5), 997–1001.
(133) Cantane, D. A.; Lima, F. H. B. *Electrocatalysis* **2012**, *3* (3–4), 324–333.
(134) Chen, A.; Ostrom, C. *Chem Rev Wash. DC U S* **2015**, *115* (21), 11999–12044.
(135) Teng, X. **2016**.
(136) Liao, F.; Lo, T. W. B.; Tsang, S. C. E. *ChemCatChem* **2015**, *7* (14), 1998–2014.
(137) Zhu, C.; Du, D.; Eychmüller, A.; Lin, Y. *Chem. Rev.* **2015**.
(138) Coutanceau, C.; Brimaud, S.; Lamy, C.; Léger, J.-M.; Dubau, L.; Rousseau, S.; Vigier, F. *Electrochimica Acta* **2008**, *53* (23), 6865–6880.
(139) Antolini, E. *J. Power Sources* **2007**, *170* (1), 1–12.
(140) Weber, M.; Mackus, A.; Verheijen, M.; van der Marel, C.; Kessels, W. *Chem. Mater.* **2012**.
(141) Park, J.; Hong, S. *Chem Soc Rev* **2012**, *41* (21), 6931–6943.
(142) Gu, J.; Zhang, Y.-W.; Tao, F. *Chem Soc Rev* **2012**, *41* (24), 8050–8065.
(143) Sankar, M.; Dimitratos, N.; Miedziak, P.; Wells, P.; Kiely, C.; Hutchings, G. *Chem Soc Rev* **2012**, *41* (24), 8099–8139.
(144) Zhang, H.; Jin, M.; Xia, Y. *Chem Soc Rev* **2012**, *41* (24), 8035–8049.

(145) Chen, X.; Cai, Z.; Chen, X.; Oyama, M. *J Mater Chem A* **2014**, *2* (2), 315–320.
(146) Zhu, C.; Guo, S.; Dong, S. *Chem. - Eur. J.* **2013**, *19* (3), 1104–1111.
(147) Christensen, P. A.; Jones, S. W. M.; Hamnett, A. *Phys. Chem. Chem. Phys.* **2013**, *15* (40), 17268.
(148) Yang, X.; Yang, Q.; Xu, J.; Lee, C.-S. *J. Mater. Chem.* **2012**, *22* (16), 8057.
(149) Datta, J.; Dutta, A.; Biswas, M. *Electrochem. Commun.* **2012**, *20*, 56–59.
(150) Zhu, C.; Guo, S.; Dong, S. *Adv. Mater.* **2012**, *24* (17), 2326–2331.
(151) Lin, S.-C.; Chen, J.-Y.; Hsieh, Y.-F.; Wu, P.-W. *Mater. Lett.* **2011**, *65* (2), 215–218.
(152) Zheng, H. T.; Chen, S.; Shen, P. K. *Electrochem. Commun.* **2007**, *9* (7), 1563–1566.
(153) Artyushkova, K.; Halevi, B.; Padilla, M.; Atanassov, P.; Baranova, E. A. *J. Electrochem. Soc.* **2015**, *162* (6), H345–H351.
(154) Du, W.; Yang, G.; Wong, E.; Deskins, N. A.; Frenkel, A. I.; Su, D.; Teng, X. *J. Am. Chem. Soc.* **2014**, *136* (31), 10862–10865.
(155) Assumpção, M. H. M. T.; Nandenha, J.; Buzzo, G. S.; Silva, J. C. M.; Spinacé, E. V.; Neto, A. O.; De Souza, R. F. B. *J. Power Sources* **2014**, *253*, 392–396.
(156) Baranova, E. A.; Padilla, M. A.; Halevi, B.; Amir, T.; Artyushkova, K.; Atanassov, P. *Electrochimica Acta* **2012**, *80*, 377–382.
(157) Kim, I.; Han, O. H.; Chae, S. A.; Paik, Y.; Kwon, S.-H.; Lee, K.-S.; Sung, Y.-E.; Kim, H. *Angew. Chem. Int. Ed.* **2011**, *50* (10), 2270–2274.
(158) Zhou, W. J.; Song, S. Q.; Li, W. Z.; Zhou, Z. H.; Sun, G. Q.; Xin, Q.; Douvartzides, S.; Tsiakaras, P. *J. Power Sources* **2005**, *140* (1), 50–58.
(159) Lamy, C.; Rousseau, S.; Belgsir, E. M.; Coutanceau, C.; Léger, J.-M. *Electrochimica Acta* **2004**, *49* (22–23), 3901–3908.
(160) Zhou, W. *Appl. Catal. B Environ.* **2003**, *46* (2), 273–285.
(161) Gralec, B.; Lewera, A.; Kulesza, P. J. *J. Power Sources* **2016**, *315*, 56–62.
(162) Huang, L.; Sorte, E. G.; Sun, S.-G.; Tong, Y. Y. J. *Chem Commun* **2015**, *51* (38), 8086–8088.
(163) Hajian, A.; Rafati, A. A.; Yurchenko, O.; Urban, G.; Afraz, A.; Najafi, M.; Bagheri, A. *J. Electrochem. Soc.* **2014**, *162* (1), B41–B46.
(164) Petrii, O. A. *J. Solid State Electrochem.* **2008**, *12* (5), 609–642.
(165) Ghumman, A.; Vink, C.; Yepez, O.; Pickup, P. G. *J. Power Sources* **2008**, *177* (1), 71–76.
(166) Fujiwara, N.; Siroma, Z.; Yamazaki, S.; Ioroi, T.; Senoh, H.; Yasuda, K. *J. Power Sources* **2008**, *185* (2), 621–626.
(167) LI Lin, M. Z.-F., YUAN Xian-Xia, XIA Xiao-Yun, DU Juan, MA Zhong. *J. Inorg. Mater.* **2014**, *29* (10), 1044.
(168) Figueiredo, M. C.; Arán-Ais, R. M.; Feliu, J. M.; Kontturi, K.; Kallio, T. *J. Catal.* **2014**, *312*, 78–86.
(169) Matsumoto, F. *Electrochemistry* **2012**, *80* (3), 132–138.
(170) Tusi, M. M.; Polanco, N. S. O.; da Silva, S. G.; Spinacé, E. V.; Neto, A. O. *Electrochem. Commun.* **2011**, *13* (2), 143–146.
(171) Mourdikoudis, S.; Chirea, M.; Zanaga, D.; Altantzis, T.; Mitrakas, M.; Bals, S.; Liz-Marzán, L. M.; Pérez-Juste, J.; Pastoriza-Santos, I. *Nanoscale* **2015**, *7* (19), 8739–8747.
(172) Dutta, A.; Mondal, A.; Datta, J. *J. Power Sources* **2015**, *283*, 104–114.
(173) Zhou, W.; Li, M.; Zhang, L.; Chan, S. H. *Electrochimica Acta* **2014**, *123*, 233–239.
(174) da Silva, S. G.; Silva, J. C. M.; Buzzo, G. S.; De Souza, R. F. B.; Spinacé, E. V.; Neto, A. O.; Assumpção, M. H. M. T. *Int. J. Hydrog. Energy* **2014**, *39* (19), 10121–10127.
(175) Song, H. M.; Anjum, D. H.; Sougrat, R.; Hedhili, M. N.; Khashab, N. M. *J. Mater. Chem.* **2012**, *22* (48), 25003.
(176) Gunji, T.; Tanabe, T.; Jeevagan, A. J.; Usui, S.; Tsuda, T.; Kaneko, S.; Saravanan, G.; Abe, H.; Matsumoto, F. *J. Power Sources* **2015**, *273*, 990–998.
(177) Yang, W.-H.; Wang, H.-H.; Chen, D.-H.; Zhou, Z.-Y.; Sun, S.-G. *Phys. Chem. Chem. Phys.* **2012**, *14* (47), 16424.

(178) He, Q.; Shyam, B.; Macounová, K.; Krtil, P.; Ramaker, D.; Mukerjee, S. *J. Am. Chem. Soc.* **2012**, *134* (20), 8655–8661.
(179) El-Shafei, A. A.; El-Maksoud, S. A. A.; Moussa, M. N. H. *J. Electroanal. Chem.* **1992**, *336* (1–2), 73–83.
(180) Calderón-Cárdenas, A.; Ortiz-Restrepo, J. E.; Mancilla-Valencia, N. D.; Torres-Rodriguez, G. A.; Lima, F. H. B.; Bolaños-Rivera, A.; Gonzalez, E. R.; Lizcano-Valbuena, W. H. *J. Braz. Chem. Soc.* **2014**.
(181) Shen, S. Y.; Zhao, T. S.; Xu, J. B. *Int. J. Hydrog. Energy* **2010**, *35* (23), 12911–12917.
(182) Hong, W.; Wang, J.; Wang, E. *Nano Res.* **2015**, *8* (7), 2308–2316.
(183) Kepeniene, V.; Tama auskaite-Tama i naite, L.; Jablonskiene, J.; Vai i niene, J.; Kondrotas, R.; Ju kenas, R.; Norkus, E. *J. Electrochem. Soc.* **2014**, *161* (14), F1354–F1359.
(184) Jin, C.; Ma, X.; Zhang, J.; Huo, Q.; Dong, R. *Electrochimica Acta* **2014**, *146*, 533–537.
(185) Matsuoka, K.; Iriyama, Y.; Abe, T.; Matsuoka, M.; Ogumi, Z. *J. Power Sources* **2005**, *150*, 27–31.
(186) Obradović, M. D.; Stančić, Z. M.; Lačnjevac, U. Č.; Radmilović, V. V.; Gavrilović-Wohlmuther, A.; Radmilović, V. R.; Gojković, S. L. *Appl. Catal. B Environ.* **2016**, *189*, 110–118.
(187) Moraes, L. P. R.; Matos, B. R.; Radtke, C.; Santiago, E. I.; Fonseca, F. C.; Amico, S. C.; Malfatti, C. F. *Int. J. Hydrog. Energy* **2016**, *41* (15), 6457–6468.
(188) Wang, Y.; Jiang, K.; Cai, W.-B. *Electrochimica Acta* **2015**, *162*, 100–107.
(189) Chen, W.; Zhang, Y.; Wei, X. *Int. J. Hydrog. Energy* **2015**, *40* (2), 1154–1162.
(190) Sheikh, A. M.; Silva, E. L.; Moares, L.; Antonini, L. M.; Abellah, M. Y.; Malfatti, C. F. *Am. J. Min. Metall.* **2014**, *2* (4), 64–69.
(191) Jiang, R.; Tran, D. T.; McClure, J. P.; Chu, D. *ACS Catal.* **2014**, *4* (8), 2577–2586.
(192) Dutta, A.; Datta, J. *J. Mater. Chem. A* **2014**, *2* (9), 3237–3250.
(193) Ahmed, M. S.; Jeon, S. *ACS Catal.* **2014**, *4* (6), 1830–1837.
(194) Wang, Y.; Shi, F.-F.; Yang, Y.-Y.; Cai, W.-B. *J. Power Sources* **2013**, *243*, 369–373.
(195) Shen, S. Y.; Zhao, T. S.; Wu, Q. X. *Int. J. Hydrog. Energy* **2012**, *37* (1), 575–582.
(196) Roy, P. S.; Bagchi, J.; Bhattacharya, S. K. *Catal. Sci. Technol.* **2012**, *2* (11), 2302.
(197) Miao, F.; Tao, B.; Chu, P. K. *Dalton Trans.* **2012**, *41* (16), 5055.
(198) Lee, K.; Kang, S. W.; Lee, S.-U.; Park, K.-H.; Lee, Y. W.; Han, S. W. *ACS Appl. Mater. Interfaces* **2012**, *4* (8), 4208–4214.
(199) Zhang, Z.; Xin, L.; Sun, K.; Li, W. *Int. J. Hydrog. Energy* **2011**, *36* (20), 12686–12697.
(200) Qi, Z.; Geng, H.; Wang, X.; Zhao, C.; Ji, H.; Zhang, C.; Xu, J.; Zhang, Z. *J. Power Sources* **2011**, *196* (14), 5823–5828.
(201) Miao, F.; Tao, B. *Electrochimica Acta* **2011**, *56* (19), 6709–6714.
(202) Li, Y. S.; Zhao, T. S. *Int. J. Hydrog. Energy* **2011**, *36* (13), 7707–7713.
(203) Shen, S. Y.; Zhao, T. S.; Xu, J. B.; Li, Y. S. *J. Power Sources* **2010**, *195* (4), 1001–1006.
(204) Maiyalagan, T.; Scott, K. *J. Power Sources* **2010**, *195* (16), 5246–5251.
(205) Singh, R. N.; Singh, A.; Anindita. *Carbon* **2009**, *47* (1), 271–278.
(206) Monyoncho, E. A.; Ntais, S.; Soares, F.; Woo, T. K.; Baranova, E. A. *J. Power Sources* **2015**, *287*, 139–149.
(207) Ma, L.; He, H.; Hsu, A.; Chen, R. *J. Power Sources* **2013**, *241*, 696–702.
(208) Ma, L.; Hsu, A.; Chen, R. *ECS Trans.* **2013**, *58* (1), 1321–1326.
(209) Anindita, A. *Open Catal. J.* **2011**, *4* (1), 88–99.
(210) Chen, Y.; Zhuang, L.; Lu, J. *Chin. J. Catal.* **2007**, *28* (10), 870–874.
(211) Bagchi, J.; Bhattacharya, S. K. *Transit. Met. Chem.* **2007**, *32* (1), 47–55.
(212) Cai, K.; Liao, Y.; Zhang, H.; Liu, J.; Lu, Z.; Huang, Z.; Chen, S.; Han, H. *ACS Appl. Mater. Interfaces* **2016**, *8* (20), 12792–12797.
(213) Hong, W.; Shang, C.; Wang, J.; Wang, E. *Electrochem. Commun.* **2014**, *48*, 65–68.
(214) Smiljanić, M.; Rakočević, Z.; Strbac, S. B. *Int. J. Electrochem. Sci.* **2013**, *8* (4), 4941–4954.
(215) Xu, J. B.; Zhao, T. S.; Shen, S. Y.; Li, Y. S. *Int. J. Hydrog. Energy* **2010**, *35* (13), 6490–6500.

(216) Cheng, F.; Dai, X.; Wang, H.; Jiang, S. P.; Zhang, M.; Xu, C. *Electrochimica Acta* **2010**, *55* (7), 2295–2298.
(217) Zhu, L. D.; Zhao, T. S.; Xu, J. B.; Liang, Z. X. *J. Power Sources* **2009**, *187* (1), 80–84.
(218) He, Q.; Chen, W.; Mukerjee, S.; Chen, S.; Laufek, F. *J. Power Sources* **2009**, *187* (2), 298–304.
(219) Neto, A. O.; da Silva, S. G.; Buzzo, G. S.; de Souza, R. F. B.; Assumpção, M. H. M. T.; Spinacé, E. V.; Silva, J. C. M. *Ionics* **2015**, *21* (2), 487–495.
(220) Shen, S. Y.; Zhao, T. S.; Xu, J. B. *Electrochimica Acta* **2010**, *55* (28), 9179–9184.
(221) Wang, P.; Lin, X.; Yang, B.; Jin, J.-M.; Hardacre, C.; Yu, N.-F.; Sun, S.-G.; Lin, W.-F. *Electrochimica Acta* **2015**, *162*, 290–299.
(222) Cai, J.; Huang, Y.; Guo, Y. *Electrochimica Acta* **2013**, *99*, 22–29.
(223) Neto, A. O.; Tusi, M. M.; de Oliveira Polanco, N. S.; da Silva, S. G.; Coelho dos Santos, M.; Spinacé, E. V. *Int. J. Hydrog. Energy* **2011**, *36* (17), 10522–10526.
(224) Du, W.; Mackenzie, K. E.; Milano, D. F.; Deskins, N. A.; Su, D.; Teng, X. *ACS Catal.* **2012**, *2* (2), 287–297.
(225) Yan, Z.; Zhang, M.; Xie, J.; Shen, P. K. *J. Power Sources* **2013**, *243*, 336–342.
(226) Liu, Q.; Liu, M.; Li, Q.; Xu, Q. *Catalysts* **2015**, *5* (3), 1068–1078.
(227) Yang, J.; Xie, Y.; Wang, R.; Jiang, B.; Tian, C.; Mu, G.; Yin, J.; Wang, B.; Fu, H. *ACS Appl. Mater. Interfaces* **2013**, *5* (14), 6571–6579.
(228) Serov, A.; Asset, T.; Padilla, M.; Matanovic, I.; Martinez, U.; Roy, A.; Artyushkova, K.; Chatenet, M.; Maillard, F.; Bayer, D.; Cremers, C.; Atanassov, P. *Appl. Catal. B Environ.* **2016**, *191*, 76–85.
(229) Mao, H.; Huang, T.; Yu, A. *Electrochimica Acta* **2015**, *174*, 1–7.
(230) Liu, H.; Adzic, R. R.; Wong, S. S. *ACS Appl. Mater. Interfaces* **2015**, *7* (47), 26145–26157.
(231) Zhao, X.; Zhang, J.; Wang, L.; Liu, Z.; Chen, W. *J. Mater. Chem. A* **2014**, *2* (48), 20933–20938.
(232) Cai, J.; Zeng, Y.; Guo, Y. *J. Power Sources* **2014**, *270*, 257–261.
(233) Wang, K.-W.; Kang, W.-D.; Wei, Y.-C.; Liu, C.-W.; Su, P.-C.; Chen, H.-S.; Chung, S.-R. *ChemCatChem* **2012**, *4* (8), 1154–1161.
(234) Kang, W.-D.; Wei, Y.-C.; Liu, C.-W.; Wang, K.-W. *Electrochem. Commun.* **2011**, *13* (2), 162–165.
(235) Wang, A.-L.; He, X.-J.; Lu, X.-F.; Xu, H.; Tong, Y.-X.; Li, G.-R. *Angew. Chem. Int. Ed.* **2015**, *54* (12), 3669–3673.
(236) Aguirre, M. del C.; Fuentes, A. S.; Filippin, A. F. *Procedia Mater. Sci.* **2015**, *9*, 3–12.
(237) Liu, J.; Ye, J.; Xu, C.; Jiang, S. P.; Tong, Y. *Electrochem. Commun.* **2007**, *9* (9), 2334–2339.
(238) Maksić, A.; Smiljanić, M.; Miljanić, Š.; Rakočević, Z.; Štrbac, S. *Electrochimica Acta* **2016**, *209*, 323–331.
(239) Sneed, B. T.; Brodsky, C. N.; Kuo, C.-H.; Lamontagne, L. K.; Jiang, Y.; Wang, Y.; Tao, F. (Feng); Huang, W.; Tsung, C.-K. *J. Am. Chem. Soc.* **2013**, *135* (39), 14691–14700.
(240) Cai, J.; Huang, Y.; Guo, Y. *Int. J. Hydrog. Energy* **2014**, *39* (32), 18256–18263.
(241) Cai, J.; Huang, Y.; Guo, Y. *Appl. Catal. B Environ.* **2014**, *150–151*, 230–237.
(242) Yu, H.; Zhou, D.; Zhu, H. *J. Solid State Electrochem.* **2014**, *18* (1), 125–131.
(243) Wang, Y.; Nguyen, T. S.; Liu, X.; Wang, X. *J. Power Sources* **2010**, *195* (9), 2619–2622.
(244) Zhan, J.; Cai, M.; Zhang, C.; Wang, C. *Electrochim Acta* **2015**, *154*, 70–76.
(245) Ren, L.; Hui, K. S.; Hui, K. N. *J Mater Chem A* **2013**, *1* (18), 5689–5694.
(246) Hassan, H. B.; Hamid, Z. A. *Int. J. Hydrog. Energy* **2011**, *36* (8), 5117–5127.
(247) Yi, Y.; Uhm, S.; Lee, J. *Electrocatalysis* **2010**, *1* (2–3), 104–107.
(248) Tarasevich, M. R.; Bogdanovskaya, V. A.; Mazin, P. V. *Russ. J. Electrochem.* **2010**, *46* (5), 542–551.
(249) Hayashi, A.; Tatsumisago, M.; Tadanaga, K.; Furukawa, Y. *Adv. Mater.* **2010**, *22* (39), 4401–4404.
(250) Cardoso, W. S.; Dias, V. L. N.; Costa, W. M.; Araujo Rodrigues, I.; Marques, E. P.; Sousa, A. G.; Boaventura, J.; Bezerra, C. W. B.; Song, C.; Liu, H.; Zhang, J.; Marques, A. L. B. *J Appl Electrochem* **2009**, *39* (1), 55–64.
(251) Tsivadze, A. Y.; Tarasevich, M. R.; Efremov, B. N.; Kapustina, N. A.; Mazin, P. V. *Dokl. Phys. Chem.* **2007**, *415* (6), 234–236.

(252) Kim, J.-W.; Park, S.-M. *J Electrochem Soc* **2003**, *150* (11), E560–E566.
(253) Casella, I. G.; Cataldi, T. R. I.; Salvi, A. M.; Desimoni, E. *Anal. Chem.* **1993**, *65* (21), 3143–50.
(254) Jin, Z.; Wang, Q.; Zheng, W.; Cui, X. *ACS Appl. Mater. Interfaces* **2016**, *8* (8), 5273–5279.
(255) Leelavathi, A.; Madras, G.; Ravishankar, N. *J. Am. Chem. Soc.* **2014**.
(256) Koper, M. T. M.; Kwon, Y.; Rodriguez, P. *Nat. Chem.* **2012**, *4* (3).
(257) de Lima, R. B.; Varela, H. *Gold Bull.* **2008**, *41* (1), 15–22.
(258) Tremiliosi-Filho, G.; Gonzalez, E. R.; Motheo, A. J.; Belgsir, E. M.; Leger, J.-M.; Lamy, C. *J. Electroanal. Chem.* **1998**, *444* (1), 31–39.
(259) Avramov-Ivic, M.; Jovanovic, V.; Vlajnic, G.; Popic, J. *J Electroanal Chem* **1997**, *423* (1–2), 119–124.
(260) Zhang, F.; Zhou, D.; Zhang, Z.; Zhou, M.; Wang, Q. *RSC Adv* **2015**, *5* (111), 91829–91835.
(261) Resta, A.; Blomquist, J.; Gustafson, J.; Karhu, H.; Mikkelsen, A.; Lundgren, E.; Uvdal, P.; Andersen, J. N. *Surf Sci* **2006**, *600* (24), 1136–1141.
(262) Tarasevich, M. R.; Korchagin, O. V. *Russ. J. Electrochem.* **2013**, *49* (7), 600–618.
(263) M. Koper, M. T.; S. Lai, S. C. *Faraday Discuss.* **2009**, *140* (0), 399–416.
(264) Asiri, H. A.; Anderson, A. B. *J Electrochem Soc* **2015**, *162* (1), F115–F122.
(265) Sheng, T.; Lin, W.-F.; Hardacre, C.; Hu, P. *J. Phys. Chem. C* **2014**, *118* (11), 5762–5772.
(266) Hibbitts, D. D.; Neurock, M. *J. Catal.* **2013**, *299* (0), 261–271.
(267) Buso-Rogero, C.; Grozovski, V.; Vidal-Iglesias, F. J.; Solla-Gullon, J.; Herrero, E.; Feliu, J. M. *J Mater Chem A* **2013**, *1* (24), 7068–7076.
(268) Melke, J.; Schoekel, A.; Gerteisen, D.; Dixon, D.; Ettingshausen, F.; Cremers, C.; Roth, C.; Ramaker, D. E. *J. Phys. Chem. C* **2012**, *116* (4), 2838–2849.
(269) Kavanagh, R.; Cao, X.-M.; Lin, W.-F.; Hardacre, C.; Hu, P. *Angew. Chem. Int. Ed.* **2012**, *51* (7), 1572–1575.
(270) Christensen, P. A.; Jones, S. W. M.; Hamnett, A. *J. Phys. Chem. C* **2012**, *116* (46), 24681–24689.
(271) Zope, B. N.; Hibbitts, D. D.; Neurock, M.; Davis, R. J. *Science* **2010**, *330* (6000), 74–78.
(272) Melke, J.; Schoekel, A.; Dixon, D.; Cremers, C.; Ramaker, D. E.; Roth, C. *J Phys Chem C* **2010**, *114* (13), 5914–5925.
(273) Colmati, F.; Tremiliosi-Filho, G.; Gonzalez, E. R.; Berná, A.; Herrero, E.; Feliu, J. M. *Faraday Discuss.* **2008**, *140*, 379–97-37.
(274) Paik, Y.; Kim, S.-S.; Han, O. H. *Electrochem. Commun.* **2009**, *11* (2), 302–304.
(275) Wang, H.-F.; Liu, Z.-P. *J Phys Chem C* **2007**, *111* (33), 12157–12160.
(276) Geraldes, A. N.; Furtunato da Silva, D.; Martins da Silva, J. C.; Antonio de Sá, O.; Spinacé, E. V.; Neto, A. O.; Coelho dos Santos, M. *J. Power Sources* **2015**, *275*, 189–199.
(277) Yang, Y.-Y.; Ren, J.; Li, Q.-X.; Zhou, Z.-Y.; Sun, S.-G.; Cai, W.-B. *ACS Catal* **2014**, *4* (3), 798–803.
(278) Zhou, Z.-Y.; Wang, Q.; Lin, J.-L.; Tian, N.; Sun, S.-G. *Electrochimica Acta* **2010**, *55* (27), 7995–7999.
(279) Christensen, P. A.; Hamnett, A.; Linares-Moya, D. *Phys. Chem. Chem. Phys.* **2011**, *13* (24), 11739–11747.
(280) Rao, V.; Cremers, C.; Stimming, U.; Cao, L.; Sun, S.; Yan, S.; Sun, G.; Xin, Q. *J. Electrochem. Soc.* **2007**, *154* (11), 1138.
(281) Zhou, Z.-Y.; Sun, S.-G. *Electrochim Acta* **2005**, *50* (25–26), 5163–5171.
(282) Bayer, D.; Cremers, C.; Baltruschat, H.; Tuebke, J. *ECS Trans* **2010**, *25* (13, Alkaline Electrochemical Power Sources), 85–93.
(283) Xia, X. H.; Liess, H.-D.; Iwasita, T. *J. Electroanal. Chem.* **1997**, *437* (1–2), 233–240.
(284) Tarnowski, D. J.; Korzeniewski, C. *J Phys Chem B* **1997**, *101* (2), 253–258.
(285) Wang, H.-F.; Liu, Z.-P. *J. Am. Chem. Soc.* **2008**, *130* (33), 10996–11004.
(286) Fang, X.; Wang, L.; Shen, P. K.; Cui, G.; Bianchini, C. *J. Power Sources* **2010**, *195* (5), 1375–1378.
(287) Christensen, P. A.; Linares-Moya, D. *J. Phys. Chem. C* **2010**, *114* (2), 1094–1101.

(288) Christensen, P. A.; Jones, S. W. M. *J. Phys. Chem. C* **2014**, *118* (51), 29760–29769.
(289) Monyoncho, E. A.; Steinmann, S. N.; Michel, C.; Baranova, E. A.; Woo, T. K.; Sautet, P. *ACS Catal.* **2016**, *6*, 4894–4906.
(290) Varcoe, J. R.; Atanassov, P.; Dekel, D. R.; Herring, A. M.; Hickner, M. A.; Kohl, P. A.; Kucernak, A. R.; Mustain, W. E.; Nijmeijer, K.; Scott, K.; Xu, T.; Zhuang, L.; Lin Zhuang; Plamen Atanassov; Kitty Nijmeijer; Keith Scott; Tongwen Xu. *Energy Environ. Sci.* **2014**, *7* (10), 3135–3191.
(291) Zeng, R.; Handsel, J.; Poynton, S. D.; Roberts, A. J.; Slade, R. C. T.; Herman, H.; Apperley, D. C.; Varcoe, J. R. *Energy Environ. Sci.* **2011**, *4* (12), 4925–4928.
(292) Baranova, E. A.; Amir, T.; Mercier, P. H. J.; Patarachao, B.; Wang, D.; Le Page, Y. *J. Appl. Electrochem.* **2010**, *40* (10), 1767–1777.
(293) In *Iron Oxides in the Laboratary*; Schwertmann, U., Cornell, R. M., Eds.; Wiley-VCH Verlag GmbH: Weinheim, Germany, 2000; pp 27–54.
(294) Brun, M.; Berthet, A.; Bertolini, J. . *J. Electron Spectrosc. Relat. Phenom.* **1999**, *104* (1–3), 55–60.
(295) Figlarz, M.; Fievet, F.; Lagier, J. P. Reduction of metal compounds to metal powders by polyols., June 22, 1984.
(296) Johansson, G.; Hedman, J.; Berndtsson, A.; Klasson, M.; Nilsson, R. *J. Electron Spectrosc. Relat. Phenom.* **1973**, *2* (3), 295–317.
(297) Kissinger, P. T.; Heineman, W. R. *J. Chem. Educ.* **1983**, *60* (9), 702.
(298) BioLogic SS. Biologic Science Instruments 2013.
(299) Hüfner, S.; Wertheim, G. K. *Phys. Rev. B* **1975**, *11* (2), 678–683.
(300) Kresse, G.; Hafner, J. *Phys. Rev. B* **1993**, *48* (17), 13115–13118.
(301) Kresse, G.; Furthmüller, J. *Phys. Rev. B* **1996**, *54* (16), 11169–11186.
(302) Perdew, J. P.; Burke, K.; Ernzerhof, M. *Phys. Rev. Lett.* **1996**, *77* (18), 3865–3868.
(303) Kresse, G.; Joubert, D. *Phys. Rev. B* **1999**, *59* (3), 1758–1775.
(304) Blöchl, P. E. *Phys. Rev. B* **1994**, *50* (24), 17953–17979.
(305) Methfessel, M.; Paxton, A. T. *Phys. Rev. B* **1989**, *40* (6), 3616–3621.
(306) Henkelman, G.; Jónsson, H. *J. Chem. Phys.* **2000**, *113* (22), 9978.
(307) Paul Fleurat-Lessard - Reaction Path http://perso.ens-lyon.fr/paul.fleurat-lessard/ReactionPath.html (accessed Nov 21, 2016).
(308) Henkelman, G.; Jónsson, H. *J. Chem. Phys.* **1999**, *111* (15), 7010.
(309) Karhánek, D.; Bučko, T.; Hafner, J. *J. Phys. Condens. Matter* **2010**, *22* (26), 265006.
(310) Mennucci, B.; Cancès, E.; Tomasi, J. *J. Phys. Chem. B* **1997**, *101* (49), 10506–10517.
(311) Frisch, M. J.; Fox, D. J.; Cioslowski, J.; Ortiz, J. V.; Foresman, J. B.; Farkas, O.; Daniels, A. D.; Dapprich, S.; Dannenberg, J. J.; Salvador, P.; Voth, G. A.; Zakrzewski, V. G.; Morokuma, K.; Martin, R. L.; Ochterski, J. W.; Pomelli, C.; Cammi, R.; Austin, A. J.; Yazyev, O.; Stratmann, R. E.; Gomperts, R.; Jaramillo, J.; Adamo, C.; Bakken, V.; Cross, J. B.; Knox, J. E.; Klene, M.; Millam, J. M.; Rega, N.; Cossi, M.; Tomasi, J.; Iyengar, S. S.; Burant, J. C.; Rendell, A.; Raghavachari, K.; Normand, J.; Kobayashi, R.; Staroverov, V. N.; Kudin, K. N.; Brothers, E.; Heyd, J. J.; Bearpark, M.; Ogliaro, F.; Peralta, J. J. E.; Montgomery, J. A.; Vreven, T.; Nakai, H.; Kitao, O.; Honda, Y.; Nakajima, T.; Ishida, M.; Hasegawa, J.; Fukuda, R.; Toyota, K.; Ehara, M.; Hada, M.; Sonnenberg, J. L.; Zheng, G.; Bloino, J.; Izmaylov, A. F.; Hratchian, H. P.; Li, X.; Caricato, M.; Nakatsuji, H.; Petersson, G. A.; Mennucci, B.; Barone, V.; Scalmani, G.; Cheeseman, J. R.; Robb, M. A.; Scuseria, G. E.; Schlegel, H. B.; Trucks, G. W. *Gaussian09*; 2013.
(312) Ashley, K.; Pons, S. *Chem Rev* **1988**, *88* (4), 673–695.
(313) Brand, I. *Z Phys Chem Muenchen Ger* **2016**, *230* (2), 133–183.
(314) Wieckowski, A.; Korzeniewski, C.; Braunschweig, B. In *Vib. Spectrosc. Electrified Interfaces*; Cuesta, A., Ed.; John Wiley & Sons, Inc., 2013; pp 266–306.
(315) Mudiyanselage, K.; Stacchiola, D. J. In *In-situ Characterization of Heterogeneous Catalysts*; John Wiley & Sons, Inc., 2013; pp 209–239.

(316) Kycia, A. H.; Su, Z.; Brosseau, C. L.; Lipkowski, J. In *Vibrational spectroscopy at electrified interfaces*; John Wiley & Sons, 2013.
(317) Zamlynny, V.; Lipkowski, J. In *Advances in Electrochemical Science and Engineering*; Wiley-VCH Verlag GmbH, 2006; Vol. 9, pp 315–376.
(318) Perez-Villar, S.; Lanz, P.; Schneider, H.; Novak, P. *Electrochim Acta* **2013**, *106*, 506–515.
(319) Lai, S. C. S.; Kleyn, S. E. F.; Rosca, V.; Koper, M. T. M. *J. Phys. Chem. C* **2008**, *112* (48), 19080–19087.
(320) Shen, Y. R. *J. Phys. Chem. C* **2012**, *116* (29), 15505–15509.
(321) Kutz, R. B.; Braunschweig, B.; Mukherjee, P.; Dlott, D. D.; Wieckowski, A. *J. Phys. Chem. Lett.* **2011**, *2* (17), 2236–2240.
(322) Greenler, R. G. *J. Chem. Phys.* **1966**, *44* (1), 310–315.
(323) Greenler, R. G. *J. Chem. Phys.* **1969**, *50* (5), 1963–1968.
(324) Bewick, A.; Kunimatsu, K. *Surf. Sci.* **1980**, *101* (1–3), 131–138.
(325) Davidson, T.; Pons, B. S.; Bewick, A.; Schmidt, P. P. *J. Electroanal. Chem. Interfacial Electrochem.* **1981**, *125* (1), 237–241.
(326) Pons, S. *J. Electroanal. Chem. Interfacial Electrochem.* **1983**, *150* (1–2), 495–504.
(327) Leung, L.-W. H.; Chang, S.-C.; Weaver, M. J. *J. Electroanal. Chem. Interfacial Electrochem.* **1989**, *266* (2), 317–336.
(328) Bewick, A.; Kunimatsu, K.; Pons, B. S. *Electrochim Acta* **1980**, *25* (4), 465–468.
(329) Bewick, A.; Kunimatsu, K.; Pons, B. S.; Russell, J. W. *J. Electroanal. Chem. Interfacial Electrochem.* **1984**, *160* (1–2), 47–61.
(330) Golden, W. G.; Dunn, D. S.; Overend, J. *J. Catal.* **1981**, *71* (2), 395–404.
(331) Golden, W. G.; Kunimatsu, K.; Seki, H. *J. Phys. Chem.* **1984**, *88* (7), 1275–1277.
(332) Bethune, D. S.; Luntz, A. C.; Sass, J. K.; Roe, D. K. *Surf Sci* **1988**, *197* (1–2), 44–66.
(333) Datta, M.; Datta, A. *Spectrosc. Lett.* **1986**, *19* (9), 993–1037.
(334) Faguy, P. W.; Richmond, W. N. *J. Electroanal. Chem.* **1996**, *410* (1), 109–113.
(335) Faguy, P. W.; Richmond, W. N.; Jackson, R. S.; Weibel, S. C.; Ball, G.; Payer, J. H. *Appl. Spectrosc.* **1998**, *52* (4), 557–564.
(336) Christensen, P. A. In *Encycl. Electrochem.*; Wiley-VCH Verlag GmbH & Co. KGaA, 2003; Vol. 3, pp 530–571.
(337) Buffeteau, T.; Desbat, B.; Turlet, J. M. *Appl Spectrosc* **1991**, *45* (3), 380–389.
(338) Buffeteau, T.; Desbat, B.; Blaudez, D.; Turlet, J. M. *Appl. Spectrosc.* **2000**, *54* (11), 1646–1650.
(339) Datta, M.; Freeman, J. J.; Jansson, R. E. W. *Spectrosc. Lett.* **1985**, *18* (4), 273–282.
(340) Datta, M.; Jansson, R. E. W.; Freeman, J. J. *Spectrosc Lett* **1986**, *19* (2), 129–139.
(341) Gollas, B.; Schennach, R.; Vieira, L. *Phys Chem Chem Phys* **2015**, *17* (19), 12870–12880.
(342) Green, M. J.; Barner, B. J.; Corn, R. M. *Rev Sci Instrum* **1991**, *62* (6), 1426–1430.
(343) Barner, B. J.; Green, M. J.; Saez, E. I.; Corn, R. M. *Anal Chem* **1991**, *63* (1), 55–60.
(344) Blaudez, D.; Buffeteau, T.; Cornut, J. C.; Desbat, B.; Escafre, N.; Pezolet, M.; Turlet, J. M. *Thin Solid Films* **1994**, *242* (1–2), 146–150.
(345) Meier, D. M.; Urakawa, A.; Mäder, R.; Baiker, A. *Rev. Sci. Instrum.* **2009**, *80* (9).
(346) Seki, H.; Kunimatsu, K.; Golden, W. G. *Appl Spectrosc* **1985**, *39* (3), 437–443.
(347) Foley, J. K.; Pons, S. *Anal. Chem.* **1985**, *57* (8), 945A–956A.
(348) Roe, D. K.; Sass, J. K.; Bethune, D. S.; Luntz, A. C. *J. Electroanal. Chem. Interfacial Electrochem.* **1987**, *216* (1–2), 293–301.
(349) Blatt, S.; Roscoe, S. G.; Zamlynny, V. *J. Electroanal. Chem.* **2010**, *649*, 102–109.
(350) Jackson, R.; Zamlynny, V. *Electrochimica Acta* **2008**, *53*, 6768–6777.
(351) HANSEN, W. N. *J Opt Soc Am* **1968**, *58* (3), 380–388.
(352) Matsui, M.; Saito, T. Infrared reflection absorption spectroscopy apparatus with improved sensitivity for electrochemical cells. JP2009250824A, October 29, 2009.
(353) Blaudez, D.; Castano, S.; Desbat, B. In *Biointerface Characterization by Advanced IR Spectroscopy*; Elsevier, 2011; pp 27–55.

(354) Zhang, L.; Chang, Q.; Chen, H.; Shao, M. *Nano Energy* **2016**.
(355) Cui, G.; Song, S.; Shen, P. K.; Kowal, A.; Bianchini, C. *J. Phys. Chem. C* **2009**, *113* (35), 15639–15642.
(356) Galea, N.; Knapp, D.; Ziegler, T. *J. Catal.* **2007**, *247* (1), 20–33.
(357) Guo, W.; Li, M.; Lu, X.; Zhu, H.; Li, Y.; Li, S.; Zhao, L. *Dalton Trans* **2013**, *42* (6), 2309–2318.
(358) Li, M.; Guo, W.; Jiang, R.; Zhao, L.; Shan, H. *Langmuir* **2010**, *26* (3), 1879–1888.
(359) Tereshchuk, P.; Da Silva, J. L. F. *J. Phys. Chem. C* **2012**, *116* (46), 24695–24705.
(360) Wang, E. D.; Xu, J. B.; Zhao, T. S. *J. Phys. Chem. C* **2010**, *114* (23), 10489–10497.
(361) Coussan, S.; Bouteiller, Y.; Perchard, J. P.; Zheng, W. Q. *J. Phys. Chem. A* **1998**, *102* (29), 5789–5793.
(362) Grimme, S.; Antony, J.; Ehrlich, S.; Krieg, H. *J. Chem. Phys.* **2010**, *132* (15), 154104.
(363) Tkatchenko, A.; Scheffler, M. *Phys. Rev. Lett.* **2009**, *102* (7).
(364) Grimme, S. *J. Comput. Chem.* **2006**, *27* (15), 1787–1799.
(365) Department of Commerce, U. S. *Computational Chemistry Comparison and Benchmark Database*; U.S Department of Commerce: USA, 2013.
(366) Humphrey, W.; Dalke, A.; Schulten, K. *J. Mol. Graph.* **1996**, *14* (1), 33–38.
(367) Accelrys Materials Studio - Scientific Computing - Confluence https://confluence.csiro.au/display/SC/Accelrys+Materials+Studio (accessed Dec 1, 2016).
(368) Momma, K.; Izumi, F. *J. Appl. Crystallogr.* **2011**, *44* (6), 1272–1276.
(369) Ammam, M.; Easton, E. B. *J. Power Sources* **2012**, *215*, 188–198.
(370) Bianchini, C.; Shen, P. K. *Chem. Rev.* **2009**, *109* (9), 4183–4206.
(371) Feng, Y.-Y.; Liu, Z.-H.; Xu, Y.; Wang, P.; Wang, W.-H.; Kong, D.-S. *J. Power Sources* **2013**, *232*, 99–105.
(372) Yu, E. H.; Krewer, U.; Scott, K. *Energies* **2010**, *3* (8), 1499–1528.
(373) Colle, V. D.; Berná, A.; Tremiliosi-Filho, G.; Herrero, E.; Feliu, J. M. *Phys. Chem. Chem. Phys.* **2008**, *10* (25), 3766.
(374) Yi, Q.; Niu, F.; Song, L.; Liu, X.; Nie, H. *Electroanalysis* **2011**, *23* (9), 2232–2240.
(375) Bagchi, J.; Bhattacharya, S. K. *Transit. Met. Chem.* **2008**, *33* (1), 113–120.
(376) Correia, M.; Moghieb, A. M.; Goforth, S.; McElwee-White, L. 2009; pp 13–21.
(377) Sun, S.; Jusys, Z.; Behm, R. J. *J. Power Sources* **2013**, *231*, 122–133.
(378) Storm, J.; Lambert, R. M.; Memmel, N.; Onsgaard, J.; Taglauer, E. *Surf. Sci.* **1999**, *436* (1–3), 259–268.
(379) Curtarolo, S.; Morgan, D.; Ceder, G. *Calphad* **2005**, *29* (3), 163–211.
(380) Tollefsen, H.; Laastad, E. O.; Raaen, S. *Surf. Sci.* **2009**, *603* (1), 197–202.
(381) Tura, J. M.; Regull, P.; Victori, L.; de Castellar, M. D. *Surf. Interface Anal.* **1988**, *11* (8), 447–449.
(382) Lewerenz, H. J.; Stucki, S.; Kötz, R. *Surf. Sci.* **1983**, *126* (1–3), 463–468.
(383) Liang, Y.; Li, J.; Xu, Q.-C.; Hu, R.-Z.; Lin, J.-D.; Liao, D.-W. *J. Alloys Compd.* **2008**, *465* (1–2), 296–304.
(384) *Standard potentials in aqueous solution*, 1st ed.; Bard, A. J., Parsons, R., Jordan, J., International Union of Pure and Applied Chemistry, Eds.; Monographs in electroanalytical chemistry and electrochemistry; M. Dekker: New York, 1985.
(385) Aricò, A. S.; Baglio, V.; Di Blasi, A.; Modica, E.; Antonucci, P. L.; Antonucci, V. *J. Electroanal. Chem.* **2003**, *557*, 167–176.
(386) *Practical surface analysis*, 2nd ed.; Briggs, D., Seah, M. P., Eds.; Wiley ; Salle + Sauerländer: Chichester ; New York : Aarau, 1990.
(387) Allagui, A.; Oudah, M.; Tuaev, X.; Ntais, S.; Almomani, F.; Baranova, E. A. *Int. J. Hydrog. Energy* **2013**, *38* (5), 2455–2463.
(388) Thepkaew, J.; Therdthianwong, S.; Therdthianwong, A.; Kucernak, A.; Wongyao, N. *Int. J. Hydrog. Energy* **2013**, *38* (22), 9454–9463.
(389) Fisher, J. M.; Cabello-Moreno, N.; Christian, E.; Thompsett, D. *Electrochem. Solid-State Lett.* **2009**, *12* (5), B77.

(390) López-Cudero, A.; Cuesta, A.; Gutiérrez, C. *J. Electroanal. Chem.* **2005**, *579* (1), 1–12.
(391) López-Cudero, A.; Cuesta, Á.; Gutiérrez, C. *J. Electroanal. Chem.* **2006**, *586* (2), 204–216.
(392) Cuesta, A.; Couto, A.; Rincón, A.; Pérez, M. C.; López-Cudero, A.; Gutiérrez, C. *J. Electroanal. Chem.* **2006**, *586* (2), 184–195.
(393) Rolison, D. R.; Hagans, P. L.; Swider, K. E.; Long, J. W. *Langmuir* **1999**, *15* (3), 774–779.
(394) Liang, Z. X.; Zhao, T. S.; Xu, J. B.; Zhu, L. D. *Electrochimica Acta* **2009**, *54* (8), 2203–2208.
(395) Xiao, L.; Zhuang, L.; Liu, Y.; Lu, J. *J. Am. Chem. Soc.* **2009**, *131* (2), 602–608.
(396) Mériaudeau, P.; Dufaux, M.; Naccache, C. In *Strong Metal-Support Interactions*; Baker, R. T. K., Tauster, S. J., Dumesic, J. A., Eds.; American Chemical Society: Washington, DC, 1986; Vol. 298, pp 118–122.
(397) Demmin, R. A.; Ko, C. S.; Gorte, R. J. In *Strong Metal-Support Interactions*; Baker, R. T. K., Tauster, S. J., Dumesic, J. A., Eds.; American Chemical Society: Washington, DC, 1986; Vol. 298, pp 48–53.
(398) Yaldagard, M.; Jahanshahi, M.; Seghatoleslami, N. *World J. Nano Sci. Eng.* **2013**, *3* (4), 121–153.
(399) Silva, J. C. M.; De Souza, R. F. B.; Parreira, L. S.; Neto, E. T.; Calegaro, M. L.; Santos, M. C. *Appl. Catal. B Environ.* **2010**, *99* (1–2), 265–271.
(400) De Souza, R. F. B.; Silva, J. C. M.; Assumpção, M. H. M. T.; Neto, A. O.; Santos, M. C. *Electrochimica Acta* **2014**, *117*, 292–298.
(401) Meriaudeau, P.; Dutel, J. F.; Dufaux, M.; Naccache, C. In *Studies in Surface Science and Catalysis*; Elsevier, 1982; Vol. 11, pp 95–104.
(402) Su, L.; Jia, W.; Schempf, A.; Lei, Y. *Electrochem. Commun.* **2009**, *11* (11), 2199–2202.
(403) Wang, M.; Guo, D.; Li, H. *J. Solid State Chem.* **2005**, *178* (6), 1996–2000.
(404) Mattos, L. V.; Noronha, F. B. *J. Power Sources* **2005**, *152*, 50–59.
(405) Meher, S. K.; Rao, G. R. *ACS Catal.* **2012**, *2* (12), 2795–2809.
(406) Birkholz, M.; Fewster, P. F. *Thin film analysis by X-Ray scattering*, 2nd reprint.; WILEY-VCH: Weinheim, 2009.
(407) Baranova, E. A.; Le Page, Y.; Ilin, D.; Bock, C.; MacDougall, B.; Mercier, P. H. J. *J. Alloys Compd.* **2009**, *471* (1–2), 387–394.
(408) Militello, M. C. *Surf. Sci. Spectra* **1994**, *3* (4), 402.
(409) Mahata, N.; Vishwanathan, V. *J. Catal.* **2000**, *196* (2), 262–270.
(410) Jin, M.; Park, J.-N.; Shon, J. K.; Kim, J. H.; Li, Z.; Park, Y.-K.; Kim, J. M. *Catal. Today* **2012**, *185* (1), 183–190.
(411) Ramaker, D. E.; de Graaf, J.; van Veen, J. A. R.; Koningsberger, D. C. *J. Catal.* **2001**, *203* (1), 7–17.
(412) Bernal, S.; Calvino, J. .; Cauqui, M. .; Gatica, J. .; Larese, C.; Pérez Omil, J. .; Pintado, J. . *Catal. Today* **1999**, *50* (2), 175–206.
(413) Allred, A. L. *J. Inorg. Nucl. Chem.* **1961**, *17* (3–4), 215–221.
(414) *Catalysis by Ceria and Related Materials*; Trovarelli, A., Ed.; Hutchings, G. J., Series Ed.; Catalytic Science Series; Imperial College Press, 2002; Vol. 2.
(415) Dole, H. A. E.; Safady, L. F.; Ntais, S.; Couillard, M.; Baranova, E. A. *J. Catal.* **2014**, *318*, 85–94.
(416) Chen, S.-Z.; Zhang, P.-Y.; Zhu, W.-P.; Chen, L.; Xu, S.-M. *Appl. Surf. Sci.* **2006**, *252* (20), 7532–7538.
(417) Taylor, J. A.; Lancaster, G. M.; Rabalais, J. W. *J. Electron Spectrosc. Relat. Phenom.* **1978**, *13* (3), 435–444.
(418) Vidaković, T.; Christov, M.; Sundmacher, K. *Electrochimica Acta* **2007**, *52* (18), 5606–5613.
(419) Fang, Y.-H.; Liu, Z.-P. *J. Phys. Chem. C* **2009**, *113* (22), 9765–9772.
(420) Nguyen, S. T.; Law, H. M.; Nguyen, H. T.; Kristian, N.; Wang, S.; Chan, S. H.; Wang, X. *Appl. Catal. B Environ.* **2009**, *91* (1–2), 507–515.
(421) Singh-Miller, N. E.; Marzari, N. *Phys. Rev. B* **2009**, *80* (23).
(422) Gu, D.; Dey, S. K.; Majhi, P. *Appl. Phys. Lett.* **2006**, *89* (8), 82907.

(423) Li, W. Y.; Iburahim, A. A.; Goto, K.; Shimizu, R. *The Absolute AES is Coming; Work Functions and Transmission of CMA*; 2005.
(424) Warule, S. S.; Chaudhari, N. S.; Kale, B. B.; Patil, K. R.; Koinkar, P. M.; More, M. A.; Murakami, R. *J. Mater. Chem.* **2012**, *22* (18), 8887.
(425) Imanishi, A.; Tsuji, E.; Nakato, Y. *J. Phys. Chem. C* **2007**, *111* (5), 2128–2132.
(426) Islam, M. N.; Hakim, M. O. *J. Mater. Sci. Lett.* **1986**, *5* (1), 63–65.
(427) Schnur, S.; Groß, A. *Catal. Today* **2011**, *165* (1), 129–137.
(428) Delpeuch, A. B.; Chatenet, M.; Rau, M. S.; Cremers, C. *Phys Chem Chem Phys* **2015**, *17* (16), 10881–10893.
(429) Ferrin, P.; Mavrikakis, M. *J. Am. Chem. Soc.* **2009**, *131* (40), 14381–14389.
(430) Ferrin, P.; Nilekar, A. U.; Greeley, J.; Mavrikakis, M.; Rossmeisl, J. *Surf. Sci.* **2008**, *602* (21), 3424–3431.
(431) Rossmeisl, J.; Ferrin, P.; Tritsaris, G. A.; Nilekar, A. U.; Koh, S.; Bae, S. E.; Brankovic, S. R.; Strasser, P.; Mavrikakis, M. *Energy Environ. Sci.* **2012**, *5* (8), 8335.
(432) Anderson, A. B.; Albu, T. V. *J. Am. Chem. Soc.* **1999**, *121* (50), 11855–11863.
(433) Lozovoi, A. Y.; Alavi, A. *Phys. Rev. B* **2003**, *68* (24).
(434) Otani, M.; Sugino, O. *Phys. Rev. B* **2006**, *73* (11).
(435) Taylor, C. D.; Wasileski, S. A.; Filhol, J.-S.; Neurock, M. *Phys. Rev. B* **2006**, *73* (16).
(436) Skúlason, E.; Karlberg, G. S.; Rossmeisl, J.; Bligaard, T.; Greeley, J.; Jónsson, H.; Nørskov, J. K. *Phys Chem Chem Phys* **2007**, *9* (25), 3241–3250.
(437) Mathew, K.; Sundararaman, R.; Letchworth-Weaver, K.; Arias, T. A.; Hennig, R. G. *J. Chem. Phys.* **2014**, *140* (8), 84106.
(438) Jinnouchi, R.; Anderson, A. B. *Phys. Rev. B* **2008**, *77* (24).
(439) Filhol, J.-S.; Neurock, M. *Angew. Chem. Int. Ed.* **2006**, *45* (3), 402–406.
(440) Steinmann, S. N.; Michel, C.; Schwiedernoch, R.; Filhol, J.-S.; Sautet, P. *ChemPhysChem* **2015**, *16* (11), 2307–2311.
(441) Janik, M. J.; Taylor, C. D.; Neurock, M. *Top. Catal.* **2007**, *46* (3–4), 306–319.
(442) Fang, Y.-H.; Wei, G.-F.; Liu, Z.-P. *Catal. Today* **2013**, *202*, 98–104.
(443) Zhao, Y.; Li, X.; Schechter, J. M.; Yang, Y. *RSC Adv.* **2016**, *6* (7), 5384–5390.
(444) Habibi, B.; Mohammadyari, S. *Int. J. Hydrog. Energy* **2015**, *40* (34), 10833–10846.
(445) Ferreira Jr., R. S.; Janete Giz, M.; Camara, G. A. *J. Electroanal. Chem.* **2013**, *697*, 15–20.
(446) Rudolph, W. W.; Fischer, D.; Irmer, G. *Dalton Trans* **2014**, *43* (8), 3174–3185.
(447) Sutton, C. C. R.; Franks, G. V.; da Silva, G. *Spectrochim. Acta. A. Mol. Biomol. Spectrosc.* **2015**, *134*, 535–542.
(448) Alcala, R.; Mavrikakis, M.; Dumesic, J. A. *J Catal* **2003**, *218* (1), 178–190.
(449) Li, H.; Calle-Vallejo, F.; Kolb, M. J.; Kwon, Y.; Li, Y.; Koper, M. T. M. *J. Am. Chem. Soc.* **2013**, *135* (38), 14329–14338.
(450) Steinmann, S. N.; Michel, C.; Schwiedernoch, R.; Wu, M.; Sautet, P. *J. Catal.* **2016**, *343*, 240–247.
(451) Zaffran, J.; Michel, C.; Auneau, F.; Delbecq, F.; Sautet, P. *ACS Catal.* **2014**, *4* (2), 464–468.
(452) Michel, C.; Zaffran, J.; Ruppert, A. M.; Matras-Michalska, J.; Jędrzejczyk, M.; Grams, J.; Sautet, P. *Chem Commun* **2014**, *50* (83), 12450–12453.
(453) Loffreda, D.; Michel, C.; Delbecq, F.; Sautet, P. *J. Catal.* **2013**, *308*, 374–385.
(454) Mattos, L. V.; Jacobs, G.; Davis, B. H.; Noronha, F. B. *Chem. Rev.* **2012**, *112* (7), 4094–4123.
(455) Besson, M.; Gallezot, P.; Pinel, C. *Chem. Rev.* **2014**, *114* (3), 1827–1870.
(456) Sutton, J. E.; Vlachos, D. G. *Ind Eng Chem Res* **2014**, Ahead of Print.
(457) Wang, J.-H.; Lee, C. S.; Lin, M. C. *J. Phys. Chem. C* **2009**, *113* (16), 6681–6688.
(458) Alcala, R.; Shabaker, J. W.; Huber, G. W.; Sanchez-Castillo, M. A.; Dumesic, J. A. *J. Phys. Chem. B* **2005**, *109* (6), 2074–2085.
(459) Mavrikakis, M.; Doren, D. J.; Barteau, M. A. *J. Phys. Chem. B* **1998**, *102* (2), 394–399.
(460) Ferrin, P.; Simonetti, D.; Kandoi, S.; Kunkes, E.; Dumesic, J. A.; Norskov, J. K.; Mavrikakis, M. *J Am Chem Soc* **2009**, *131* (16), 5809–5815.

Table A.1: Summary of alkaline DEFCs tests showing the catalysts used, the operating conditions, and power density obtained

Anode	Synthesis	Support	Membrane (AEM)	Cathode	Operating conditions/Temperature	Power ($mW\ cm^{-2}$)	Ref
Pt	commercial	Ni	Teflon	MnO_2	1 M Ethanol + 3 M KOH/O_2 T = room temp	14.6	[1]
	$NaBH_4$ reduction	C	A-600, Tokuyama	Pt/C	1 M Ethanol + 0.5 M NaOH; T = 20-80 ^oC	12	[2]
	$NaBH_4$ reduction	C	Nafion® 117	Pt/C	J_{O2} = 150 $cm^3\ min^{-1}$; 2 M Ethanol + 2 M KOH; T = 75 ^{o} C	3	[3]
	Polyol and impregnation	C	Nafion® 115	Pt/C	J_{O2} = 120 $cm^3\ min^{-1}$; 1 M Ethanol; T = 90 ^oC	10.85	[4]
	Polyol	C	Nafion 117, DuPont	Pt/C	J_{O2} = 45 $cm^3\ min^{-1}$; 1 M Ethanol; T = 80 ^oC	~21 mW	[5]
Pt-Pd	Polyol and impregnation	C	Nafion® 115	Pt/C	J_{O2} = 120 $cm^3\ min^{-1}$; 1 M Ethanol; T = 90 ^oC	11.97	[4]
	Solid state polymerization (for PNVC-V_2O_5) and $NaBH_4$ reduction	PNVC – V_2O_5	A-006, Tokuyama	Pt/C	J_{O2} = 100 sccm; 1 M Ethanol + 0.5 M NaOH; T = 40 ^oC	30	[6]
Pt-Au	$NaBH_4$ reduction	C	Tokuyama (A-600)	Pt/C	1 M Ethanol + 0.5 M NaOH; T = 20-80 ^oC	35	[2]
	$NaBH_4$ reduction	C	Nafion® 117	Pt/C	J_{O2} = 150 $cm^3\ min^{-1}$; 2 M Ethanol + 2 M KOH; T = 75 ^{o} C (room temperature)	9 (PtAu 70:30)	[3]
Pt-W	Polyol and impregnation	C	Nafion® 115	Pt/C	J_{O2} = 120 $cm^3\ min^{-1}$; 1 M Ethanol; T = 90 ^oC	15.88	[4]
Pt-Ru	commercial	C	PBI/KOH	Pt/C	2 M Ethanol + 2 M KOH; T = 75, 90 ^oC	49.20, 60.95	[7]
	commercial		AAEM-C, AAEM-E, Nafion® 115	Pt black	J_{O2} = 2000 sccm; 2 M Ethanol/ O_2; T = 50 ^oC	1.71, 2.09, 7.42	[8]
	Polyol and impregnation	C	Nafion® 115	Pt/C	J_{O2} = 120 $cm^3\ min^{-1}$; 1 M Ethanol; T = 90 ^oC	28.54	[4]
	commercially		AAEM, Tokuyama	Pt black	Jo_2= 100$cm^3 min^{-1}$; 1 M EtOH + 0.5 M NaOH; T = room temperature	58	[9]
	commercially	C	KOH	MnO_2	2 M Ethanol + 3 M KOH/O_2; T = 25 ^oC	16	[10]

	Commercial	C	PBI/KOH	MnO_2/C	2 M Ethanol + 2 M KOH/air; T = 60 °C	30	[11]
	commercial	C	CEM (Na^+) (Nafion® 112)	Pt/C	2 M Ethanol + 2 M KOH/0.2 MPa O_2; T = 90 °C	58.87	[12]
	commercial	C	AEM (A-201)	Pt/C	1 M Ethanol + 0.25 M KOH/O_2; T = 50 °C	22.4	[13]
	Polyol reduction	C	Nafion® 117, DuPont	Pt/C	J_{O2} = 45 cm^3 min^{-1}; 1 M Ethanol; T = 80 °C	~50 mW	[5]
Pt-Sn	Reducing metal precursors in EG and impregnation	C	Nafion® 115	Pt/C	J_{O2} = 120 cm^3 min^{-1}; 1 M Ethanol; T = 90 °C	52.22	[4]
	Polyol reduction process with EG	C	Nafion® 117, DuPont	Pt/C	J_{O2} = 45 cm^3 min^{-1}; 1 M Ethanol; T = 80 °C	~67 mW	[5]
	*commercial catalysts were used	C	Nafion® 117	Pt/C	J_{O2} = 100 cm^3 min^{-1}; 1 M Ethanol; T = 80 °C	~1.2	[14]
	Mixing solution of metal precursors in EG with carbon slurry then acidifying	C	Nafion® 115	Pt/C	1 M Ethanol; T = 90 °C	61.2 (Pt_2Sn_1)	[15]
	Metal precursors in THF in presence of a surfactant to form colloidal precursor which is then dispersed on carbon powder	C	Nafion® 117	Pt/C	EtoH T = 110 °C	28	[16]
Pd	dimethylformamide co-	C	A-201, Tokuyama	Acta Hypermec^T	J_{O2} = 100 sccm; 3 M Ethanol + 5 M KOH; T = 40 °C	56	[17]

	reduction method			M			
	THF added to a suspension of MWCNT and Pd metal precursor	MWCNT	A-600, Tokuyama	Acta Hypermec ™, K14	J_{O2} = 200 sccm; 10 wt% Ethanol + 2 M KOH; T =20-22, 80 °C	18.4, 73	[18]
	Impregnation/reduction method	C	Nafion® 117 (DuPont)	Pt/C	2 M Ethanol + 6 M NaOH; T = 100 °C	30.1	[19]
	$NaBH_4$ reduction	C	A-201, Tokuyama	Acta Hypermec ™	J_{O2} = 100 sccm; 1, 3 M Ethanol + 1, 5 M KOH/O_2; T = 60 °C	33, 67	[20]
	Impregnation and $NaBH_4$ reduction	C	A-201, Tokuyama	MnO_2	J_{O2} = 300 sccm; 3 M Ethanol + 3 M KOH; T = 60, 70, 80 °C	67, 82, 98	[21]
	Simultaneous reduction method	C	AEM (A-201)	Fe–Co Hypermec ™, K14	J_{O2} = 100 sccm; 1 M Ethanol + 1 M KOH/O_2; T = 100 °C	40	[22]
	$NaBH_4$ reduction	C	PBI/KOH	MnO_2/C	2 M Ethanol + 2 M KOH/air; T = 60 °C	16	[11]
	$NaBH_4$ assisted EG reduction	C	A-600, Tokuyama	Acta Hypermec™, K-14	5 M Ethanol + 5 M KOH; T = 25 °C	16.8	[23]
	$NaBH_4$ reduction	TNTA	A-201, Tokuyama	Fe-Co/C	J_{O2} = 100 cm^3 min^{-1}; 10 wt% Ethanol + 2 M KOH; T = 80 °C	335	[24]
	Electroless method	C	A-600, Tokuyama	Fe–Co/C	J_{O2} = 200 cm^3 min^{-1}; 10 wt% Ethanol + 2 M KOH; T = 25, 80 °C	18, 120	[25]
Pd-Au	dimethylformamide co-reduction method	C	A-201, Tokuyama	Acta HYMPER MEC™	J_{O2} = 100 sccm; 3 M Ethanol + 5 M KOH; T = 40 °C	57.5	[17]
Pd-Ir	$NaBH_4$ reduction	C	Nafion® 117	Pt/C	J_{O2} = 150 cm^3 min^{-1}; 2 M Ethanol + 2 M KOH; T = 70 °C	10 (70:30)	[26]
Pd-Sn	Impregnation/reduction method	C	Nafion® 117, DuPont	Pt/C	2 M Ethanol + 6 M NaOH; T = 100 °C	27.2	[19]
Pd-Ni		C	CEM (Na^+) (Nafion® 211), A-201,	Acta Hypermec ™, K14	3 M Ethanol + 5 M NaOH/O_2; T = 60, 90 °C	100, 135, 90, 115	[27]

			Tokuyama				
		C	CEM (Na^+) (Nafion® 117)	Pt/C	3 M Ethanol + 5 M NaOH/4 M H_2O_2 + 1 M H_2SO_4; T = 60 °C	240	[28]
		C	CEM (Na^+) (Nafion® 117)	Au/Ni–Cr foam	3 M Ethanol + 5 M NaOH/4 M H_2O_2 + 1 M H_2SO_4; T = 60 °C	200	[29]
		C	A-201, Tokuyama	Acta Hypermec ™, K14	3 M Ethanol + 5 M KOH/4 M H_2O_2; T = 80 °C	160	[30]
	Impregnation/reduction method	C	Nafion® 117 (DuPont)	Pt/C	2 M Ethanol + 6 M NaOH; T = 100 °C	19.8	[19]
	Simultaneous reduction method	C	AEM (A-201)	Fe–Co Hypermec ™, K14	J_{O2} = 100 sccm; 1 M Ethanol + 1 M KOH/O_2		[22]
	Mixing PdNi/C with PTFE in EtOH and brushing catalysts on surface of nickel foam	C	A-201, Tokuyama	Fe–Co Hypermec ™, K14	J_{O2} = 100 sccm; 3 M Ethanol + 5 M KOH/O_2; T = 80 °C	130	[31]
			A-600, Tokuyama	Acta Hypermec ™, K14	Ethanol + KOH/O_2; T = 60 °C		[32]
	$NaBH_4$ reduction	C	A-201, Tokuyama	Acta Hypermec ™	J_{O2} = 100 sccm; 1, 3 M Ethanol + 1, 5 M KOH/O_2; T = 60 °C	44, 90	[20]
Pd-Ru	Impregnation and $NaBH_4$ reduction	C	A-201, Tokuyama	MnO_2	J_{O2} = 300 sccm; 3 M Ethanol + 3 M KOH; T = 60, 70, 80 °C	123, 151, 176	[21]
	Impregnation method	C	A-201, Tokuyama	MnO_2	J_{O2} = 300 sccm; 3 M Ethanol + 3 M KOH; T = 80 °C	160	[33]
PtRu black	commercial		PVA/TiO_2	MnO_2/C	2 M Ethanol + 4 M KOH; T = room temperature	8.0	[34]
	commercial		AEM (A-201)	Pt black	J_{O2} = 100 sccm; 1 M Ethanol + 0.5 M KOH/O_2; T = room temperature	58	[9]
	commercial	C	PVA/HAP	MnO_2	2 M Ethanol + 8 M KOH; T = room temperature	10.74	[35]
RuV	H_2 reduction 430 °C	C	PBI/KOH	TMPhP/C	Jo_2 = 200 cm^3 min^{-1}; 2 M EtOH + 3 M NaOH; T = 80 °C	100	[36]

Pt black	commercial		Teflon	MnO_2/C/Ni	2 M Ethanol + 3 M KOH/O_2; T = 25 ^oC		[37]
	commercial		Teflon	MnO_2	2 M Ethanol + 3 M KOH/O_2; T = 45 ^oC	55	[38]
	commercial		KOH	MnO_2	2 M Ethanol + 3 M KOH/O_2; T = 25 ^oC		[10]
Acta Hypermec™	commercial		A-201, Tokuyama	Acta Hypermec™, K14	J_{O2} = 100 sccm; 3 M Ethanol + 7 M KOH/O_2; T = 40 ^oC	60	[39]
	commercial		PVA/TMAPS	Acta Hypermec™, K14	J_{O2} = 50 sccm; 3 M Ethanol + 5 M KOH/ O_2; T = 60 ^oC	50	[40]
	commercial		A-600, Tokuyama	Acta Hypermec™, K14, Pt/C	J_{O2} = 150 cm^3 min^{-1}; 10 wt% Ethanol + 10 wt% KOH/O_2; T = 60 ^oC	80, 72	[41]
NiCo		C	Mg–Al CO32–LDH	FeCo/C	10 wt% Ethanol + 10 wt% KOH/air; T = 80 ^oC	65	[42]
RuNi	H_2 reduction at high temperature	C	CEM (Na^+) (Nafion117)	N_4Co/C	2 M Ethanol + 6 M NaOH/O_2; T = 60 ^oC	~ 40	[43]
	Heat treatment at 430 ^oC with H_2	C	PBI/KOH	CoN_4/C	4 M Ethanol + 8 M KOH/O_2; T = 60 ^oC	~55	[44]
	Synthesis on XC72 soot	C	PBI	Acetylene soot promoted by CoN_4	4 M Ethanol + 8 M KOH; T = 60 ^oC	60	[45]
Ni–Fe–Co HYPERMEC™			A-201, Tokuyama	Fe-Co Hypermec™	J_{O2} = 100 sccm; 1 M Ethanol + 1 M KOH; T = 40 ^oC		[46]
Au	$NaBH_4$ reduction	C	Nafion® 117	Pt/C	J_{O2} = 150 cm^3 min^{-1}; 2 M (1 M) Ethanol + 2 M (1M) KOH; T = 75 ^{o} C (room temperature)	1.6 (PtAu 70:30)	[3]
PdNiSn	Impregnation/reduction method	C	Nafion® 117 (DuPont)	Pt/C	2 M Ethanol + 6 M NaOH; T = 100 ^oC	27.1	[19]
PtRuW	Polyol impregnation	C	Nafion® 115	Pt/C	J_{O2} = 120 cm^3 min^{-1}; 1 M Ethanol; T = 90 ^oC	38.54	[4]

Pd-(Ni-Zn)	Spontaneous deposition	C	A-006, Tokuyama	Fe–Co Hypermec ™, K-14	Jo_2 = 200 cm^3 min^{-1}; 10 wt% Ethanol + 2 M KOH; T = 20, 80 °C	58, 170	[47]
PtRuMo	Polyol impregnation	C	Nafion® 115	Pt/C	J_{O2} = 120 cm^3 min^{-1}; 1 M Ethanol; T = 90 °C	23.34	[4]
Pd-$La(OH)_3$	Microwave	C	AEM, Qianqiu Corporation	MnO_2/C	6 M Ethanol + 6 M KOH, T = room temperature		[48]
$Pd(DBA)_2$	commercial		A-600, Tokuyama	Fe–Co Hypermec ™	5 wt% Ethanol + 5 wt% KOH, T = room temperature	31	[49]
Pd-CeO_2	Electroless method	C	A-600, Tokuyama	Fe–Co/C	J_{O2} = 200 cm^3 min^{-1}; 10 wt% Ethanol + 2 M KOH; T = 25, 80 °C	66, 140	[25]

Legend: C = carbon, CMS = carbon microspheres, MWCNT = multi-walled carbon nanotubes, EG = ethylene glycol, TNTA = Titanium nanotube arrays, NP = nanoparticles

Table A.1 References

1 A. Verma, A. K. Jha and S. Basu, *J. Power Sources*, 2005, **141**, 30–34.
2 A. Dutta, A. Mondal and J. Datta, *J. Power Sources*, 2015, **283**, 104–114.
3 S. G. da Silva, J. C. M. Silva, G. S. Buzzo, R. F. B. De Souza, E. V. Spinacé, A. O. Neto and M. H. M. T. Assumpção, *Int. J. Hydrog. Energy*, 2014, **39**, 10121–10127.
4 W. Zhou, *Appl. Catal. B Environ.*, 2003, **46**, 273–285.
5 I. Kim, O. H. Han, S. A. Chae, Y. Paik, S.-H. Kwon, K.-S. Lee, Y.-E. Sung and H. Kim, *Angew. Chem. Int. Ed.*, 2011, **50**, 2270–2274.
6 J. Datta, A. Dutta and M. Biswas, *Electrochem. Commun.*, 2012, **20**, 56–59.
7 H. Hou, G. Sun, R. He, Z. Wu and B. Sun, *J. Power Sources*, 2008, **182**, 95–99.
8 J. R. Varcoe, R. C. T. Slade, E. L. H. Yee, S. D. Poynton and D. J. Driscoll, *J. Power Sources*, 2007, **173**, 194–199.
9 N. Fujiwara, Z. Siroma, S. Yamazaki, T. Ioroi, H. Senoh and K. Yasuda, *J. Power Sources*, 2008, **185**, 621–626.
10 A. Verma and S. Basu, *J. Power Sources*, 2007, **174**, 180–185.
11 H. Hou, S. Wang, Q. Jiang, W. Jin, L. Jiang and G. Sun, *J. Power Sources*, 2011, **196**, 3244–3248.
12 H. Hou, S. Wang, W. Jin, Q. Jiang, L. Sun, L. Jiang and G. Sun, *Int. J. Hydrog. Energy*, 2011, **36**, 5104–5109.
13 M. Unlu, D. Abbott, N. Ramaswamy, X. Ren, S. Mukerjee and P. A. Kohl, *J Electrochem Soc*, 2011, **158**, B1423–B1431.
14 M. H. M. T. Assumpção, J. Nandenha, G. S. Buzzo, J. C. M. Silva, E. V. Spinacé, A. O. Neto and R. F. B. De Souza, *J. Power Sources*, 2014, **253**, 392–396.
15 W. J. Zhou, S. Q. Song, W. Z. Li, Z. H. Zhou, G. Q. Sun, Q. Xin, S. Douvartzides and P. Tsiakaras, *J. Power Sources*, 2005, **140**, 50–58.
16 C. Lamy, S. Rousseau, E. M. Belgsir, C. Coutanceau and J.-M. Léger, *Electrochimica Acta*, 2004, **49**, 3901–3908.
17 J. B. Xu, T. S. Zhao, S. Y. Shen and Y. S. Li, *Int. J. Hydrog. Energy*, 2010, **35**, 6490–6500.
18 V. Bambagioni, C. Bianchini, A. Marchionni, J. Filippi, F. Vizza, J. Teddy, P. Serp and M. Zhiani, *J. Power Sources*, 2009, **190**, 241–251.
19 L. P. R. Moraes, B. R. Matos, C. Radtke, E. I. Santiago, F. C. Fonseca, S. C. Amico and C. F. Malfatti, *Int. J. Hydrog. Energy*, 2016, **41**, 6457–6468.
20 S. Y. Shen, T. S. Zhao, J. B. Xu and Y. S. Li, *J. Power Sources*, 2010, **195**, 1001–1006.
21 L. Ma, H. He, A. Hsu and R. Chen, *J. Power Sources*, 2013, **241**, 696–702.
22 S. Y. Shen, T. S. Zhao and Q. X. Wu, *Int. J. Hydrog. Energy*, 2012, **37**, 575–582.
23 R. M. Modibedi, T. Mehlo, K. I. Ozoemena and M. K. Mathe, *Int. J. Hydrog. Energy*, 2015, **40**, 15605–15612.
24 Y. Chen, M. Bellini, M. Bevilacqua, P. Fornasiero, A. Lavacchi, H. A. Miller, L. Wang and F. Vizza, *ChemSusChem*, 2015, **8**, 524–533.
25 V. Bambagioni, C. Bianchini, Y. Chen, J. Filippi, P. Fornasiero, M. Innocenti, A. Lavacchi, A. Marchionni, W. Oberhauser and F. Vizza, *ChemSusChem*, 2012, **5**, 1266–1273.
26 A. O. Neto, S. G. da Silva, G. S. Buzzo, R. F. B. de Souza, M. H. M. T. Assumpção, E. V. Spinacé and J. C. M. Silva, *Ionics*, 2015, **21**, 487–495.
27 L. An and T. S. Zhao, *Energy Env. Sci*, 2011, **4**, 2213–2217.
28 L. An, T. S. Zhao, R. Chen and Q. X. Wu, *J. Power Sources*, 2011, **196**, 6219–6222.
29 L. An, T. S. Zhao and J. B. Xu, *Int. J. Hydrog. Energy*, 2011, **36**, 13089–13095.

30 L. An, T. S. Zhao, L. Zeng and X. H. Yan, *Int. J. Hydrog. Energy*, 2014, **39**, 2320–2324.
31 Y. S. Li and T. S. Zhao, *Int. J. Hydrog. Energy*, 2011, **36**, 7707–7713.
32 Y. S. Li, T. S. Zhao and R. Chen, *J Power Sources*, 2011, **196**, 133–139.
33 L. Ma, A. Hsu and R. Chen, *ECS Trans.*, 2013, **58**, 1321–1326.
34 C.-C. Yang, S.-J. Chiu, K.-T. Lee, W.-C. Chien, C.-T. Lin and C.-A. Huang, *J. Power Sources*, 2008, **184**, 44–51.
35 C.-C. Yang, Y.-J. Lee, S.-J. Chiu, K.-T. Lee, W.-C. Chien, C.-T. Lin and C.-A. Huang, *J. Appl. Electrochem.*, 2008, **38**, 1329–1337.
36 A. D. Modestov, M. R. Tarasevich, A. Y. Leykin and V. Y. Filimonov, *J. Power Sources*, 2009, **188**, 502–506.
37 A. Verma and S. Basu, *J. Power Sources*, 2005, **145**, 282–285.
38 D. Gaurava, A. Verma, D. K. Sharma and S. Basu, *Fuel Cells*, 2010, **10**, 591–596.
39 Y. S. Li, T. S. Zhao and Z. X. Liang, *J. Power Sources*, 2009, **187**, 387–392.
40 E. D. Wang, T. S. Zhao and W. W. Yang, *Int. J. Hydrog. Energy*, 2010, **35**, 2183–2189.
41 M. Zhiani, H. A. Gasteiger, M. Piana and S. Catanorchi, *Int. J. Hydrog. Energy*, 2011, **36**, 5110–5116.
42 A. Hayashi, M. Tatsumisago, K. Tadanaga and Y. Furukawa, *Adv. Mater.*, 2010, **22**, 4401–4404.
43 A. Y. Tsivadze, M. R. Tarasevich, B. N. Efremov, N. A. Kapustina and P. V. Mazin, *Dokl. Phys. Chem.*, 2007, **415**, 234–236.
44 M. R. Tarasevich, V. A. Bogdanovskaya and P. V. Mazin, *Russ. J. Electrochem.*, 2010, **46**, 542–551.
45 A. Y. Tsivadze, M. R. Tarasevich, V. N. Andreev and V. A. Bogdanovskaya, *Russ. J. Gen. Chem.*, 2007, **77**, 783–789.
46 Y. S. Li, T. S. Zhao and Z. X. Liang, *J Power Sources*, 2009, **190**, 223–229.
47 C. Bianchini, V. Bambagioni, J. Filippi, A. Marchionni, F. Vizza, P. Bert and A. Tampucci, *Electrochem. Commun.*, 2009, **11**, 1077–1080.
48 H. Yu, D. Zhou and H. Zhu, *J. Solid State Electrochem.*, 2014, **18**, 125–131.
49 M. Zhiani, S. Majidi, H. Rostami and M. M. Taghiabadi, *Int. J. Hydrog. Energy*, 2015, **40**, 568–576.

Appendix

1 Supporting information chapter four

Figure A1-1 demonstrates that setting the angle of incidence to the range between 60 and 64 degrees and keeping the thin-cavity distance as small as possible should yield the best MSEFS at the surface. The obtained values of the MSEFS are about twice lower compared to highly reflective metal surfaces for which MSEFS reaches 4x enhancement. However, the values close to the magnitude of 2 indicate that there should be at least 2x enhancements with respect to the incident light.

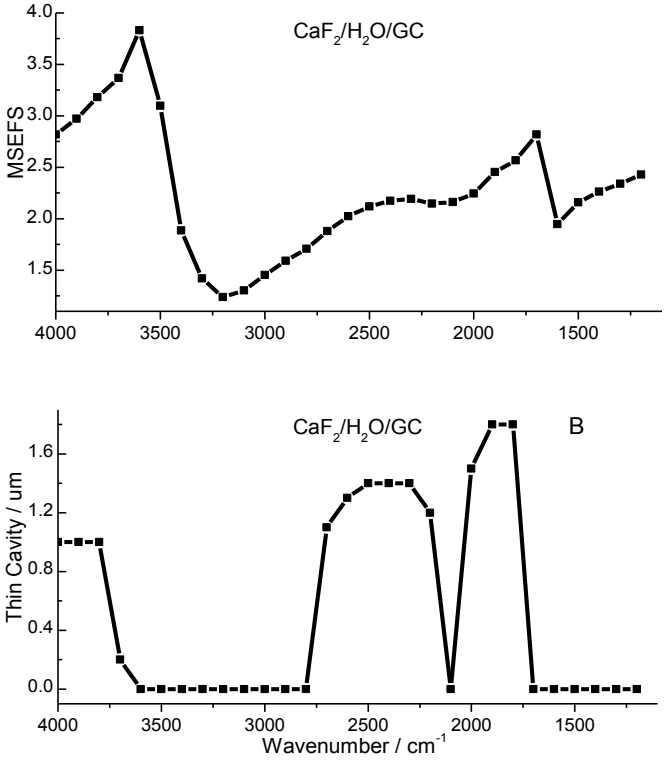

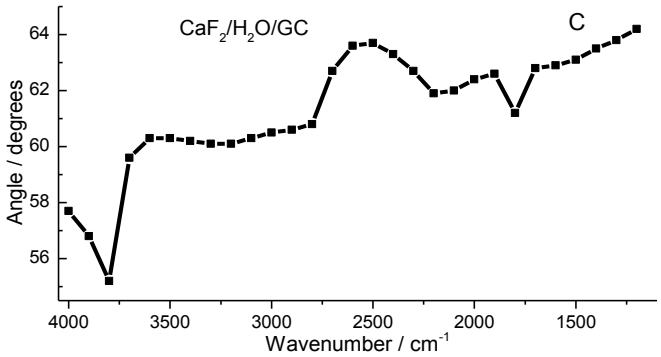

Figure A1-1: Coordinates of the global maximum in the MSEFS for $CaF_2/H_2O/GC$ system calculated in the mid infrared region for the beam of ±3º convergence (Figures with values obtained with a convergence of 5 was used.) Panels A, B, and C show the optimum values of the MSEFS, the electrolyte thin cavity thickness and the angle of incidence, respectively.

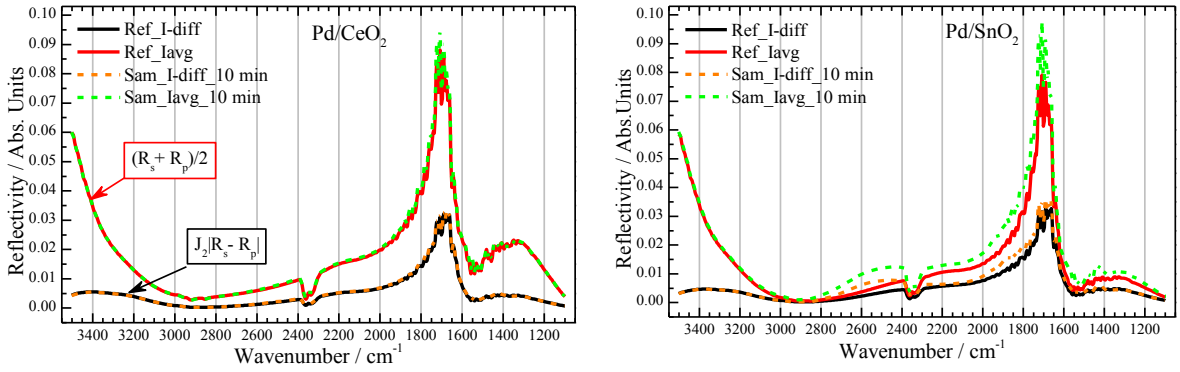

(a) (b)

Figure A1-2: The sample and reference reflectivity spectra data for ethanol electrooxidation on Pd/CeO_2 and Pd/SnO_2. The reflectivities for Pd/TiO_2 and Pd/C were similar to what is shown here.

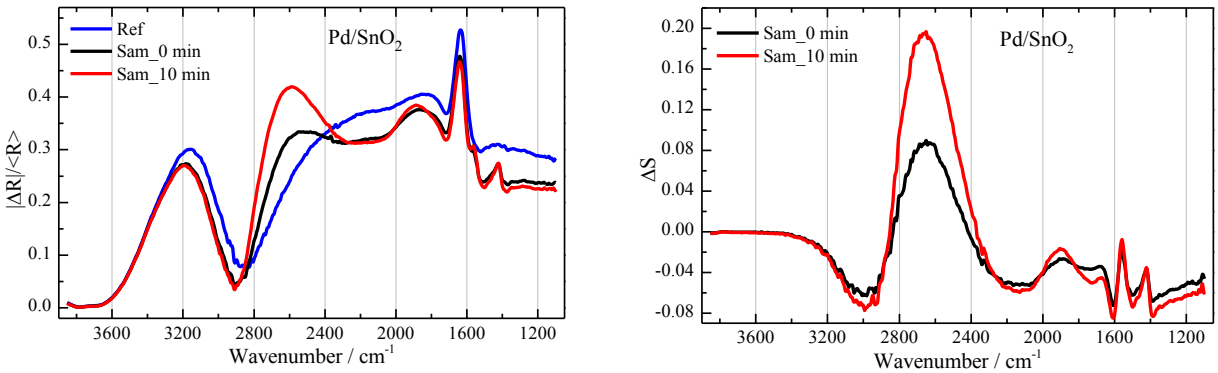

(a) (b)

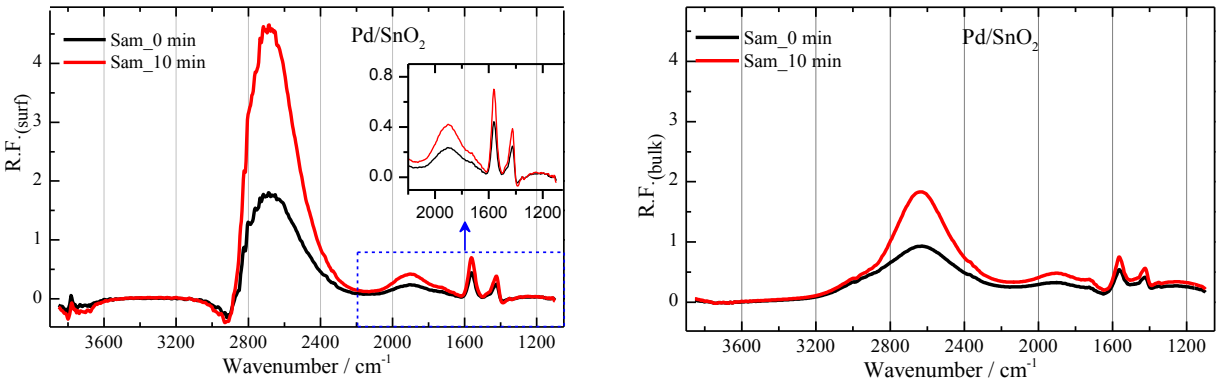

Figure A1-3: Processed spectra for ethanol electrooxidation on Pd/SnO_2 to show reproducibility of spectra features reported. Sample spectra were recorded at -0.15 V/ Hg/HgO in 1M (KOH+EtOH) electrolyte.

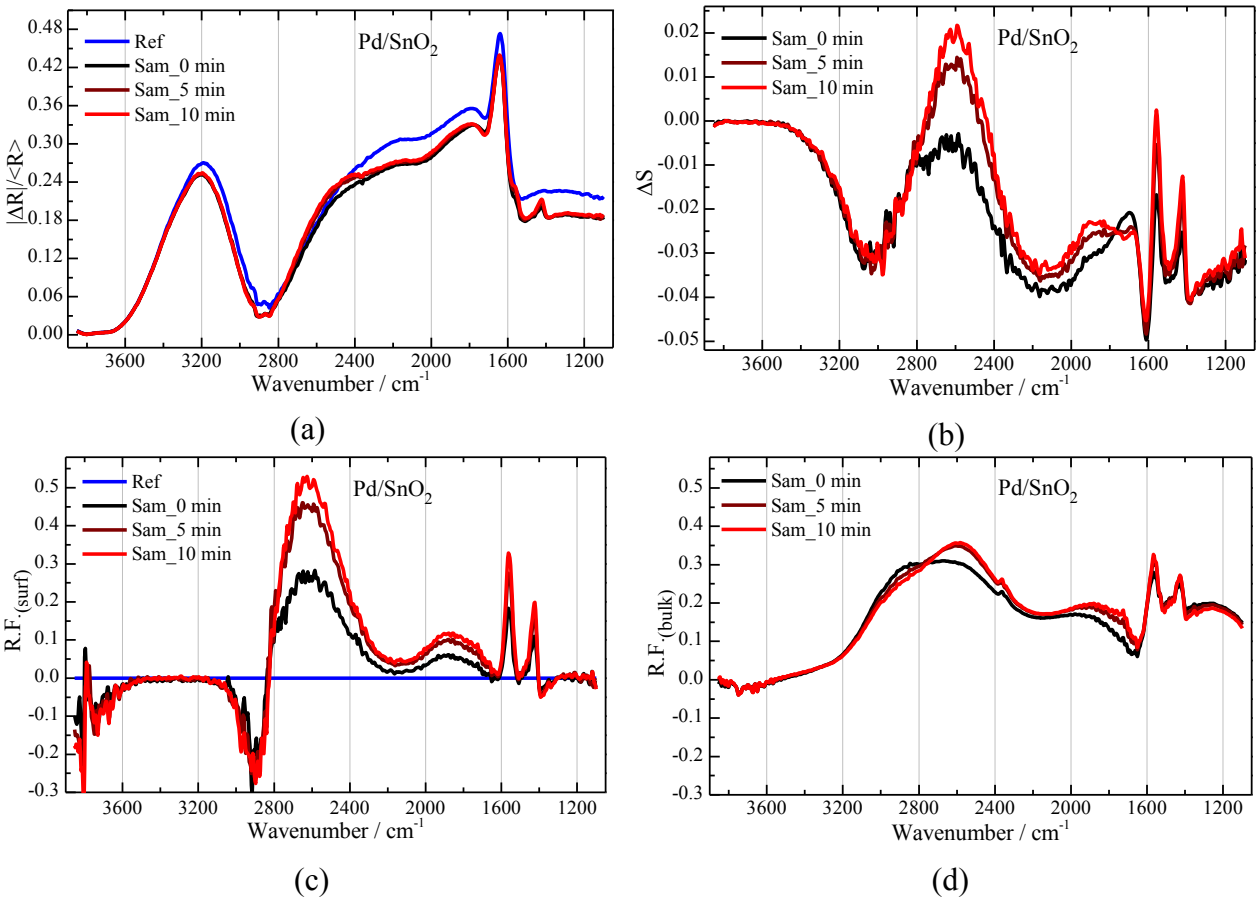

Figure A1-4: Processed spectra for ethanol electrooxidation on Pd/SnO_2 to show reproducibility of spectra features reported. Sample spectra were recorded at -0.15 V/ Hg/HgO in (1M KOH + 0.2M EtOH) electrolyte.

2 Supporting information for chapter six

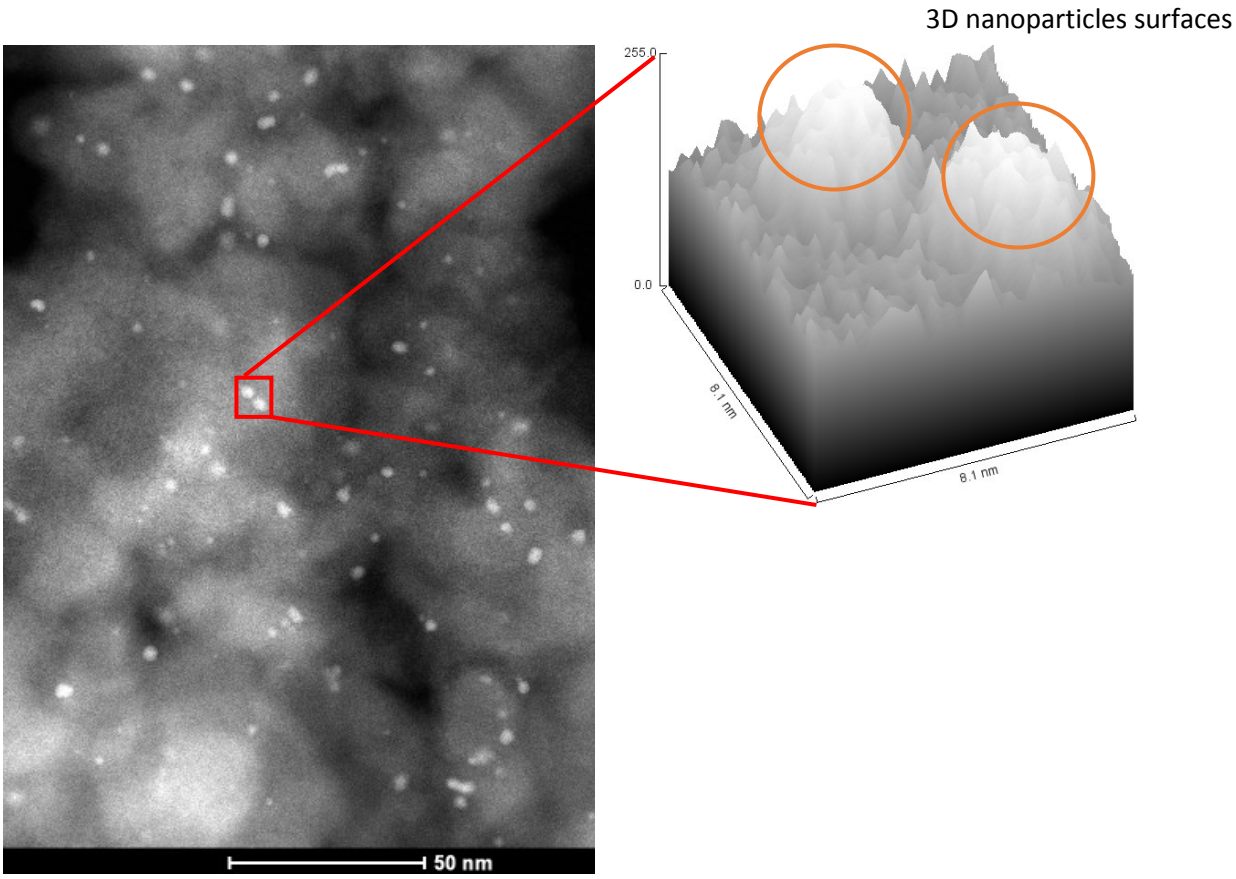

Figure A2-1: STEM micrographs for $Pd_{95}Ru_5/C$ with a zoomed in 3D surface to show the texture of the nanoparticles

Figure A2-2 provides evidence that that 100% Ru nanoparticles are not good electrocatalyst for ethanol oxidation. The insert figure show that glassy carbon does not oxidize ethanol in the conditions used in this study.

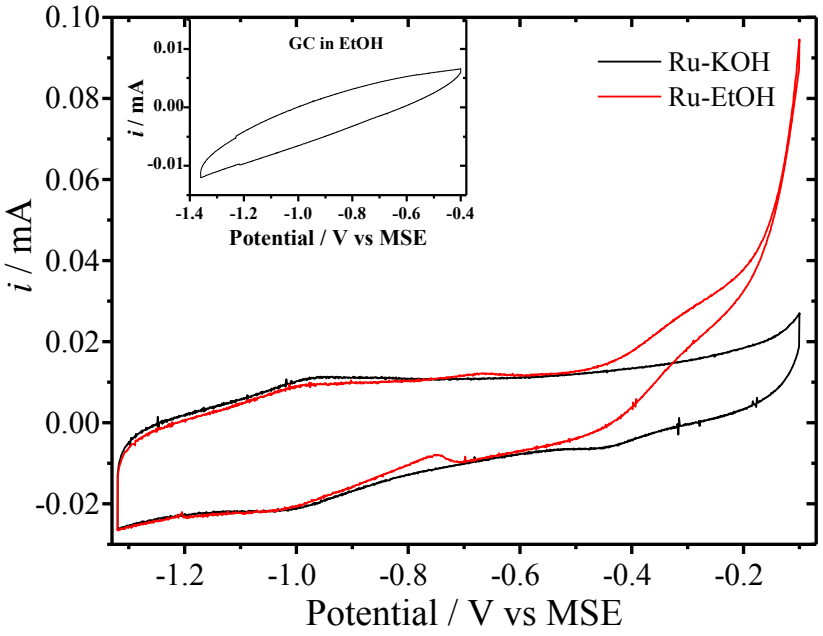

Figure A2-2: CVs for Ru/C in 1M KOH with and without ethanol, scan rate 20 mVs^{-1}. Insert is CV from glassy carbon electrode without a catalyst in 1M KOH+1M ethanol.

3 Supporting information for chapter seven

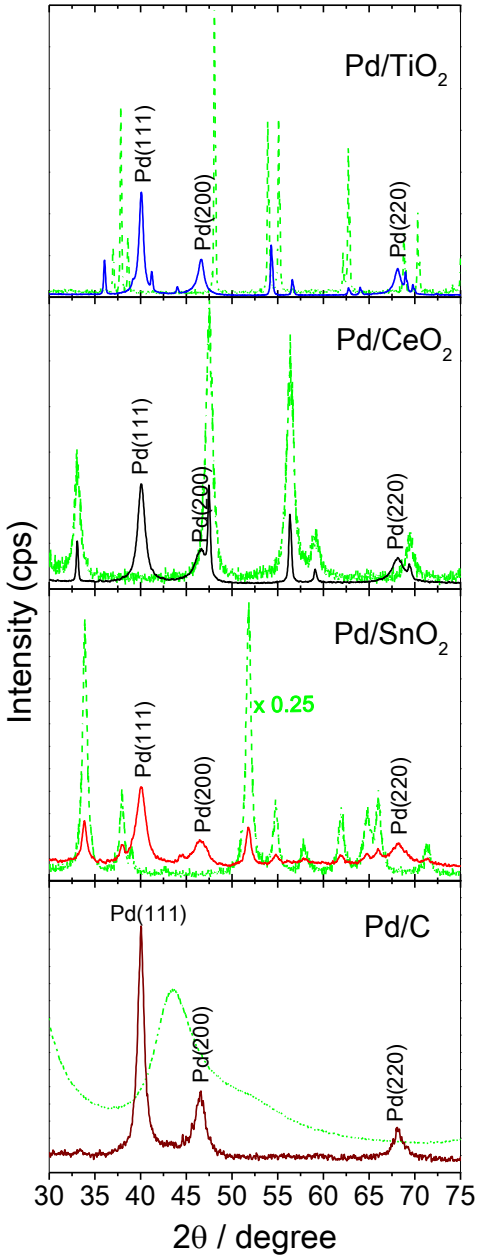

Figure A3-1: XRD patterns of supported Pd nanoparticles (solid lines) and pure support (dashed green lines) of the supports tested as shown. The face-centred cubic (fcc) diffractions for Pd structure are shown

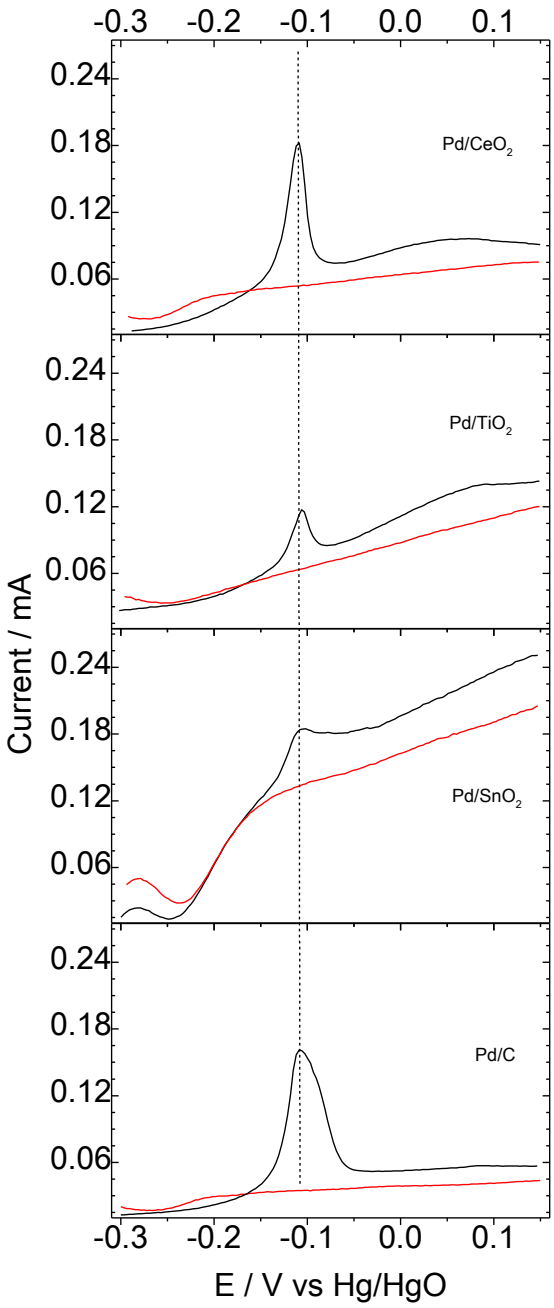

Figure A3-2: The first (black lines) and second (red lines) cycles (forward scan) of CO stripping voltammograms of the four catalysts as indicated at $v = 25$ mV s^{-1}. The area between the two voltammograms was used to calculate the electrochemical active surface area (ECSA).

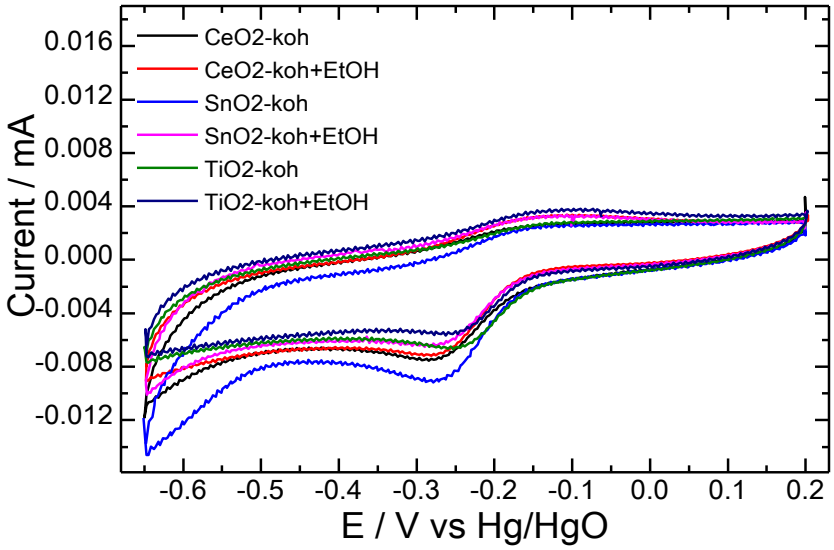

Figure A3-3: CVs of the supports in 1M KOH and in 1M (KOH + EtOH) confirming that the supports have no catalytic activity for ethanol electrooxidation in alkaline media

4 Supporting information for chapter eight

4.1 Physical characterization of Pd/C nanoparticles

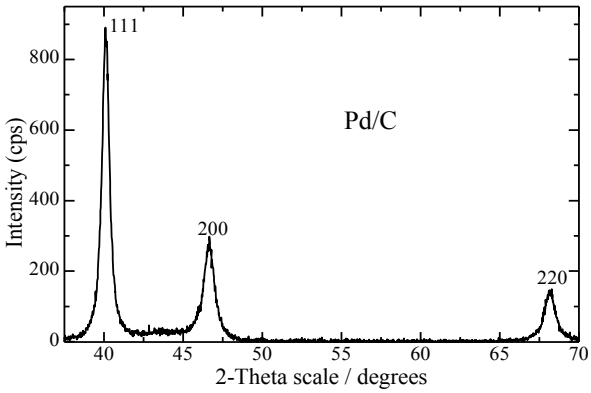

(a)

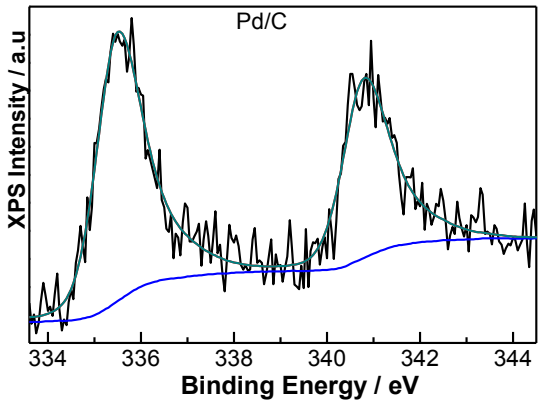

(b)

Figure A4-1: (a) the X-ray diffraction pattern and (b) the Pd3d peak of the XPS spectrum

4.2 Infrared Spectra

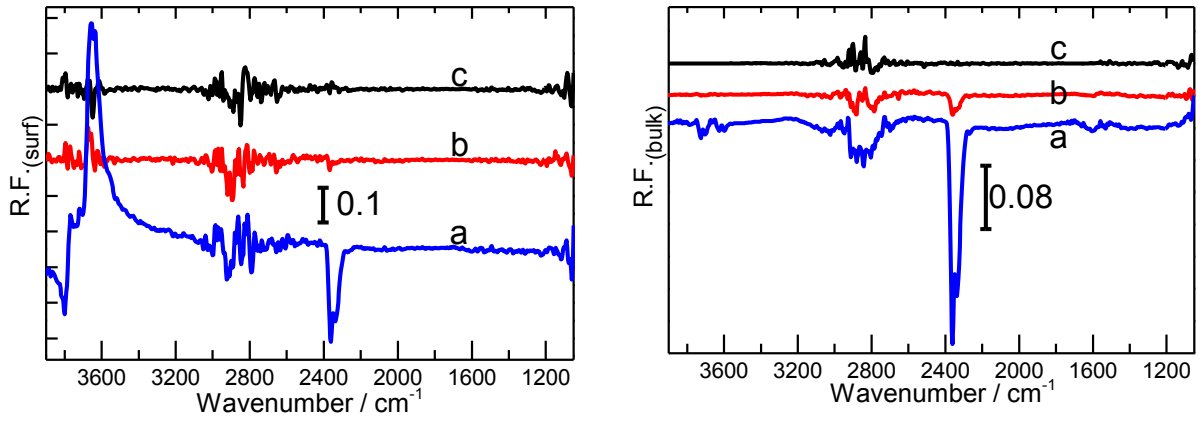

Figure A4-2: Background PM-IRRAS spectra of Pd/C in 1M (KOH+EtOH) at open circuit potentials (OCP) tracking the level of CO_2 in the optical path after; (a) 2.5 hrs, (b) 30 minutes, and (c) 3 minutes before measurements were commenced. The reference spectrum is the last OCP spectrum before measurements were taken and is the same reference used to process sample spectra discussed in main text. The left panel is for surface species while the right panel is for atmospheric/liquid-phase species.

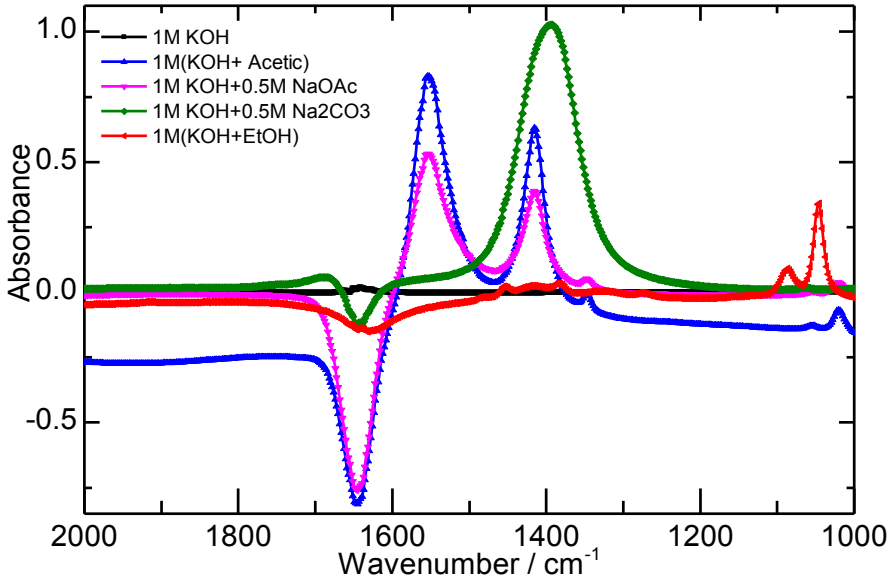

Figure A4-3: Transmission infrared spectra for 1M KOH and 1M KOH mixed with 1M acetic acid (CH_3COOH), 0.5M sodium acetate (CH_3COONa), 0.5M sodium carbonate (Na_2CO_3), and 1M ethanol (C_2H_5OH). The transmission spectra were collected after a background correction of 1M KOH hence a straight line is expected for 1M KOH solution. The negative peak at 1645 cm^{-1}

corresponds to decreased water vibrations due to addition of the respective organic species. The spectra intensities were normalized to the same scale as described in text for easy comparison

Figure A4-4 is to show what species would be contributing to the broad peak observed between 2400 cm^{-1} and 2700 cm^{-1} of the PM-IRRAS spectra reported in the main text Figure 2. Figure A4-4 (a) shows the DFT simulated IR spectra of potential ethanol electrooxidation intermediates. It shows that ethoxy ($CH_3CH_2O^-$) and geminal-diol are the potential candidates eliminating acetaldehyde and acetic acid. However, the experimental transmission spectrum for acetic [Figure A4-4 (b), blue curve] shows that acetic acid has three overlapping peaks at 2400 – 2700 cm^{-1}. In summary, the potential candidates for the broad peak at 2400 – 2700 cm^{-1} would be ascribed to a combination of ethoxy, geminal-diol, and acetic acid.

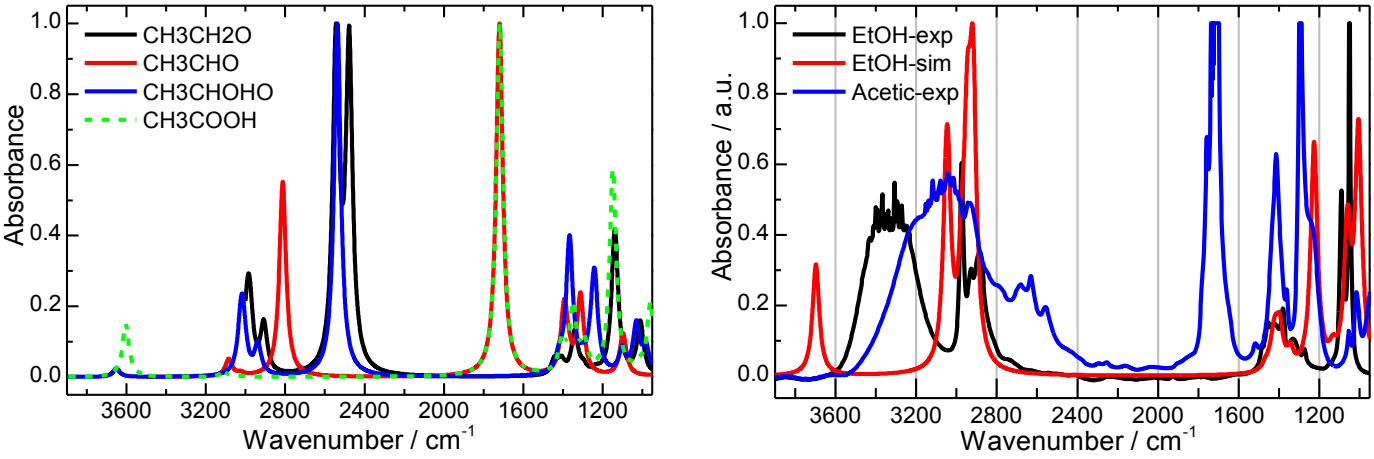

(a) (b)

Figure A4-4: The simulated infrared spectra for ethoxy (CH_3CH_2O), acetaldehyde (CH_3CHO), hydrated acetaldehyde (CH_3CHOHO), and acetic acid (CH_3COOH) (a), and the transmission spectra for ethanol (EtOH-exp) and acetic acid (Acetic-exp) together with the simulated spectra for ethanol (EtOH-sim) (b). See text for details.

4.3 Optimized geometry structures of ethanol intermediates on Pd surfaces

Pd(111): The most important intermediates on Pd(111) surface are depicted in Figure A4-5. The reactant, ethanol, adsorbs at the top site via the lone pair electrons of the oxygen atom, with the O–H bond positioned almost parallel to the surface. The first oxidation of ethanol [Figure A4-5(a)] leads to three possible intermediates: 1-hydroxyethyl [CH_3CHOH, Figure A4-5(b)], 2-hydroxyethyl [CH_2CH_2OH, Figure A4-5(c)], and ethoxy [CH_3CH_2O, Figure A4-5(d)]. While the dehydrogenated carbon atoms bind on top sites, oxygen prefers to bind to a bridge site. The second oxidation step towards acetic acid might lead to one of four intermediates, which are obtained either by removing a proton and an electron (we will use the term "dehydrogenation" indistinguishably) or by the addition of a hydroxyl group, i.e., forming a C–OH bond. Acetaldehyde adsorbs on the surface as C(top) O(bridge) [Figure A4-5(g)] while its hydrate, a gem-diol, adsorbs as expected via the oxygen atoms of the hydroxyl groups on top sites [Figure A4-5 (e)]. The enol adsorbs on a bridge site (di-sigma) [Figure A4-5(h)]. The only species that has no equivalent in solution is 1-hydroxyethylidene [CH_3COH, Figure A4-5(f)], which adsorbs on a top site, similar to Pt(111).[13] Although the 3rd oxidation step (+3) could lead to a multitude of intermediates, the ones that can subsequently form acetic acid in one elementary step are limited: $CH_3C(OH)_2$, CH_3CO and $CH_3CHO(OH)$. The latter is clearly too high in energy (0.38 eV higher than $CH_3C(OH)_2$) and thus is discarded from this study. The acetyl [CH_3CO, Figure A4-5(i)] adsorbs in a C(top) O(top) mode, i.e., across a bridge site. Unsurprisingly, the de-hydrogenated geminal-diol [$CH_3C(OH)_2$, Figure A4-5(j)] adsorbs in a C(top) mode. At the 4th degree of oxidation, acetic acid [CH_3COOH, Figure A4-5(k)], adsorbs perpendicular to the metal surface, i.e., with one oxygen in a top position and the OH pointing into a hollow site. Last, at the 5th degree of oxidation, the adsorption of an acetate [CH_3COO, Figure A4-5(l)] species is of some interest as well in alkaline media, although it would need to be formally reduced in a pure electron transfer reaction before desorbing into solution. The CH_3COO adsorbs in the bidentate mode with both oxygen atoms in a top position, characteristic for yloxy carbonyls.

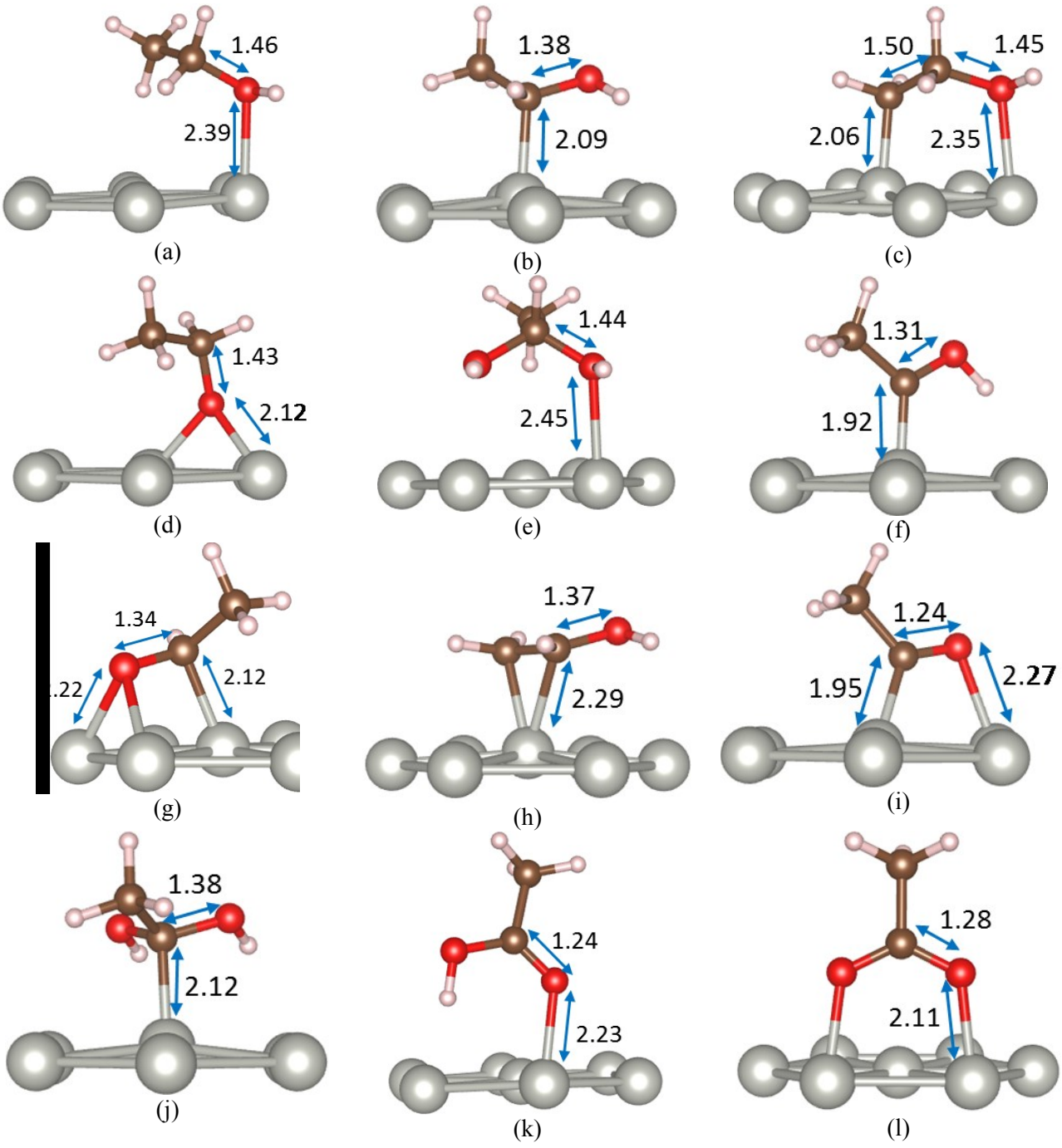

Figure A4-5: The side views of the most stable geometric structures of intermediates involved in ethanol electrooxidation on Pd(111) leading to acetate formation. The intermediates are presented in sequence at each oxidation step. Main distances in ethanol gas phase for reference: C–C = 1.51 Å, C–O = 1.44 Å, C–H = 1.10 Å, O–H = 0.97 Å.

Pd(100): The most important intermediates on Pd(100) surface are depicted in Figure A4-6.

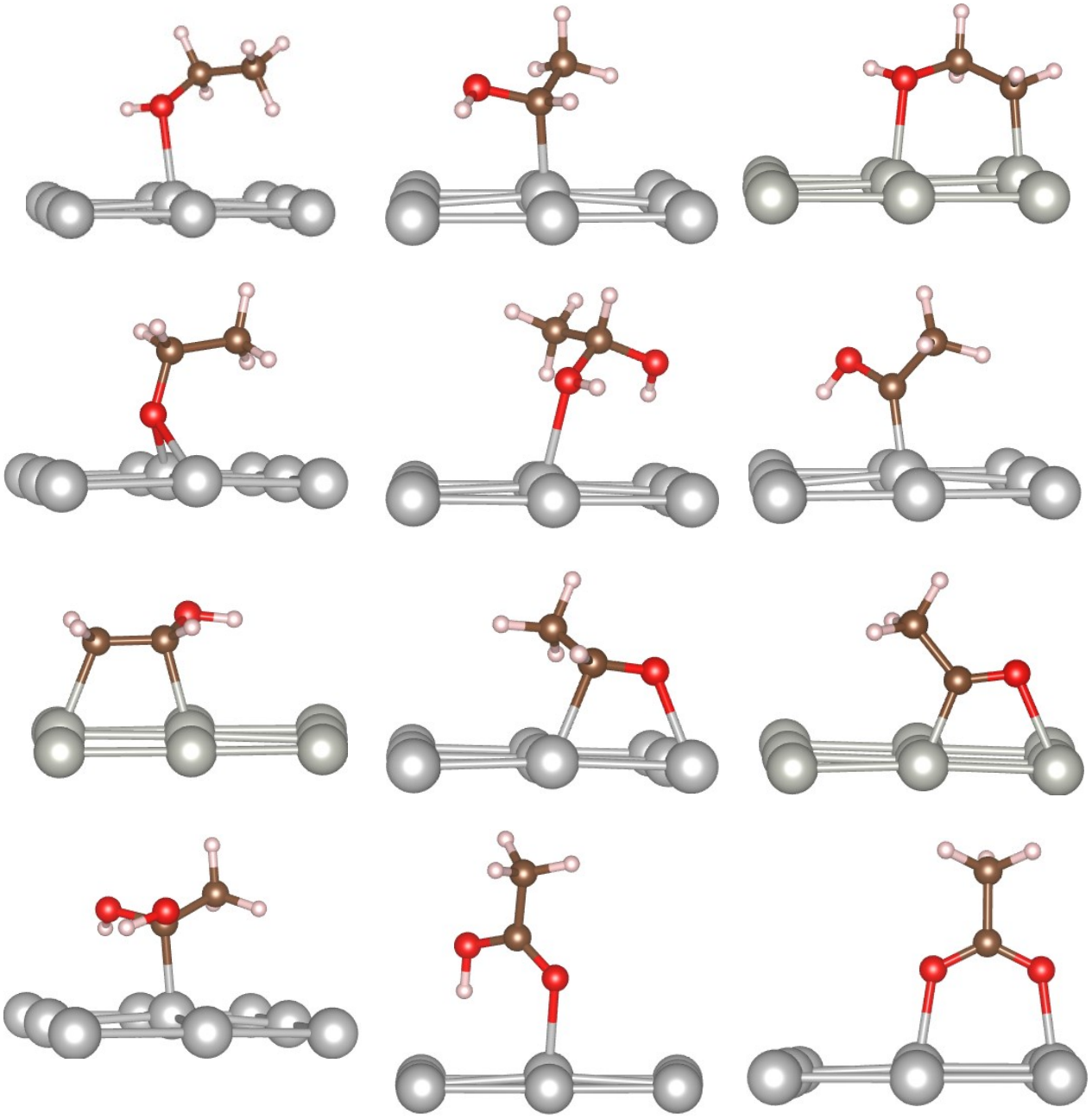

Figure A4-6: The side views of the most stable geometric structures of intermediates involved in ethanol electrooxidation on Pd(100) leading to acetate formation. The species are presented in order of stability as shown in Figure 4 (b).

5 Supporting information for chapter nine

Table A5-1: Summary of the DFT adsorption energies of important intermediates for EOR

Surface	C_{ads}		O_{ads}	CO_{ads}		CH_{3ads}		CH_3CO_{ads}		CH_3COO
	eV	site	eV	eV	site	eV	site	eV	Mode	eV
Ag (111)	-3.65 -3.60	fcc hcp	-3.84	-0.18	fcc	-1.00	top	-0.89	n_1u_1(C)	-2.16
Au (111)	-4.66 -4.56	fcc hcp	-3.43	-0.30	fcc	-1.31	top	-1.29	n1u1(C)	-1.63
Cu (111)	-5.04 -5.00	fcc hcp	-4.98	-0.90	fcc	-1.28	top	-1.28	n1u1(C)	-2.55
Pd (111)	-7.13	hcp	-4.76	-2.04	fcc	-1.76	top	-2.11	n1u1(C)	-2.28
Pt (111)	-7.34 -7.23	fcc hcp	-4.72	-1.84	fcc	-2.07	top	-2.35	n1u1(C)	-2.29
Ir (111)	-7.46	hcp	-5.16	-1.74	brg	-1.97	top	-2.56	n1u1(C)	-2.78
Ni (111)	-6.85	hcp	-5.70	-1.90	fcc	-1.60	top	-2.03	n1u1(C)	-2.76
Pb (111)	-4.30	hcp	-4.92	n/a	n/a	-1.15	top	-0.84	n_1u_1(C)	-2.59
Rh (111)	-7.49	hcp	-5.47	-1.97	fcc	-1.84	top	-2.47	n1u1(C)	-2.79
Cd (0001)	-3.81	hcp	-4.68	n/a	n/a	-1.12	top	-0.84	n_1u_1(C)	-2.52
Co (0001)	-7.14	hcp	-6.06	-1.75	fcc	-1.48	fcc	-2.08	n_1u_1(C)	-2.92
Hf (0001)	-8.16	hcp	-8.97	-1.73	hcp	-2.63	fcc	-4.85	n_2u_4	-4.57
Os (0001)	-7.86	hcp	-6.14	-2.04	top	-1.83	top	-2.51	n_1u_1(C)	-3.27
Re (0001)	-7.55	hcp	-6.91	-1.61	fcc	-1.48	top	-2.40	n1u1(C)	-3.28
Ru (0001)	-6.88	hcp	-6.32	-1.85	hcp	-1.72	top	-2.35	n1u1(C)	-3.19
Sc (0001)	-7.92	hcp	-9.73	-3.58	n_2u_4	-2.73	fcc	-4.98	n_2u_4	-5.09
Ti (0001)	-7.91	hcp	-8.77	-1.90	hcp	-2.70	fcc	-4.94	n_2u_4	-4.52
Tl (0001)	-3.84	hcp	-4.87	-0.17	hcp	-0.88	top	-0.68	n_1u_1(C)	-2.43
Y (0001)	-7.77	hcp	-9.47	-3.13	n_2u_4	-2.53	fcc	-4.43	n_2u_4	-4.97
Zn (0001)	-4.24	hcp	-5.18	-0.07	top	-1.12	top	-0.84	n_1u_1(C)	-2.58

Table A5-2: Detailed bond analysis for CH_3CO to explain observed trends

Surface	CH_3CO Bond distances in Angs			
	Atomic distances		Calculated	
	M – C	M – O	M – C	M – O
Ag (111)	2.21	2.18	2.21	2.90
Au (111)	2.21	2.18	2.12	3.49
Cu (111)	2.05	2.02	1.96	2.16
Pd (111)	2.14	2.11	1.95	2.27
Pt (111)	2.16	2.13	1.96	2.23
Ir (111)	2.13	2.10	1.98	2.15
Ni (111)	2.02	1.99	1.85	2.00
Pb (111)	2.52	2.49	2.51	3.14
Rh (111)	2.11	2.08	1.95	2.14
Cd (0001)	2.29	2.26	2.31	2.66
Co (0001)	2.02	1.99	1.87	2.01
Hf (0001)	2.36	2.33	2.34	2.21
Os (0001)	2.12	2.09	2.04	2.15
Re (0001)	2.14	2.11	2.05	2.15
Ru (0001)	2.11	2.08	2.01	2.16
Sc (0001)	2.41	2.38	2.25	2.12
Tc (0001)	2.12	2.09	2.04	2.14
Ti (0001)	2.24	2.21	2.15	2.05
Tl (0001)	2.48	2.45	2.56	2.93
Y (0001)	2.59	2.56	2.45	2.26
Zn (0001)	2.14	2.11	2.08	2.34

Table A5-3: Reaction energies of the key intermediates during ethanol electrooxidation at 0 and 0.26 V/ RHE

Metal (facet)	CH_3CO from ethanol		CH_3COO from ethanol		CH_3COO from acetyl		CH_3 + CO
	0 V	**0.26 V**	**0 V**	**0.26 V**	**0 V**	**0.26 V**	
Ag (111)	1.79	1.01	0.96	-0.34	-0.83	-1.35	0.80
Au (111)	1.38	0.60	1.49	0.19	0.10	-0.42	0.77
Cu (111)	1.40	0.62	0.57	-0.73	-0.84	-1.36	0.19
Pd (111)	0.57	-0.21	0.84	-0.46	0.27	-0.25	-0.60
Pt (111)	0.33	-0.45	0.83	-0.47	0.50	-0.02	-0.48
Ir (111)	0.12	-0.66	0.34	-0.96	0.22	-0.30	-0.09
Ni (111)	0.65	-0.13	0.36	-0.94	-0.29	-0.81	-0.37
Pb (111)	1.84	1.06	0.52	-0.78	-1.32	-1.84	--
Rh (111)	0.21	-0.57	0.33	-0.97	0.12	-0.40	-0.24
Cd (0001)	1.84	1.06	0.60	-0.70	-1.24	-1.76	--
Co (0001)	0.60	-0.18	-0.20	-1.10	-0.40	-0.92	-0.05
Hf (0001)	-2.17	-2.95	-1.46	-2.76	0.72	0.20	1.59
Os (0001)	0.17	-0.61	-0.15	-1.45	-0.32	-0.84	-0.27
Re (0001)	0.28	-0.50	-0.16	-1.46	-0.44	-0.96	0.40
Ru (0001)	0.33	-0.45	-0.07	-1.37	-0.41	-0.93	-0.12
Sc (0001)	-2.30	-3.08	-1.97	-3.27	0.33	-0.19	-0.24
Ti (0001)	-2.26	-3.04	-1.41	-2.71	0.85	0.33	1.44
Tl (0001)	2.00	1.22	0.69	-0.61	-1.31	-1.83	--
Y (0001)	-1.75	-2.53	-1.85	-3.15	-0.10	-0.62	-0.14
Zn (0001)	1.84	1.06	0.54	-0.76	-1.30	-1.82	0.75